Structure and assembly of nuclear pore complexes by correlative AFM and super-resolution microscopy

Anthony Vial

THÈSE POUR OBTENIR LE GRADE DE DOCTEUR DE L'UNIVERSITÉ DE MONTPELLIER

En Biologie-Santé, spécialité Biophysique

École doctorale Sciences Chimiques et Biologiques pour la Santé (CBS2 n°168)

Unité de recherche Centre de Biologie Structurale CNRS UMR5048 – UM – INSERM U 1054

Structure and assembly of nuclear pore complexes by correlative AFM and super-resolution microscopy

Présentée par Anthony Vial
Le 9 décembre 2021

Sous la direction de : Dr Christine Doucet et Dr Pierre-Emmanuel Milhiet

Devant le jury composé de

Victor SHAHIN, Pr, University of Münster, Institute of physiology II, Medical Faculty.	Rapporteur
Felix RICO, Pr, Université Aix-Marseille, Laboratoire Adhésion et Inflammation, LAI INSERM U1067	Rapporteur
Shotaro OTSUKA, Dr, University of Vienna, Max Perutz labs, Vienna Biocenter.	Examinateur
Csilla GERGELY, Pr, Université de Montpellier, Laboratoire Charles Coulomb, L2C-UMR5221 CNRS.	Examinatrice Présidente du jury
Pierre-Emmanuel MILHIET, Dr, Université de Montpellier, Centre de Biochimie Structurale, CNRS UMR5048 - UM - INSERM U1054.	Directeur de thèse
Christine DOUCET, Dr, Université de Montpellier, Centre de Biochimie Structurale, CNRS UMR 5048 - UM - INSERM U 1054.	Co-encadrante

UNIVERSITÉ DE MONTPELLIER

Acknowledgements

Firstly, I would like to thank all the members of the jury, Pr. Victor Shahin, Pr. Felix Rico, Pr. Csilla Gergely and Dr. Shotaro Otsuka for accepting to review my research work. I would like to especially thank Pr. Rico, who participated in all my thesis committees and followed my progress all along, as well as Céline Verheggen and Ariane Abrieu for their constructive comments and suggestions on my work during these committees.

I would like to express my deepest appreciation to my thesis directors, Dr. Pierre-Emmanuel Milhiet and Dr. Christine Doucet. Pierre-Emmanuel for giving me the opportunity to join the CBS as an engineer and to continue as a PhD student. For his trust in me which allowed me to be involved in several projects and to learn new techniques, like High-speed AFM and super-resolution microscopy. He has always been available for me if I had questions, even on his busiest days, and I do not think I could have had a better director. Christine for everything: from her confidence in my ability to do a PhD while I was not sure in myself, to the help in experiments and analysis, as well as her support in all the aspects of this PhD. I certainly would not have been able to achieve this work without her and I do not know how to express all the gratitude I have.

I would like to thank all present and past members of my team at the CBS, especially Dr. Luca Costa. Luca was the first person to introduce me to AFM when I arrived as a totally ignorant “kid” to the ESRF. He taught me most of what I know about AFM and transmitted his passion for it. I really enjoyed working with you at the ESRF and the CBS. My professional career would have been completely different if I had not met Luca. Thank you for the support, answers to my numerous questions about AFM and for the outside activities - football, hiking, and cycling expeditions. Finally, thanks to the Italian national football team for not qualifying for the FIFA World Cup 2018, so that I could enjoy the title without hearing Luca talking about Italy supposedly playing better than France.

I would like to also thank Fabio Comin, who gave me the chance to join ESRF and enter the academic domain.

Thanks to all the people from the team who contributed to this work: Patrice Dosset who helped us a lot with analysis, Thales Fernandes for the help and discussions on experiments and data. Thanks to Laurent Fernandez for the support in the first and the last years of my PhD.

Thanks to people who helped me learning and managing super-resolution microscopy techniques. Antoine Le Gall, Jean-Bernard Fiche and Emmanuel Margeat for their help on the setup and answers to my questions on fluorescence microscopy and STORM. Marie-Pierre Blanchard and Julio Mateos Langerak for their help in setting STED microscopy on NPCs on the MRI platform. I would like to especially thank Orestis Faklaris for his help in setting up STORM imaging and analysis where his experience on NPC has been precious.

I would like to thank all the people I had the opportunity to collaborate with at the CBS on different projects and especially the people involved in the study of septins.

I would like to thank all the members of the CBS, where I spent seven years and always enjoyed the atmosphere. Thanks for collaborative work and social interactions. Thank you, Nathalie Sibille, for rich discussions and good advice during my PhD. Especially thanks to the PhD students of CBS 60, Sara Rombouts, Oscar Saavedra, Julian Gurgo and Baptiste Guilhas for their help and support during these years.

Merci à ma famille, mes parents, mon frère Sylvain et à ma grand-mère Manou qui m'ont soutenu et ont fait de moi la personne que je suis aujourd'hui.

Finally, and most importantly I would like to thank my dear Zhanna and my wonderful son Victor for all the support during this journey, the review of my manuscript, and all the joy in life we have together.

Abstract

A characteristic feature of eukaryotic cells is the physical isolation of their genetic material by the nuclear envelope (NE), a double lipid bilayer composed of an inner and outer nuclear membrane separated by a lumen. Across this barrier are the nuclear pore complexes (NPCs), the only gateways between the nucleus and cytoplasm. They are made of multiple copies of around 30 proteins called nucleoporins. During interphase, proliferating cells have to duplicate their genetic material, organelles, membranes and enzymatic tools, to split them between daughter cells. While DNA replication is widely studied, duplication of other materials is largely unexplored. In most cases, this is just a matter of protein and lipid synthesis, yet the NPC replication is a complex process involving macromolecular assembly combined with membrane remodelling. Moreover, the nuclear permeability barrier must remain intact during the whole process, underlining that protein assembly and membrane fusion must be tightly coordinated. Interphase pore assembly occurs by *de novo* insertion of new pore units in the NE, which requires the local fusion of the inner and outer nuclear membranes. The fusion process must involve a close apposition of the two membranes, generating locally a complex combination of positive and negative curvature in the bilayers.

A recent study showed that interphase assembly of the NPC is a directional process that initiates at the inner nuclear membrane. That a highly symmetrical protein complex assembles in an asymmetric manner is extremely intriguing. The objective was to elucidate the precise evolution of the protein structure and membrane topography during this process. In this context, the goal of my thesis was to investigate the detailed sequence of events of NPC assembly at the molecular and topographic level. Atomic Force Microscopy (AFM) is a technique of choice, as it produces high-resolution topographies of single nano-objects. Moreover, correlative Single Molecule Localization Microscopy (SMLM) can add compositional information, with a similar resolution. As AFM is a contact technique, I first had to develop a protocol to purify and open human cell nuclei in a manner that does not affect the structure of NPCs and the surrounding NE. Then I measured for the first time the topography and mechanical properties of the human NPC nucleoplasmic side, together with SMLM images of the main basket component Tpr. My results demonstrate a large range of flexibility in the conformations of this structure which questioned the usually admitted protruding structure of the basket.

Then, I used differential immuno-labelling to discriminate mature NPCs from intermediates, and record their topography. In addition, SMLM on POM121, an early player in interphase assembly, revealed that this transmembrane nucleoporin acts as a seeding point in early intermediates. POM121 concentration then increases at this seeding point and grows, until the formation segregates towards a ring structure in NPC interphase intermediates.

Finally, using quantitative measurements of NPC structure based on Stimulated Emission Depletion Microscopy combined with small interfering RNA treatment against a set of nucleoporins, I have been able to characterize the contribution of several nucleoporins to the kinetics of assembly and structure of NPC interphase intermediates.

Taken together, these results demonstrated how AFM can be used as a nanotool to investigate the inner nuclear membrane of human cells and especially NPCs. They also reveal the high variability of NPC basket structure and bring new information to understand the complex process of NPC interphase assembly.

Résumé

Les pores nucléaires (NPC) sont les seules passerelles entre le noyau et le cytoplasme. Ils sont constitués de plusieurs copies d'une trentaine de protéines appelées nucléoporines. Pendant l'interphase, les cellules en prolifération doivent dupliquer leur matériel génétique, organelles, membranes et outils enzymatiques, pour les répartir entre les cellules filles. Dans la plupart des cas, il s'agit simplement d'une question de synthèse de protéines et de lipides, or la réplication du NPC est un processus complexe impliquant un assemblage macromoléculaire combiné à un remodelage membranaire. De plus, la barrière de perméabilité nucléaire doit rester intacte pendant tout le processus, ce qui souligne que l'assemblage des protéines et la fusion des membranes doivent être étroitement coordonnés. L'assemblage des pores en interphase se produit par l'insertion de novo de nouveaux pores dans l'EN, ce qui nécessite la fusion locale des membranes nucléaires interne et externe. Le processus de fusion doit impliquer l'apposition étroite des deux membranes, générant localement une combinaison complexe de courbures positive et négative dans les bicouches.

Une étude récente a montré que l'assemblage du NPC en interphase est un processus directionnel qui commence au niveau de la membrane nucléaire interne. Le fait qu'un complexe protéique hautement symétrique s'assemble de manière asymétrique est extrêmement intriguant. Nous avons voulu comprendre l'évolution précise de la structure protéique et de la topographie de la membrane au cours de ce processus. Dans ce contexte, le but de ma thèse était d'étudier la séquence détaillée des événements d'assemblage du NPC au niveau moléculaire et topographique. La microscopie à force atomique (AFM) est une technique de choix pour cela, car elle produit des images topographiques à haute résolution d'objets nanoscopiques. De plus, la corrélation avec la microscopie de localisation de molécules uniques (SMLM) peut ajouter des informations sur la composition, avec une résolution similaire. L'AFM étant une technique nécessitant d'entrer en contact avec l'échantillon, j'ai d'abord dû mettre au point un protocole pour purifier et ouvrir les noyaux de cellules humaines d'une manière qui n'affecte pas la structure des NPCs et de l'EN autour. Ensuite, j'ai mesuré pour la première fois la topographie et les propriétés mécaniques de la face nucléoplasmique de NPCs humains, ainsi que des images SMLM du composant principal du panier, Tpr. Mes résultats démontrent une large gamme de flexibilité dans les conformations de cette structure, ce qui remet en question la structure protubérante du panier habituellement admise.

Ensuite, j'ai utilisé l'immunomarquage différentiel pour discriminer les NPCs matures des intermédiaires, et enregistrer leur topographie. De plus, le SMLM sur POM121, un acteur précoce de l'assemblage en interphase, a révélé que cette nucléoporine transmembranaire agit comme un point d'ancrage dans les intermédiaires précoces. La concentration de POM121 augmente ensuite à ce point d'ancrage et croît, pour finalement être ségrégée vers une structure en anneau dans les intermédiaires de l'interphase du NPC.

Enfin, en utilisant des mesures quantitatives de la structure des NPC basées sur la microscopie à déplétion par émission stimulée, combinées à des traitements par ARN interférent contre un ensemble de nucléoporines, j'ai pu caractériser la contribution de plusieurs nucléoporines à la cinétique d'assemblage et à la structure en interphase des intermédiaires de NPCs.

Pris ensemble, ces résultats ont démontré comment l'AFM peut être utilisé comme un nano-outil pour étudier la membrane nucléaire interne des cellules humaines et en particulier des NPCs. Ils révèlent également la grande variabilité de la structure du panier des NPC et

apportent de nouvelles informations pour comprendre l'assemblage en l'interphase des NPC.

Table of contents

Abbreviations

AFM – Atomic Force Microscopy
EM – Electron Microscopy
FG – phenylalanine-glycine
HS-AFM – High-Speed Atomic Force Microscopy
INM – Inner Nuclear Membrane
NE – Nuclear Envelope
NES – Nuclear Export Signal
NLS – Nuclear Localization Signal
NPC – Nuclear Pore Complex
NTR – Nuclear Transport Receptor
Nup – Nucleoporin
ONM – Outer Nuclear Membrane
PALM – Photo-Activated Localization Microscopy
PSF – Point Spread Function
SMLM – Single-Molecule Localization Microscopy
STED – STimulated Emission Depletion
STORM – STochastic Optical Reconstruction Microscopy
TIRF – Total Internal Reflection Fluorescence

Introduction

Preamble

Regarding the introduction of this manuscript, the study of the Nuclear Pore Complex is such a vast subject that it would require several books to cover all the knowledge acquired since they were first imaged in the 1940s. Thus, the following introduction aims at giving enough elements and context to understand the work and advances achieved during the thesis. Consequently, the introduction on the NPC will not be exhaustive and I apologize to the authors whose work was not cited or discussed although the entire literature on the NPC allows us to, step by step, better understand this intriguing cellular complex.

My PhD work mainly focuses on the study of the Nuclear Pore Complex structure and interphase assembly. In addition, I occasionally worked in parallel on the study of the membrane remodelling operated by septins on a model supported lipid bilayer. This work, which I started before the thesis at the *Centre de Biologie Structurale*, led to a publication as a co-first author(Vial *et al.*, 2021). Although several aspects in the instrumental approach are similar, and the fact that it also focuses on the study of protein assemblies during interaction with membranes, the biological context appears to be quite different between the two topics. Moreover, the time assigned to this side project was far less than for the study of the NPC. For these reasons, I decided not to present this work in the main part of the manuscript and added it only, as well as other works, as an annexe.

Introduction

Eukaryota represent one of the three domains of life, along with Bacteria and Archaea. The main characteristic of Eukaryota that differentiates them from other domains is the physical isolation of their genetic material from the rest of the cell by endomembranes. Scientists have for a long time observed differences in the internal structure of cells, like the presence of a nucleus. Yet the first occurrence of the term "eukaryote" was made by a French zoologist and marine biologist, Edouard Chatton, in a study trying to establish a new classification of protists in *"Pansporella perplexa: Réflexions sur la Biologie et la Phylogénie des Protozoaires" (1925)*.

This essay on *Pansporella perplexa*, an amebae that he discovered in 1906, aimed at finding the phylogenetic group of this species. Discussing the characteristics of this organism and its position in the family tree of protists along the article, he will finally create a specific group for it, *Sporamœbidæ*.

However, the unique traits of *Pansporella perplexa* forced Chatton to review entirely the relationship between protists. This process led him to the final figures of his article where he delivers a hypothetical general classification of these organisms. By separating some protists - now classified as prokaryotic organisms - from others presenting a "true nucleus" in their cellular organization, he uses for the first time the word "eukaryotes". This term was later recommended by André Lwoff, a former Chatton's student and a future Nobel prize laureate, to Roger Stanier and Cornelis van Niel for "The Concept of Bacterium", a masterpiece in the building of the actual three-domain model (Sapp, 2005).

In parallel, Ellsworth Dougherty independently proposed the terminology of prokaryote and eukaryote, probably inspired after reading Chatton's work. In addition, Chatton's article demonstrates that his vision was not limited to the world of protists since he included metazoan in this tree as well.

All these works led to the conclusion that the study of the nucleus, and especially its membranous boundary, would be a key to better understand cellular functions of prokaryotes and eukaryotes, as well as to study the evolution of primitive forms of life.

In the meantime, several scientific advances allowed a better classification of these organisms and the development of new instruments offered an opportunity to investigate more deeply the nature and the organization of the nuclear membrane present in eukaryotes. The development of the first electron microscopes in the 1930's gave the opportunity to H. G. Callan to study the membrane of giant *Xenopus laevis* and *Triturus cristatus* nuclei with this technique (Figure 1) and observe for the first time what will be later named a nuclear pore complex (NPC) (Callan, Randall and Tomlin, 1949; Watson, 1959).

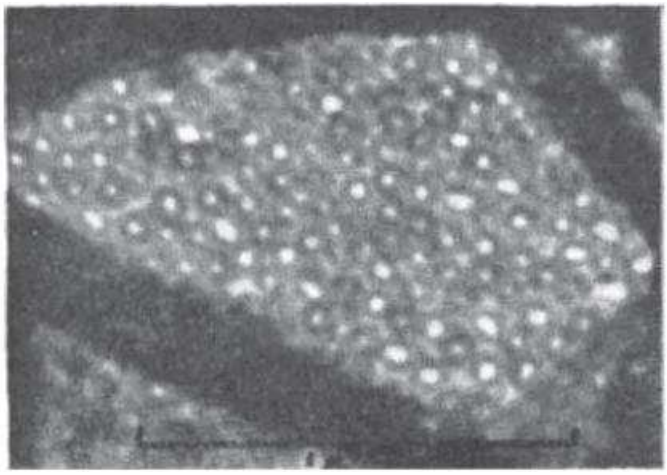

Figure 1: Nuclear membrane from Triturus cristatus observed by electron microscopy (EM) by H.G. Callan in 1949 was the first report of the porous nature of this membrane (Callan, Randall and Tomlin, 1949). Scale bar is 1 µm.

The discovery of the porous nature of the eukaryotic nucleus opened a new field of investigation in biophysics, centered on the understanding of the NPC functions and regulation and the nucleo-cytoplasmic transport that is still highly active. Indeed, many questions about the NPC remain open because of its extraordinarily complex structure and implication in many cellular processes.

1. Eukaryotes and nucleus

1.1. An element of the endomembrane system

As explained before, eukaryotic organisms are mainly defined by the presence of a "true nucleus" responsible for the protection of the genome. The isolation of the genetic material is fulfilled by a double lipid bilayer separated by a 40-50 nm lumen (Watson, 1959; Rothballer, Schwartz and Kutay, 2013) named the nuclear envelope (NE), which is continuous with another part of the endomembrane system, the endoplasmic reticulum. Other organelles are found in most eukaryotes like the Golgi apparatus and this system is completed by lysosomes and vacuoles. Eukaryotes also carry mitochondria, that provide energy to the cell, and a cytoskeleton composed of three types of filaments: actin filaments, intermediate filaments, and microtubules.

This extraordinarily complex and optimized system relying on intense membrane trafficking between organelles is believed to have appeared early in the evolution process (Figure 2). The last eukaryotic common ancestor (LECA) whose emergence is estimated between one billion and one billion and a half years ago most probably already possessed these well differentiated organelles (Liashkovich and Shahin, 2017; Rout and Field, 2017). This organism acquired mitochondria through an endosymbiosis event.

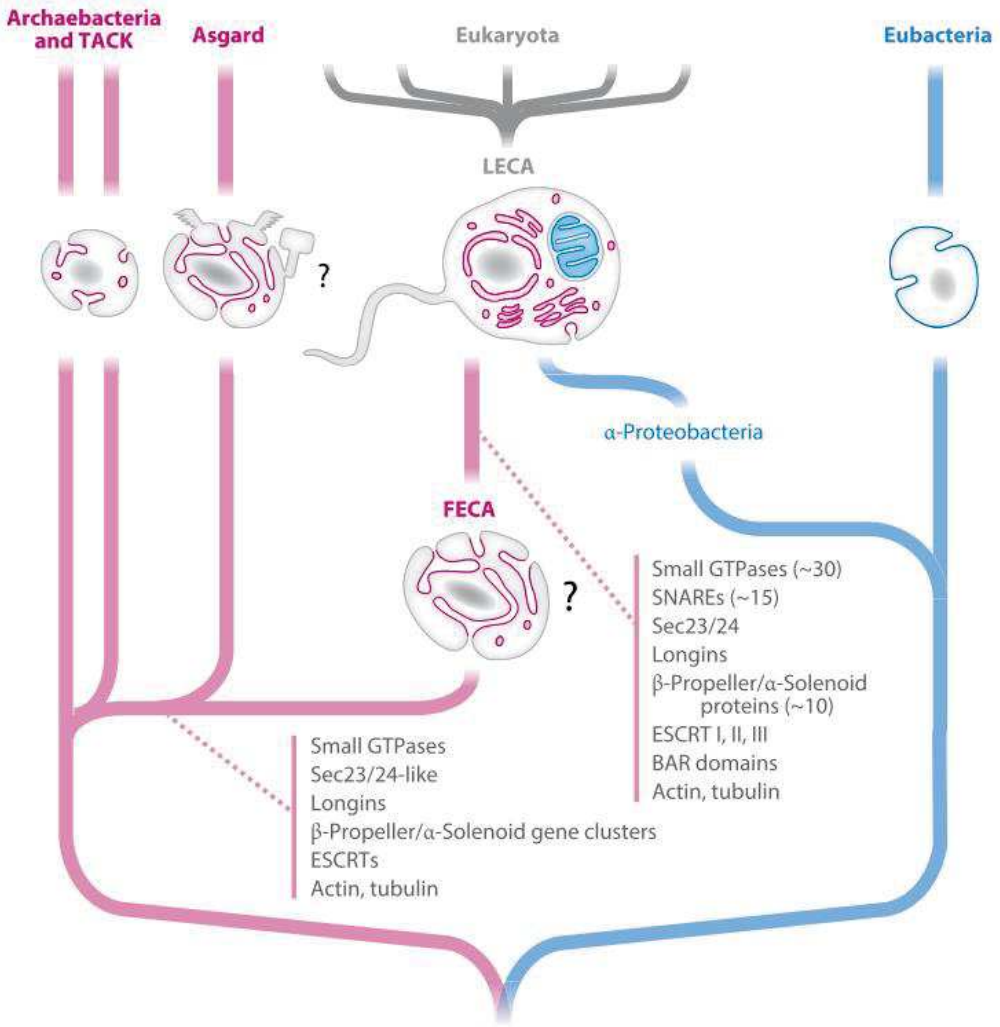

Figure 2: Model of emergence of Eukaryota by Rout and Field (Rout and Field, 2017). According to the last model, eukaryotic organisms emerged from Archea which closest related family are Asgard. They might early have developed organelle-like structures and later acquired an α-Proteobacteria by endosymbiosis.

While the appearance of the endomembrane system remains unclear, recent work reveals new organisms, like an anaerobic *Asgard archaeon* related to *Lokiarchaeota* (Imachi *et al.*, 2020), MK-D1, which has no visible organelle-like structure and which could explain the origin of this membrane complexity. MK-D1 lives in an almost oxygen-free environment and is the closest related to eukaryotes. It has long arms that could have allowed engulfment of bacteria tolerant to oxygen which would later become the mitochondria while the core globular part of MK-D1 could be the basis of the cell nucleus.

The emergence of the nucleus and the rest of the endomembrane is tightly linked to the evolution of protein complexes, which can deform and shape into a particular topology a membrane that otherwise would be flat. This property is key for deforming membranes to build organelles. One hypothesis is that this ability to shape membranes has been inherited from a common ancestor. The common primitive membrane coat proteins, or coatomers, acquired the property to coat vesicles trafficked between organelles. They have evolved in different complexes spread among the different organelles. The relationship between membrane shaping complexes has been demonstrated through similarities observed in the protein structures containing α-solenoids and β-propellers motifs (Rout and Field, 2017). One of these coatomers is the NPC.

NPC as an element of the endomembrane system has been related to the family of vesicle coating proteins like clathrin, COPI and COPII. These coatomers, even though they act in different places in cell membranes, all share structural similarities with some of the nucleoporins present in the NPC since they share a common ancestor. COPII proteins which act on the ER membrane to shape transport vesicles addressed to the Golgi membrane are considered as the closest to the NPC type of coatomer. Acting on the ER, which is continuous with the NE where NPCs sit, COPII shares with the NPC the protein Sec13 as a common component. This suggests the ancestral proto-NPC might have emerged from the divergence from COPII (Rout and Field, 2017).

In addition, recent work based on the assumption of a common ancestor between clathrin and some scaffold Nups of the NPC demonstrated this evolutionary relationship between them (Liashkovich *et al.*, 2015). Using an inhibitor of the clathrin coat assembly which binds the β-propeller N-terminal domain of clathrin, Liashkovich et al. showed that this inhibitor alters NPC permeability barrier and NPC structure by interfering in the interaction between the β-propellers motifs present in scaffold Nups. This result was interpreted as an indication of the common protein motifs shared with NPC scaffold Nups and clathrin.

1.2. Characteristics of the nucleus

The biggest component of the endomembrane system is the nucleus. The cell nucleus encloses the nuclear genome of eukaryotes with its NE and the access to the nucleoplasm is highly regulated. The only gateway to it is the NPC, the biggest complex of eukaryotic cells, and each nucleus possesses thousands of them.

This central organelle is indirectly connected to the cell wall by a chain of different elements of the cytoskeleton (Figure 3) (Jahed *et al.*, 2016). Lamins are intermediate filaments forming a meshwork at the inner part of the NE. They are linked to the cytoskeleton through LINC complexes, composed of a trimer of SUN proteins, anchored in the INM, whose SUN domain interacts with a KASH peptide of a Nesprin protein, located in the ONM. Nesprins are bound to cytoplasmic elements of the cytoskeleton like actin, microtubules or other intermediates filaments connected to the plasma membrane. This chain of interactions will transmit force from the cell wall to the nucleus and is especially important for cell polarization or movement. Thus, the nucleus will be indirectly affected by external forces applied to the cell.

In eukaryotes, the NE acts as a barrier to prevent corruption of the genomic information. This function is performed by both the nuclear membrane and the NPC. The nuclear membrane is a double lipid-bilayer, supported by lamins, and acts as an enclosure wall around the DNA. Within this wall, NPCs perform as a permeability barrier that carefully controls which elements can cross the border. This unique gate between the cytoplasm and nucleoplasm regulates the import and export of proteins across the NE. This property is referred to as the permeability barrier.

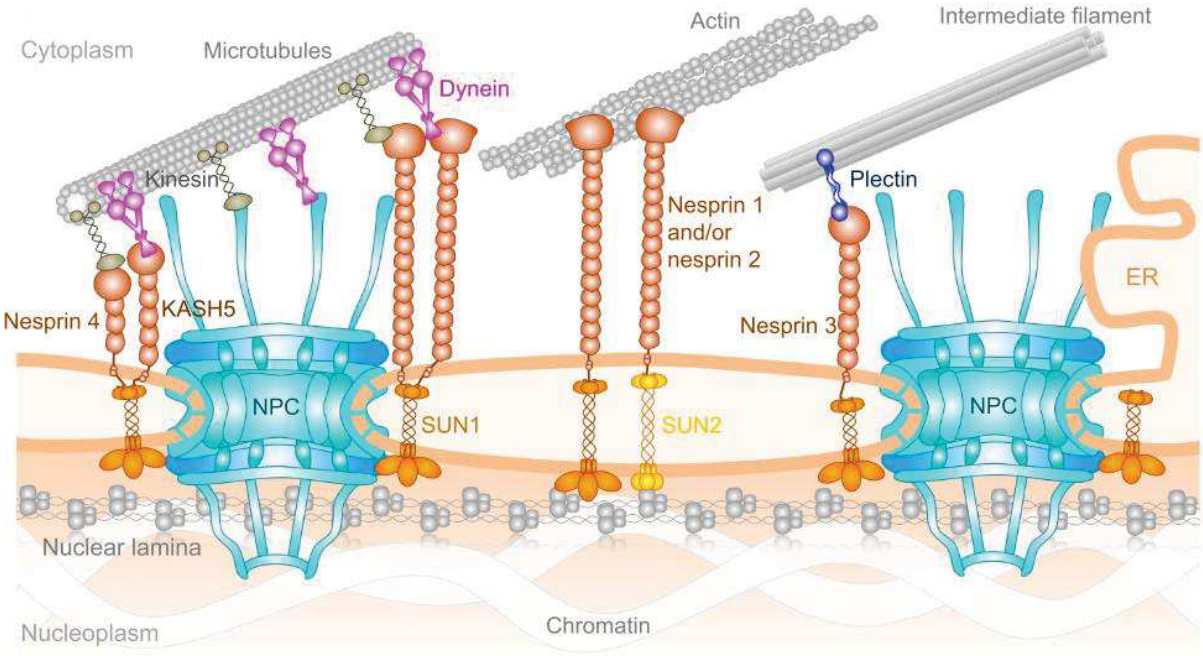

Figure 3: Connections of the nucleus with cytoskeleton as represented by Jahed et al. (Jahed et al., 2016)

This configuration separates the transcription of genes into RNA, that takes place inside the nucleus, from the translation of RNA into proteins that is performed by ribosomes in the cytoplasm. Gene expression is thus regulated by the import of transcription factors inside the nucleus and export of the corresponding mRNA towards the cytoplasm where it will reach ribosomes to be translated. For many transcription factors, their activity is *de facto* regulated at the level of nucleo-cytoplasmic shuttling. Indeed, post-translational modifications can regulate the accessibility of transport sequences, which in turn controls the nucleoplasmic concentration of these factors. This underlines that functional NPCs are essential for eukaryotic cells to function properly and to produce all the proteins required for their metabolism and their regulation.

2. The Nuclear Pore Complex, an essential element of the nucleus

2.1. NPC structure

The nuclear pore complex is a highly conserved structure present in all eukaryotic organisms and an essential element of the cell. In metazoan, it is composed of around 30 different proteins, present in several copies that assemble in a pore structure inserted into the NE and has a diameter of around 120 nm. In total, up to 1000 nucleoporins (Nups) (Schwartz, 2016) assemble together to form the NPC. The Nups names are in general based on their molecular weight.

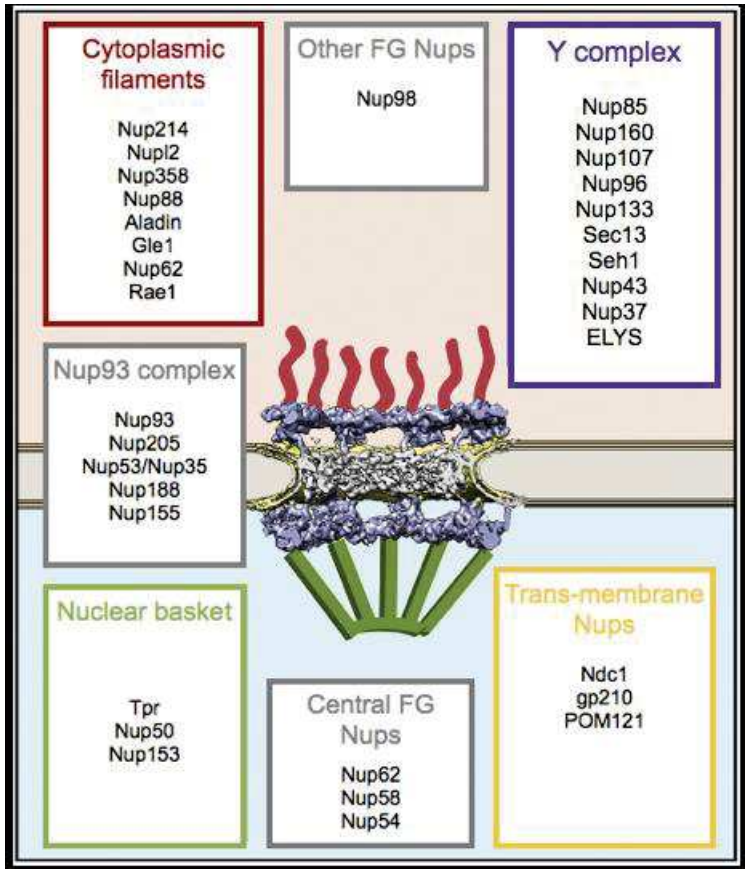

Figure 4: Description of the structure and composition of human NPC and its different sub-complexes (adapted from Knockenhauer and Schwartz, 2016).

The pore structure exhibits an eightfold rotational symmetry (Gall, 1967) around its central channel and is composed of several subcomplexes (Figure 4). These are defined as stable protein complexes made up of several Nups, that remain together even outside of the NPC environment, for example during mitosis. They are biochemically associated and can be isolated by pull-down experiments. Moreover, members of the same subcomplexes can associate together as early as during translation, close to NPCs (Lautier *et al.*, 2021).

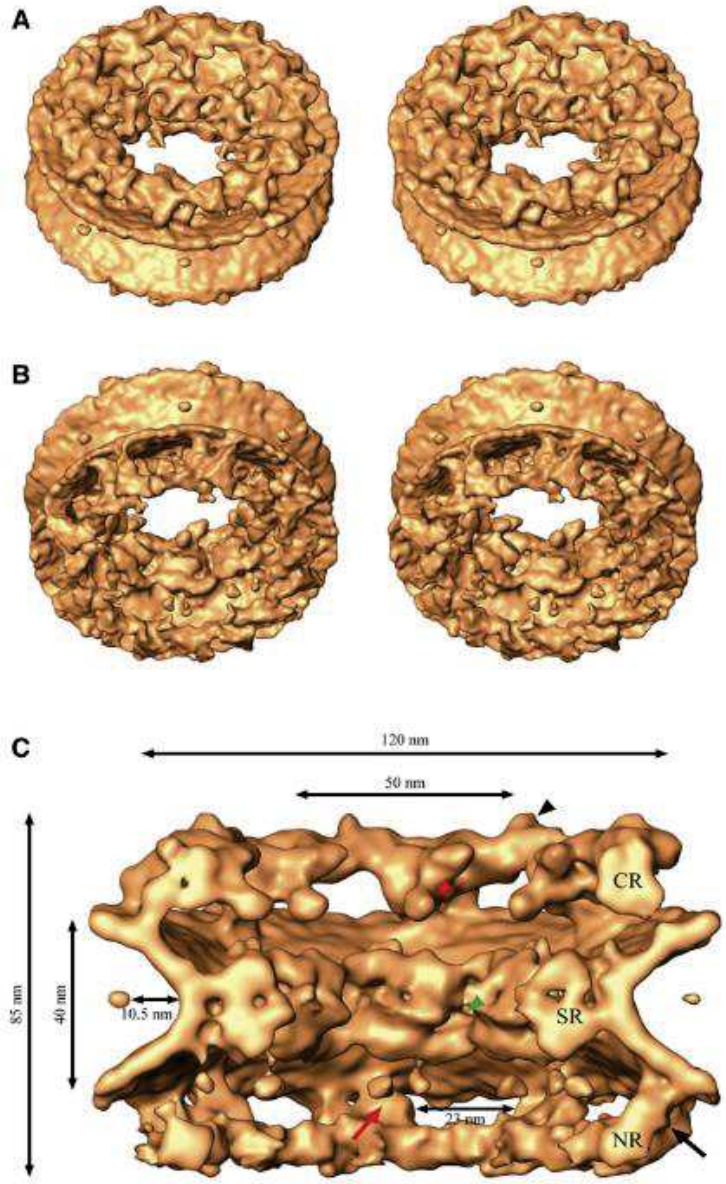

Figure 5: Reconstruction by cryo-EM tomography of the human NPC showing the overall structure of the cytoplasmic ring (CR), spoke ring (SR) and nuclear ring (NR). (A) View from the cytoplasmic side, (B) view from the nucleoplasmic side, (C) cross-section of the NPC, (Maimon et al., 2012).

Even though the composition and number of Nups varies between species, the overall NPC structure is rather conserved and homology between the different sub-complexes is high (Lin and Hoelz, 2019). Nucleoporins are divided into three groups, based on their role within the pore:

- Scaffold Nups, that constitute the NPC shell and stabilize the highly curved membrane at the junction between the inner and outer nuclear membranes (INM and ONM). They are arranged as a hollow barrel and their distribution is symmetric across the plane of the nuclear envelope. Scaffold Nups are organized as an inner pore ring, localized at the fusion plane between INM and ONM (Kosinski *et al.*, 2016) and the nuclear and cytoplasmic rings, that both share almost the same protein composition (except for ELYS which is only nucleoplasmic) and are anchored to the inner pore ring (Figure 5).

- A small subset of Nups are transmembrane proteins most likely positioned in the same plane as the inner pore ring; they anchor the NPC to the nuclear membrane (Antonin *et al.*, 2005). In mammals, there are three transmembrane Nups: POM121, gp210 and Ndc1. Among them, gp210 is absent in many mammalian cell types and thus dispensable for the stability of the NPC (Eriksson, Rustum and Hallberg, 2004; Olsson, Schéele and Ekblom, 2004). Transmembrane Nups are poorly conserved across species except for Ndc1.

- The peripheral Nups: Nups located in the central channel are characterized by the abundance of FG (phenylalanine-glycine)-rich repeats in their sequences. These domains are intrinsically disordered and, combined together, they form a hydrogel (Frey, Richter and Görlich, 2006). Located at the center of the scaffold structure, they ensure the permeability barrier of the NPC channel. Attached to the scaffold are another two asymmetric structures: a basket protruding towards the nucleoplasm, composed of eight filaments that join in a nuclear ring and eight cytoplasmic filaments anchored to the cytoplasmic ring (schematized in Figure 4).

A main component of NPCs is the Y-complex (also known as Nup107-Nup160 complex in metazoans, Nup84 complex in yeast), named after its shape. In higher eukaryotes it comprises Nup107, Nup160, Nup133, Nup96, Nup85, Nup37, Sec13, Seh1,

and Nup43 (Figure 6). This complex is the major constituent of the nuclear and cytoplasmic rings. Each of these rings are organized as two concentric rings of Y-complex arranged in an eightfold symmetry (in total 16 Y-complexes) around the NPC channel (Figure 6). ELYS is also often considered as a member of the Y-complex even though it is only present in the nuclear ring (Sabinina *et al.*, 2021).

Nups of the Y-complex are mainly composed of two specific structural domains: α-solenoids and β-propellers. Interestingly, these folds are evolutionarily well conserved among eukaryotes and shared with other membrane coating protein complexes (Field and Rout, 2019). This illustrates their ability to interact with biological membranes and stabilize membrane curvature.

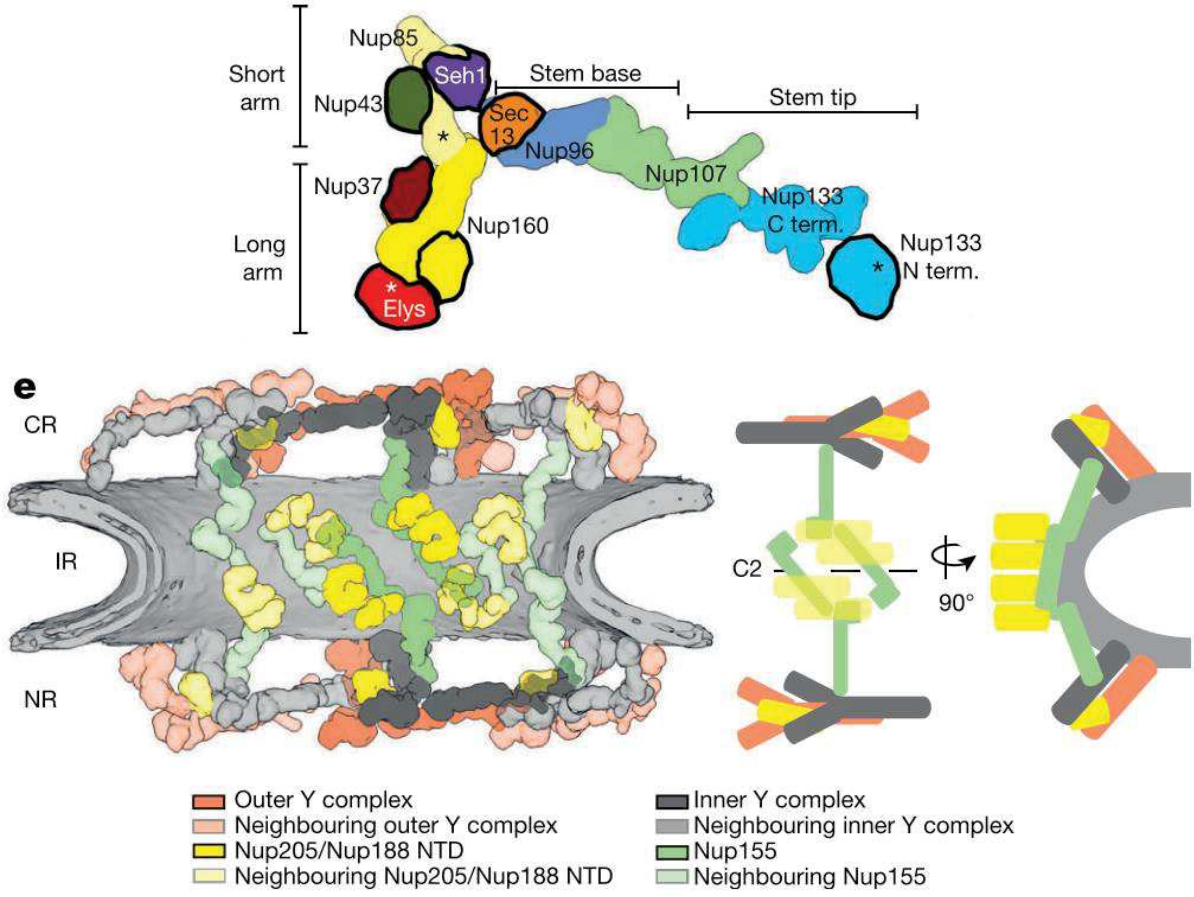

Figure 6: Structure and arrangement of the Y-complex (Von Appen et al., 2015). The top figure represents the structure of the Y-complex. The bottom figure shows the overall arrangement of Y-complexes and Nups members of the inner ring where we can also observe the Nup155 bridges (green). CR= cytoplasmic ring; NR= nucleoplasmic ring; IR= inner ring.

Nuclear and cytoplasmic rings are linked to the inner pore ring via Nup155 bridges (in green in figure 6) (Kosinski *et al.*, 2016). The rest of the inner pore ring is composed of 32 copies of Nup93, Nup205, Nup53/35, Nup188 and Nup155 again, which will serve as anchors for the FG-Nups of the central channel.

The exact structure of these three rings is a subject of intense research. The most resolved ensemble view of the human NPC observed *in situ* is the cryo-EM structure of the outer rings by von Appen et al. (von Appen *et al.*, 2015) and that of the inner ring by Kosinski et al. (Kosinski *et al.*, 2016).

For Nups of the central channel, no clear picture has been resolved yet. Nup62, Nup58 and Nup54, that form most of the permeability barrier, contain both structured and intrinsically disordered FG-repeats, preventing any conventional structural study. Cytoplasmic filaments were long thought to extend towards the cytoplasm but it appears that they point towards the centre of the NPC (Fernandez-Martinez *et al.*, 2016a) with a predicted role of Nup358 and Nup214 in stabilizing the cytoplasmic ring structure (Huang *et al.*, 2020).

On the nucleoplasmic side of the NPC, the nuclear basket is composed of three Nups, Nup50, Nup153 and Tpr. Nup153 is known to be the linker between the nuclear ring and the rest of the basket (Walther *et al.*, 2001) and a recent work has also pointed at the role of Nup133 (present in the Y-complex) to stabilize the basket (Souquet *et al.*, 2018). Most of the basket structure is then composed of Tpr that contains coiled-coiled domains. Tpr would form the eight filaments attached to the nuclear ring that join together at the end of the basket (Figure 7) (Allen *et al.*, 1997) as it has been suggested by Krull et al. in HeLa cells (Krull *et al.*, 2004).

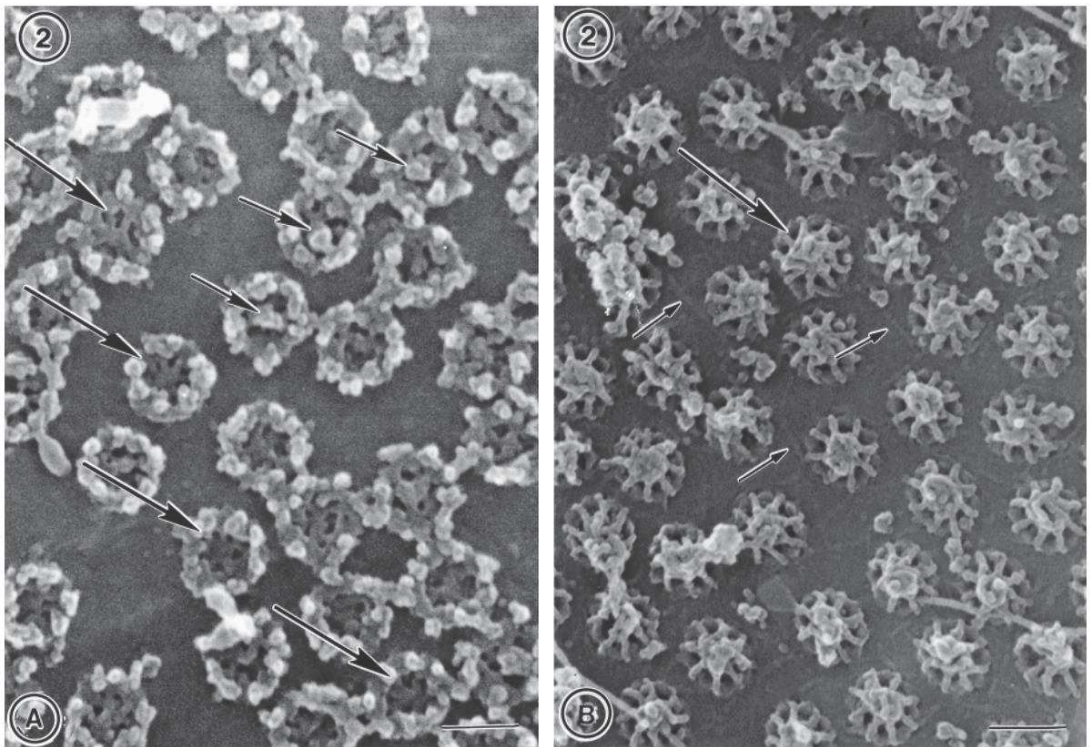

Figure 7: NPC cytoplasmic (left) and nucleoplasmic (right) sides of Xenopus laevis NE observed by SEM (Allen et al., 1997). Scale bars are 100 nm.

Tpr's N-terminal domain, which contains an alpha-helix predicted to form a coiled-coiled structure, was studied by various structural approaches including SEM (Hase, Kuznetsov and Cordes, 2001). It exhibits a rod-like structure of 2-3 nm width. Contrary to its C-terminal domain that does not exhibit coiled-coiled nor rod-like structures, its N-terminal domain is composed of evolutionarily conserved polypeptides (Kuznetsov *et al.*, 2002).

In total, full-length Tpr has four predicted coiled-coils. A crystallographic structural study of a part of Tpr encompassing half of a coiled-coil domain showed that this Nup assembles as two dimers in a tetramer with antiparallel orientation forming a chain with a total length of 175.6 Å (Figure 8) (Pal *et al.*, 2017). Although this structure of an isolated fragment of Tpr can help to develop a hypothesis on the NPC basket structure, its overall arrangement remains unclear.

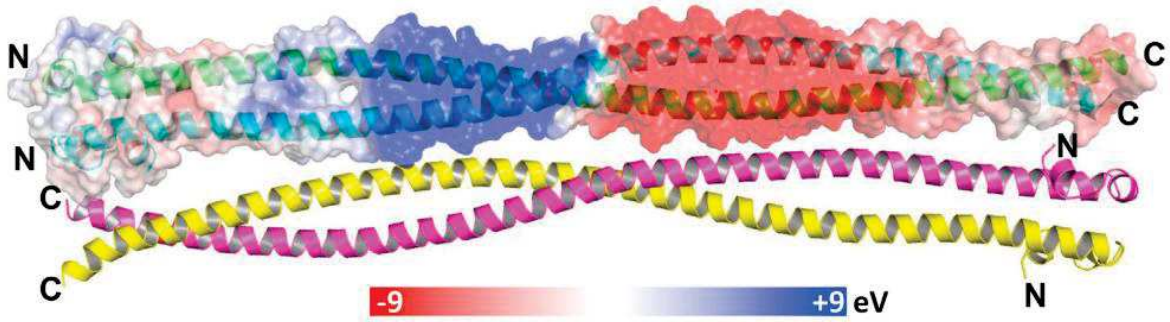

Figure 8: Structure of Tpr[1-142] exhibiting the tetrameric antiparallel orientation that is determined by the surface charges.(Pal et al., 2017).

To conclude on NPC structure, the experimental works that tried to solve the structural architecture of the NPC are mainly based on biochemical analysis and reconstructed EM structure of Nups that can be associated through an integrative modelling approach with docking predicted or known crystal structures of proteins, providing the best view of how NPC is organized (Kim *et al.*, 2018). However, these approaches have some limitations since they rely on the assumption of the eight-fold rotational symmetry of all the Nups, specifically with the EM approach that imposes this symmetry for the reconstructed 3D structure. In addition, analogy between structures observed in other organisms, often used to predict the organization of subcomplexes, might introduce some bias due to a certain variability among eukaryota. Finally, some NPC sub-structures have never been solved at high resolution due to their flexibility.

2.2 Structural variability

Although the overall structure of the NPC is quite well conserved among eukaryotes, scientists have explored the different levels of variability of the NPC.

The first level is the variation between species. From yeast to human, as well as plants, NPC homology is present but the different subcomplexes and structures of Nups have evolved in many ways (Figure 9) (Brohawn *et al.*, 2009). Some Nups that seem essential to the NPC assembly in humans (*e.g.* POM121), are absent in other organisms. In addition, functions attributed to a single Nup in a species can be accomplished by two

separate ones in another eukaryote. This evolution-driven variability greatly limits the transposition of some of the structural advances from one organism to another.

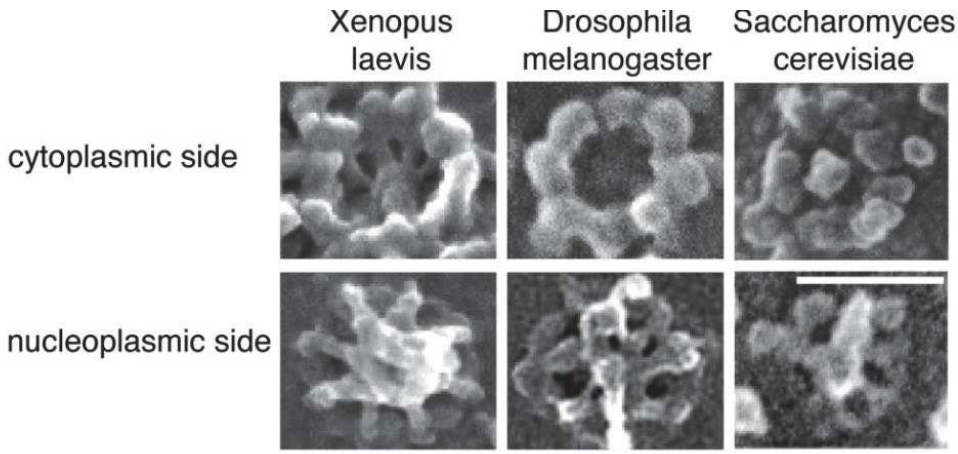

Figure 9: Difference in the structure of the peripheral elements of the NPC in different organisms observed by SEM (Brohawn et al., 2009). Scale bar is 100 nm.

The second level of variability concerns higher eukaryotes and is linked to the diversity of tissues and cell types. A study on Nups stoichiometry has shown that the NPC composition can vary between cell types, and this influences the NPC structure and functions (D'Angelo *et al.*, 2012; Ori *et al.*, 2013).

It was long assumed that the NPC structure deforms to allow the translocation of large cargos in their native folding, such as proteasomes, that are 11 nm by 15 nm (Savulescu *et al.*, 2011). This flexibility presumably relies on conformational changes within the pore, meaning that the interaction surfaces between Nups are dynamic and protean. This ability of the NPC to modify its conformation could partly find its origin in the lumenal region of the NPC where integral membrane Nups reside. In *Xenopus laevis,* a recent study has proposed an independent rearrangement of some of the eight subunits of the lumenal ring (Zhang *et al.*, 2020). This structure is presumably composed of the transmembrane Nups like gp210, POM121 and NDC1. Two alternative interaction modes of adjacent subunits in the luminal ring could also affect the conformation of the inner ring (Figure 10). The authors have shown that in some cases, the two conformations co-exist in a single NPC, resulting in an elliptic global shape. In addition, adaptation in the interaction surfaces between subcomplexes is also observed in the canonical NPC structure: for example, the nuclear and cytoplasmic rings contain two rings each of Y-complexes organized head-to-

tail (Figure 6). Because of the curved membrane surface, the diameters of the stacked rings of Y-complexes slightly differ, implying minor differences in the interaction surfaces between adjacent Y-complexes (discussed in (Lin and Hoelz, 2019).

A previous study in human cells (Rabut, Doye and Ellenberg, 2004), as well as a more recent study in yeast (Hakhverdyan *et al.*, 2021), have also shown that even within the core scaffold, Nups have variable exchange rates and are not permanently located at the NPC. This study also demonstrates that degradation of a proportion of a given Nup in the NPC can be compensated by higher exchange rate of this Nup without compromising NPC functions. This confirms a certain flexibility in the NPC structure and a certain redundancy among Nups.

Another type of NPC variability is the plasticity of NPCs during development. In *Xenopus laevis* oocytes, it has been demonstrated by super-resolution experiments that the size of the NPC central channel varies depending on the oocyte stage and this could be linked to the variation of translocation rates between stages (Sellés *et al.*, 2017). In this study, Sellés et al. observe a reduction of the central channel and gp210 ring diameters from stage II to stage VI of the oocyte development. At the same time, they showed that the number of NPC per nucleus increases while their density decreases.

Previous studies (Schlune *et al.*, 2006; Sommerville, 2010) have shown that the high-level of transcriptional activity at early stages drops at later stages. These results thus suggest that the NPC diameter and the amount of RNA passing through the NPC are strongly related. A higher activity could result in a higher RNA export that will influence the structure of the NPC. It has been shown recently that cellular energy depletion constricts the pore and reduces the diffusion and active transport through NPCs (Zimmerli *et al.*, 2020).

Similarly, external forces applied to the cell nucleus influence the size and nuclear permeability barrier of NPCs. By observing YAP, a mechano-sensitive transcription activator, during experiments with an AFM applying force on the nucleus it was shown that this force is sufficient to trigger the import of YAP into the nucleus (Elosegui-Artola *et al.*,

2017). This translocation is allowed by the reduced mechanical restriction of YAP, due to partial opening of the pore channel in response to force. It was proposed that mechanical stability is required for proper control of nucleo-cytoplasmic transport.

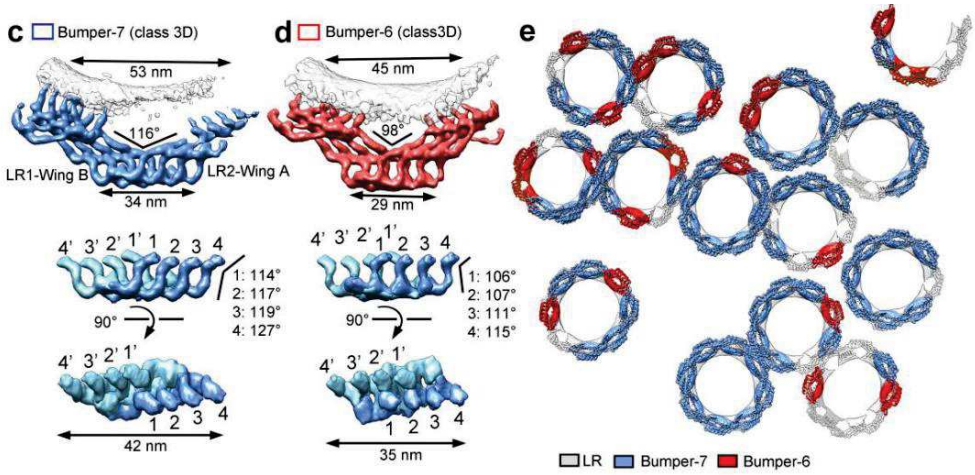

Figure 10: Two conformations of the NPC lumenal ring Nups Bumper-6 and Bumper-7, as described by Zhang et al. (Zhang et al., 2020)

Concerning the nuclear basket, flexibility is most probably the reason why this structure is missing in the recent structural publications. Tpr and its predicted long coiled-coiled domains could change conformation to let through a large translocation complex for example and could also depend on its interaction status with euchromatin present in the proximity of the NPC. This diversity of structures in the peripheral Nups has been explored by AFM in *Xenopus laevis* oocytes. Indeed, there is a large dispersion in the conformation of structures like the nucleoplasmic basket (Liashkovich *et al.*, 2011; Stanley, Fassati and Hoogenboom, 2018). AFM imaging revealed that the basket can exhibit both typical symmetric arrangement of filaments protruding several tens of nanometers above the nucleoplasmic ring as well as other entanglement where basket filaments seem to join lower at the NPC central channel (Figure 11). These two examples are at the extreme of a full spectrum of conformations adopted by the NPC basket.

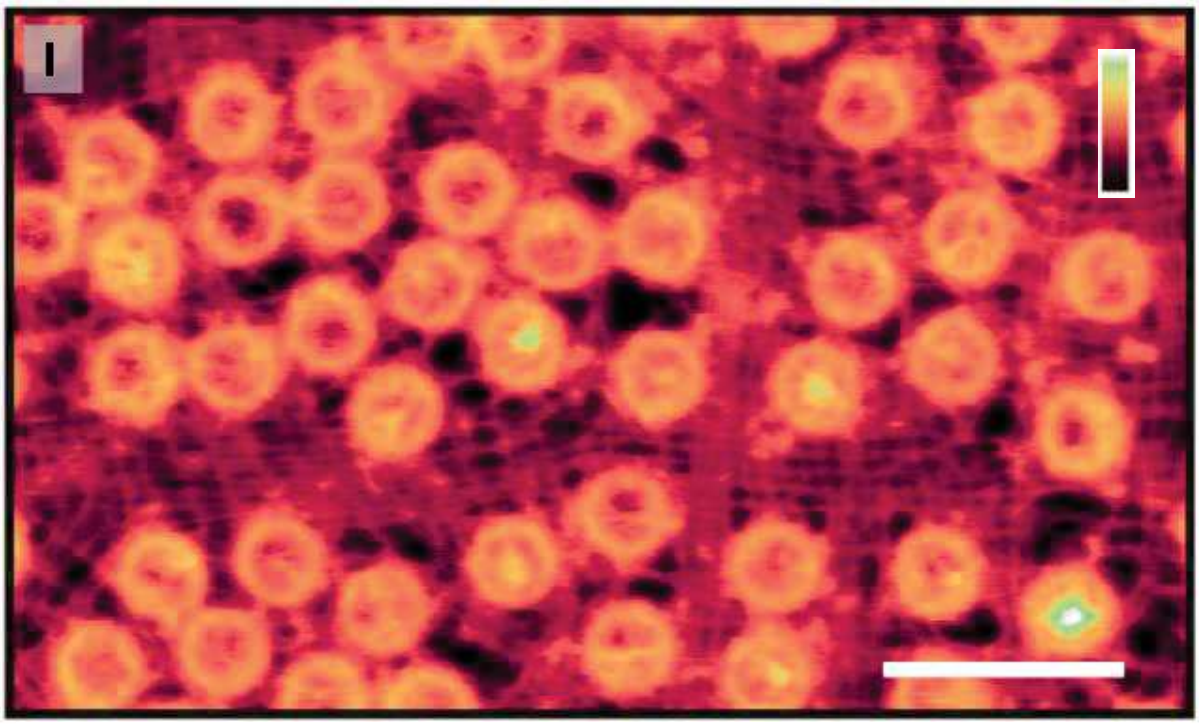

Figure 11: Xenopus NPC nucleoplasmic side exhibiting a high variability in the basket structure, Stanley et al. 2018. Scale bar is 300 nm, colour scale 0-100 nm.

Finally, some studies showed that NPCs can exceptionally assemble as a structure composed of nine subunits instead of eight (Löschberger *et al.*, 2014; Thevathasan *et al.*, 2019). This suggests that NPC structure can handle a certain degree of variability. However, how this translates at the molecular level is not clear.

2.3. Anchoring within the nuclear envelope

NPCs are very stable in the nuclear envelope since they do not diffuse and keep more or less their position of insertion (Rabut, Doye and Ellenberg, 2004). The INM and ONM of the nuclear envelope are linked by the LINC complexes. SUN proteins are INM transmembrane trimeric proteins. Their luminal domain consists of a long coiled-coiled region followed by a SUN domain, which interacts with the KASH peptide of a partner (nesprins for instance) anchored in the ONM. It was speculated that these complexes act as rulers to maintain the 40-50 nm distance between the INM and ONM (Rothballer, Schwartz and Kutay, 2013). At the top of ONM, nesprins interact with the cytoskeleton. On

the INM, SUN proteins interact with lamins and other INM structural proteins such as emerin.

SUN1 and SUN2 are associated at the INM with lamin A. Lamins are intermediate filaments that form a meshwork underneath the nuclear envelope and are responsible for keeping the overall structure of the nucleus. A fraction of SUN1 is associated with a fraction of the NPCs (Liu *et al.*, 2007) and could be responsible for stabilizing the NPC structure through its nuclear envelope distance regulation and its interaction with lamin A.

There are two types of lamins expressed in mammals. Lamin A and C (LaA and LaC) are A-type lamins expressed by the same gene while B-type lamins comprise lamin B1 and lamin B2 (LaB1 and LaB2). These different lamins form distinct networks of filaments. Among them, LaC preferentially interacts with NPCs through its association with Tpr: this interaction could be responsible for the anchoring of NPCs (Xie *et al.*, 2016; Turgay *et al.*, 2017). Mutations in the gene coding for A-type lamins are responsible for laminopathies like progeria (De Sandre-Giovannoli *et al.*, 2003), which induces symptoms that resemble ageing and are linked to abnormal nuclear shape leading to an increased cell death in an organism.

Moreover the NPC interacts with the cytoskeleton through the interaction of Nup358 with microtubules (Jahed *et al.*, 2016). Anchoring of the NPC to the nuclear envelope and cytoskeleton components is important to ensure proper functions of this complex even during cell migration when traction forces are exerted on the nucleus.

3. Nuclear pore complex functions

Each cell has hundreds of NPCs that are more or less evenly distributed in the NE. For example, the mammalian NE has a density of 6-7 NPCs per µm² (Dultz and Ellenberg, 2010). Its crucial position within the NE underlines its main role as the only gateway for nucleo-cytoplasmic transport but a number of Nups fulfil many other functions in eukaryotic cells (Hezwani and Fahrenkrog, 2017) discussed further.

3.1. Nucleo-cytoplasmic transport of proteins

An essential function of the NPC is the control of the nucleo-cytoplasmic transport. The inner pore ring, composed of Nup205, Nup188, Nup93, Nup155 and Nup53/35, forms the plane were most of the action concerning transport takes place. In the middle of the inner pore ring, a set of three Nups, Nup62, Nup58 and Nup54 with intrinsically disordered structures containing FG-repeats acts as a hydrogel. This pattern of thousands of FG-repeats has been shown to be responsible for the permeability barrier and control of the translocation through the NPC in yeast (Strawn *et al.*, 2004; Patel *et al.*, 2007).

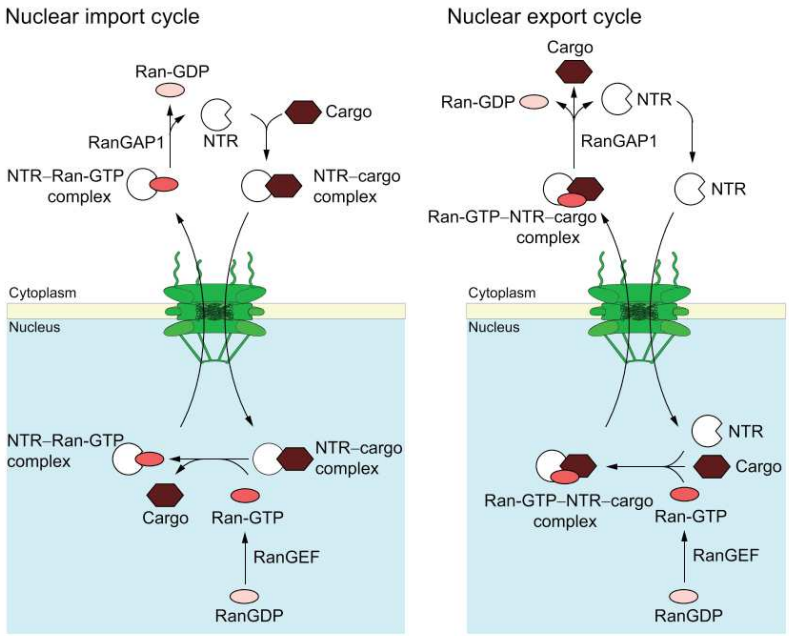

Figure 12: Schematic of the nuclear import (left) and nuclear export (right) cycles (Antonin et al., 2016).

The permeability barrier is a mix of passive diffusion and active transport of molecules. Small molecules (< 40 kDa or 5 nm hydrodynamic radius) can freely diffuse through the NPC while larger elements (> 40 kDa or 5 nm hydrodynamic radius) rely on an active transport mechanism for import and export (Knockenhauer and Schwartz, 2016). Association of a cargo protein to a nuclear transport receptor (NTR), that specifically interacts with FG-repeats, is required for translocation through the nuclear pore. Binding to NTRs is mediated by specific sequences in the cargo proteins: NLS (nuclear localization signal) for nuclear import or NES (nuclear export signal) for nuclear export. Transport is driven by a Ran-GTP/Ran-GDP gradient between the cytoplasm and nucleoplasm (Figure 12).

Among peripheral Nups that contain FG-motifs, some, like Nup214 and Nup358, are present in the cytoplasmic filaments, as well as Nup98 found at cytoplasmic filaments and in the scaffold. They serve as low affinity binding sites that facilitates the initiation of nuclear import while at the basket, the Nup153 FG-repeats might be involved in the initiation of export (Wente, 2000).

To control this transport, the high concentration of FG-repeats from different Nups, located in the central channel of the NPC, acts as a sieve that facilitates or prevents translocation. While early models implied that the transport through the NPC was regulated by the presence or absence of a plug at the central channel, more recent works have shown that this is not true. These investigations have, for example, used the power of atomic force microscopy (AFM) and high-speed atomic force microscopy (HS-AFM) to try to decipher the phenomenon governing this permeability barrier (Liashkovich *et al.*, 2012; Bestembayeva *et al.*, 2015; Sakiyama *et al.*, 2016; Mohamed *et al.*, 2017, 2020; Stanley, Fassati and Hoogenboom, 2017). These results, which mainly focused on the cytoplasmic side of the NPC, revealed that the FG-Nups of the central channel are in fact highly dynamic. These observations along with others helped to build several models (forest, virtual gating, polymer brush and selective phase/ hydrogel) to describe this mechanism (Wente and Rout, 2010; Schmidt and Görlich, 2016). Research effort is also put into attempts to rebuild artificial pores functionalized with FG-Nups to better understand their collective behaviours (Stanley *et al.*, 2019).

All in all, such organization and dynamics of the central channel is responsible for the control of import/export of proteins, RNAs etc.

3.2. mRNA control and export

A consequence of the transport role of the NPC is gene regulation. As described earlier, the physical barrier of the nuclear envelope around chromatin implies that transcription of DNA into RNA occurs inside the nucleus. Gene expression is dependent on the recruitment of transcription factors on chromatin. To reach a specific gene and trigger its expression, these transcription factors must be imported through the NPC. Import of repressors is as important as the one of transcription factors since it will have a direct effect on the correct silencing of genes. Thus, the NPC transport function plays a regulatory role on the production of mRNA in the cell.

The specific mRNA that codes for a protein of interest needs to be later exported into the cytoplasm to reach ribosomes where it will be translated. Here again the NPC is the only way out for mRNA and thus plays a crucial role in cells.

While the export of other types of RNA is similar to the one of proteins via cargo, even though the export of ribosomes still remains unclear, the mRNA export is quite different. First, mRNA is not exported as a single element, but because of its instability, it is bound to several proteins and forms what is called a messenger ribonucleoprotein (mRNP). TRAMP (Trf4–Air2–Mtr4p polyadenylation) complex and exosome protein complexes perform quality control of mRNPs and mature ones are then recruited to the NPC basket.

Mature mRNPs are bound to several Nxf1-Nxt1 heterodimers that will transport them through the NPC. This export is driven by ATP and Nxf1-Nxt1 will be removed when mRNP reaches the cytoplasm leading to a proper mRNA export and ready for transcription.

3.3. Genome organization, gene expression and regulation

The nuclear envelope surrounds the genome of eukaryotic cells and is essential to preserve its integrity. Each chromosome occupies a defined territory that can change between cell types and metabolic states of the cell (Mateos-Langerak *et al.*, 2007). The genome organization is also linked to its interaction with the nuclear envelope.

It has been observed for a long time that while heterochromatin accumulates at the NE, the close vicinity of NPCs is occupied by euchromatin. Chromatin decondensation plays a role in gene expression. In general, localization of genes in the proximity of the nuclear envelope, specifically the nuclear lamina, is associated with gene silencing. Though NPCs are shown to bind silent and active genes, their role in gene regulation is versatile and varies regarding Nups associations.

This role has been mainly investigated in *Saccharomyces cerevisiae* because this model organism is well suited for genomic studies. Indeed, its small size, easy culture, small genome and short generation time allow the study of gene addition or deletion in a eukaryotic context.

The NPC has first been identified as a transcription regulator both negative and positive. While early studies identified it as a gene silencing element, in agreement with its location in the periphery of the nucleus, further works have shown Nups association with promoters of active genes. One important aspect of this process is the location of active genes, since the activation of several genes drives their relocation to the periphery of the nucleus and more specifically NPC-tethering, underlying the role of the NPC in gene expression (D'Angelo, 2018).

In metazoan, research about the role of the NPC in genome regulation is more recent. Some studies have also pointed at an implication of NPC in gene silencing while other work have underlined a role in activation of gene expression (Raices and D'Angelo, 2017; D'Angelo, 2018). In these organisms, two types of regulation have been identified:

the association of genes with NPCs and regulation by free intranuclear Nups which are also present outside of the NPC.

A good example of the gene regulation by Nups away from NPCs is Nup98 that is required for the initiation of transcription at developmental genes loci in *Drosophila* (Capelson *et al.*, 2010; Kalverda *et al.*, 2010) but also binds to a subset of inactive genes. Consistently, Nup98 and other Nups bound to genes in the nuclear interior are mostly dynamic (they shuttle in and out of the NPC) or known to possess an intranuclear fraction.

In mammals, Nup98 is known to shuttle between NPC and nuclear interior in a transcription-dependent manner (Griffis *et al.*, 2002). Indeed, it was also described to regulate gene expression through binding with silent chromatin domains (Liang *et al.*, 2013) that are involved in development and differentiation in higher eukaryotes. Nup98 association with a soluble form of POM121, sPOM121, that has no transmembrane domain also localize at several genes' promoters, targeting multiple genes (Franks *et al.*, 2016). Among these genes are some transcription factors like Myc, that activate the expression of many genes and can stimulate cell proliferation.

Like Nup98, Nup153 can control the expression of developmental genes. In embryonic stem cells, Nup153 is a mediator for the recruitment of the polycomb-repressive complex 1 (PRC1) responsible for some of the gene silencing. This association permits to keep these cells as pluripotent stem cells (Jacinto, Benner and Hetzer, 2015; Raices and D'Angelo, 2017). Several other Nups are suspected to be associated with gene loci and in general little is known about this aspect of Nups functions.

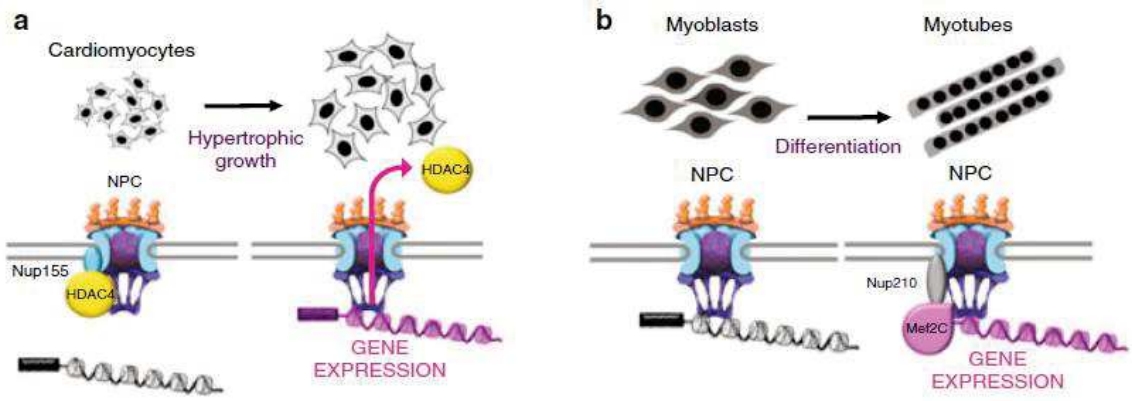

Figure 13: Examples of gene expression regulation at NPC. a) Binding of HDAC4 to Nup155 prevents association of muscle genes with NPC while its export allows the expression of these genes for hypertrophic growth. b) Nup210 (also called gp210) recruits the transcription factor Mef2C to regulate sarcomeric and muscle structural genes that are associated with nuclear pores.

In addition to this intranuclear genome binding, Nups can also be associated with genes at NPCs (Figure 13). This gene regulation at NPC has been particularly shown in mammalian muscle cells. In resting cardiomyocytes for example, binding of the histone deacetylase HDAC4 to Nup155 is responsible for preventing the association of muscle genes with NPCs while its export allows the expression of these genes when the hypertrophic growth of these cells is induced (Kehat *et al.*, 2011).

Another example is the differentiation of myoblasts into myotubes by the regulation of gene expression by the transmembrane gp210 that is specifically expressed and added to NPC during differentiation (D'Angelo, 2018). Gene regulation at NPC is also in good agreement with the different structure of chromatin at NPC compared to the rest of the nuclear periphery.

Although this description of the implication is not exhaustive, it underlines an essential role of the NPC and Nups in gene expression and regulation.

3.4. NPC and nucleoporins roles in mitosis

Not only do Nups exhibit key functions in interphase, but they also play a crucial role during mitosis. In higher eukaryotes, the NE and the NPCs disassemble at the beginning

of prophase through a phosphorylation process of Nups and then reform as soon as chromosome segregation onset.

During mitosis, the NE – including transmembrane Nups – resides in the endoplasmic reticulum, while soluble Nups are released in the cytoplasm. Some of them are involved in crucial steps of the mitosis process. First, members of the Y-complex were involved in the Spindle Assembly Checkpoint: Nup107 and Nup133 localize at kinetochores, supramolecular protein assemblies that attach to centromeres of paired sister chromatids (Belgareh *et al.*, 2001) and link them to microtubules to permit their segregation during mitosis. Indeed, the entire Y-complex localizes at kinetochores during mitosis. Among these Nups, deletion of Seh1, which is the only Nup member of the Y-complex whose depletion does not affect NPC assembly, results in disruption of the Y-complex localization at kinetochores and defects in chromosomes segregation (Zuccolo *et al.*, 2007).

Another Nup associated with kinetochores is Nup358. This peripheral constituent of the cytoplasmic filaments of the NPC is recruited a bit later, after binding of the microtubules to the kinetochores. Depletion of Nup358 is associated with mis-localization of RanGAP1 that seems to disrupt microtubules-kinetochores interactions (Joseph *et al.*, 2004). Nup358 is also known to be important for sumoylation of chromosomal passenger complex (CPC) components and topoisomerase IIα (TopoIIα) that is important for correct progression in anaphase (Dawlaty *et al.*, 2008).

Some of the previously mentioned Nups play a role in centrosomes positioning during early mitosis as well. In G2 phase, this function relies on the anchoring of the dynein-dynactin that is mediated by Nup133 and Nup358 through two independent processes (Splinter *et al.*, 2010; Bolhy *et al.*, 2011). This association with NPCs during the transition between G2/prophase prevents defects of positioning of the mitotic spindle and helps to assure genome integrity during mitosis.

This control of the formation of spindles relies on a checkpoint of their assembly that involves several other Nups. Among them, Tpr, the main constituent of the NPC basket, is essential for the correct function of the spindle assembly checkpoint (SAC) complex (Sang

et al., 2008). Depletion of Tpr or its yeast homologues were shown to dissociate Mad1 and Mad2, two members of the SAC, from NPCs location during interphase and makes Tpr an essential player of the SAC checkpoint machinery.

Similarly, Nup153 is another basket Nup important for SAC since its depletion in HeLa cells leads to increased number of multinucleated cells and multipolar spindle formation because of the hypophosphorylation of Mad1 (Lussi *et al.*, 2010). In addition to SAC regulation, Nup153 plays a role in cytokinesis during mitosis since its depletion leads to an increase of microtubule mid-bodies structures and a failure in cytokinesis (Mackay, Elgort and Ullman, 2009).

Other Nups are probably important during mitosis (Chatel and Fahrenkrog, 2011) but nucleoporins are mainly involved in microtubule nucleation from kinetochores, microtubule-kinetochore attachment, spindle assembly, SAC and cytokinesis.

4. NPC assembly, two main processes to rule them all

4.1. Challenges and complexity of NPC assembly

The assembly of NPCs is an extraordinarily complex process. Because of its numerous constituents and its specific position at the nuclear envelope, NPC assembly is a highly coordinated process of both protein recruitment and membrane remodelling.

The process of NPC assembly has for a long time remained unclear. It is only recently, that this complex combination of recruitment of more than a thousand of proteins through the nuclear envelope has been described to proceed by two distinct mechanisms occurring at different moments of the cell cycle, post-mitotic assembly and interphase assembly (Figure 14) (Doucet, Talamas and Hetzer, 2010; Dultz and Ellenberg, 2010).

At the entry into mitosis, phosphorylation of Nups and other INM proteins like lamins triggers the disassembly of NPCs and the NE. As we saw before, several Nups are implicated in crucial steps of mitosis. Later, at the end of the mitotic process, the NPC must reassemble around chromatin at the same time as the NE to allow complete engulfment of the genetic material by the NE (Figure 14). These post-mitotically assembled NPCs must also be present in sufficient numbers, complete and functional to allow rapid progression of the cell cycle thanks to a proper translocation mechanism. The post-mitotic assembly occurs on the timescale of around 12 minutes (Dultz *et al.*, 2008; Anderson *et al.*, 2009).

The challenges for interphase assembly are of a completely different nature. The number of NPCs must double before the next mitosis where they will be split into the daughter cells. While the recruitment of all Nups is also a key point, this process takes place in a membranous environment. Insertion of a new NPC takes place in an intact nuclear envelope where the INM and the ONM have to fuse at the end of the process to create a channel in the NE (Figure 14). This important membrane remodelling process of interphase assembly must be highly coordinated with the recruitment of the different Nups to prevent any leakage between the nucleus and the cytoplasm. Symptomatic of the different cellular context in

which it happens, interphase assembly occurs on a timescale of an hour (Dultz and Ellenberg, 2010).

Because the interphase assembly process is slow, it is incompatible with a very rapid cell division that occurs at early stages of development in *Drosophila melanogaster,* for instance. In this particular case, a third NPC assembly pathway has been identified. Some regions of the ER are packed with pre-assembled NPCs called *annulate lamellae*. In fact, these NPCs contain most Nups except for the asymmetric domains (cytoplasmic filaments and nuclear basket) (Soupart and Strong, 1974; Spindler and Hemleben, 1982). In early embryos of *D. melanogaster*, *annulate lamellae* are more abundant, and they are used to rapidly assemble new NPCs alternatively to the slow process of interphase assembly that would be limiting in this fast growth phase. This process suggests that large patches of ER containing *annulate lamella*e can be integrated into the NE, followed by the recruitment of peripheral Nups to end up with complete and functional NPCs (Lénárt and Ellenberg, 2003; Hampoelz *et al.*, 2016).

Post-mitotic and interphase assembly represent different challenges and mechanisms for NPC assembly that will be later explained in more detail. This difference is related to the cellular environments in which pores assemble. Indeed, assembly processes are biochemically adapted to the matrices in which pores assemble: nuclear membrane or naked chromatin. Interestingly, ELYS, which is critical for NPC assembly at the surface of chromatin, is only present in organisms with an open mitosis. This reflects that NPCs have evolved to adapt to their membrane environment, but also to the constraints related to their assembly process. During post-mitotic assembly, the reformation of NPCs is initiated by the seeding of ELYS at the surface of chromatin, thanks to its capacity to bind DNA through an AT-hook motif (Rasala *et al.*, 2006; Franz *et al.*, 2007). Different homologs of ELYS have been found between vertebrates and fungi while it is absent in yeast (Rasala *et al.*, 2006). This is remarkable since yeast undergoes closed mitosis, analogous to interphase. Higher eukaryotes have NPC assembly during both interphase and mitosis. A study has shown that the homolog of vertebrate ELYS in *Aspergillus nidulans* lacks the AT-hook motif characteristic of the vertebrate ELYS proteins important to initiate NPC assembly on chromatin during mitosis by recruiting Pom121- and Ndc1-containing vesicles (Liu *et al.*, 2009). During mitosis, the *Aspergillus*

nidulans ELYS remains associated with the NE and no seeding on chromatin is observed. The *Aspergillus nidulans* ELYS is also dispensable for NPC assembly. This suggests that the evolution of the complexity and length of the vertebrate ELYS has led to acquisition of new functions that are not shared with fungi but that allows ELYS to recruit vertebrate Nups members of the Y-complex on chromatin during postmitotic NPC assembly.

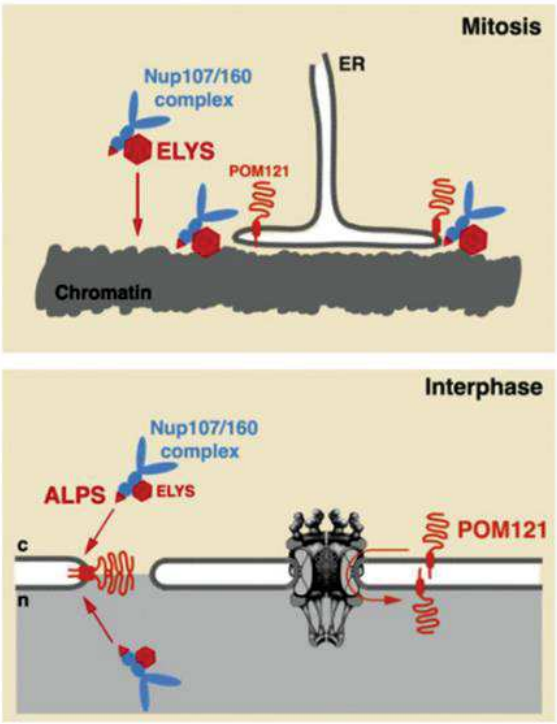

Figure 14: Two NPC assembly processes represented by Doucet et al. (Doucet, Talamas and Hetzer, 2010). Mitosis assembly is triggered by seeding of ELYS onto chromatin. Others Nups will be recruited in the context of a reforming NE to build a full NPC. Interphase assembly consists in a de novo insertion of new pores in an intact NE with POM121 being the earliest Nup recruited.

4.2. Post-mitotic NPC assembly

As mentioned before, this process is initiated by the DNA-interacting motif present in ELYS. Concomitant recruitment of the rest of the Y-complex leads to the formation of pre-pores, structures that gets embedded within the reforming NE through their interaction with the transmembrane Nups POM121 and Ndc1, that functionally link NPC assembly and nuclear envelope reformation at the end of mitosis (Antonin *et al.*, 2005; Mansfeld *et al.*, 2006; Franz *et al.*, 2007). This reformation of the NE has been proposed to be based on the remodelling of

endoplasmic reticulum membrane and its capacity to form sheets. ER provides the lipids necessary for the NE reformation, mediated by DNA-binding proteins present in the ER (Anderson and Hetzer, 2007). Fenestrated ER sheets were also shown to assemble close to the chromatin in which the holes would slowly shrink to a size close to the NPC diameter where scaffold Nups would insert (Otsuka *et al.*, 2018). Recruitment of the remaining Nups and sealing of the nuclear envelope result in functional NPCs that are not evenly distributed within the nuclear envelope: indeed post-mitotic pore assembly is delayed in the so-called 'core regions' where the dense spindle microtubules first need to be removed from the chromatin surface (Otsuka *et al.*, 2018). As a result, these areas are almost devoid of pores at the end of mitosis and undergo very active NPC interphase assembly in early G1 phase of the cell cycle (Otsuka *et al.*, 2016; Mimura *et al.*, 2017). The whole post-mitotic assembly process is relatively fast and happens on the timescale of around 12 minutes (Anderson and Hetzer, 2008; Dultz *et al.*, 2008).

After the first steps of assembly, NDC1 interacts with Nup53, a membrane-binding Nup of the inner ring complex that is then recruited at these NPC formation sites (Vollmer *et al.*, 2012). Through Nup53 specific interaction with Nup155 (Eisenhardt, Redolfi and Antonin, 2014), subsequent recruitment of NPC inner ring Nups occurs, followed by peripheral Nups that will lead to complete functional NPCs at the end of mitosis (Figure 15) (Otsuka and Ellenberg, 2018).

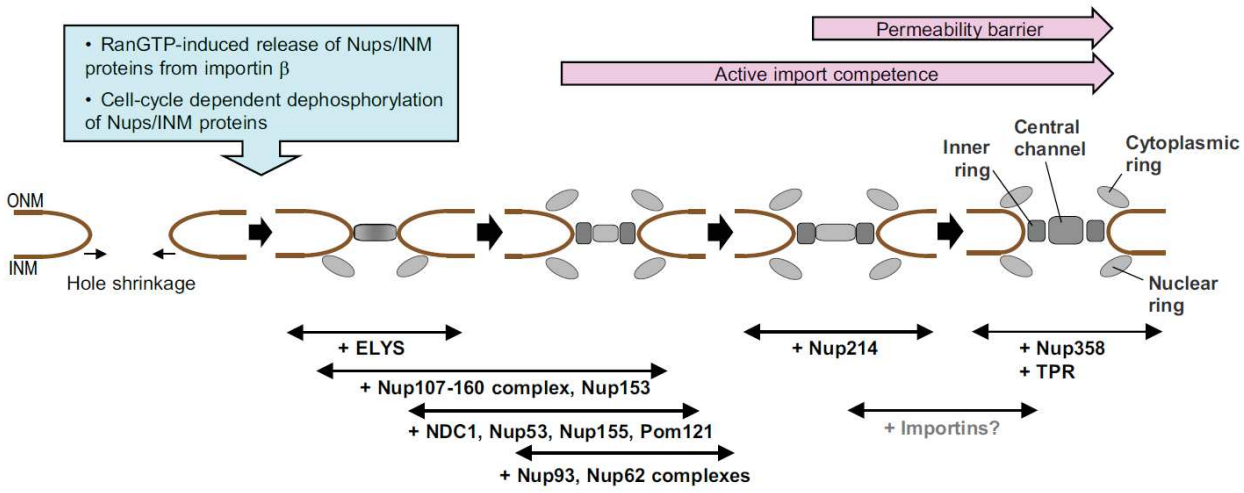

Figure 15: The different steps of post-mitotic assembly of NPC and the successive recruitment of Nups as described by Otsuka et al. (Otsuka and Ellenberg, 2018).

4.3. Topology of NPC interphase assembly

On the other hand, during interphase, the number of NPCs must double before the next mitosis as they will be split between the two daughter cells. In contrast to post-mitotic assembly, the formation of new NPCs occurs in the context of an intact nuclear envelope that must keep its permeability barrier integrity. Thus, the formation of these new NPCs must occur in a manner that does not disrupt the nuclear envelope and is not a source of leakage because of the formation of incomplete NPCs. While for some time, hypotheses were made about the possibility of a "division" of pre-existing NPCs to form new channels, later studies described a *de novo* formation of NPC into the NE (D'Angelo *et al.*, 2006; Doucet, Talamas and Hetzer, 2010; Dultz and Ellenberg, 2010).

This idea of a potential specific interphase assembly of the NPC had first been suggested by an electron microscopy study of Maul et al. in 1971 (Maul, Price and Lieberman, 1971). Their experimental approach was to stimulate the entry in mitosis of lymphocytes by treatment with phytohemagglutinin (PHA) for 48h and to image their nuclei with an electron microscope before they would undergo mitosis. The PHA has the property to change the metabolic activity of these cells from a resting state to a much more active one by inducing blast transformation. The observation of control and PHA-treated lymphocytes showed a higher number and higher density of NPCs in PHA-treated cells with around twice as many NPCs. These results suggested that the number of NPCs must at least double before the next cell mitosis and thus supported the assumption of NPC assembly during interphase. This study also showed that NPC assembly is stimulated in cells with higher metabolism.

Besides this observation, Maul et al. used rat kidney cell nuclei to study the distribution of NPCs in the NE. Their experiments show a non-random distribution of NPCs within the NE that is characterized by a minimal distance between NPCs that could be determined by the physical properties of the complex and membrane curvature and later described through modelling approaches (Torbati, Lele and Agrawal, 2016). Another observation was the apparition of specific frequencies in the pore-to-pore distance that also suggest a typical distance between NPCs. This distance could be determined by the position and structure of the genetic material present under the nuclear envelope.

An interesting observation was made: the presence of particle-free patches on the ONM, located in the typical distance range from surrounding NPCs. This suggested that new pores may assemble in these areas. Indeed, searching for prospective NPC assembly sites, several objects were identified. They exhibit a granular electron-opaque (see NPC 11, 12 and 15 in Figure 16) structure smaller than fully assembled NPCs and are correlated with an absence of heterochromatin at their nucleoplasmic side. These assembly sites are often associated with a circular electron-opaque structure, wider than a normal NPC and visible on the nucleoplasmic side (see the second consecutive image in Figure 16).

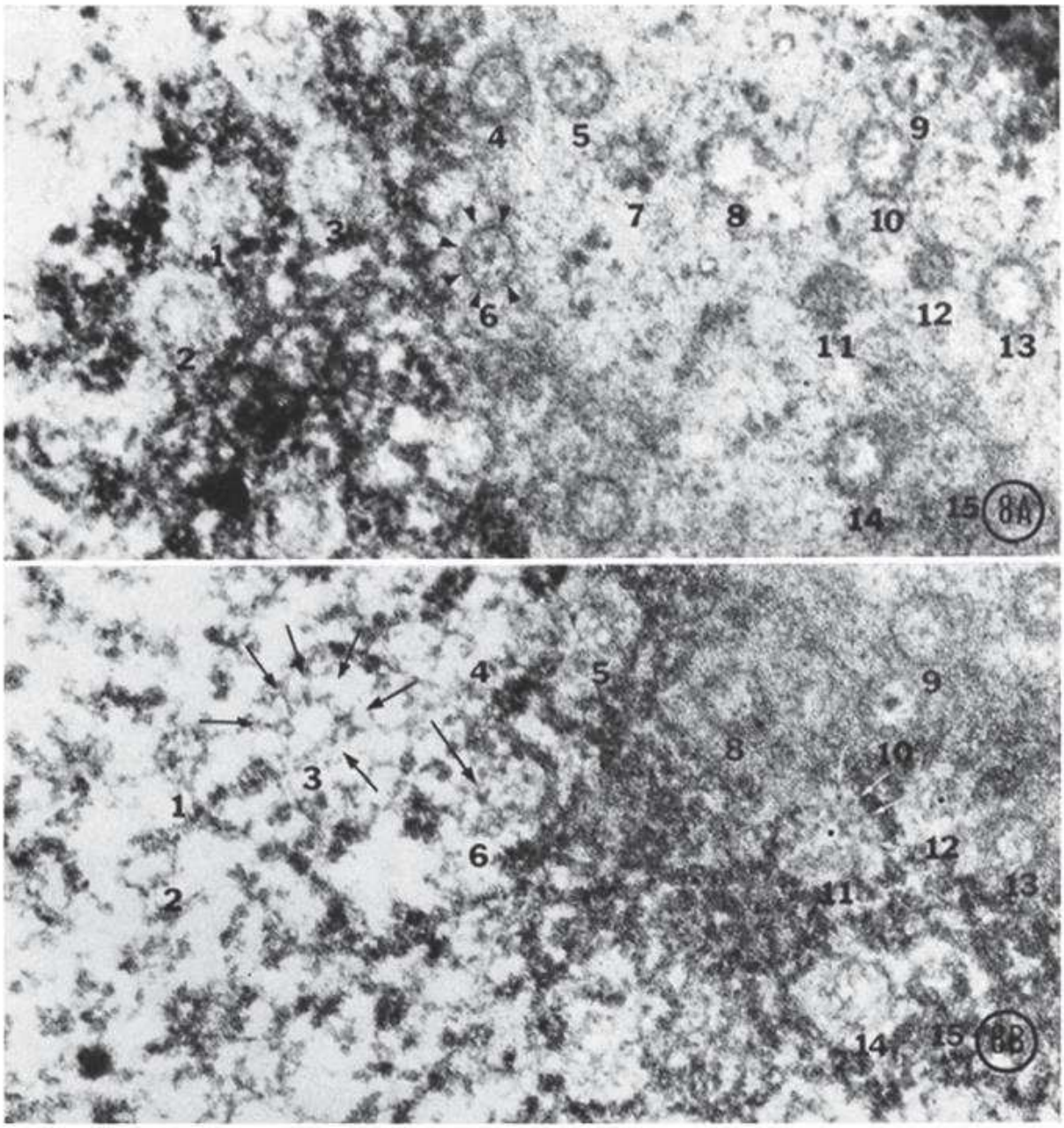

Figure 16: NPC assembly sites (11, 12 and 15) observed by Maul et al. in 1971. The images correspond to two consecutive sections parallel to the nuclear envelope (Maul, Price and Lieberman, 1971).

Finally, this study shed the first light on the possible directionality of the interphase NPC assembly process. Cross-sections of the nuclear envelope showed the presence of an electron-opaque structure that is present at the INM and bends the INM towards the ONM (Figure 17). It resembles the structures observed before in the face-on view of the ONM (NPC 11, 12 and 15 in Figure 16, electron-opaque area). These indentations of the INM were also observed in freeze-etched nuclear membranes of stimulated lymphocytes but no such structure was observed at the ONM. Only bare areas of membrane, slightly larger than the NPC were visible, like the ones observed in rat kidney cells (Figure 18). Even though their role is not clear, the hypothesis of a correlation of this ONM bare area and the INM indentation in the NPC interphase assembly process has been formulated as a hypothesis.

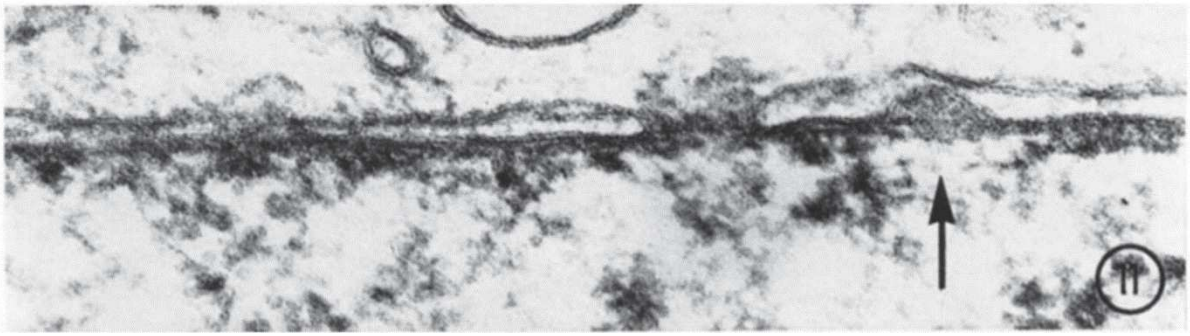

Figure 17: Cross-section of the nuclear envelope exhibiting an indentation at the INM corresponding to putative NPC interphase assembly site (Maul, Price and Lieberman, 1971).

It is only forty-five years later that this first observation and intuition of Maul et al. was confirmed by another electron microscopy study (Otsuka *et al.*, 2016). The fact that these events are spread on a large timescale (on the order of the cell cycle) and on a large area makes the study of interphase pore assembly rather difficult. The occurrence of pore intermediates at a given time is thus low. To enrich these events, Otsuka et al. used a structural characteristic of the freshly divided nuclei in telophase: the simultaneous assembly of numerous pores in a specific region of the growing NE.

At this stage, after reformation of the NE, there is a high number of *de novo* interphase assembly events, more specifically in the inner-core regions (Figure 19). This high rate of insertion of new NPCs is synchronized and thus can be used to study the kinetics of assembly with techniques based on an averaging strategy. By using time-points from anaphase onset

occurrence in the cells, Otsuka et al. reconstituted the kinetics of interphase pore assembly in early G1 phase in mammalian cells.

Otsuka et al. focused on the so-called “core-regions”, where the spindle microtubules disassemble. These regions of the NE after mitosis display a delay in the reformation of the NE leading to the formation of bare NE areas devoid of NPCs (Vietri *et al.*, 2015). While non-core regions are known to be the place where post-mitotic NPC assembly mainly occurs, the assembly of new NPCs in the “core regions” is triggered later, during early G1 phase. Otsuka et al. quantified this higher probability of NPC interphase assembly and showed that assembly in inner-core regions was higher than in non-core regions during the first hour after mitosis, a moment where this interphase assembly is known to be very active (Maul *et al.*, 1972).

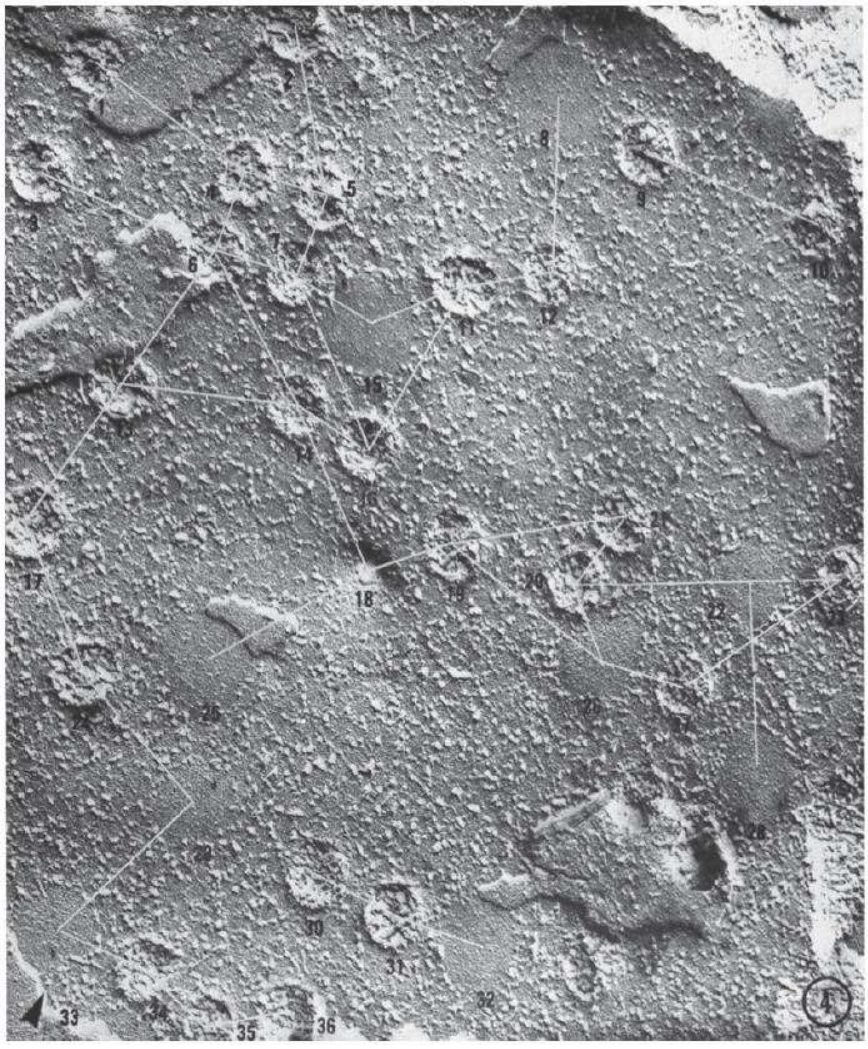

Figure 18: ONM of cells exhibiting smooth area of membrane that could correspond to NPC interphase intermediates (Maul, Price and Lieberman, 1971). White lines illustrate distance between NPCs and potential NPC assembly sites.

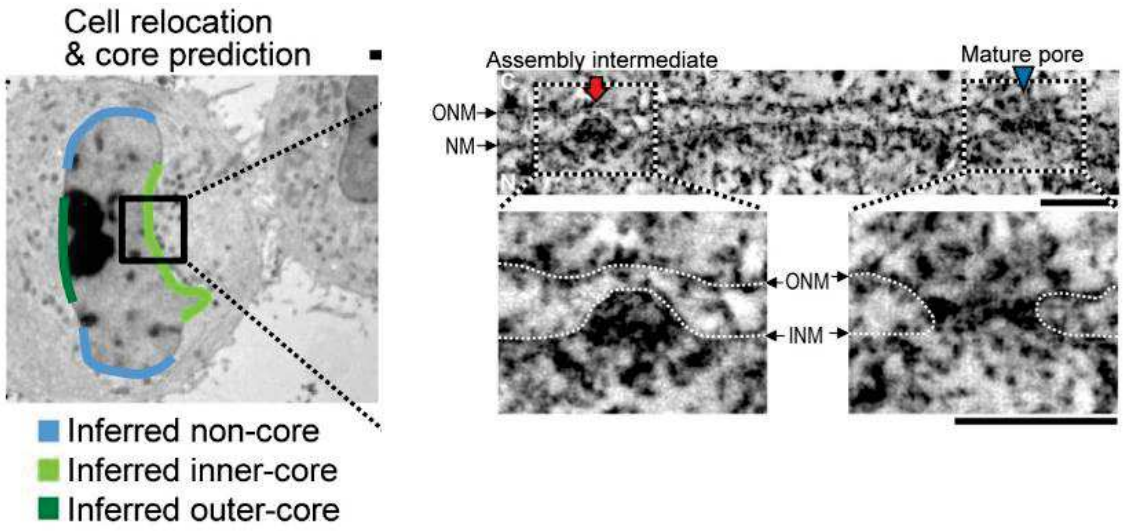

Figure 19: EM image of a cell with core and non-core regions of the NE identified by Otsuka et al. INM invagination and mature pore as observed by Otsuka et al. using EM. Dashed lines represent the membrane of the NE. Scale bar 100 nm.

Focusing on this area, Otsuka et al. have been able to observe depressions in the INM and describe the evolution of the structure of NPC assembly intermediates. The nuclear pore assembly in interphase requires high coordination of membrane remodelling and protein recruitment. For the membrane remodelling, Otsuka et al. clearly confirmed that this process occurs from the INM where assembly sites exhibit hollows increasing in depth from 16 to 22 nm, where it reaches the ONM. The deformation of the ONM was however small and observed only for the intermediates showing the deepest INM deformation. Progression in membrane remodelling is also visible as the membrane deformation area increases in diameter. Accordingly, the electron-opaque structure occupying the membrane depression increases from 51 to 58 nm in diameter (Figure 19 and 20).

Otsuka et al. thus further studied the structure of the complex formed by proteins visible in places where INM deformation was observed. Doing so and using the same time-points as before, they were able to describe distinct stages of the formation of an NPC in interphase and associated INM membrane deformation.

Averaging tens of structures for each time-point, they describe a protein assembly composed of two different structures. The main one is the central “mushroom” that grows laterally and vertically and seems to be responsible for the INM deformation. The other

element present is a ring structure around the "mushroom" that is present from the earliest step observed and does not seem to change a lot, except that its diameter seems slightly smaller in the first time point at 19 minutes time-point. Another remarkable aspect is the eight-fold rotational symmetry of this ring, noticeable from the earliest time point and characteristic of NPCs. In comparison with the image of a mature NPC observed in this study, the ring structure appears similar to the nucleoplasmic or cytoplasmic ring (Figure 20).

This study strongly supports the directionality of NPC assembly during interphase, that occurs by an inside-out extrusion of the nuclear envelope and offers a particularly important description of some of its steps. The formation is mediated by a mushroom-like central structure that associates with members of the nuclear ring around it that might stabilize the membrane while the central "mushroom" is growing towards the ONM until its fusion and final maturation of NPC.

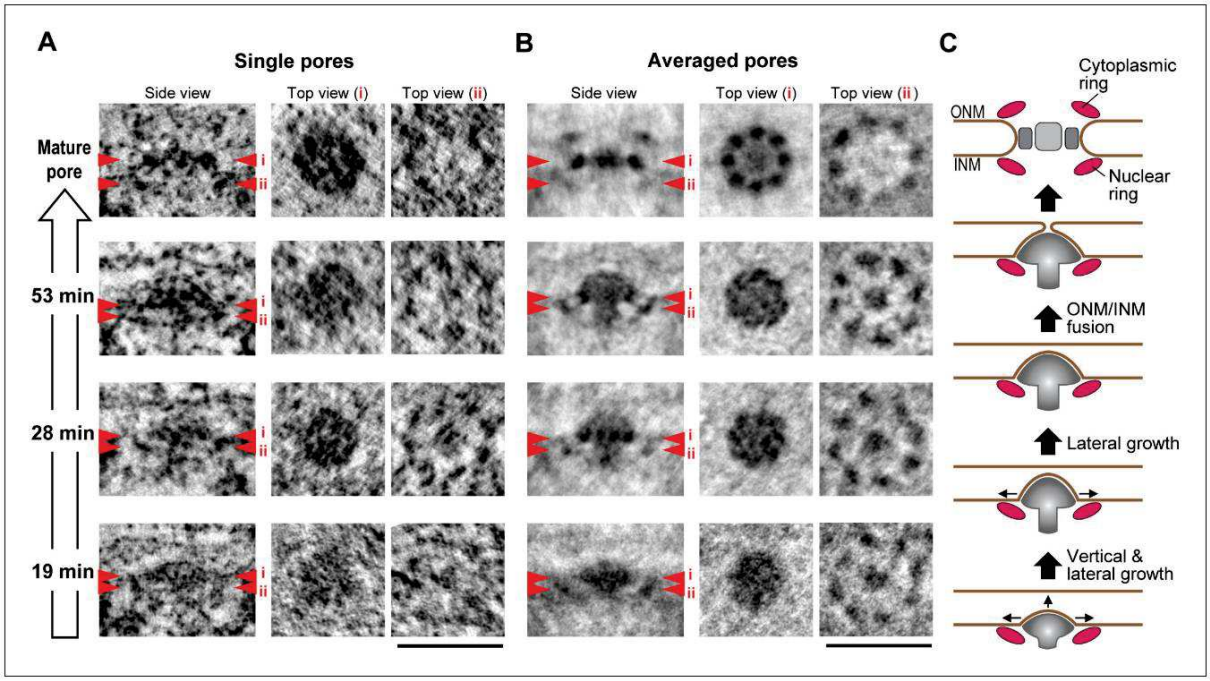

Figure 20: Model for NPC interphase assembly by Otsuka et al. Images of single and averaged pores observed by EM at specific time points after anaphase onset. Side views of the average structure show a central "mushroom" shape growing towards the ONM over time. Top views exhibit an eight-fold rotational symmetry from the earliest stages of assembly. Scale bars 100 nm.

Although this work shows that interphase assembly starts from the nucleoplasm and can detail some steps, many aspects of this process remain unclear. First, the early steps

presented in the paper already present a complex combination of a “mushroom” and a ring structure that might not be the starting point of this assembly and the earliest intermediate structures are thus missed. These very early structures are known to contain early Nups that are members of the transmembrane Nups (Dultz and Ellenberg, 2010) and might not be easily distinguishable on electron microscopy images.

In addition, the comparison of late intermediates structures with mature NPCs shows a quite different morphology that underline a drastic change in the structure concomitant with INM and ONM fusion. These last steps of assembly are missing most probably because of the short time scale at which they occur, preventing Otsuka et al. from catching this event. Thus, assembly and positioning of key elements of the NPC like the cytoplasmic ring remains unclear.

Finally, this study does not address in detail the order of recruitment of Nups and proteins responsible for these structures along the assembly and maturation of the nascent NPC.

4.4. Yeast as a model for interphase assembly

Yeast is a unicellular eukaryotic organism that belongs to the kingdom of fungi which has been widely used as the first model to decipher NPC assembly in an intact NE. Yeasts like *Saccharomyces cerevisiae* possess a specific trait: during cell division, they undergo a closed mitosis. It means that their NE never disassembles. In consequence, their NPC assembly always occurs in a membranous context analogous to interphase assembly of higher eukaryotes (Winey *et al.*, 1997). For this reason, and because it is easy to manipulate their genome to investigate the role of specific genes and proteins, yeasts have been widely used in an attempt to understand the process of NPC interphase assembly. However, the low conservation of Nups between yeasts and other organisms makes it difficult to transpose the observations on NPC assembly to higher eukaryotes. Still, their study allows extracting trends about the process.

4.5. *Xenopus laevis* oocyte model

Xenopus laevis oocytes have also been used as a model system to study NPC assembly. Nuclei can be assembled *in vitro* from *Xenopus* egg extracts and this strategy has been extensively used to study the mechanisms of NE and NPC post-mitotic assembly. Several works adapted the standard nuclear assembly procedure to study the incorporation of new pores in the sealed NE during nuclear expansion (D'Angelo *et al.*, 2006; Doucet, Talamas and Hetzer, 2010; Fichtman *et al.*, 2010).

Besides the use of egg extracts to recapitulate NPC assembly pathways, direct purification of nuclei from *Xenopus laevis* is a standard sample preparation to study NPC by AFM. The large size of the nuclei (around 200 µm in diameter, ≈ ten times larger than mammalian nuclei) allows one to manually open them and remove chromatin with a micro-pipette. The higher density of NPCs in this system is also interesting for sampling of NPC topography and characteristics by AFM which is a slow technique generally not suited for statistics. This approach allowed high resolution AFM imaging of complete NPCs from both cytoplasmic and nucleoplasmic side (Kramer *et al.*, 2008; Sakiyama *et al.*, 2016; Stanley, Fassati and Hoogenboom, 2018), as shown in Figure 21.

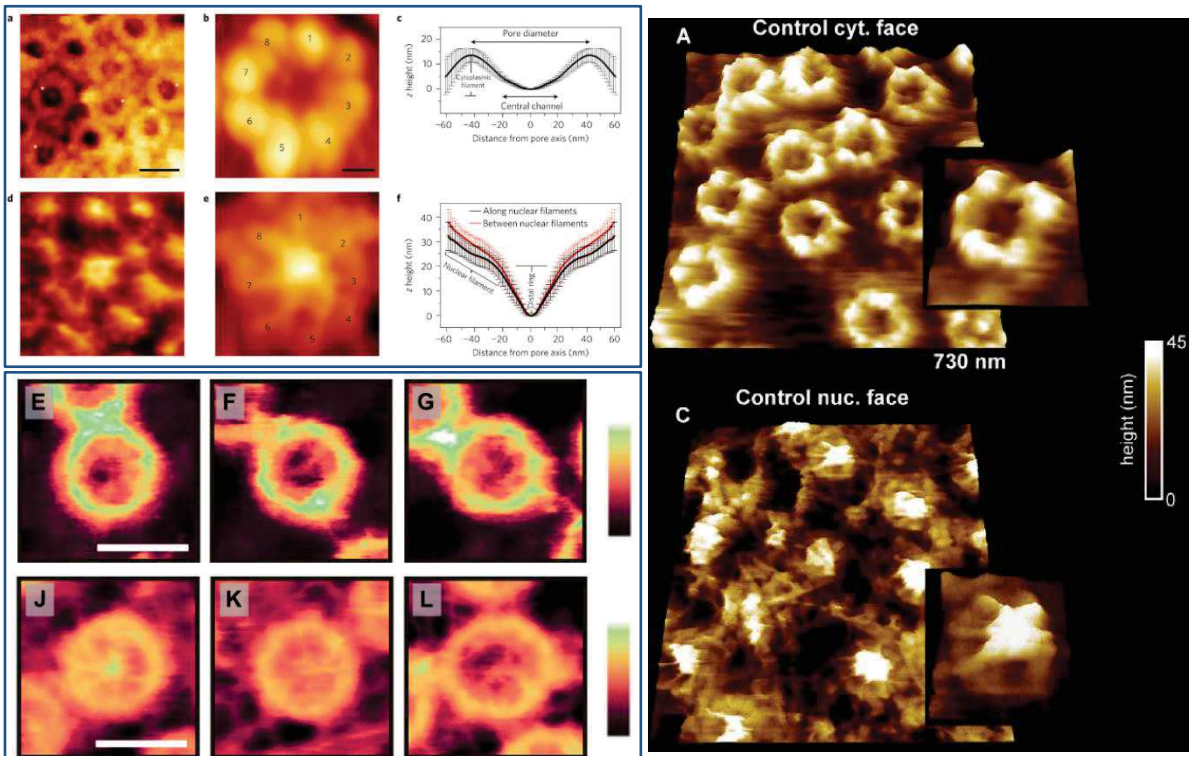

Figure 21: NPCs in Xenopus laevis observed from both cytoplasmic and nucleoplasmic side by AFM by Sakiyama et al. (top left panel), Stanley et al. (bottom left panel) and Kramer et al. (right panel).

Xenopus NEs could be an interesting system to study NPC assembly, as this model organism is closer to a human NPC than yeast for instance. However, there are several drawbacks since oocytes correspond to a specific stage of development that does not reflect the NPC state in somatic cells. For example, Sellès et al. showed that the NPC diameter can vary depending on the oocyte development stage (Sellés *et al.*, 2017) and Stanley et al. revealed specific perpendicularly organized lamina and the NPC (Stanley, Fassati and Hoogenboom, 2018) which is different from the one known in somatic cells (Turgay *et al.*, 2017). Moreover, it is not clear in which stages NPC assembly is active.

4.6. Key players of the NPC interphase assembly

NPC interphase assembly is characterized by the formation of an invagination at the INM surrounded by a ring-like structure with an eight-fold rotational symmetry. Electron microscopy provides a high-resolution view of this characteristic topology, but other techniques are required to identify the proteins and Nups involved in this process and understand the key roles they play.

All Nups must be recruited at a certain point of the interphase assembly process but other proteins are involved or essential for correct assembly. Little is known about the early steps of interphase assembly while it is expected that peripheral Nups like cytoplasmic filaments are most probably recruited at late stages. However, the membranous context in which NPCs assemble during interphase points at an essential role of the transmembrane Nups in this process.

The roles of the three vertebrate transmembrane Nups - gp210, Ndc1 and POM121 - have thus been investigated. While gp210 is conserved among most organisms, its presence for interphase NPC formation appears dispensable in mammalian cells (Eriksson, Rustum and Hallberg, 2004; Antonin *et al.*, 2005; Stavru *et al.*, 2006).

Ndc1 is also a fairly well conserved Nup, present from yeast to mammals (Lau, Delmar and Forbes, 2006). Its role in NPC assembly has been shown *in vivo* and *in vitro* by RNA interference experiments in vertebrate cells where its depletion strongly affects the NPC and

NE reformation after mitosis (Mansfeld *et al.*, 2006; Stavru *et al.*, 2006). Ndc1, a crucial membrane-integral Nup of metazoan NPCs presumably anchors the NPC inner ring since the analysis by Mansfeld *et al.* suggests a functional link between Ndc1 and Nup93, Nup205 and Nup53. Indeed, the study showed direct *in vitro* interaction of Ndc1 with Nup53. This interaction has been further investigated (Eisenhardt, Redolfi and Antonin, 2014) and it was shown in *Xenopus laevis* that the Nup53 binding site with Ndc1 overlaps with a membrane bending region of Nup53. This suggests that the interaction of these two Nups might be regulated by membrane insertion.

Indeed, the ability to bind or coat membranes is a key aspect of NPCs, which is functionally relevant but also supported by a high degree of conservation between Nups and membrane coats such as COP proteins. As mentioned above, Nup53 is one of these membrane binding Nups. In addition to the interaction with Ndc1, Nup53 is associated with other elements of the NE, which suggests their role during the early steps of NPC assembly. First, Nup53 interacts with Nup93, Nup205 and Nup155 to form stable complexes and is associated with the lamina through an interaction with lamin B in human cells (Hawryluk-Gara, Shibuya and Wozniak, 2005). In yeast, overexpression of Nup53 results in INM extensions inside the nucleoplasm with the formation of incompletely assembled NPCs (Marelli *et al.*, 2001). Nup53 has also been shown to directly bind and deform membranes *in vitro* through a C-terminal binding domain. Moreover, membrane binding and bending depends on Nup53 dimerization (Vollmer *et al.*, 2012). Other works have further determined that Nup53 is required for NPC and NE assembly and that it specifically interacts with Nup155, which is the Nup bridging the inner and outer rings of the NPC (Hawryluk-Gara *et al.*, 2008; Eisenhardt, Redolfi and Antonin, 2014). This binding is essential for NPC assembly, probably because it allows correct assembling with the Y-complexes of the outer rings. Altogether, these data suggest a role of Nup53 in the early stages of NPC interphase assembly, and possibly in membrane deformation.

POM121 is a transmembrane Nup conserved in vertebrates, and the most important regarding NPC interphase assembly. It has one transmembrane domain, a short luminal part and on the other side of the transmembrane domain, there is a long unstructured domain pointing towards the NPC central channel when POM121 is at the NPC. POM121 has been

shown to link NPC to the NE (Antonin *et al.*, 2005) and is essential for NPC interphase assembly (Doucet, Talamas and Hetzer, 2010; Funakoshi *et al.*, 2011). Most importantly, POM121 is the earliest Nup detected at assembly sites in interphase and is present before the Y-complex (Figure 22) (Dultz and Ellenberg, 2010).

This kinetics of recruitment of POM121 is indeed different between post-mitotic and interphase assembly. In post-mitotic assembly, the seeding event for NPC assembly is the recruitment of the Y-complex on chromatin, mediated by ELYS, while the order is inverse for interphase assembly (Doucet and Hetzer, 2010; Doucet, Talamas and Hetzer, 2010).

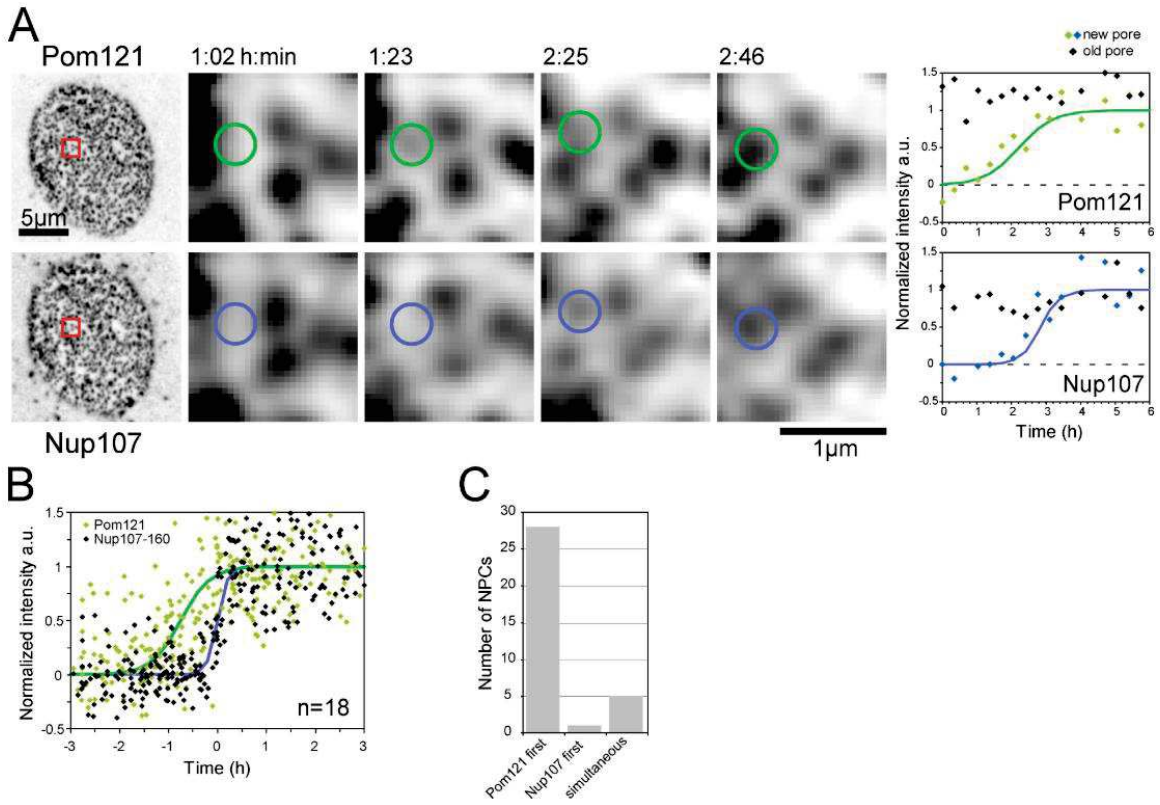

Figure 22: Live imaging of Nups recruitment of Nups during interphase assembly by Dultz et al. (Dultz et al., 2010) revealed that POM121 is the earliest Nup at assembly sites and that its kinetic of recruitment is slower than the one of Nup107.

POM121 recruitment during interphase is slower than other Nups and thus is viewed as a limiting element of interphase assembly (Doucet, Talamas and Hetzer, 2010; Dultz and Ellenberg, 2010). siRNA against POM121 inhibits NPC interphase assembly and results in areas devoid of pores but does not affect NPC post-mitotic assembly (Doucet, Talamas and Hetzer, 2010). These results suggest that POM121 is an essential early player in interphase assembly

but is dispensable for post-mitotic assembly. The interphase assembly function also relies on POM121 localisation at the INM thanks to a domain interacting with INM and lamin B (Funakoshi *et al.*, 2011). The correct function of the NLS signal of POM121 is essential for its proper import and targeting to the INM (Yavuz *et al.*, 2010). These observations take all their significance now that interphase assembly is known to proceed from the INM.

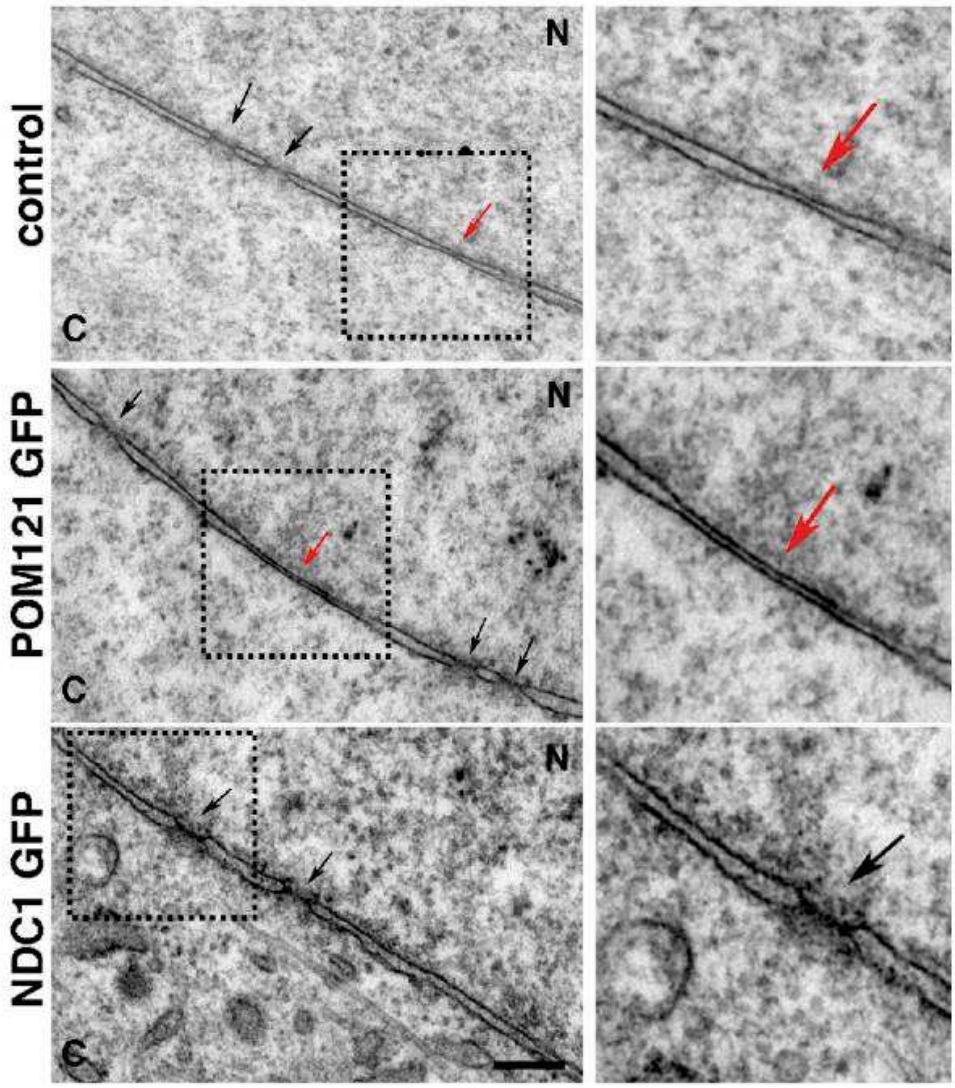

Figure 23: POM121 overexpression results in large patches of INM and ONM in close proximity in comparison with overexpression of membrane integral Nup NDC1 and control (Talamas and Hetzer, 2011). N and C respectively indicates nucleoplasm and cytoplasm. Black arrows indicate NPCs, red arrows indicate INM and ONM close apposition areas. Scale bar is 200 nm.

Finally, overexpression of POM121 in cells induces long stretches of close apposition between the INM and ONM (Figure 23), which suggests a role of POM121 in bringing together these membranes. But its luminal domain is too short to bridge the two nuclear membranes, suggesting that POM121 must rely on partners, like SUN1, for this task.

Nup153 is another key element of NPC interphase assembly. It was shown in yeast that its homolog, Nup1 and Nup60, have membrane binding domains and can bend membranes *in vitro* and reshape the NE. It functionally interacts with other Nups involved in NPC formation (Mészáros *et al.*, 2015). Experiments in vertebrate cells demonstrated that Nup153 can directly bind lipid membranes and that it is required for proper interphase assembly. Nup153 recruits the Y-complex at the INM and thus might be among the early Nups involved at NPC assembly sites (Vollmer, Lorenz, Moreno-Andrés, Bodenhöfer, De Magistris, *et al.*, 2015). These data suggest an evolutionarily conserved role of Nup153 in interphase assembly.

Several Nups can directly interact with membranes, especially among the Y-complex. Nup133 has a membrane curvature sensing motif, which is an amphipathic helix that can sense specific membrane curvature and was suggested to be essential for interphase assembly (Walther *et al.*, 2003; Doucet, Talamas and Hetzer, 2010; Doucet *et al.*, 2015). Recent work has questioned the requirement of Nup133 since the deletion of Nup133 in embryonic stem cells concluded that it is dispensable for interphase assembly (Souquet *et al.*, 2018). In this study, the NPC number in fact doubled during interphase even in the absence of Nup133, but proper nuclear basket assembly was affected. An increased dynamics of Nup153 *in vivo* has been observed which might be an alternative pathway for correct interphase assembly since an amphipathic helix motif has been reported in Nup153 (Vollmer, Lorenz, Moreno-Andrés, Bodenhöfer, De Magistris, *et al.*, 2015).

Among non-Nups proteins involved in interphase assembly, Talamas and Hetzer demonstrated the essential role of SUN1 in early stages (Talamas and Hetzer, 2011). SUN1, which links the INM and ONM, is sometimes associated with NPCs and this fraction seems to be enriched at interphase assembly sites. Moreover, its depletion results in defects in interphase assembly. One interpretation of these results is that the control of the distance between the INM and the ONM is a key parameter for interphase assembly. ER-membrane bending proteins which contains hairpins inserting in lipid membranes like Reticulon-4a might also play a role. The conserved YOP/Rtn family was shown to be important for *de novo* insertion of NPC in yeast and *Xenopus laevis* since their inhibition prevented NPC assembly (Dawson *et al.*, 2009). Hairpins could contribute to some specific stages of assembly including membrane remodelling actions.

Membrane remodelling observed in NPC interphase assembly is possible because of the specific recruitment of proteins, mainly Nups, involved at these specific assembling sites. Other Nups known to be implicated in membrane remodelling somewhere else in the cell such as Sec13 might also help in this process. The role of FG-repeats containing Nups has also been reported as a stabilizer of the assembly sites (Onischenko *et al.*, 2017). Finally, the specific concave deformation of the INM could be facilitated by the presence of specific geometric lipids (Fichtman *et al.*, 2010)

Recent works have tried to understand the kinetics of interphase assembly. Experiments in yeast performed by Onischenko *et al.* used metabolic labelling applied to NPC to try to better understand the process of interphase assembly in this organism (Onischenko *et al.*, 2020). Their results suggest that NPC individual sub-complexes form in a minute timescale, while the co-assembling of these subcomplexes is limiting and completes in an hour-long process delayed by the slow recruitment of peripheral Nups.

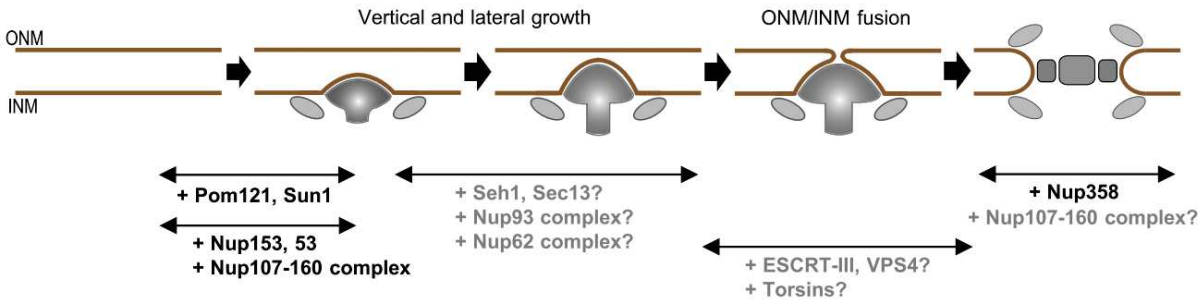

Figure 24: Model interphase assembly Otsuka et al. 2018

In conclusion, NPC interphase assembly is a complex process which requires the synchronized action of Nups and non-Nups proteins to assemble, bend and fuse the two membranes of the nuclear envelope. The exact kinetics and sequence of actions and proteins involved in this process is still poorly known. However certain aspects of this assembly have been described in the literature (see model in Figure 24). POM121 is essential for interphase assembly and up to now the earliest protein identified at assembling sites. SUN1 is also an important player of these early steps. The following steps of assembly most probably require membrane bending activity that could be performed by proteins like Nup53 or reticulons. Nup153 can also bend membranes and is then responsible for the recruitment of the Y-

complex to the INM. Intermediate stages of the assembly and fusion process are less known and implication of several proteins (Seh1, Sec13, Nup93 complex, Nup62 complex, ESCRT-III etc…) has been suggested. Finally, Nup358, present in cytoplasmic filaments as well as peripheral Nups are probably recruited in the last step.

4.7. Importance in cancer

NPC assembly would be a very interesting pathway to target to cure cancer. It is important to say that NPCs are extremely stable. In particular, most nucleoporins constituting the NPC scaffold only turn over during mitotic NPC disassembly (Rabut, Doye and Ellenberg, 2004). As a consequence, NPCs are not renewed in non-dividing (post-mitotic) tissues (Savas *et al.*, 2012). NPC assembly is thus a process specifically active in dividing cells. This may be even more critical in cancer cells as high metabolic activity increases the number of NPCs per nucleus (Maul, Price and Lieberman, 1971; Maul *et al.*, 1972; Many *et al.*, 1981). As a matter of fact, chemotherapy-resistant cells have more NPCs per nucleus than their drug-sensitive counterparts and it has been shown that depletion of Tpr regulates the number of NPCs per nucleus (McCloskey, Ibarra and Hetzer, 2018). Moreover, inhibition of nucleo-cytoplasmic transport reverts drug resistance (Lewin *et al.*, 2007). Altogether, these facts suggest that impairing NPC assembly, without harming the function of mature pores, could be a very interesting strategy to specifically impair cancer cells proliferation, with low toxicity against non-proliferative tissues. Moreover, as post-mitotic and interphase assembly pathways are different in mammalian cells, specifically altering the post-mitotic pathway may be even more interesting. However, this goal requires understanding of the mechanistic differences between post-mitotic and interphase assembly. Deciphering both processes is primordial to develop therapeutic approaches able to efficiently target post-mitotic assembly which is essential for cell proliferation. This is why filling the gap in the knowledge about how the NPC assembles in interphase is of major importance in cancer research.

POM121 appears as one of the most interesting Nups to target for cancer treatment since it is essential for interphase assembly. A recent study has shown that POM121 was upregulated in prostate cancer cells and that the Nups composition of the NPCs was altered

in advanced prostate cancer cells in comparison with primary tumour. This resulted in a higher number of NPCs correlated with the stage and aggressiveness of the tumour (Rodriguez-Bravo *et al.*, 2018). Overexpression of POM121 in prostate cancer cells promoted proliferation and drug resistance. They propose that this role in the carcinogenesis and cancer aggressiveness is linked to the role in nucleocytoplasmic transport of POM121. Through the interaction of POM121 with Importin-β, increased levels of POM121 induced higher import of the key oncogenic transcription factors MYC and E2F1, as well as AR and GATA2, two prostate cancer-specific transcription factors. One target suggested by the authors is the POM121-Importin-β axis which plays a specific role in transport. Treatment with Importazole could reduce the lethality of prostate cancer patients (Lim and Wong, 2018; Rodriguez-Bravo *et al.*, 2018).

In addition, a recent work demonstrated that inhibition of NPC formation selectively induces cancer cell death (Sakuma *et al.*, 2021). In melanoma, Sakuma et al. identify Nup160 and Nup93 as essential elements for NPC interphase assembly. These Nups present in the Y-complex and inner ring are in the scaffold of the NPC and thus are important for proper NPC structure. Their inhibition in melanoma also inhibited NPC formation which led to cancer cell death. In comparison normal cells only had to undergo an arrest in their cell cycle but could survive afterwards.

Finally, understanding interphase assembly could allow us to find a way to stimulate the formation of NPCs in aging cells and regenerate the permeability barrier, whose defects in senescent cells is often linked to alterations in the DNA (Martins *et al.*, 2020).

In conclusion, deciphering NPC interphase assembly appears important in understanding its role in the proliferation of cancer cells and might open a new strategy to develop new cancer treatments.

5. High-resolution microscopy techniques to study to the NPC

5.1. Microscopy challenges of NPC investigation

Light microscopy is one of the most popular tools to study the internal structure of cells. But the investigation of NPC by microscopy techniques presents several challenges. Conventional light microscopy techniques for *in situ* study of biological samples, like widefield or confocal microscopy, have a limited resolution because of the diffraction limit. Thus, the NPC with its diameter of around 120 nm and its insertion in a 40-50 nm thick NE is too small to allow standard microscopy to reveal the details of its organization and structure. The microscopy tools to investigate the NPC structure have remained limited to electron microscopy for a long time.

The development of scanning probe microscopy techniques, like AFM, has opened the way for the investigation of the NPC structure in the context of purified NE with a resolution of a few nanometers.

More recently, the development of new super-resolution techniques pushed the limit of the resolution of optical microscopy down to a few nanometers and became a particularly well-suited approach to reconstruct the structure and composition of the NPC.

In the following paragraphs, I will present the high-resolution microscopy techniques that have been used to investigate the NPC (except EM described above). I will also show the potential of these techniques to reveal new characteristics of the NPC.

5.2. Atomic Force Microscopy

5.2.1. Introduction

Atomic Force Microscopy (AFM) is a scanning probe microscopy technique derived from Scanning Tunneling Microscopy (STM). In 1982, Gerd Binning and Heinrich Rohrer used a fine metallic tip to scan the surface of a conductive sample. The precise scanning movement of the tip was controlled by a piezo stage. By imposing a current that would be kept constant

using an electronic feedback loop plugged on a piezo, they were able to image the topography of surfaces of CalrSn4 and gold at the atomic scale. The topography was reconstructed by recording the movement of the piezo (Z direction) when the tip was scanned (in X and Y directions) over the sample. This invention, for which they were awarded the Nobel Prize in Physics in 1986, led them to the design of another type of microscope, the AFM.

To probe non-conductive samples, Binning and Rohrer used probes consisting of a micrometric cantilever equipped with a nanometric tip at its end. A laser is positioned at the end of the backside of the cantilever and reflected on a four-quadrant photodiode. Then by putting the tip in contact with the sample and scanning it as they did with STM, it was possible to record the deflection of the cantilever that would be modulated by the sample's topography.

5.2.2. AFM principle

Modern AFM microscopes have improved in terms of instrumentation, but the basic principle remains the same. To resolve the nanoscale topography of a sample, a nanometric tip is approached to the sample's surface and is used to probe the interaction forces acting between the tip and the sample. This probe is composed of a cantilever with the tip positioned at its extremity. A laser is reflected at the end of the cantilever towards a 4-quadrants photodiode; position of the reflected spot on the photodiode measures the change in the deflection of the cantilever. If a change in the tip-sample's interaction force occurs, it is measured by a change of the vertical position of the reflected spot on the photodiode (Figure 25).

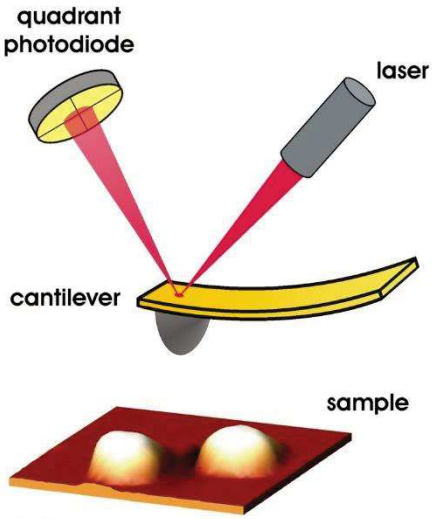

Figure 25: AFM principle. A laser is reflected at the back of a cantilever equipped with a nanometric tip at its end. By measuring the deflection of the reflected laser beam with a photodiode when the tip is in contact with the sample it is possible to reconstruct its topography at the nanometric scale by scanning a small area.

In modern AFMs, we generally use a closed loop to perform imaging. This means that the position of the Z piezo, positioned in the cantilever holder or under the sample, is regulated then by an electronic control system that keep constant the tip-sample interaction by a feedback loop that vertically moves the Z piezo to counterbalance a change in this interaction. This change is generally created by a change in the topography of the sample. By recording the position of the Z piezo, whose calibration in nm/V is known, it is thus possible to reconstruct the 3D topography at the nanometer scale. AFM can be performed, in air, liquid, or vacuum.

The force *F* applied to the sample can be precisely calculated using Hooke's law after determination of the spring constant of the cantilever, *k*:

$$F = k * z$$

where z is the deflection of the cantilever.

5.2.3. Cantilever and tip

AFM probes are composed of micrometric cantilevers, rectangular or triangular in shape, coated with a reflective layer at their backside and equipped with a tip at their end (Figure 26). Made in silicon nitride, silicon or quartz-like material, the typical cantilever's length ranges from a few microns to several hundreds of microns and the spring constant is determined by its dimensions (length, width, thickness) and its composition. For biological applications, the cantilevers used usually have a spring constant below 1 N/m.

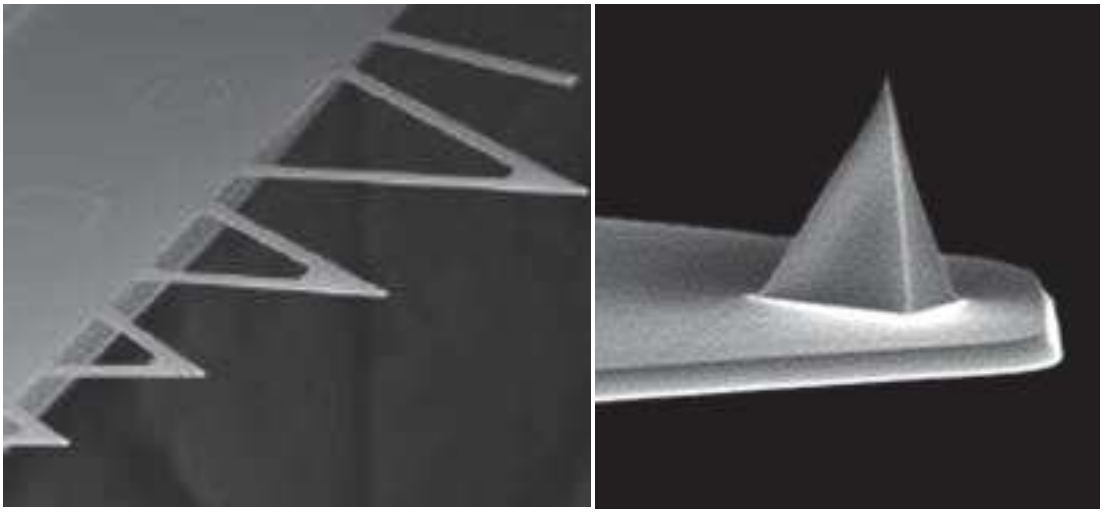

Figure 26: Cantilevers and tip of a Bruker MSNL AFM probe (https://www.brukerafmprobes.com/p-3710-msnl-10.aspx)

The tip's shape is variable and is often a pyramid or a cone of several micrometers height. It has a small apex whose tip radius can go down to the nanometer.

5.2.4. Forces involved in AFM

The interaction forces acting between the AFM tip and a sample are of two types, attractive and repulsive. In liquid, the experimental conditions used during my PhD, these interactions are dominated by repulsive forces originating from ionic and interatomic interactions, in addition to the contact force with the sample and/or substrate. In relation with electrostatic interactions, double layer forces occur between charged objects across liquids and act over distances that are comparable to the Debye length (on the order of a nanometer) (Israelachvili, 1992). Short distance Vander Waals attractive forces are negligeable due the low Hamaker Constant (10^{-20} J). The strength of these forces increases with the magnitude of the

surface charge density (or the electrical surface potential). These forces can be attractive or repulsive but can also be efficiently screened by the presence of ions in the imaging solution. Solvation forces could also be present in liquid. They are explained by the organisation of liquid molecules at the interface with the surface which will differ from the organisation in the rest of the solution and create a specific layer at this interface.

In air, other forces that vary depending on the electrostatic or magnetic properties of the tip and sample might also be present. In addition, capillarity force is the main attractive force in an ambient environment where a water bridge forms in between the AFM tip and sample when approached within nanometric distance range, which is responsible for the jump to contact between them.

In all conditions, mechanical contact force which corresponds to the repulsive part of the curve can be analysed to extract properties of a sample. For example, by fitting the slope of this repulsive part with a cantilever for which the spring constant has been calibrated, the stiffness of the sample can be extracted.

5.2.5. Scanning

Scanning of the sample is performed by the XY piezo system or piezo tube. Piezos can precisely control the movements of the tip or sample at the nanometric scale. But one of their drawbacks is the hysteresis effect when they move. This means that their movement is not linear, so the use in open loop can lead to image distortion due to this hysteresis. On most AFM, and specially on the JPK Nanowizard 4 that has been used for this work, XY piezos are coupled with sensors in a closed loop to correct for the hysteresis.

To reconstruct a 3D topographical image of the sample, the size of the scanning area is defined in the AFM control software with a fixed pixel resolution, typically 256 x 256 or 512 x 512 pixels[2]. Depending on the imaging mode used, the tip is scanned forward and backward over each line of the image or performs a force curve measurement at each pixel of the image. The image is then reconstructed by determination of the topography for each pixel.

5.2.6. Resolution and limitations due to tip convolution

The power of AFM is to reach nanometric resolution for the topography of a native sample, a level of resolution hardly achievable for many techniques, especially for optical techniques used in life science. But this high-resolution has some limits. While in Z, the resolution achievable is in the order of the Angstrom thanks to the high precision offered by piezo systems, lateral resolution of an AFM is limited by the size of the tip. In fact, the AFM image obtained is always a convolution between the topography of the sample and the shape of the tip (Figure 27). Thus, the best resolution is obtained with the tip with the smallest tip radius which at best is around 1 nm. The exact size of the tip apex is in general not known and can vary between each tip within a certain range. For example, Bruker MSNL tip radius has a nominal value of 2 nm that can in fact vary from 2 to 12 nm and thus can strongly affect the resolution obtained during AFM imaging. It is important to mention that with the same applied force, a smaller tip exerts more pressure for a given area than a larger one on the sample and can damage it more easily, especially in the case of soft biological samples.

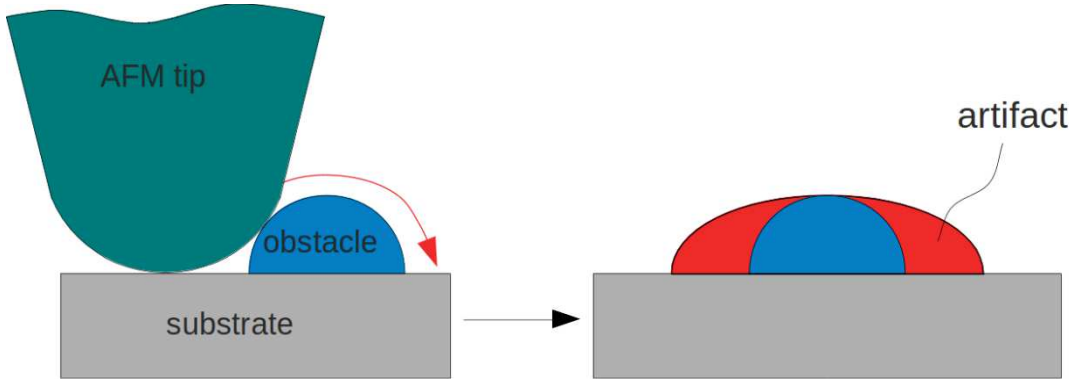

Figure 27: Tip convolution and resulting artefact (red) in AFM imaging (https://myscope.training/legacy/spm/background/convolution.php)

5.2.7. Imaging modes

AFM has been the basis for development of numerous derived techniques able to probe different parameters in samples. Here I will focus on the main classical AFM imaging modes and the one used in this work which are contact, tapping and Quantitative Imaging (QI) mode.

Contact mode is the simplest mode that was used on the original AFM setup. The principle is to approach the AFM tip in contact with the sample so that the deflection increases once the contact is established. By keeping constant this deflection on the photodiode with a feedback loop, this allows the sample to be observed at a constant applied force during the forward and backward tip scanning. In this mode, it is important to try to minimize the force applied since the tip is in constant contact with the sample during the scan. Too high forces might result in destruction of the sample by the tip scanning or in damaging the tip.

Tapping mode or intermittent contact mode is an AFM imaging mode based on the characteristic that the AFM cantilever can be considered as a harmonic oscillator. Thus, it possesses a resonant frequency that can be used to oscillate the cantilever at a certain amplitude. Instead of the deflection in contact, it is the amplitude of oscillation that will be kept constant by the feedback loop. This mode allows more gentle imaging conditions for the sample since the tip enters in contact with the sample only on a small part of the oscillation cycle and minimizes friction forces.

The oscillation is controlled by the excitation of the cantilever with a small piezo-electric element which is driven at a frequency slightly shifted from the resonant frequency. As the topography changes, the amplitude slightly increases or decreases, and the feedback loop allows reconstruction of this topography at constant amplitude.

Tapping mode can give extra information about the sample thanks to another parameter that can be measured, the phase. The phase is in fact the phase shift between the driving excitation and the oscillation of the cantilever. This parameter can give information about the viscoelasticity of the sample since its value depends on the energy dissipated in the sample which is influenced by these properties.

Finally, QI is a mode based on the measurement of a force curve at each pixel of the reconstructed AFM topography image. Like contact mode, it allows to obtain an AFM image at a specific force without the impact of a lateral scanning since the tip retracts completely between each pixel. The main drawback of this technique is that the imaging time is longer because of this approach-retract performed at each pixel and the acquisition time of each curve must be sufficient to keep the cantilever in quasi-static conditions.

However, QI mode has several advantages, the main one being the possibility to extract mechanical information from each image. By saving each force curve, several parameters can be measured for each pixel, *e.g*. maximum adhesion force, stiffness of the sample etc. Other properties like Young's Modulus or contact point image (image at zero force applied) can be calculated using mechanical contact models and are used to better characterize samples at the nanometric scale (Figure 28).

All these modes can be used with specific piezos and probes with a higher resonance frequency. This configuration, known as High-Speed AFM (HS-AFM) or fast AFM, allows to measure dynamic events with a speed up to several images per second.

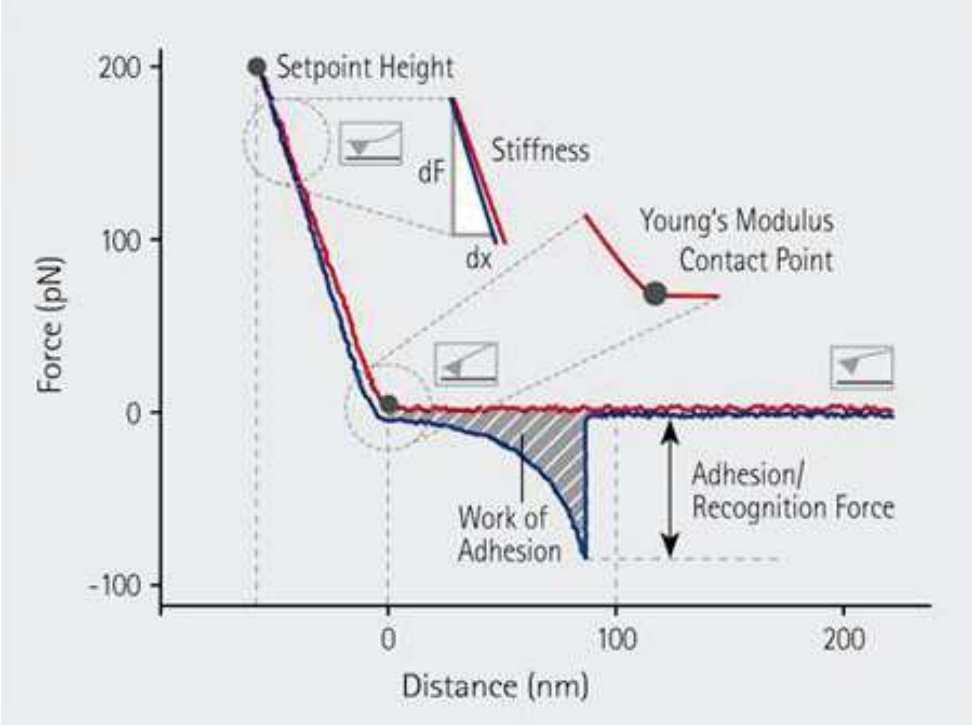

Figure 28: Parameters that can be determined from QI curves on a JPK AFM (https://www.jpk.com/products/atomic-force-microscopy/qi-mode)

5.2.8. Mechanical model

Several mechanical models have been developed to extract intrinsic properties of samples. Among them, the Hertz/Sneddon model allows to describe the contact mechanics of deformable objects without adhesion forces, which is generally observed in liquid on biological samples. The model can be used for calculations with different tip shapes. Thus, in this work, the Hertz/Sneddon model is the best suited for the analysis. Recent advances in

AFM cantilever calibration have allowed better characterization of these properties in a reproducible manner (Schillers *et al.*, 2017). However, using standard calibration approaches on commercial AFM microscopes, the results of the values calculated from mechanical models remain qualitative for complex biological samples. In addition, the models are generally valid for homogenous samples, which is not our case and therefore our approach can only give an approximation of the mechanical properties.

Using a pyramidal tip in these experiments it is possible to apply the equation below in Figure 29 to extract stiffness and effective Young's Modulus (Rico *et al.*, 2005). To perform these measurements on the sample, the data processing software provided with our JPK Nanowizard 4 AFM was used. It allows to model this contact and calculate sample properties.

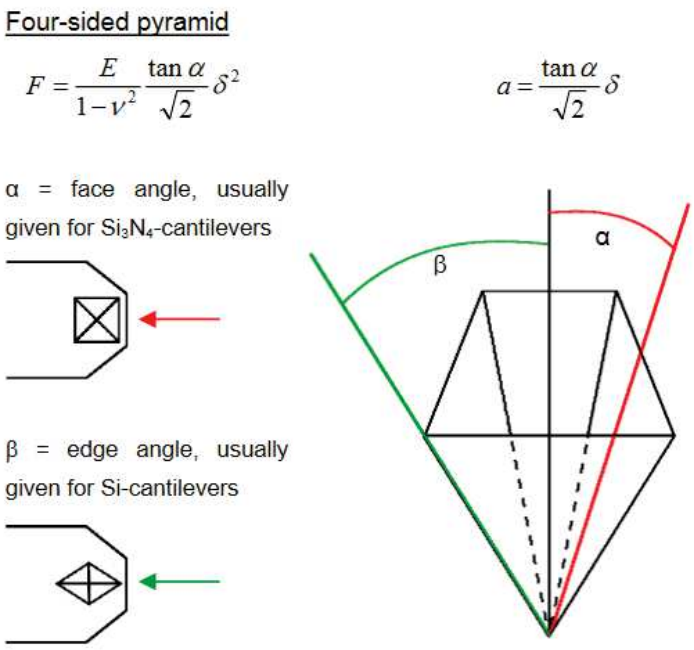

Figure 29: Equation describing the force between sample and a four-sided pyramidal tip. By fixing the tip geometry it is possible to extract an effective Young Modulus with the force and indentation parameters extracted from QI force curves.

5.3. Fluorescence and TIRF microscopy

While AFM is a remarkable tool to investigate the shape of biological samples at a nanometric scale, the obtained topography does not give information on the composition of the imaged structures. A way to identify elements is to combine AFM with other techniques, which can shed light on the specific signature of the element of interest. One way to do so is to tag these elements with fluorescent molecules and correlate AFM topography with optical fluorescence microscopy. This approach allows to identify the presence of this element in the structures imaged by AFM, especially, in the case of single molecule localization microscopy (SMLM) whose resolution is of the same order as that of AFM (Collart-Dutilleul *et al.*, 2014; Dahmane *et al.*, 2019).

Fluorescence microscopy has been widely used to characterize biological samples. Fluorescence is the property of certain molecules to emit light upon excitation with a light source. The fluorescent molecule can absorb photons from the light source if their energy (inversely proportional to their wavelength) corresponds to the energy difference between the electronic ground state and an electronic excited state of a fluorophore. In this case, after excitation, the excited molecule returns to its ground state, which results in the change in energy level and thus in the emission of photons. This is described by the Jablonski diagram (Figure 30).

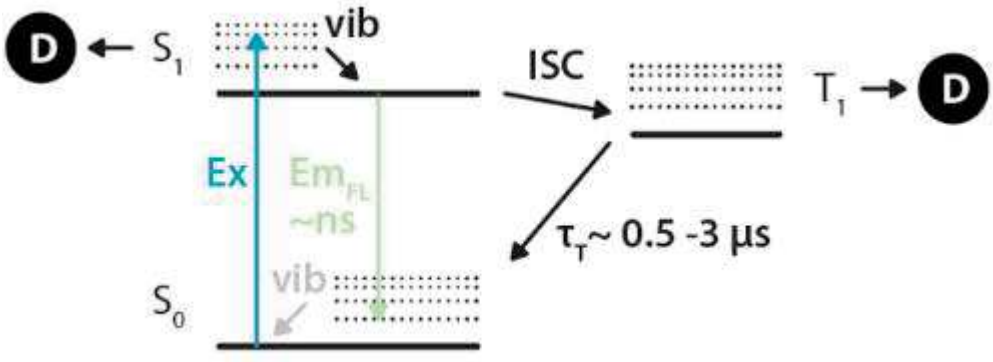

Figure 30: Jablonski diagrams showing processes that compete with fluorescence emission. The excited S1 state might convert to a longer lived and dark triplet state (T1) or to various other dark states, as indicated by 'D'. Adapted from Vangindertael et al., 2018.

Photons absorbed by the molecule will be converted into emitted photons. The ratio between absorbed and emitted photons is called Quantum yield and is an intrinsic property of the fluorescent dye. Moreover, the wavelength of the emitted photon is shifted towards a higher wavelength. This is due to the small amount of energy lost through a non-radiative process before the transition to ground state. The wavelength varies depending on the difference in energy levels and can be translated into absorption and emission spectra of a unique fluorophore (Figure 31). Fluorescence of organic molecules occurs on a timescale of the order of nanoseconds. A fraction of the fluorophores does not emit photons after excitation and can be sent to a "dark state". This dark state can be permanent when no fluorescence signal can be recovered from the molecule and is called bleaching. Or it can be transitory, in the case of triplet state, where the fluorophore passes by a dark state before returning to its ground state in a non-radiative manner.

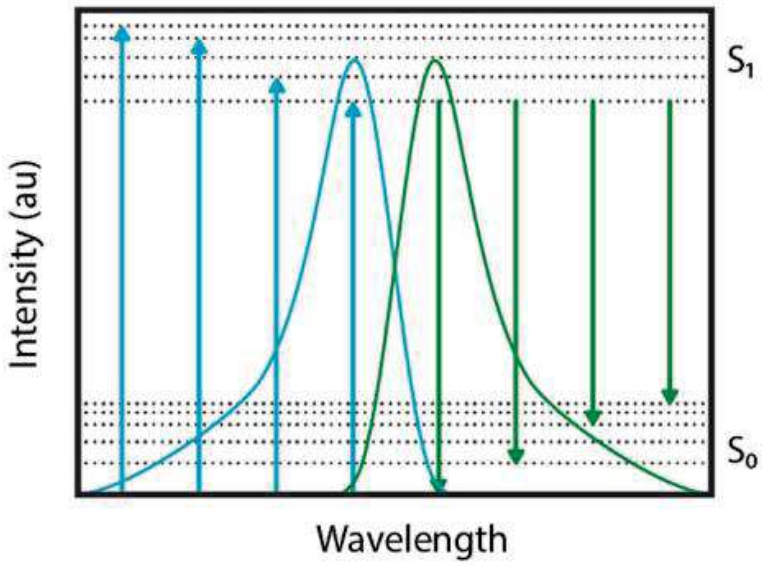

Figure 31: Absorption (blue) and emission (green) spectra of a fluorophore depending on the energy level gaps (dashed lines). Adapted from Vangindertael et al., 2018.

Fluorescence microscopy aims at collecting, in general, the emitted photons from a sample in which an element of interest is labelled with a fluorophore. Using an objective which transmits the light towards a camera, it is possible to obtain a fluorescence image of the sample. The simplest system, called epifluorescence, sends a large beam perpendicularly to the glass coverslip to illuminate through the whole sample and to obtain ensemble fluorescent

images (Figure 32). In this configuration, fluorophores that are out of the focal plane also contribute to the image and thus deteriorate the signal to noise ratio.

One way to overcome and obtain a better image with less background noise is to use Total Internal Reflection Fluorescence (TIRF) microscopy. TIRF microscopy uses the fact that, according to the different refraction indices of the glass coverslip and the medium, there is a critical angle at which the incident laser beam is totally reflected by the coverslip. The interesting characteristic of this configuration is that TIRF illumination results in the formation of an evanescent field of light on the other side of the coverslip that will excite the sample only in a range of few hundreds of nanometers from the coverslip (typically <300 nm) depending on the laser wavelength. To do so, the incident laser beam is aligned off the center of the objective, towards the side (Figure 32). TIRF microscopy has thus an improved signal to noise ratio. However, the small thickness of the evanescent field limits its use to thin samples or to the basal membranes of cells in contact with the coverslip for example.

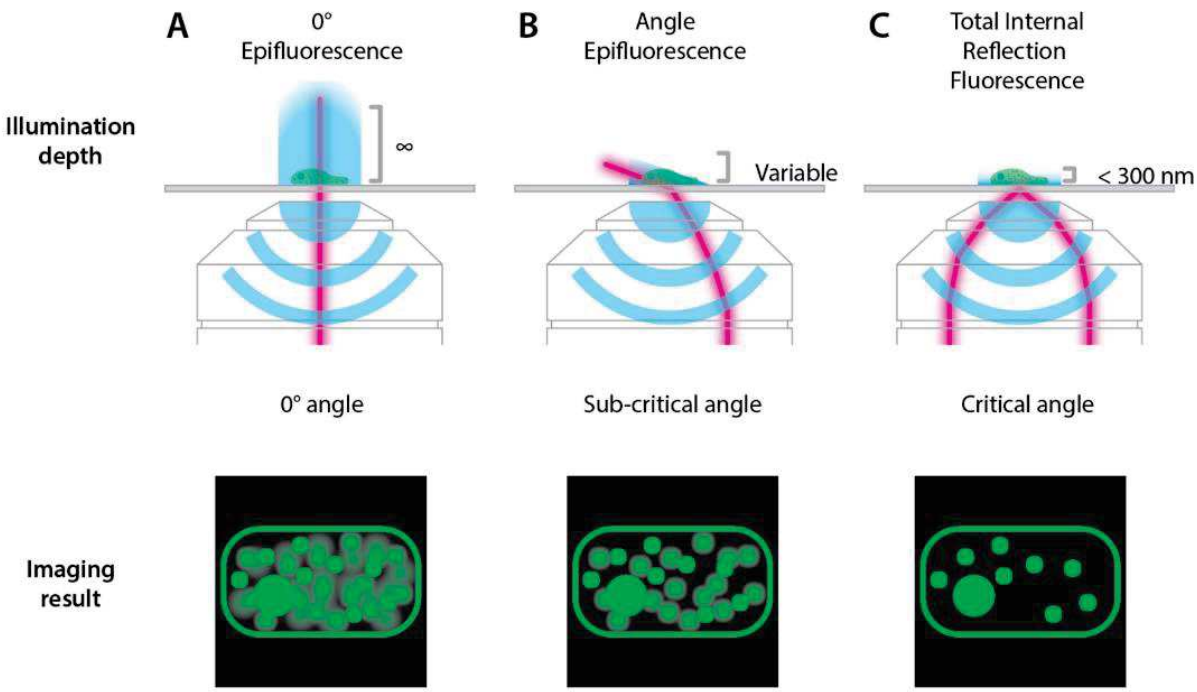

Figure 32: Epifluorescence, angle epifluorescence (also known as Hilo) and TIRF microscopy illumination scheme and corresponding image illustration of the signal to noise ratio. Adapted from Vangindertael et al., 2018.

While an illumination scheme like TIRF improves the quality of the fluorescent image, this optical microscopy technique still bears a limitation in the resolution of the imaged object. This spatial limitation is due to the diffraction of the light through the optical path. As a result, when imaging a single molecule with an optical microscope, instead of a punctual source, the molecule appears as a larger pattern called Airy disc or Point Spread Function (PSF) (Figure 33). The resolution limit depends on the wavelength and is described by:

$$d = \frac{0.61\lambda}{NA}$$

where d is the limit of resolution, λ is the wavelength of the light, and NA is the numerical aperture of the objective. The resolution limit in fluorescence microscopy is typically between 200 and 300 nm with high numerical aperture objectives.

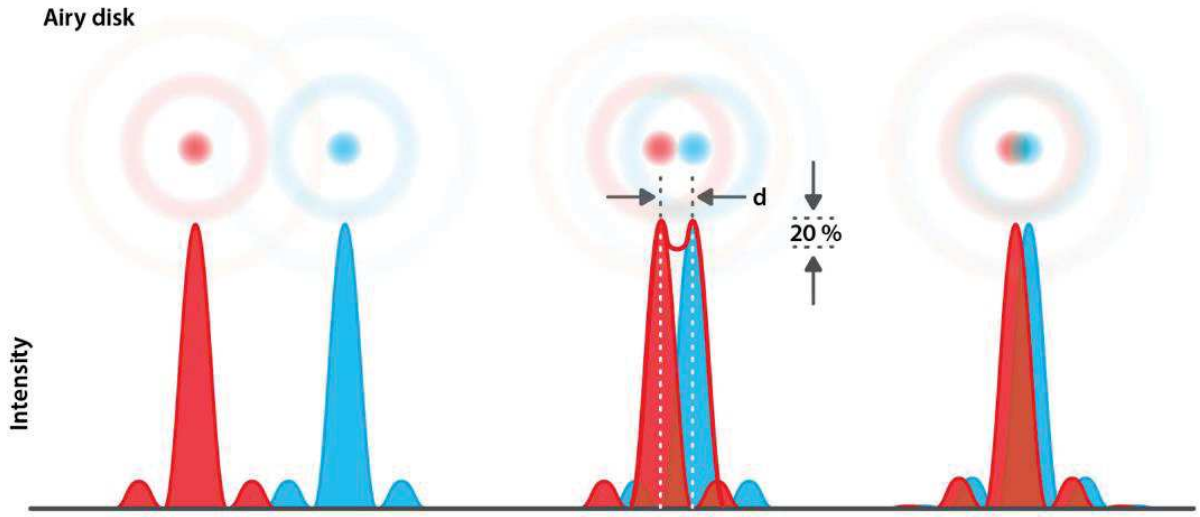

Figure 33: PSF of two fluorophores (represented as red and blue) in close proximity illustrating the limit of resolution. Adapted from Vangindertael et al., 2018.

The PSF of a single molecule is represented in Figure 33 (red and blue molecules). Two molecules can be resolved if the distance between them is above the diffraction limit. Below, the emission from the two excited molecules cannot be distinguished. This minimal distance is referred to as the Rayleigh criteria and represents the limit in standard fluorescence microscopy. The resolution achievable in standard fluorescence microscopy is a limiting factor in the study of biological samples. Indeed, many structures and complexes in organisms are smaller than the best resolution possible with this technique. Thus, their study was limited to

general organisation or position within an organism. To characterize nanoscale structures, organisation, and functions of a great variety of sophisticated biological elements present in a cell by fluorescence microscopy, the development of new techniques was required.

5.4. Stimulated Emission Depletion microscopy

This quest has led to the development of super-resolution microscopy techniques that could overcome this resolution limit. The first technology that has been developed is STimulated Emission Depletion (STED) microscopy (Hell and Wichmann, 1994). It is derived from a confocal microscope, where the laser beam is focused in a small confocal volume in which the fluorescence is measured while scanning the samples to reconstruct an image. While this approach is also diffraction limited, STED uses a second laser to deplete part of the fluorescence signal coming from the excited confocal volume.

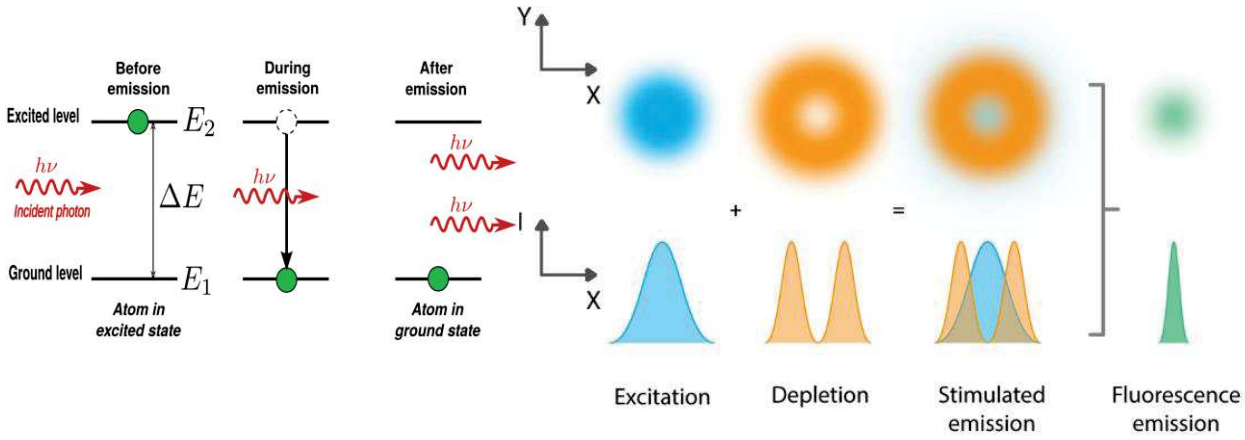

Figure 34: Left: Stimulated Emission principle - an incoming photon interacts with an excited state, leading to the depopulation of the excited state and the emission of a second photon at the same wavelength as the incident photon. (https://en.wikipedia.org/wiki/Stimulated_emission).

Right: STED principle. The confocal excitation beam is approximately Gaussian in shape while the depletion beam is donut shaped, with a central region of near zero intensity. After stimulated emission of fluorophores in the donut region, spontaneous emission from the center most molecules can be recorded. Adapted from Vangindertael et al., 2018.

The depletion principle uses the phenomenon of stimulated emission. Stimulated emission is observed when a photon interacts with an excited electron (for example by excitation of a fluorophore by a light source). In this case, the interaction of the electron with the photon causes its de-excitation which results in the emission of a photon whose

wavelength is the same as the incident photon. Using a doughnut shaped depletion beam, generally in the red or far-red spectra, aligned with the confocal spot and shone a few nanoseconds after the excitation pulse, it stimulates the emission of the fluorescence within the doughnut-shape depletion beam. Appropriate filtering allows to measure only the fluorescence emission coming from a reduced volume at the center of the doughnut (Figure 34).

This technique gives the possibility to get images at the resolution of a few tens of nanometers. NPCs have been widely characterized with this technique since their 120 nm diameter allows STED microscopy and improved resolution to visualize individual subunits of its architecture (Figure 35) (Göttfert *et al.*, 2013).

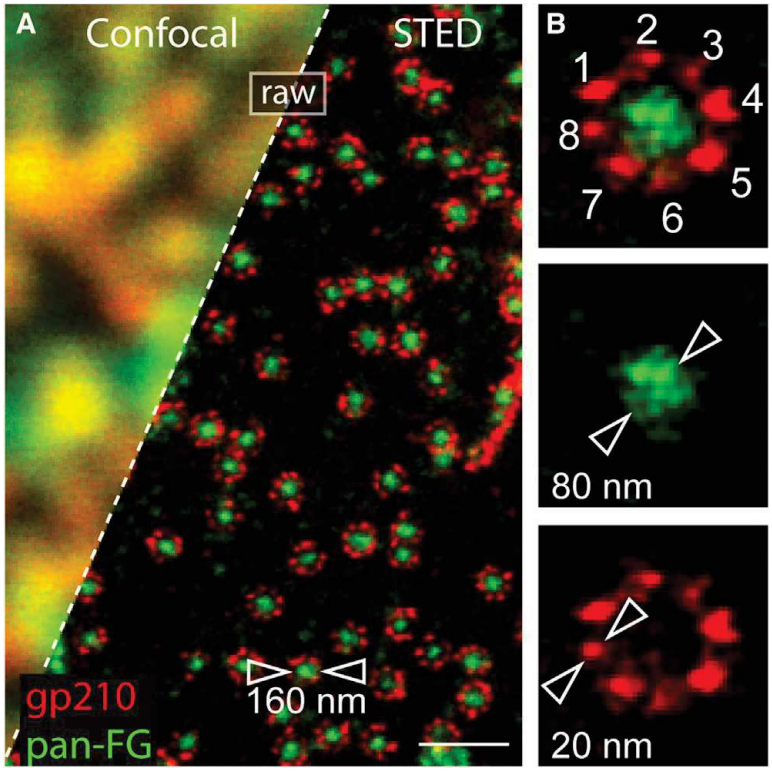

Figure 35: Gain resolution on NPC between confocal and STED microscopy where FG-repeats (green) and gp210 (red) are labelled (Göttfert et al., 2013). Scale bar is 500 nm.

Finally, recent advances allowed the development of a new technique called MINFLUX which has shown the possibility to reach a resolution of a few nanometers using optical microscopy on NPCs (Gwosch *et al.*, 2019).

5.5. Single-Molecule Localization Microscopy

The resolution of a single molecule in optical microscopy is in general limited by the fact that the PSF of fluorophores is much larger than the size of the molecule. Thus, the PSFs of the molecules of interest overlap and single molecules cannot be distinguished unless they meet the Rayleigh criteria.

To overcome this problem, single molecule localization microscopy (SMLM) techniques have been developed. In other fluorescence techniques, a single molecule resolution cannot be achieved because all fluorophores are emitting at the same time. The SMLM techniques use properties of fluorophores to reach stochastic activation, so that only a fraction of the fluorophores emits at the same time. By lighting on only this fraction, it is possible to have sufficiently sparse PSFs which do not overlap. The first SMLM technique developed is called Photo-Activation Localization Microscopy (PALM) and uses photoactivatable proteins emitting light upon activation (Betzig *et al.*, 2006; Hess, Girirajan and Mason, 2006). The principle of SMLM is to acquire thousands of frames where each contains only a subset of emitting molecules. Afterwards, individual PSFs are fitted by a 2D gaussian to determine the precise location of each single molecule. Individual localizations from each frame are then compiled into a reconstructed image where corrections linked for example to sample drift are also taken into account (see illustration in Figure 36, adapted from Khater *et al.* (Khater, Nabi and Hamarneh, 2020)). SMLM allows the acquisition of super-resolved images of labelled elements of interest with a typical resolution of 20 nm.

STochastic Optical Reconstruction Microscopy (STORM) (Rust, Bates and Zhuang, 2006) is another SMLM technique that does not require photoactivatable proteins and is a precursor of directSTORM (dSTORM) (Heilemann *et al.*, 2008). dSTORM uses the physical properties of fluorophores to be sent into a dark state upon excitation. By exciting with a high laser power a sample labelled with fluorophores adapted to STORM because of their physical properties, it is possible to put most of them into a dark triplet state while a smaller sparse subset keep emitting. As in PALM, single molecule localizations are fitted to reconstruct a super-resolved STORM image. A particularly well-suited fluorophore for STORM is AlexaFluor 647. To obtain the particular blinking of AlexaFluor647 specific reducing medium conditions

are required to allow its excitation towards the dark reversible triplet state. Using additional optical elements that affect the PSF of fluorophores depending on their position relatively to the focal plane, it is also possible to perform 3D STORM to determine more precisely the position of a specific subcomplex in the NPC relative to others (Sabinina *et al.*, 2021).

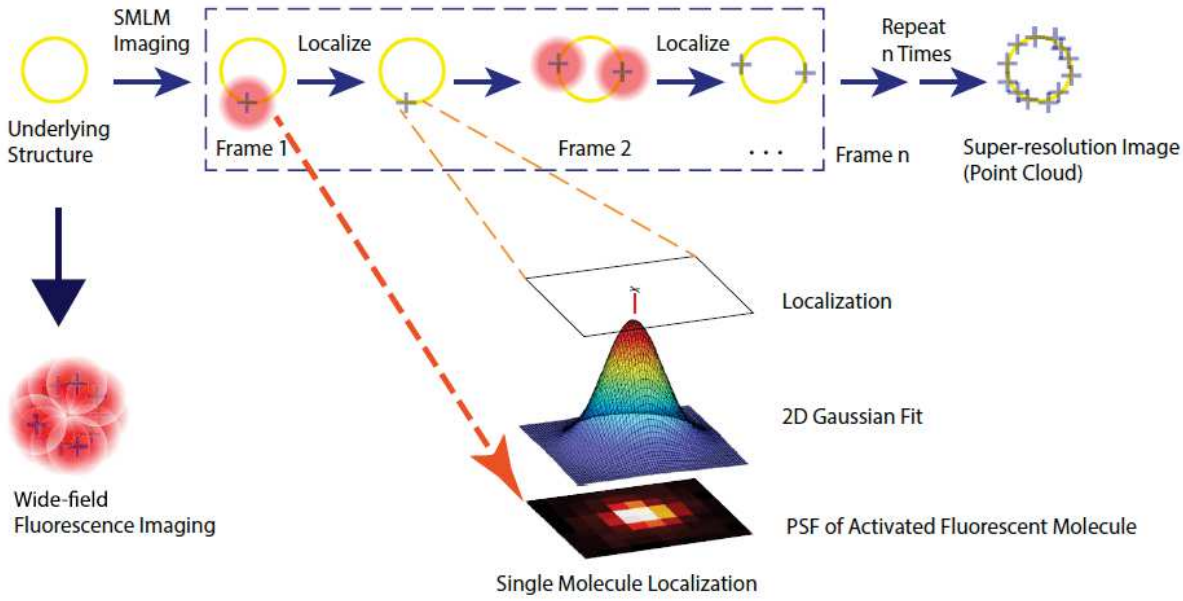

Figure 36: SMLM principle. A structure of interest is fluorescently labelled. Widefield fluorescence imaging cannot resolve it. By recording n frames in which only few molecules per frame are emitting fluorescence, it is possible to fit the PSF of single molecules by a 2D gaussian and to precisely determine its position. All localizations are then assembled into a super-resolution image which corresponds to a map of localizations. Illustration from Khater et al, 2020.

In SMLM, localization precision is determined by the 2D gaussian fit of the Airy disc observed for each single molecule. The localization precision σ is determined by the following equation from Thompson *et al.* (Thompson, Larson and Webb, 2002):

$$\sigma = \sqrt{\frac{s^2}{N} + \frac{\left(\frac{a^2}{12}\right)}{N} + \frac{4\sqrt{\pi}s^3b^2}{aN^2}}$$

where σ is the localization precision, s is the standard deviation of the Gaussian fit of the PSF, N is the number of photons captured, a is the pixel size of the detector and b is the standard deviation of the background fluorescence. The first term under the square root corresponds to the photon shot noise, the second to the pixilation noise, and the last one to the

background noise from the sample. With small effective pixel size and low background noise, the equation can be simplified to:

$$\sigma \approx \frac{s}{\sqrt{N}}$$

This simplification implies that higher the number of photons collected, better the precision.

The application of STORM microscopy is particularly interesting in case of the NPC imaging since it allows to resolve individual subunits of the NPC and can be combined with other microscopy techniques like AFM, giving similar lateral resolution on biological samples (Dahmane *et al.*, 2019).

Thesis problematic

The current knowledge of the NPC assembly process revealed major differences depending on the phase of the cell cycle. While post-mitotic assembly and its recruitment of Nups to chromatin, followed by ER membrane vesicles around these proto-NPCs, is well described, the interphase assembly process remains unclear. During interphase, cells have to duplicate their constituents before the next mitosis, and NPC replication is a complex process involving macromolecular assembly combined with membrane remodelling. Indeed, the two membranes composing the nuclear envelope must fuse locally. Moreover, the nuclear permeability barrier must remain intact during the whole process, underlining that protein assembly and membrane fusion must be tightly coordinated. The investigation of interphase assembly therefore requires monitoring both protein recruitment and membrane remodelling.

Most of the work on NPC assembly has been done on purified *Xenopus laevis* oocyte nuclei because they offer convenient and fast preparation of the sample, allowing to study and to differentiate processes happening inside or outside the nucleus, and finally, when manually opened with micro-pipettes, they offer a large flat area of nuclear envelope densely populated with NPCs.

Although this model seems interesting, it has its limitations in understanding NPC assembly in eukaryotic cells. Firstly, it corresponds to the specific stages of *Xenopus laevis* oocytes, and some publications have already shown that the structure of these NPCs changes depending on the oocyte stage (Sellés *et al.*, 2017). Another important aspect is the difference between organisms of the NPC components that are often homologous and playing the same roles but showing a different molecular structure as it has been observed between yeast and mammalian for example. Finally, it is not clear if NPCs are still assembling at this stage of development.

A study published at the very beginning of my thesis demonstrated that in human cells, interphase pore assembly occurs from the nucleoplasmic side of the nuclear envelope (Otsuka *et al.*, 2016). These results have shown large remodelling of the inner nuclear membrane and

an early eight-fold symmetry organization of the nascent pores. A very intriguing question that stems from this observation is how a symmetric pore can assemble in an asymmetric manner. Indeed, the protein-membrane interfaces must be dramatically different in the assembling intermediates located on one side of the NE as compared to the mature pore embedded at fusion sites between the INM and the ONM. But due to the limitations of the techniques used, there is a lack of details and resolution of the components present and the less ordered part of the NPC. These results urge to develop a new strategy to purify mammalian nuclei to access the inner nuclear membrane and resolve early pore intermediates at higher resolution. Importantly, being able to assess the topography of the membrane and assembling complexes, together with their protein composition appears necessary to understand the detailed sequence of events leading from a progressive and asymmetric recruitment of factors to a fully symmetric and functional NPC.

Thus, to decipher NPC interphase assembly, the aim of this work is to study this process directly on open mammalian cells nuclei and to monitor at the same time protein recruitment at NPC assembly sites and nuclear envelope remodelling at the nanoscale. Scientific publications have already identified several key early components of this assembly. Among them is POM121, a transmembrane Nup essential for interphase NPC assembly and involved in the membrane deformation process. It is the earliest protein observed at NPC assembly sites so far (Dultz and Ellenberg, 2010). Thus, we can identify pore intermediates, based on a differential POM121 / mAb414 staining (mAb414 is a widely used antibody that only stains fully assembled pores).

The goal is to gather information about membrane remodelling and protein recruitment at these assembly sites by combining fluorescence microscopy with Atomic Force Microscopy (AFM) to get the topography of the nuclear membranes and nuclear pores, either fully or partially assembled. By developing a protocol to purify and open nuclei from U2OS human cells, with the inner nuclear membrane accessible to the AFM tip the objectives are:

- Image of the nucleoplasmic side of human NPCs by AFM to get the nanometer scale topography of the inner nuclear membrane that would give information on membrane deformation and 3D structure of pore intermediates; that are expected to vary depending on

the different stages of pore assembly. And get information about NPC basket structure that is not completely resolved.

- Use of super-resolution techniques, like STimulated Emission Depletion (STED) or Stochastic Optical Reconstruction Microscopy (dSTORM) to observe NPCs, since their diameter is around 120 nm. This allows resolving the position of POM121 in fully assembled NPCs and observing intermediate structures based on the POM121 fluorescent signal.

- Combine dSTORM and AFM to correlate topographic structure and proteins recruitment at the nanoscale.

- Use siRNAs treatment against specific nucleoporins to accumulate pore intermediates at a specific stage of assemblies and record their structure and nucleoporin composition. This will document at which stage each nucleoporin is critical for the assembly to proceed.

Material and methods

6. Materials and methods

6.1. Cell culture and siRNA treatment

Several cell lines derived from the U2OS cell line have been used for the experiments. U2OS cells (originally called 2T) were isolated in 1964 from a tibial osteosarcoma of a fifteen year old girl (Ponten and Saksela, 1967). These adherent cells have a relatively large and flat nucleus that is interesting in our study because it allows a large number of NPCs in the same focal plane for microscopy. The four cell lines used are U2OS, U2OS/POM121-GFP, U2OS/Nup96-GFP and U2OS-Nup96-SNAP and will be referred this way along the manuscript.

While U2OS is the native cell line, U2OS/POM121-GFP is a modified cell line that expresses the transmembrane nucleoporin POM121 from rat, C-terminally fused with three EGFP. Finally U2OS/Nup96-GFP and U2OS/Nup96-SNAP are CRISPR/CAS9 modified cell lines that express Nup96 C-terminally fused to mEGFP or the self-labelling SNAP tag (Thevathasan *et al.*, 2019).

All cells were cultivated in DMEM + Glutamax medium supplemented with 10% foetal bovine serum at 37°C with regulated CO_2 level of 5 %. Cultured cells were controlled for mycoplasma contamination regularly and were grown without any antibiotic treatment.

For siRNA transfection, 1.5 million cells were seeded in 10cm plates. The day after they were transfected with 1.25 nmol of siRNA and 10 uL of Lipofectamine 2000 (Invitrogen) according to the manufacturer's recommendations. Medium was changed after 4-6 hours. Transfection was repeated 48h later in identical conditions. Cells were lysed or imaged the day after.

6.2. Nuclei purification and opening

For the nuclei purification procedure (Figure 37), 40 million cells were grown in four 75 cm² flasks as described above. In case of siRNA treatment, cells were grown in 10 cm plates and were treated as described above prior to lysis. Cell lysis procedure remained consistent for all the cell lines.

All cells from the four flasks were trypsinized and resuspended in 30 mL culture medium and counted to ensure a minimum number of 30 million cells. They were then centrifuged for 5 minutes at 1000 rpm and at 4°C. Cells are then washed by the same process with successively DPBS and Hypotonic Buffer (HB) composed of 50 mM Tris pH 7.5 supplemented with 1 mM DTT and Complete (Roche) to make the cells swell. Finally, the end pellet was resuspended in HB at 40 million cells/mL. Cells in HB were then left on ice for 45 minutes to allow rigidification of the plasma membrane and swelling.

After this incubation, cells have sedimented and a small volume of clear supernatant is removed from the tube. Cells are loaded in a Dounce homogenizer equipped with a tight pestle. Typically, 10 (up to 15) strokes are done with the piston to break most of the cells without breaking their nuclei. To ensure a correct solution of intact nuclei, the piston remained in the liquid during the whole process and was removed by a fast movement only at the end to avoid the formation of bubbles.

After the lysis step, the crude extract was mainly composed of intact nuclei, but cellular debris, unbroken cells, and pieces of chromatin from the few broken nuclei were also present. To eliminate these undesired components several centrifugation steps were performed to extract only intact nuclei.

The lysate was centrifuged on a sucrose cushion. To do so, 5 mL of S500 buffer (10 mM HEPES pH 7.5, 2.5 mM $MgCl_2$, 50 mM KCl, 500 mM Sucrose, supplemented by 1 mM DTT and Complete) was put in a 15 mL falcon tube and the extract was loaded at the top. Centrifugation for 15 minutes at 300 g leads to accumulation of intact nuclei and unbroken cells in the pellet. Supernatant containing mainly remains of plasma membrane was discarded. Pellet was

resuspended in 5 mL S500 and centrifuged for 3 minutes at 300 g leading to segregation between unbroken cells in the pellet and intact nuclei in the supernatant. Finally, this supernatant was centrifuged one last time for 15 minutes at 300 g. The resulting pellet composed of almost only intact nuclei was then resuspended in S500 at a concentration of 1 million nuclei/mL.

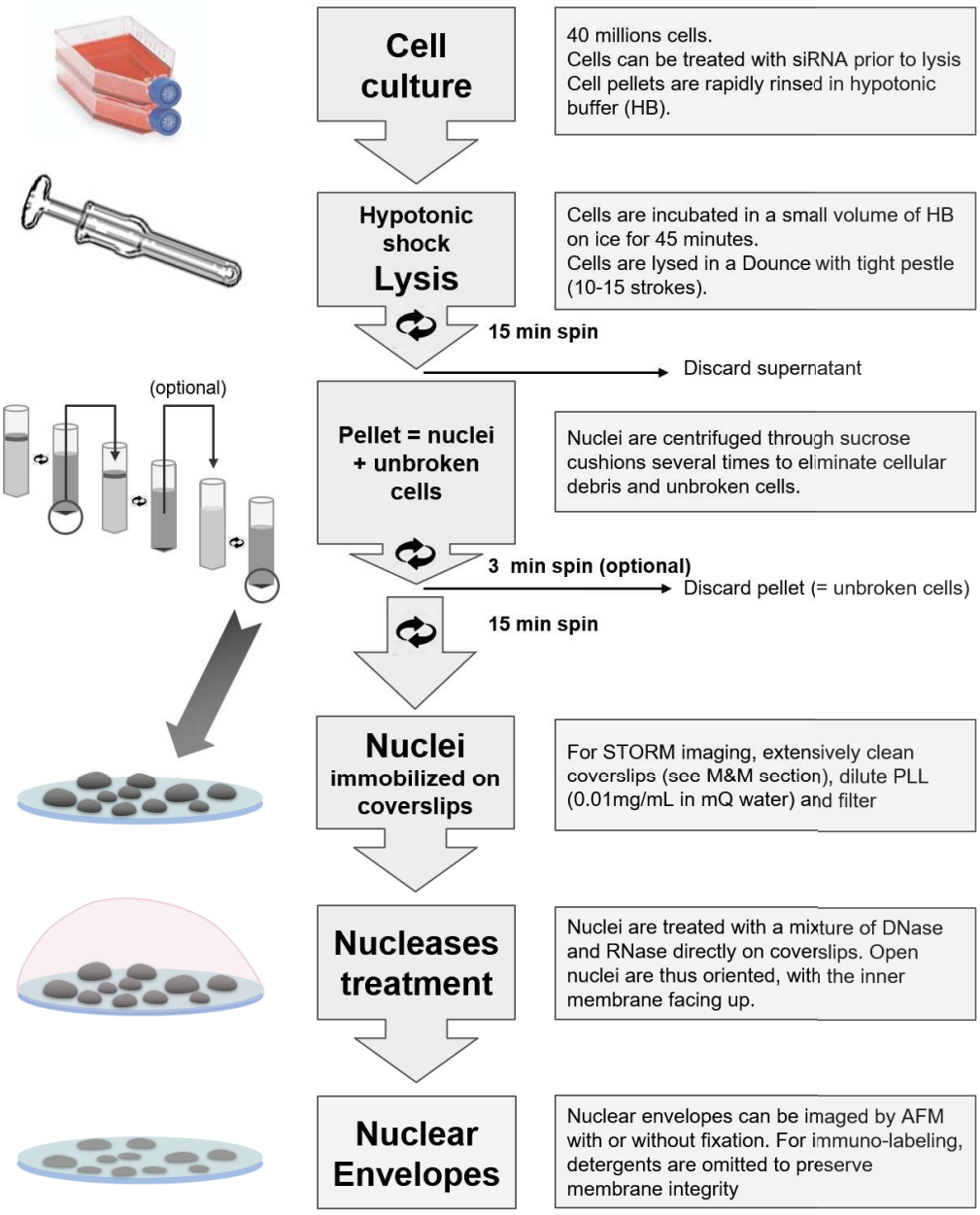

Figure 37: Purification process. U2OS cells are broken thanks to hypotonic shock lysis. The solution is then purified through centrifugation steps to keep only intact nuclei. Nuclei are then immobilized on a clean coverslip and treated with nucleases to obtain flat purified NEs.

To open nuclei, 250 µl of nuclei solution was deposited on a clean 25mm high-precision glass coverslip coated for 2 minutes with Poly-L-lysine diluted (1:10) in water (0.01 mg/ml final concentration) at room temperature. The nuclei were incubated for 15 minutes to allow their attachment to the surface. The coverslip was rinsed two times with S500 to remove weakly attached nuclei.

The opening procedure is based on a combination of osmotic shock and nuclease treatment and derived from the methods described by Ori et al. (Ori, Andrés-Pons and Beck, 2014). NE-A and NE-B buffers were pre-warmed at 30°C. 200 µl of NE-A buffer (0.1 mM MgCl2 + 30U DNAse I + 250U RNAse + 1 mM DTT in 0.5 mL) was put onto the immobilized nuclei for 30 seconds, then 800 µl of NE-B (0.1 mM MgCl2, 20 mM Tris pH 8.5, 10% sucrose + 1mM DTT) was added to the coverslip. The mixed solutions were then left for incubations on the sample for at least 35 minutes before rinsing with S500.

The sample was then fixed for 5 minutes with 4% PFA and stored in a fridge. Fixation is not mandatory but prolongs the lifetime of open nuclei from 1-2 days to 1 week.

6.3. Labelling strategy

In most cases labelling was performed by indirect immunofluorescence using primary antibodies directed against the protein of interest in combination with a secondary antibody carrying fluorophores. This approach allows a great versatility to juggle between various microscopies (conventional, STED, STORM) and versatile double or triple labelling.

For NPC labelling, the mAb414 antibody was used. mAb414 is a widely used antibody that mainly recognises Nup62 but also Nup153, Nup214 and Nup358 (Davis and Blobel, 1986). It is directed against some FG-repeat motifs present in these proteins and is a standard marker broadly used to label mature NPCs. Primary mAb414 antibody with directly attached fluorophore has been used as well as unlabelled one.

Labelling of different Nups and other proteins included in this study (like SUN1) was mainly performed by immunofluorescence. Wheat-germ-agglutinin (WGA) was used in some experiments on intact nuclei for NPC labelling.

Table 1 : Antibodies used to label Nups and proteins in fluorescence microscopy experiments

Supplier	Ref	Protein	Type	Conjugated	References / dilution
BioLegend	682202	**mAb414**	mouse mono	Alexa 594	1:1000
abcam	ab124770	**SUN1**	rabbit mono [EPR6554]		1:1000
Covance		**mAb414**	mouse mono		IF 1:2000, STED 1:500
Abcam	ab84516	**Tpr**	rabbit		McCloskey et al, 2018 (1:200)
Genetex	GTX102128	**POM121**	rabbit		McCloskey et al, 2018 (1:200)
abcam	ab53540	**ELYS**	mouse		Kane et al, 2018 (1:200)
abcam	ab96462	**Nup153**	mouse [SA1]		McCloskey et al, 2018 (1:200)
Thermo Scientific	PA5-19468	**Lamin B1**	rabbit		1:500

For U2OS/POM121-GFP and U2OS/Nup96-GFP cells, the GFP fluorescence was measured directly. For U2OS/Nup96-SNAP cells, Nup96 labelling was done by using a SNAP ligand conjugated with AlexaFluor 647 (NEB) according to the protocol described by Thevathasan et al. (Thevathasan *et al.*, 2019). For AFM imaging, this protocol was slightly modified by removing all detergents present in buffers to preserve the integrity of the lipid membrane of the NE.

For immunofluorescence in cells, cells were plated on a clean coverslip (sonicated 30 minutes in 1M KOH before rinsing and sterilized under UV for 20 minutes) and let to adhere and grow for 24h. Cells were then washed twice in PBS and fixed for 5 minutes with 4% PFA. Primary antibody labelling was performed with primary antibody in immunofluorescence buffer (IF buffer = 10 mg/ml BSA, 0.1% Triton, 0.02% SDS in PBS) for 1 hour. The sample was then rinsed with IF buffer to remove unbound antibodies. Secondary antibody was then added at 1-10 µg/mL in IF buffer (depending on the application) and incubated on the sample for 30 minutes. Samples were finally fixed with 4% PFA for 5 minutes. For light microscopy experiments like STED and confocal microscopy, coverslips were then mounted with Vectashield against a glass slide and sealed with nail polish for later imaging.

6.4. AFM imaging

Atomic force microscopy was performed on a JPK Nanowizard 4 combined with a CellHesion Z stage. Experiments were performed in liquid in Nuclei Imaging Buffer (NIB) (10 mM HEPES pH 7.5, 2.5 mM MgCl2, 83 mM KCl, 17 mM NaCl derived from Kramer *et al.* (Kramer *et al.*, 2007). qp-Bio-T and qp-Bio-AC probes were used for intact nuclei while Bruker MSNL probes using cantilever E (0.1 N/m) or Olympus OTR4 probes (0.12 N/m) were used for open nuclei. Both MSNL and OTR4 probes have pyramidal tips with a nominal tip radius of 2 nm for MSNL and 7 nm for OTR4. The spring constant of the cantilever was calibrated, prior to imaging, by acquisition of a force versus distance curve on a rigid, clean glass coverslip. Optical lever sensitivity was calibrated with a linear fit of the repulsive part of the force curve assuming the displacement of the force sensor (in nm) to be equal to the deflection of the cantilever (in V), therefore leading to the calibration parameter in [nm/V]. Spring constant was calibrated by recording the thermal noise of the cantilever and calculating the spring constant with the Sader method.

Images were recorded at resolution of 256 x 256 pixels in Quantitative Imaging (QI) mode, which consists in performing a force-curve at each pixel of the image and reconstructing the topography by using the height at 80 % of the maximum applied force. The maximum force setpoint was below 300 pN to minimize the force applied on the soft biological sample while keeping the acquisition time short enough to avoid drift and facilitate the correlation with the super-resolution image. The length of the force curve was 200-300 nm with a Z movement speed of typically 30 µm/s.

6.5. Correlative AFM/Fluorescence

To allow correlative fluorescence imaging of the sample, the AFM was mounted on a custom-made microscope based on a Zeiss Observer D1 inverted microscope (Figure 38).

The microscope was coupled with four laser lines, composed of a Oxxius Near-UV Violet 405 nm laser (100 mW), a Coherent Obis 488 nm laser (50 mW), a Coherent Sapphire 561 nm laser 100 (mW) and Coherent Obis 641 nm laser (100 mW) or a MPB 642 nm laser

(1W) for STORM. All laser lines were combined in the same optic path using dichroic mirrors and directed to an acousto-optic tunable filter (AOTF) to select which laser is sent to the sample and control its intensity. The laser beam is then enlarged and focused in the back focal plane of the microscope's objective by two lenses and deviated by a polarized beam splitter just before the objective.

Total Internal Reflection Fluorescence (TIRF) illumination was achieved by laterally translating the polarized beam splitter to move the beam to the side of the back focal plane. To allow TIRF, a high-numerical aperture objective is necessary. Thus, the objective used in this microscope was an oil immersion Zeiss α-Plan-Apochromat 100X, 1.46 N.A. DIC.

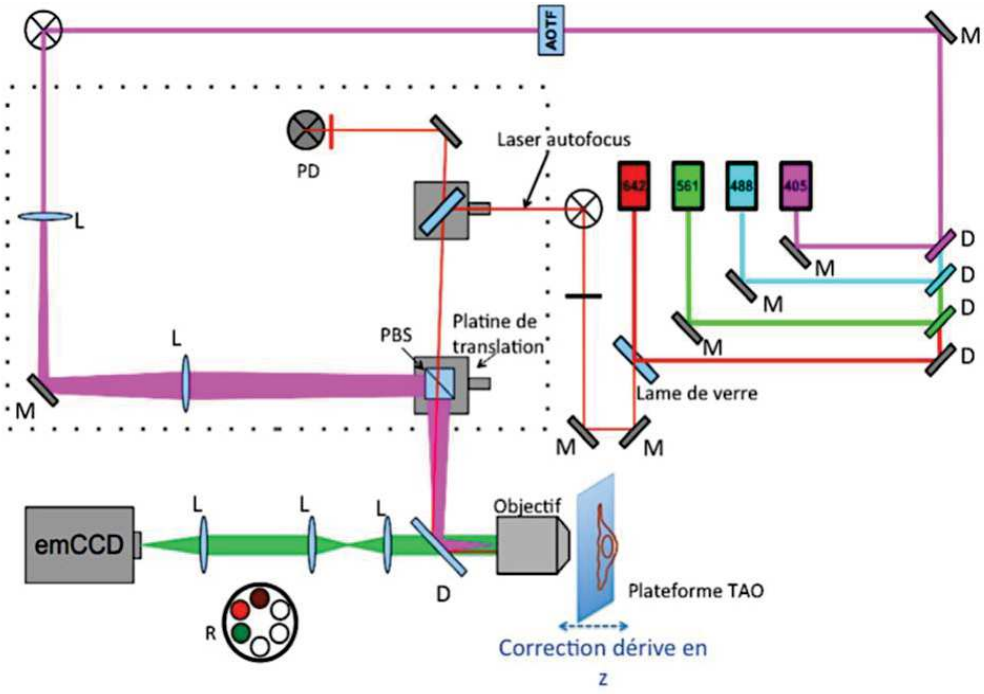

Figure 38: Schematic of the setup used for correlative AFM/fluorescence microscopy. M: mirror, D: dichroic mirror, L: lens, R: filter wheel, PD: 4-quadrant photodiode (autofocus), PBS: polarized beam splitter.

Fluorescence emission signal was then returned to a filter wheel placed in front of an Andor Xion Ultra 897 emCCD 512x512 pixels², with a pixel dimension of 16 µm. A 2x telescope was placed in front of the camera to obtain a final image magnification of 200, corresponding to a pixel size of 81.3 nm. Acquisition of the images was controlled by a Labview program developed in the lab. For correlation with AFM, the AFM cantilever was roughly placed at the

center of the objective, based on the field of view in binoculars of the microscope. Then, using the emCCD, under white light illumination, the tip was more precisely aligned with the area of interest to scan a nucleus. Finally, the TIRF image was imported into the JPK imaging software using the emCCD camera pixel calibration for matching scales. This image was then shifted to match with the AFM topography. Generally, the border of the nucleus was used for coarse alignment, then a specific NPCs pattern for fine alignment.

To keep the focus constant during STORM acquisition, a small amount from one of the visible lasers was sent to another optical path and positioned in TIRF configuration. The reflected beam was then sent to a 4-quadrant photodiode (PD) to keep its position constant on the PD by a feedback loop directly controlling the stage (CellHesion) in Z.

6.6. STORM experiments

STORM experiments were performed on the correlative setup presented before. Proteins of interest in cells and nuclei were labelled with AlexaFluor 647.

An oxygen-scavenging buffer based on PBS including 10% glucose and containing 40 µg/mL glucose oxidase, and 50 µg/mL catalase, supplemented with 25 mM mercaptoethylamine (MEA) and Tetraspeck (1/1000) fluorescent beads was loaded on the sample. 1,2 mL of this solution was used to fill the AttoFluor. A glass coverslip was put on top of the AttoFluor to limit oxygen exchange with the ambient atmosphere.

STORM acquisition was performed by illuminating the sample with a 642 nm laser, set to 500 mW nominal power to obtain 3-7 kW/cm² on the sample. 30 000 frames, with an acquisition speed of 20-30 ms were recorded. 0-0.1 kW/cm² of 405 nm was sometimes used for conversion from the dark state. The acquisition area was chosen so that a nucleus surrounded by several Tetraspek fiducial markers was visible.

STORM analysis was performed using Fiji plug-in Thunderstorm. Drift was corrected thanks to the fiducial markers or in some cases by cross-correlation. To reconstruct the image, localizations were filtered to keep only intensity (number of photons) between 50 and 5000,

localization precision below 45 nm and standard deviation of the fit of the PSF between 90 and 180 nm. For diameter measurements, analysis was performed using SMAP (Ries, 2020).

6.7. STED experiments and data analysis

For STED experiments, fixed cells were immuno-labelled with primary antibodies, at a 1:200 dilution in most cases and secondary antibodies conjugated to either Alexa Fluor 594 (Molecular Probes or BioLegend) or Star 580, and Star RED or Star635P (Abberior).

The focus was adjusted on the lower surface of nuclei, which is large and flat in U20S cells and ensures a large number of NPCs being in focus at the same time. To avoid photo-bleaching, a single image was acquired for an entire nucleus.

STED images were acquired on an Abberior Instrument Expert Line STED super-resolution microscope (Abberior Instruments GmbH, Göttingen, Germany), using 561- and 640-nm pulsed excitation laser sources and a pulsed STED laser operating at 775 nm and an 80-MHz repetition rate. The fluorescence excitation and collection were performed using a 100×/1.40 numerical aperture (NA) Plan Super Apochromat 1.4 oil immersion objective (Olympus, Southend-on-Sea, UK). All acquisition operations were controlled by Imspector software (Abberior Instruments GmbH, Germany). Image series were recorded using Imspector software with the following parameters: pixel dwell time, 3 µs; 10 repetitions; pixel size, 15 nm per pixel, de-excitation power (measured in the back focal plane of the objective), 250-300mW, pulse duration, 8ns with a delay of 700ps.

As a general workflow for STED analysis, images were loaded and analyzed in Matlab (MathWorks) and the statistical and graphical representations were done in Python, using mostly the numpy, pandas and matplotlib libraries. All analyses were performed on normalized images.

For automated pore detection, a gaussian filter was applied to the images (sigma = 2). For mature NPCs detection, local maxima were collected in the mAb414 channel image, with an intensity threshold (Th1) being applied. For Pore Intermediate detection, local

maxima were collected in the POM121 channel; maxima were kept if their POM121 intensities were above a given threshold (Th2), AND the POM121 / mAb414 intensity ratio was also above a third threshold (Th3). The three thresholds were found empirically; the accuracy of the detection algorithm was systematically visually inspected. As acquisition parameters were conserved in all experiments, all data were analyzed with the same thresholding parameters.

Individual pores were then analysed for their intensity profiles from normalized, non-filtered images. For this, we measured intensity profiles along a line centered on pore (mAb414 position for mature NPCs, POM121 localisation for pore intermediates), with a total length of 150nm and a 25nm step. The line was then rotated 19 times with an angle of pi/20. The resulting 20 intensity profiles in each channel were then averaged, and recorded as individual rotationally averaged intensity profiles. These profiles were then fitted with gaussians to extract geometric characteristics (pore diameter, FWHM, amplitude, distances…).

6.8 AFM image processing

AFM images were treated using Gwyddion software. Images were corrected by subtracting the mean plane, applying line correction and sometimes removing horizontal lines. Aberrant pixels (very high or very low) due to problems in the force curve were sometimes corrected by using mask which interpolates a pixel with surrounded pixels. For crops around NPCs, data from images with scan sizes of 1 to 3 µm were used and crops of 300 nm x 300 nm were extracted. The Z scale was always ranging from 0 to 150 nm which is sufficient for the topography around NPCs. The offset and tilt of the nucleoplasmic ring was corrected using the Matlab algorithm from Stanley et al. (Stanley, Fassati and Hoogenboom, 2018).

For mechanical measurements from QI data, we used JPK data processing software. Experimentally calibrated spring constant was used for calculations, force curve baseline offset and tilt was subtracted before tip vertical position correction. Tip-sample contact point was determined using the Hertz/Sneddon model for a quadratic pyramid in the software with

tip pyramid angles modified to match MSNL probe geometry. The stiffness was measured by fitting the repulsive part of the force from the contact point over 20 nm.

Results

To decipher and understand in more detail the process of human NPC interphase assembly, it was important to observe both the composition and the structure of single assembly intermediates at high-resolution in a preserved NE. This information can be provided by combining AFM and fluorescence microscopy in a correlative manner on nuclei purified from cells. While AFM can document the topography of the NPCs at the nanometer scale, super-resolved fluorescence microscopy techniques like STORM can sub-localize Nups present in the NPC and intermediates with a resolution in the same order as that obtained with AFM.

This approach purifying nuclei from human cells in a manner that preserved NE and NPCs. Then, AFM imaging had to be optimized to acquire topography of NPCs in the context of an intact purified nucleus.

Investigating interphase assembly required additional development in the sample preparation to allow the AFM tip to access the INM, where early events of the interphase assembly occur. Sites of pore assembly were identified thanks to the presence of POM121, an early player in interphase assembly. It was then possible to determine the local topography of the pore intermediate and the surrounding membrane, and to precisely localize specific Nups at this place. Our aim was to describe the role of the different elements involved in interphase assembly which were still poorly understood.

7. AFM observation of NPC from ONM on purified nucleus

The first step of the thesis work was to test the possibility to image the topography of NPCs and potentially interphase assembly intermediates directly on purified intact nuclei. It represented a challenge because of the poroelastic nature of the nucleus (Wei *et al.*, 2016) which makes AFM difficult since imaging could trigger a mechanical deformation and oscillation of the NE. We used QI mode for AFM with a loading rate of 8 to 10 µm/s to avoid this phenomenon.

Investigation of the NPC by AFM requires the extraction of the nucleus from the cell to access the NE with the tip. To do so cells were broken by hypotonic lysis and mechanical shearing of the plasma membrane while preserving nuclei. These were isolated from the crude cell lysate by a series of centrifugations through sucrose cushions (see Material and methods for more details). This procedure allowed obtaining a solution of purified nuclei with a concentration of 1 million nuclei per mL in S500 buffer from U2OS adherent cells (Figure 39). The purified nuclei were then deposited on a glass coverslip for further microscopy imaging.

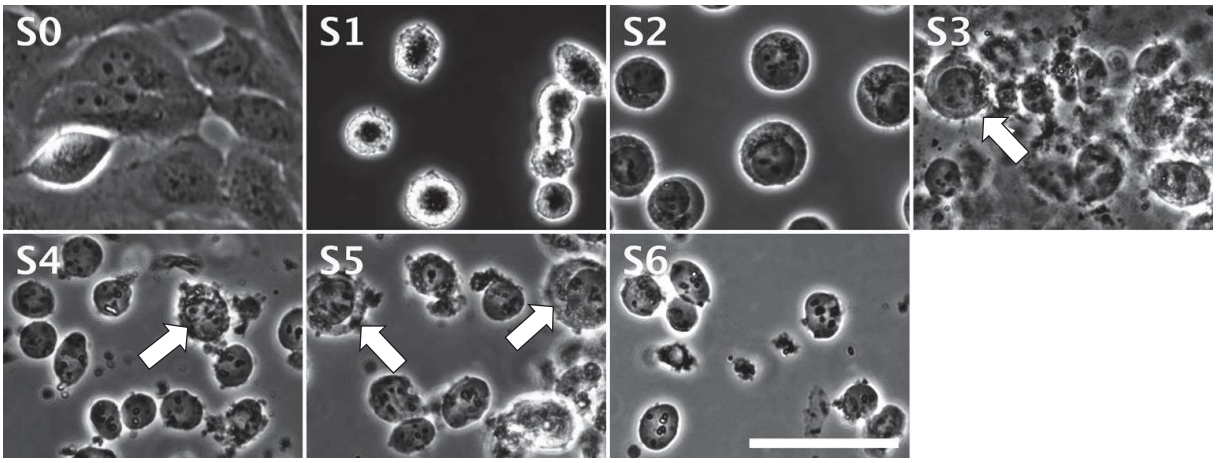

Figure 39: Sample images acquired at different steps of the nuclear envelope preparation procedure. S0- Adherent cells. S1- Trypsinized cells. S2- Intact cells submitted to hypotonic shock. S3- Crude cell extract after mechanical shearing. Intact cells are indicated by an arrow. S4- Total nuclei fraction after centrifugation through sucrose cushion. Remaining intact cells are indicated by arrows. S5- Preclearing pellet. Remaining intact cells are indicated by arrows. S6- Final nuclei fraction.

Epifluorescence of purified nuclei labelled with WGA-Alexa488 (see Materials and methods) was correlated with AFM topography (Figure 40 and 42). The first AFM image of the NPC on purified nuclei was obtained on a nucleus that spontaneously opened (Figure 40). While on the right side of the nucleus, the NE was ruptured, a small band of preserved NE was still present on the left of the nucleus (white arrow in Figure 40).

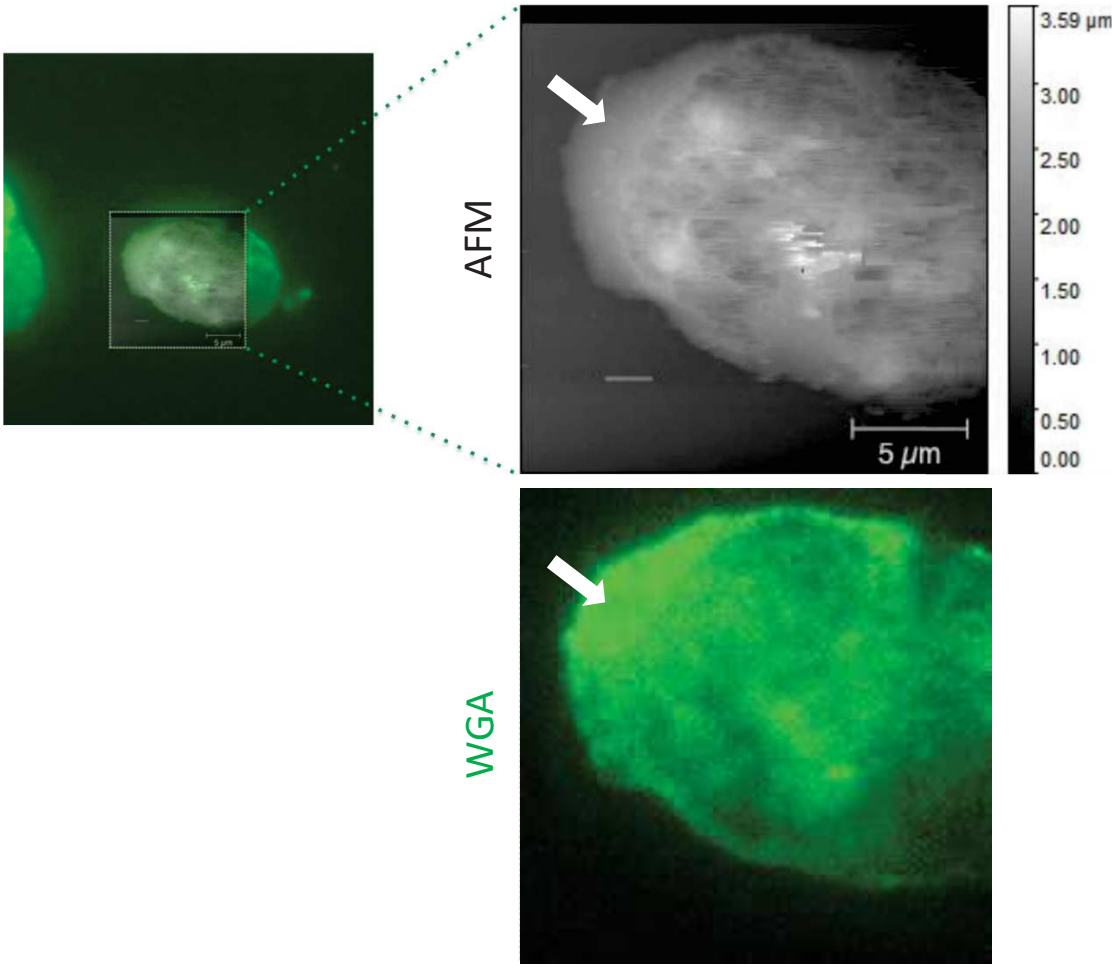

Figure 40: Correlative AFM/ fluorescence of a spontaneously opened nucleus labelled with WGA. Correlation of the topography (grey scale image) and fluorescence (green) reveals a small band of preserved NE on the left of the nucleus (see white arrow).

Scanning of this area by AFM further revealed the presence of ring structures of around 80 nm in diameter (see blue rings in Figure 41) which matches the expected diameter of the cytoplasmic face of the NPC.

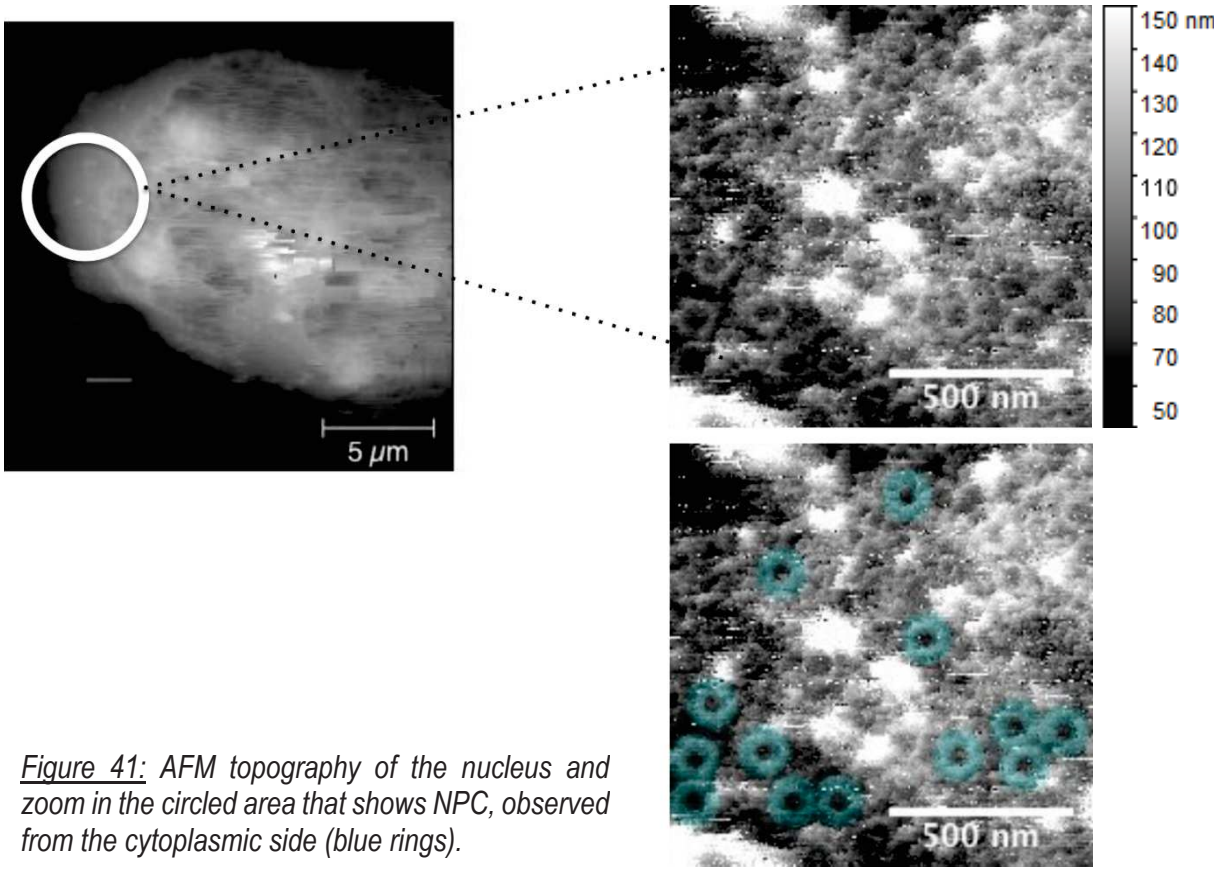

Figure 41: AFM topography of the nucleus and zoom in the circled area that shows NPC, observed from the cytoplasmic side (blue rings).

Improvements made in the purification procedure, like the use of a Dounce homogenizer, allowed a better preservation of the nuclei and imaging by AFM of the topography of an entire nucleus that could be correlated with the fluorescence image (Figure 42).

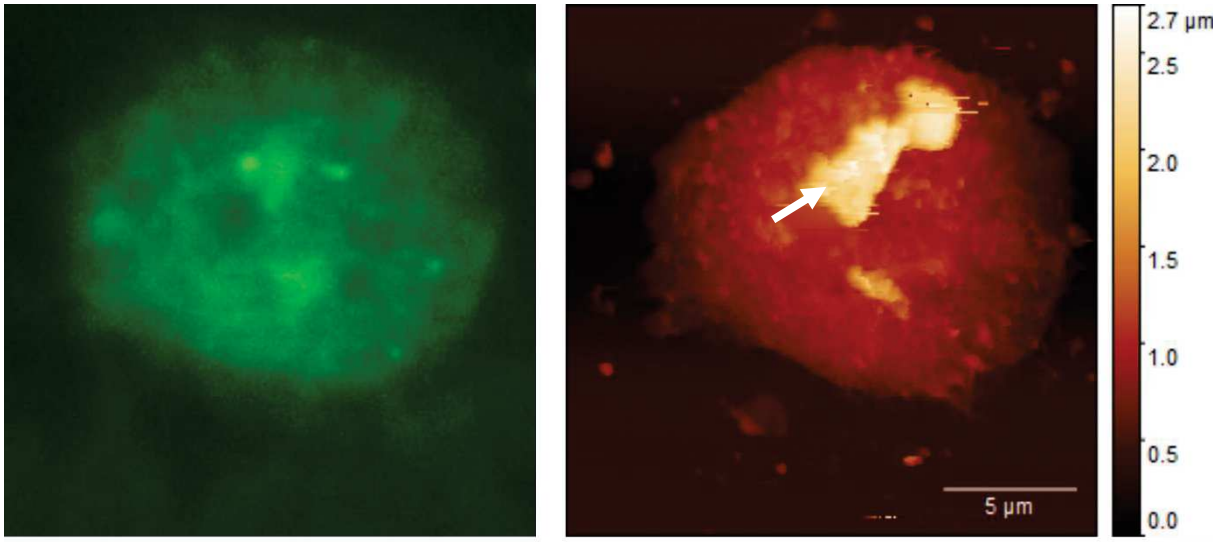

Figure 42: Correlative fluorescence (left)/AFM (right) of an intact nucleus labelled with WGA. White arrow indicates higher protrusion that could correspond to part of the ER.

The overall shape of the nucleus could be well aligned between the epifluorescence image labelled with WGA even though direct correlation of individual NPC was not possible due to the low image quality of the epifluorescence image. The AFM image of the nucleus showed the membrane shape was well preserved. The protrusion with a higher topography at the top could correspond to a fragment of the ER still connected with the NE (white arrow).

Imaged at a higher magnification, the surface of the non-fixed cell nucleus revealed rings present at the NE surface (see black arrows in Figure 43). Cytoplasmic filaments were not visible in the AFM image, probably because of their small diameter and flexibility or because these filaments can also collapse into the pore opening (Fernandez-Martinez *et al.*, 2016b). Thus, the ring shape topography corresponds to the cytoplasmic rings. The structure resembles what has been observed by AFM in *Xenopus laevis* on intact nuclei (Jäggi, Franco-Obregón and Ensslin, 2003), or purified NEs (Kramer *et al.*, 2008; Bestembayeva *et al.*, 2015; Sakiyama *et al.*, 2016; Stanley, Fassati and Hoogenboom, 2018) and air-dried nuclei from myotubes cells (Asally *et al.*, 2011). It is however important to mention that the membrane topography appeared much more corrugated and heterogeneous as compared to that of *Xenopus*.

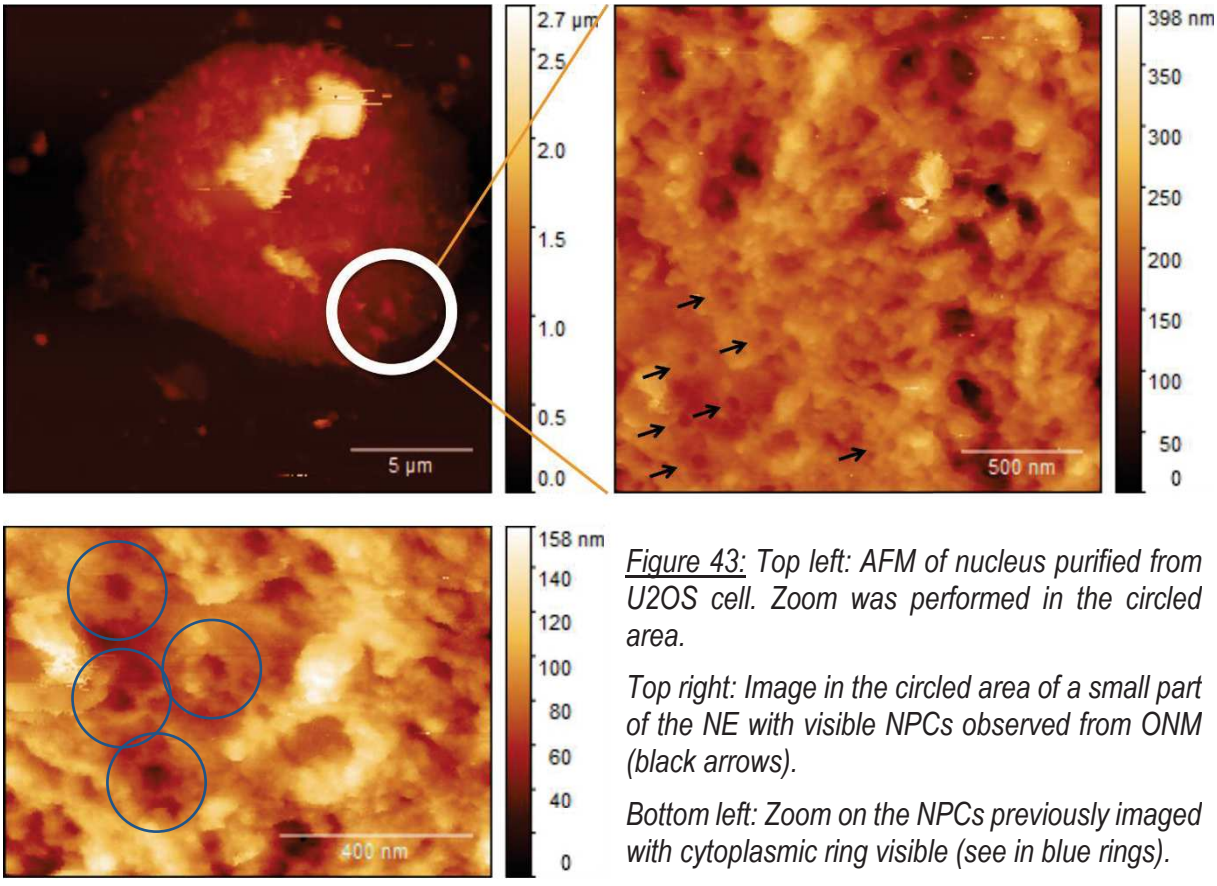

Figure 43: Top left: AFM of nucleus purified from U2OS cell. Zoom was performed in the circled area.

Top right: Image in the circled area of a small part of the NE with visible NPCs observed from ONM (black arrows).

Bottom left: Zoom on the NPCs previously imaged with cytoplasmic ring visible (see in blue rings).

The rim of the nucleoplasmic ring was about 20 nm thick with a diameter at the top of the rim around 80 nm and the eight-fold rotational symmetry could be guessed in the most zoomed images (Figure 44).

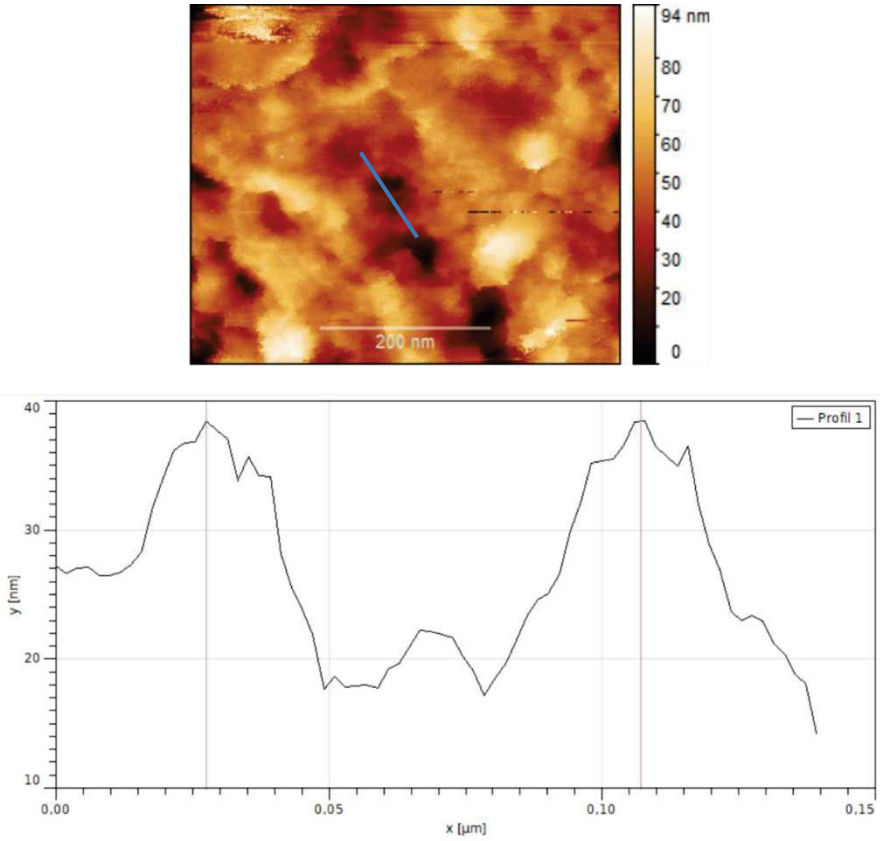

Figure 44: Image of an NPC with profile (blue line and graph) of the NPC showing 79,5 nm peak to peak distance at the top of the rim.

To conclude this part, the data presented here represent to our knowledge the first AFM images of human NPCs observed directly on an intact nucleus in liquid. Otsuka et al. revealed at the very beginning of my thesis that most of the early steps of interphase assembly occur at the INM. Thus, I then focused mainly on the AFM imaging of the NPC nucleoplasmic side and rather than optimizing AFM imaging of NPCs in intact nuclei. However, this purification approach could be used to better understand *in situ* processes like nucleocytoplasmic transport directly at the NPC gate.

8. Investigation of NPC from INM by correlative AFM and fluorescence

8.1 Controlled nuclei purification and opening

Current approach was to image NPCs by AFM on purified nuclei or NE to investigate the topography of interphase assembly intermediates. However, important results from Otsuka et al. (Otsuka *et al.*, 2016) showed that during interphase most of NPC assembly takes place on the INM. Consequently, further strategy has to be revisited. To study intermediate structures and especially early ones where POM121 is involved, nuclei had to be opened while NE and NPC orientation was thoroughly controlled to allow the AFM tip to access the inside of the nucleus. To do so, nuclei were first immobilized on glass coverslips and were treated to be opened. Importantly, no detergents could be used since the topography of the preserved INM at these assembly sites was to be observed. Thus, the goal of this part of my work was to tune the different steps of the protocol to open nuclei in a manner that preserves NPCs.

Adaptation of an existing protocol for purification of NE (Ori, Andrés-Pons and Beck, 2014) allowed opening of the U2OS cells nuclei in a manner that preserves the NE and controls its orientation. The key point of this new protocol was to perform it not in solution, but after attachment of the nuclei to a coverslip so that NEs are oriented with the INM facing up. This protocol combines an osmotic shock with a nuclease treatment to create a hole in the NE while DNase and RNase would digest all nucleic acids. Attaching the nuclei to the coverslip ensured that the part of the NE stuck to the glass remained in the specific orientation with its INM facing up. The nucleus ended up open on the coverslip in different configurations (Figure 45 and 46). Nuclei could open from the side and a have top and bottom NE on top of each other or presented a hole at the center of the nucleus.

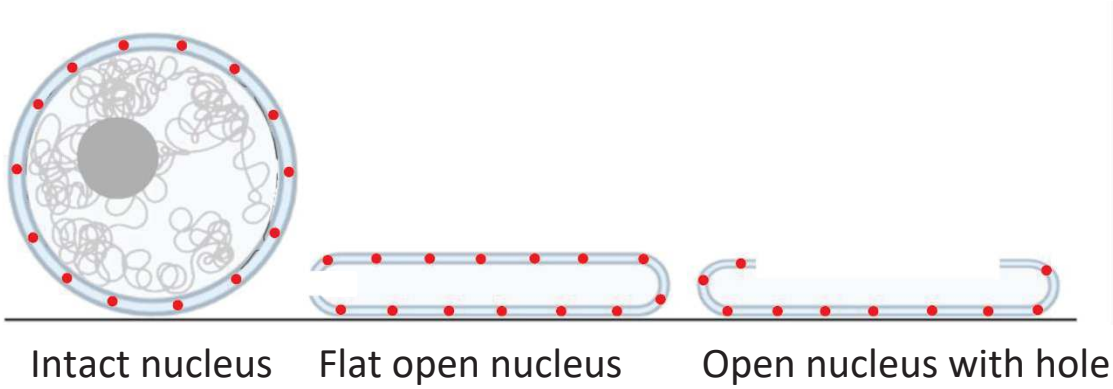

Figure 45: Different configuration of NE (blue) with NPCs represented as red dots. Left figure represents an intact nucleus where top and bottom regions of the NE can be separated by confocal microscopy. Centre and right figure represent two ways nuclei can open using our protocol, either flat or exhibiting a hole in the NE. In these two cases, no separation between top and bottom is possible by confocal microscopy and signal of NE and NPCs doubles in areas where both regions are present.

Effect of the opening procedure is presented in Figure 46. Compared to the control (left image in figure 46), opening treatment resulted in flat nuclei devoid of chromatin. The topology of the remaining NE could differ since the opening point was not manually controlled. This sometimes resulted in a collapse of the upper sheet onto the lower sheet of the NE (central panel in Figure 46); in this case, no INM is accessible. In contrast, nuclei could exhibit a large piece of the top NE missing which gives access to the INM for AFM imaging. The different configurations of opening are easily distinguishable thanks to the two-fold difference in NPC density - because the two collapsed sheets of NE are not axially resolved.

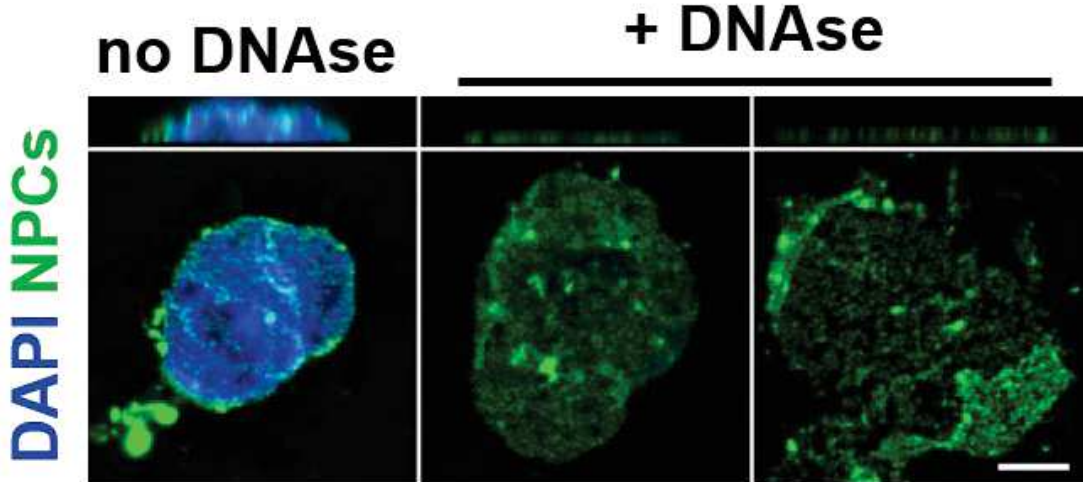

Figure 46: Effect of the opening treatment of nuclei observed by confocal microscopy. 3D-confocal imaging of nuclei isolated from U2OS and treated or not with nucleases. The chromatin was labelled with Hoechst (blue) and NPCs with WGA (green). Top panels show XZ sections; bottom panels show the basal nuclear membrane. Left panel: Nucleus without treatment. Central panel: Treated nucleus with two layers of collapsed NE. Right panel: Treated nuclei opened with accessible INM. Scale bar is 5 µm.

While the general topology of the NEs was preserved, the integrity of the NE at several levels had to be controlled:

- Integrity of the lipid bilayer, to make sure that no significant tears would happen,
- integrity of the protein organization
- integrity of pore organization and structure.

To do so, the first control was to use a lipid dye to measure the lipid membrane signal from the nuclear membrane. By confocal microscopy, it was first observed that the lipid membrane of the NE remained present at places where nuclei were opened (Figure 47). NPC labelling of an open nucleus revealed the presence of a hole in the nucleus, which could be deduced from the lower NPC density in this place where only the NE attached to the coverslip remained (left image in Figure 47). There was also a two-fold difference in lipid dye intensity between the open and closed regions, as depicted in figure 47. The intensity pattern suggests that indeed the bottom NE sheet is preserved during opening.

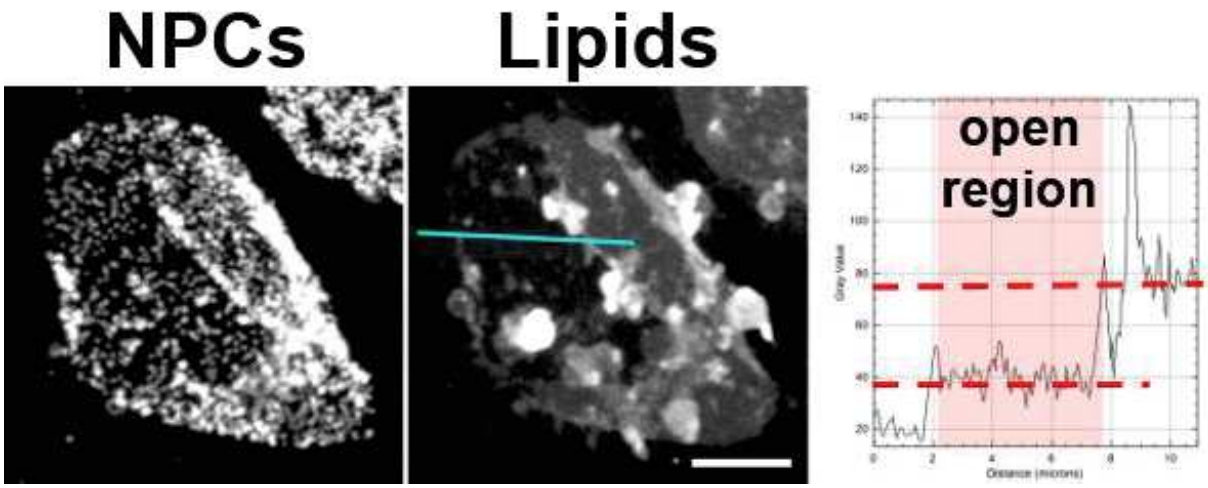

Figure 47: Confocal imaging of an open nucleus. NPCs are labelled with WGA (left), lipids with DiOC6 (center). Scale bar is 5 µm. The right panel shows the intensity profile of the lipid dye along the cyan section.

Another important element of the NE envelope is the underlying lamin meshwork which is essential for its mechanical stability. It was chosen to check lamin organization as a readout for protein organization at the NE. The results (Figure 48) indicate that the lamin meshwork continuity can be affected by the opening procedure in some cases and depended on the way the nucleus opened. In comparison with a control untreated nucleus (Figure 48a and 48b), the lamin staining exhibited important tears in nuclei where very large patches of

NE are sheared away (Figure 48c and 48d). Yet the lamin staining appeared homogeneous in nuclei exhibiting a central hole (Figure 48e or 48f) with a large band of the top layer of the NE surrounding this hole. Thus, for further studies, this type of open nuclei was preferentially chosen for AFM imaging.

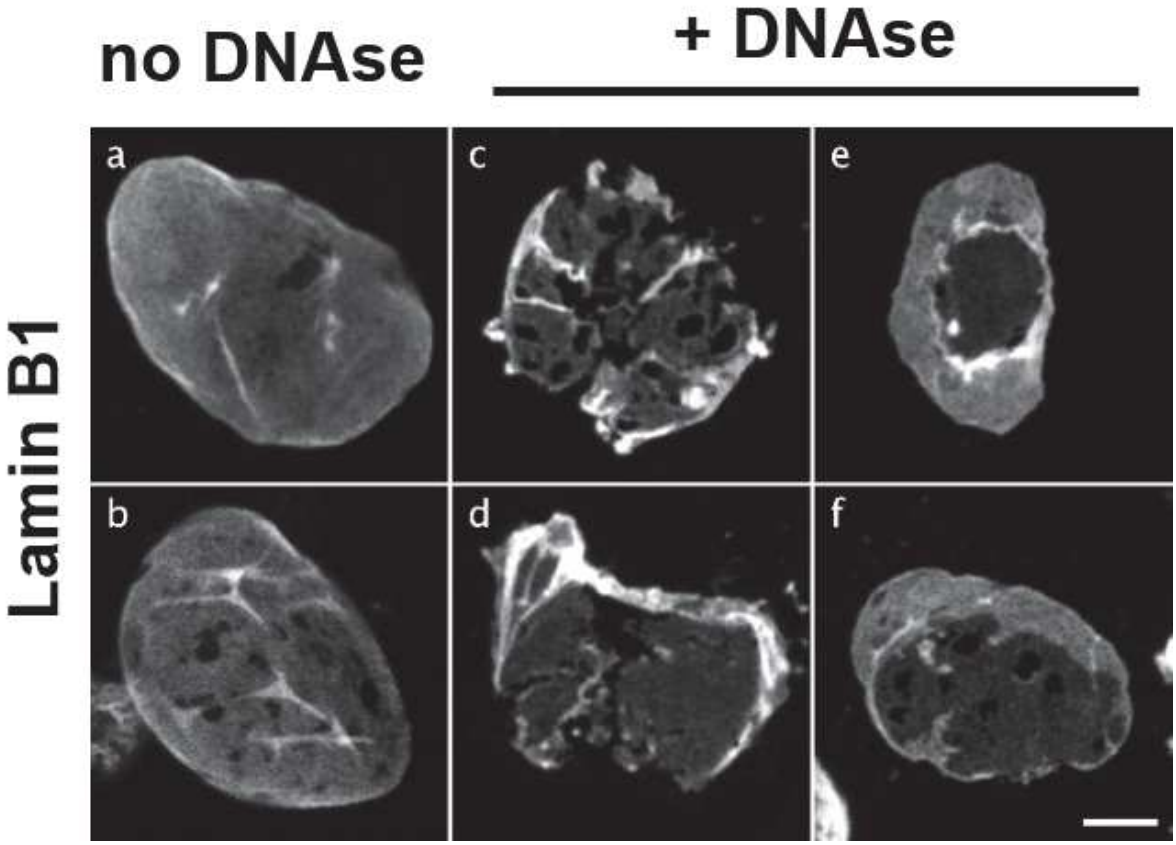

Figure 48: Confocal imaging of nuclei treated (c-f) or not (a-b) with nucleases and labelled with anti-lamin B1. Well-circumscribed openings (e) better preserve membrane integrity, translated in homogenous lamin staining; scale bar is 5 µm.

Finally, the integrity of NPCs in open nuclei was checked. To quantify this, U2OS/Nup96-SNAP cells were analysed by STORM imaging. Thevathasan *et al.* had demonstrated that NPCs could be used as a reference standard for quantitative super resolution microscopy (Thevathasan *et al.*, 2019). The U2OS cell line was used with endogenous Nup96 fused to a SNAP tag (named Nup96-SNAP), and labelled pores with a SNAP-ligand coupled with AlexaFluor 647 to control how NPCs were affected by the current protocol. Both the radius and the density of NPCs in cells, intact nuclei and open nuclei were then measured.

STORM reconstructed images revealed the image of the different subunits of Nup96 in the NPC (doubly labelled with mAb414 that recognizes the FG-Nup of the central channel). STORM images were similar between all three conditions and the overlay between TIRF acquired mAb414 signal and Nup96 STORM signal showed a very good correlation (Figure 49).

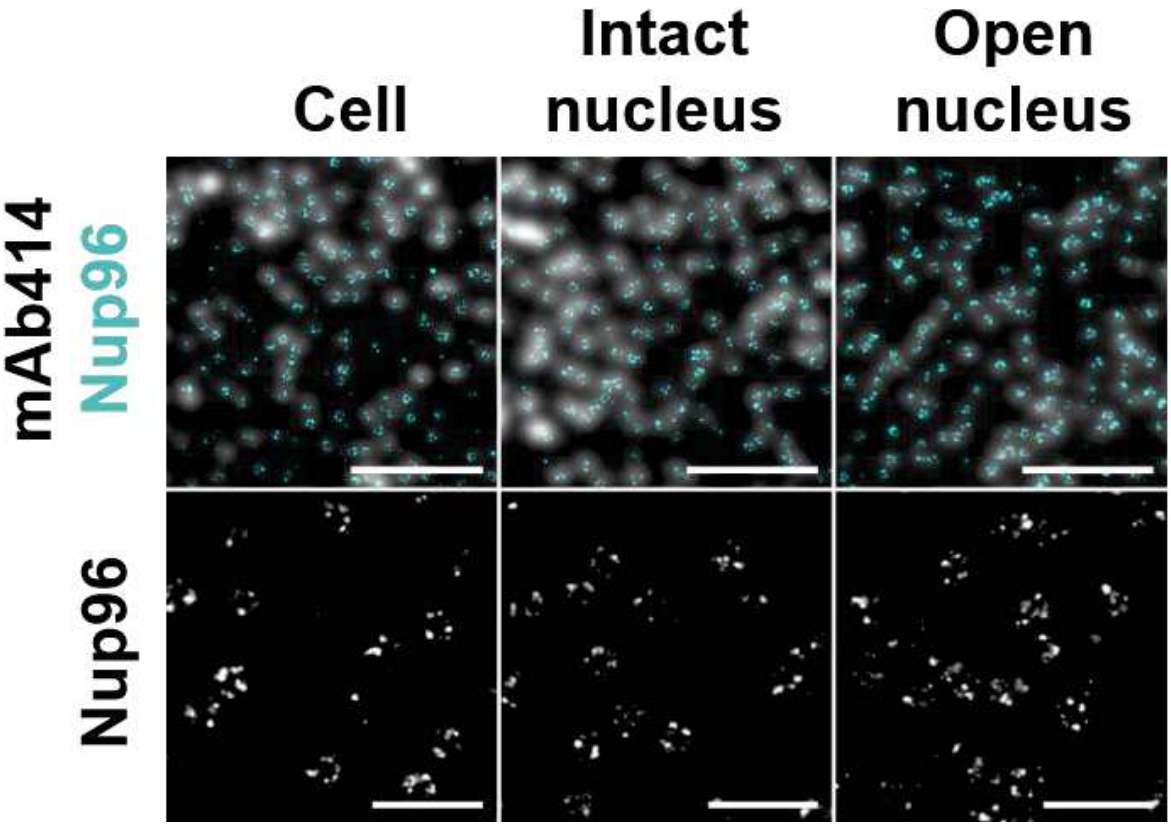

Figure 49: Nuclei and nuclear envelopes were extracted from U2OS/Nup96-SNAP. Intact cells, intact nuclei or open nuclei were labelled with mAb414 and AF647-SNAP ligand. Diffraction-limited (mAb414) and STORM images (Nup96-SNAP) were acquired in TIRF illumination; scale bars are 2 µm (top) and 500nm (bottom).

The NPC density was quantified under the three conditions which remained similar from cells to open nuclei with a value close to 4 NPC/µm² (Figure 50). This confirmed that NPC organization was not perturbed in open nuclei chosen according to the criteria discussed previously (a central hole). Finally, to check the integrity of NPCs, the radius of Nup96-SNAP rings was measured. Thevathasan *et al.* measured an average radius of 53.7 nm in cells (Thevathasan *et al.*, 2019) using an in house Matlab program. With the help of the same program, which was freely available, a mean pore radius in cells, purified intact nuclei and open nuclei was measured to be 56 ±2.9 nm, 55.6 ±3.4 nm and 56.5 ±2.9 nm respectively.

These measurements are very close to the expected values and, most importantly, show that NE preparation does not impact the structure of NPCs, at least at the scaffold level.

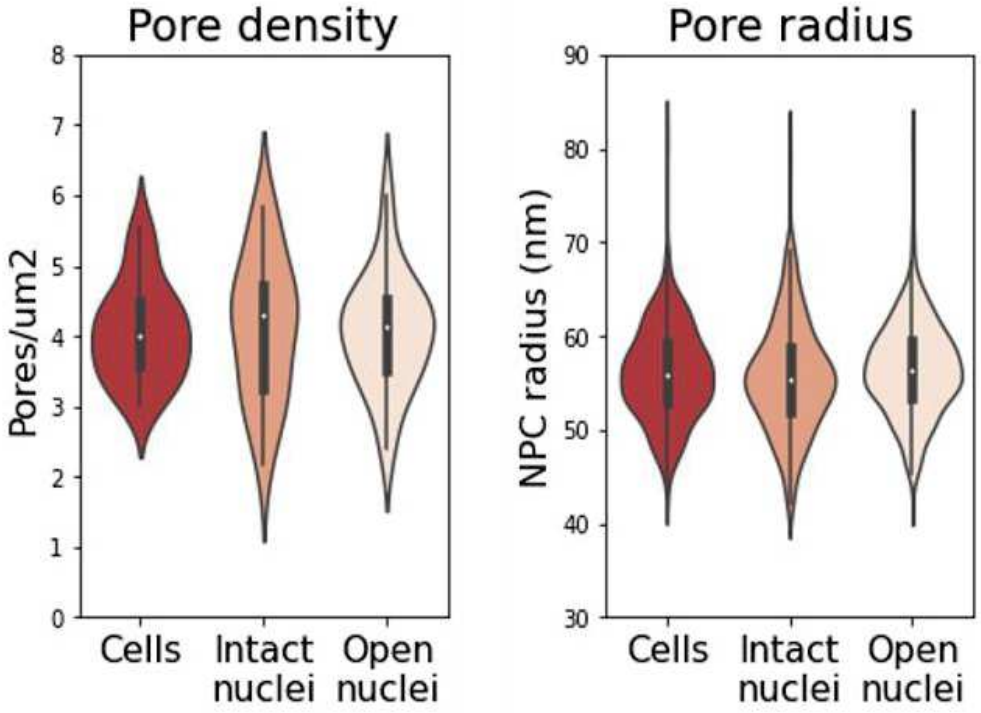

Figure 50: Pore density measured from confocal images (n>20 nuclei); NPC radii measured from STORM images as exemplified in D (n≥3 nuclei).

In conclusion, the updated approach allows opening human cell nuclei in a manner that does not affect the structure nor organization of NPCs and offers the possibility to access and study the INM and nucleoplasmic side of NPCs by AFM.

8.2. AFM imaging of NPC from INM

With this NE preparation protocol in hand, AFM was used to investigate the INM. It is possible to observe the structure of the NPC basket, which is poorly described regarding other microscopy techniques.

After opening, nuclei were fixed, and NPCs were doubly labelled with mAb414 combined with other Nups staining. mAb414 mostly stains Nup358, Nup214, Nup153 and Nup62 (Davis and Blobel, 1986)), and thus labels fully assembled pores. The coverslip carrying open nuclei was placed on our correlative AFM/Fluorescence setup for imaging. A typical nucleus chosen for the experiment is presented in Figure 51. This nucleus exhibits a hole in its center with the top part of the NE generally preserved around this hole.

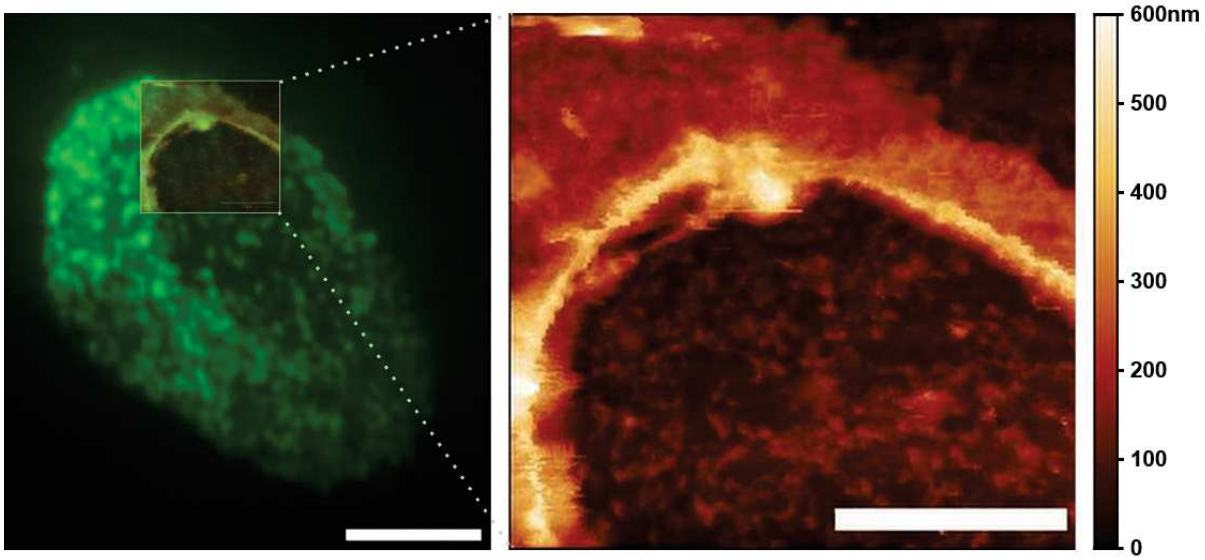

Figure 51: Correlative fluorescence / AFM image of an open nucleus isolated from U2OS overexpressing POM121-GFP. left: TIRF image of the entire nucleus overlaid with the region scanned by AFM. right: height image acquired by AFM, encompassing the opening border. Scale bars are 5um (left), 2um (right).

After acquisition of a TIRF image of the nucleus, the AFM tip was manually placed over the nucleus using the emCCD camera (see details in Material and methods). TIRF and AFM images were manually overlayed in the JPK software, using calibration of fluorescence image pixel size, and aligning large structures. Areas where the INM was accessible for the AFM imaging were easily distinguishable because of the lower density of NPCs which appears as individual dots in the TIRF image.

This configuration allows imaging of both the cytoplasmic (see black arrows in Figure 52) and nucleoplasmic side of NPCs (white arrows in Figure 52). In both cases, NPCs observed by AFM appeared as rings corresponding to the scaffold structure of the NPC. However, the density of NPCs viewed from the cytoplasmic side (top NE) was higher. This indicates that the formation of a hole in the NE has resulted in the shrinking of its top part to the sides. In contrast, the density of NPCs viewed from the nucleoplasmic side, and thus attached to the coverslip, was not affected.

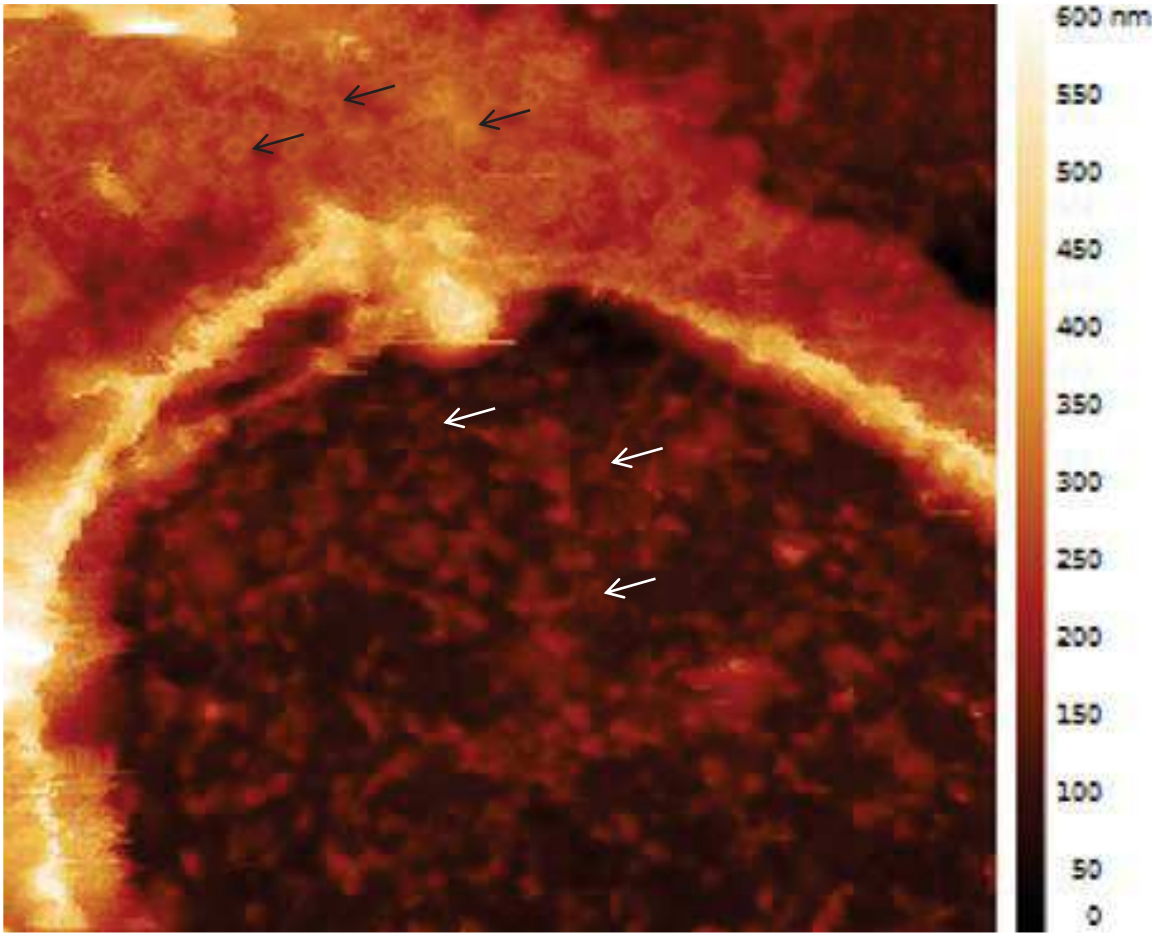

Figure 52: Cytoplasmic (black arrows) and nucleoplasmic (white arrows) NPC observed by AFM. Scan width is 5 µm.

On the ONM, no other elements than NPCs are visible. On the contrary, on the INM the topography is much more corrugated and exhibits many unidentified structures in addition to NPCs. These structures, that could correspond to lamins, proteins, remains of chromatin or patches of membranes, affect the topography at the INM and thus does not facilitate the identification and imaging of NPCs. Correlation and identification of NPCs was facilitated by the specific pattern they form, which allowed aligning of the individual NPCs with their fluorescent TIRF signal. This approach allowed to identify mature NPCs using the signal from mAb414 antibody used for labelling (blue circles in Figure 53).

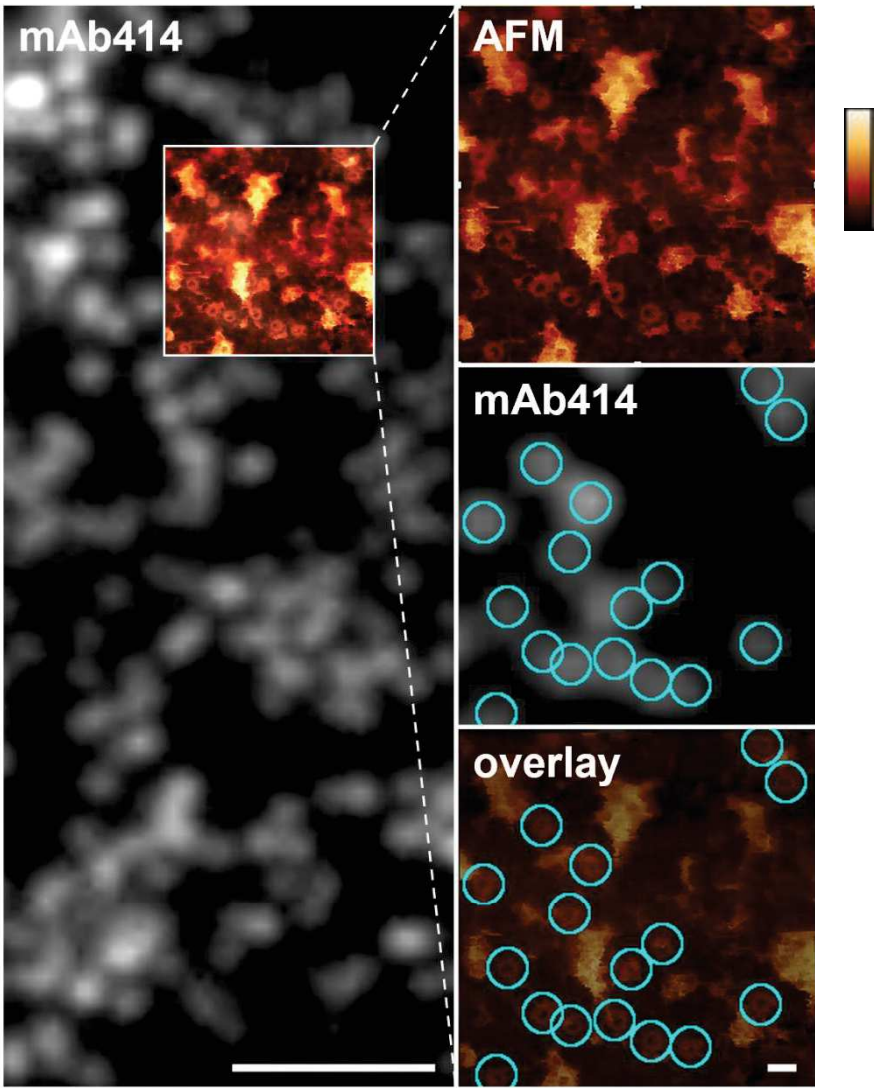

Figure 53: Correlative TIRF/AFM image of the inner nuclear envelope of an open nucleus. NPCs are labeled with mAb414 and visualized as fluorescent dots that coincide with ring-like structures in the AFM image. Scale bars are 2um and 200nm.

Similarly to what has been observed in *Xenopus laevis* oocytes, these formally identified NPC nucleoplasmic structures were composed of a scaffold ring associated with basket components. However, contrary to the text-book image of a protruding fish-trap like basket, this structure seemed to adopt a very diverse range of conformations with a basket often lower than the rim of the nucleoplasmic ring (see Figure 54). This heterogeneity in the basket structure has recently been reported by Stanley et al. in an AFM study in *Xenopus laevis* oocytes (Stanley, Fassati and Hoogenboom, 2018).

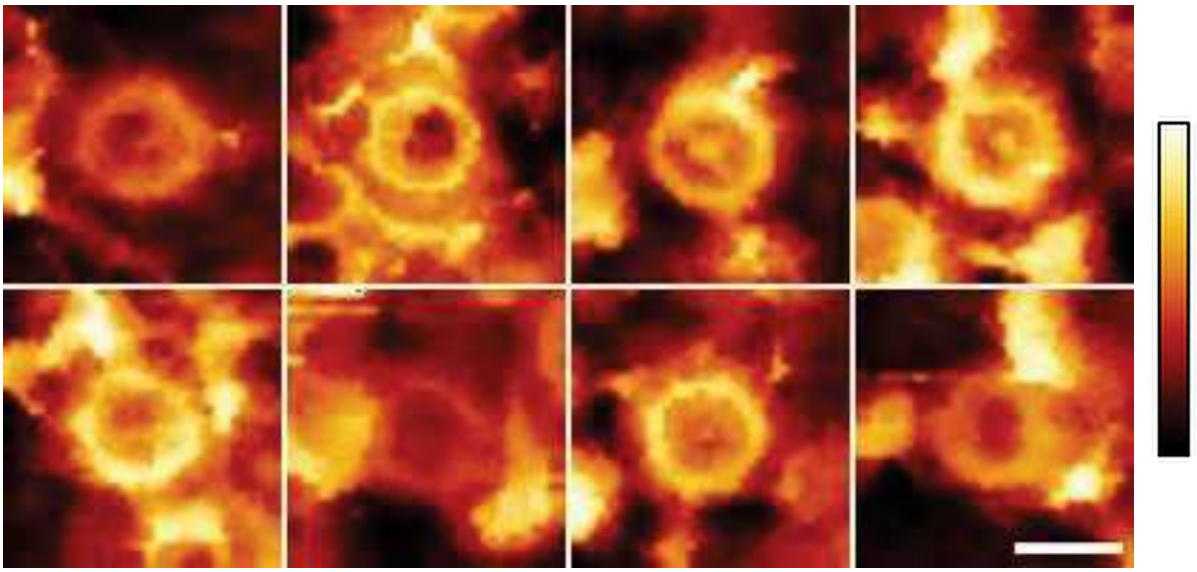

Figure 54: Representative samples of human nuclear pores (nucleoplasmic face) imaged by AFM. Scale bar is 100 nm. Height colour scale is 0-150 nm

An average NPC height image was reconstructed from 170 images recorded with the same resolution. From this mean NPC, the diameter taken at the ridge of the ring is 81.3 nm while the centre of the basket is 16.4 nm below the nucleoplasmic ring (Figure 55). These values are very close to similar measurements made in *X. laevis* NPCs (Liashkovich *et al.*, 2011; Stanley, Fassati and Hoogenboom, 2018). The central hollow in the mean NPC confirms the qualitative appreciation that the most NPCs do not exhibit a *bona fide* protruding basket.

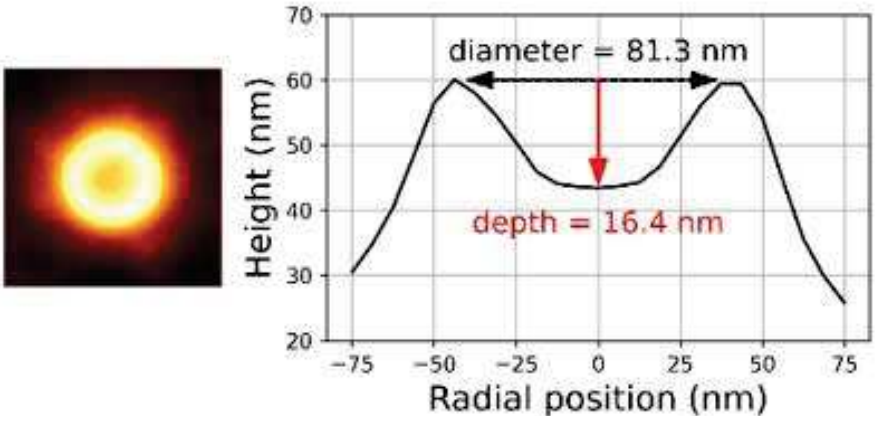

Figure 55: Left: Average NPC image (nucleoplasmic) obtained from 170 individual NPCs. 300nm crops from AFM scans were manually aligned and averaged. right: Resulting pore profile, with diameter and central depth indicated.

To better characterise the several conformations of the basket, a topographical analysis approach based on rotationally averaged height profiles of individual NPCs was developed. For each NPC height profiles along a 150 nm line rotated 20 times around the central channel symmetry axis was measured, and the resulting profiles were averaged (see details in Figure 56 and Material and Methods). These rotationally averaged height profiles were analysed for 210 individual NPCs and a diameter and a depth value was extracted for each.

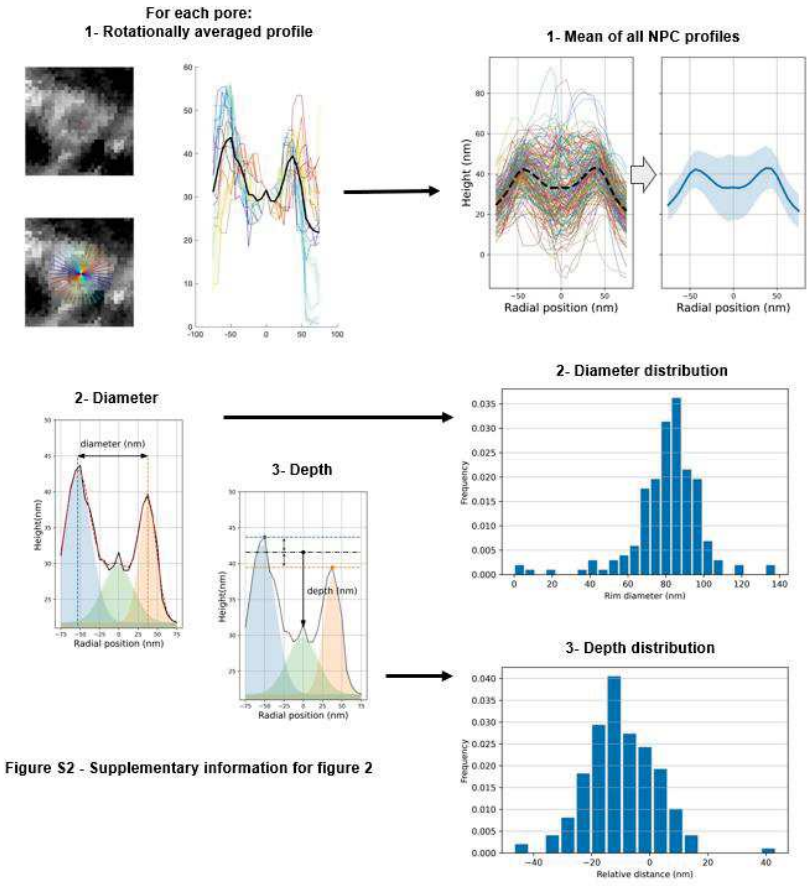

Figure S2 - Supplementary information for figure 2

Figure 56: Methods for rotationally averaging AFM profiles on NPCs.

1- A profile is drawn on a crop of the AFM image, centered on the NPC and rotated around it to measure 20 profiles. These profiles are then averaged to draw an averaged profile (black continuous line). This averaged profile is used for all further analysis, like the mean of all NPC profiles with corresponding standard deviation.

2- For each pore, the rotationally averaged profile is fitted with three gaussians to measure NPC ring diameter and depth of the center of the basket as indicated on the figure. The depth is calculated from the mean ring height.

The mean of all NPC height profiles and their standard deviation were calculated (Figure 57, left). Importantly, the standard deviation is much higher at the centre of NPCs than in the ring area (lower left panel in Figure 57). It was possible to qualitatively identify three categories of pores based on the structure of the central basket: i) NPCs with no clear central basket structure; exhibiting a lower topography at the centre of the NPC (blue crop and profile in Figure 57 right panel); ii) the standard and expected protruding basket with a central point higher than the NPC nucleoplasmic rim (orange crop and profile in Figure 57 right panel); iii) NPCs with visible basket filaments and distal ring lower than the NPC rim (green crop and profile in Figure 57 right panel).

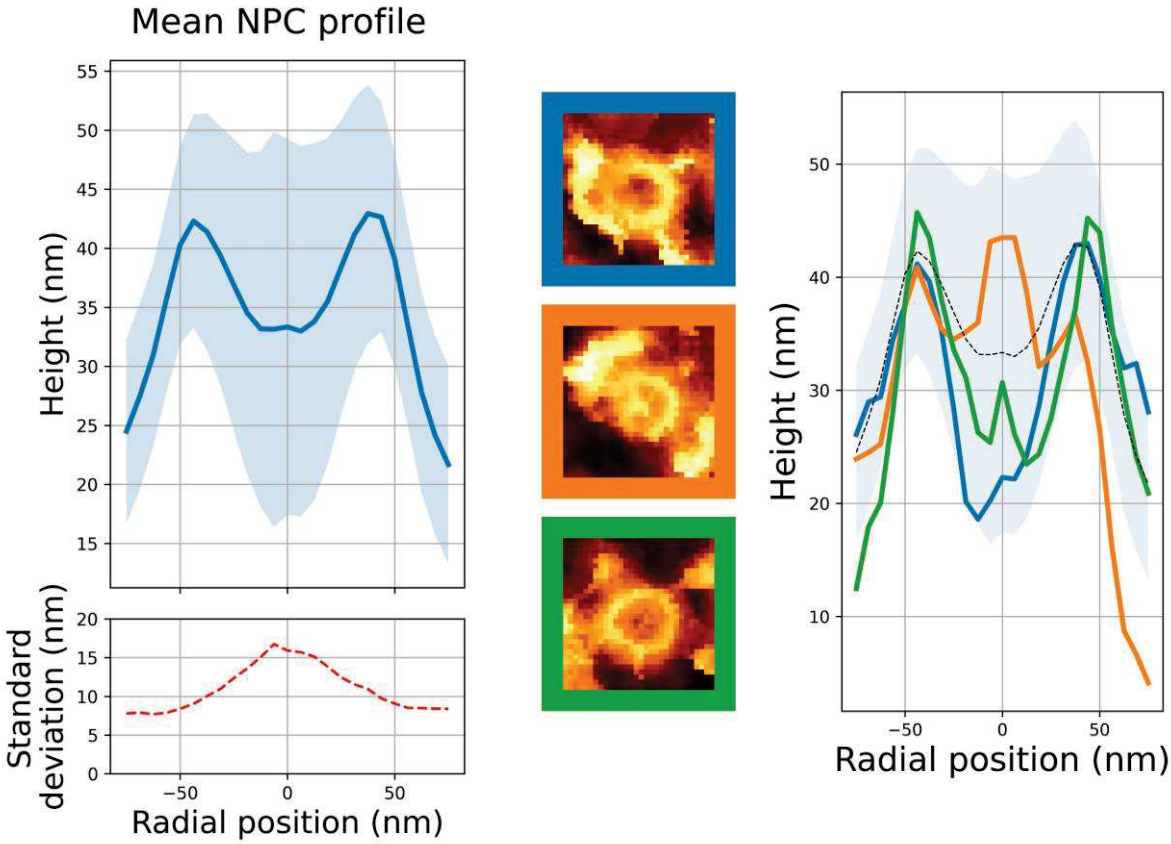

Figure 57: Left - Mean of rotationally averaged NPC height profiles (n=210). The standard deviation (shaded area in the top panel) is plotted in the bottom panel. Right - Three configurations of NPC nucleoplasmic region and their respective height profile. "empty" (blue), protruding (orange) and low basket (green), with standard deviation from left graph for comparison.

Next, using correlative AFM and STORM, the presence of Tpr in these structures was confirmed. Figure 58 shows a representative AFM topography image of NPCs labelled with Tpr. The correlative STORM image confirms that Tpr is present in all NPC basket conformations

as can be seen in the overlay image as well as in the 3D topographic AFM image correlated with the signal from the STORM reconstructed image.

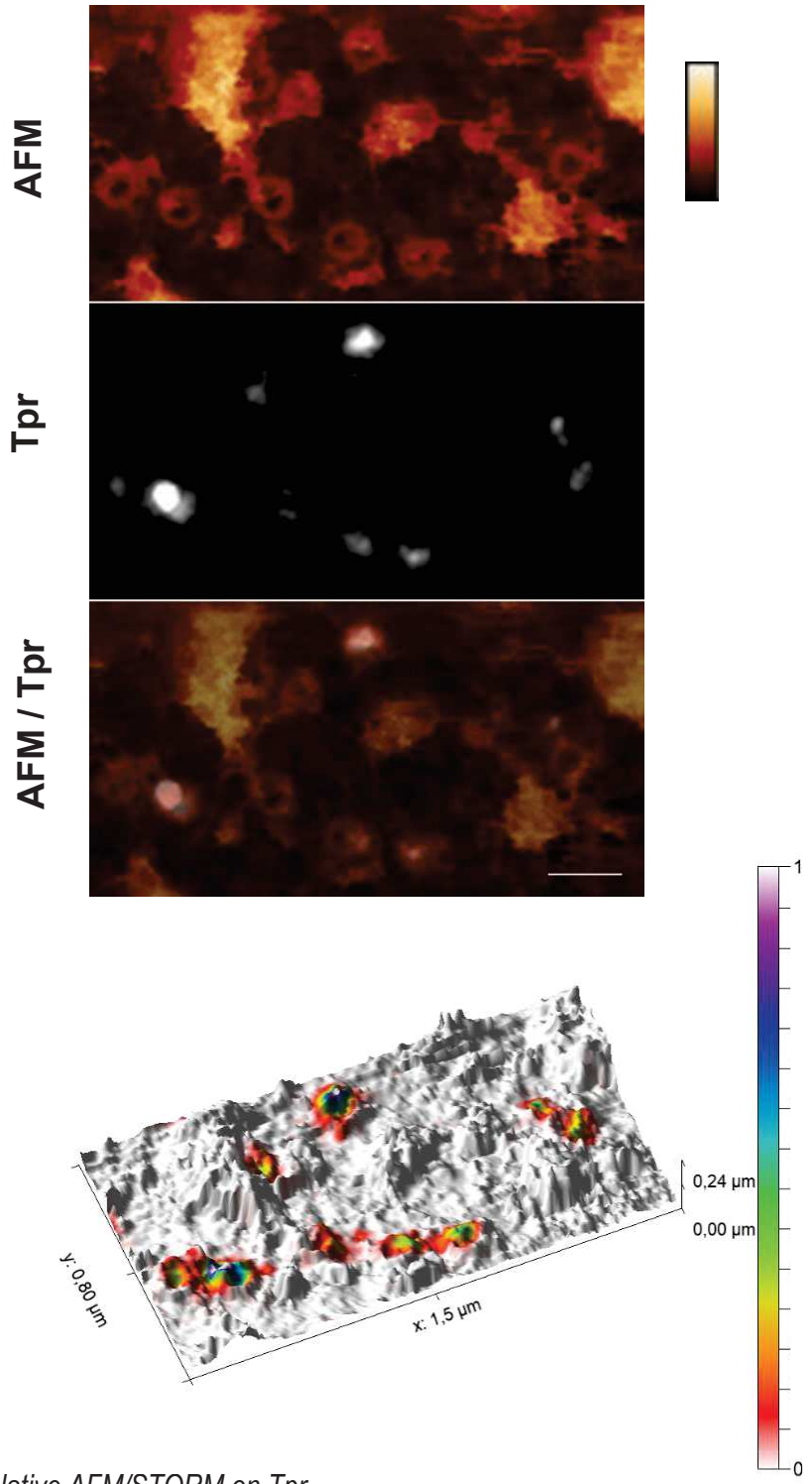

Figure 58: Correlative AFM/STORM on Tpr.

Top: AFM, STORM image of Tpr and correlation between AFM and STORM. AFM colour scale is 0-150 nm. The structures inside the nucleoplasmic ring match with STORM signal from Tpr. Scale bar 200 nm.

Bottom: 3D representation of the AFM topography with overlapping colour scale corresponding to Tpr STORM signal (Arbitrary unit)

However, details in individual NPCs revealed that depending on the basket conformation, the localization of Tpr differs. In the first example (Figure 59), a strong Tpr signal is visible and centered on the protruding basket while in the second case where no basket is visible the fluorescence STORM signal is located at the rim of the NPC nucleoplasmic ring and even outside of it. Finally in the last case where the basket structure is present but lower than the nucleoplasmic ring, Tpr is present both in the center of the NPC and on the ring with a center of mass shifted to the side of the NPC. In all cases, the structure visible in the topography correlates well with the STORM fluorescent signal of Tpr.

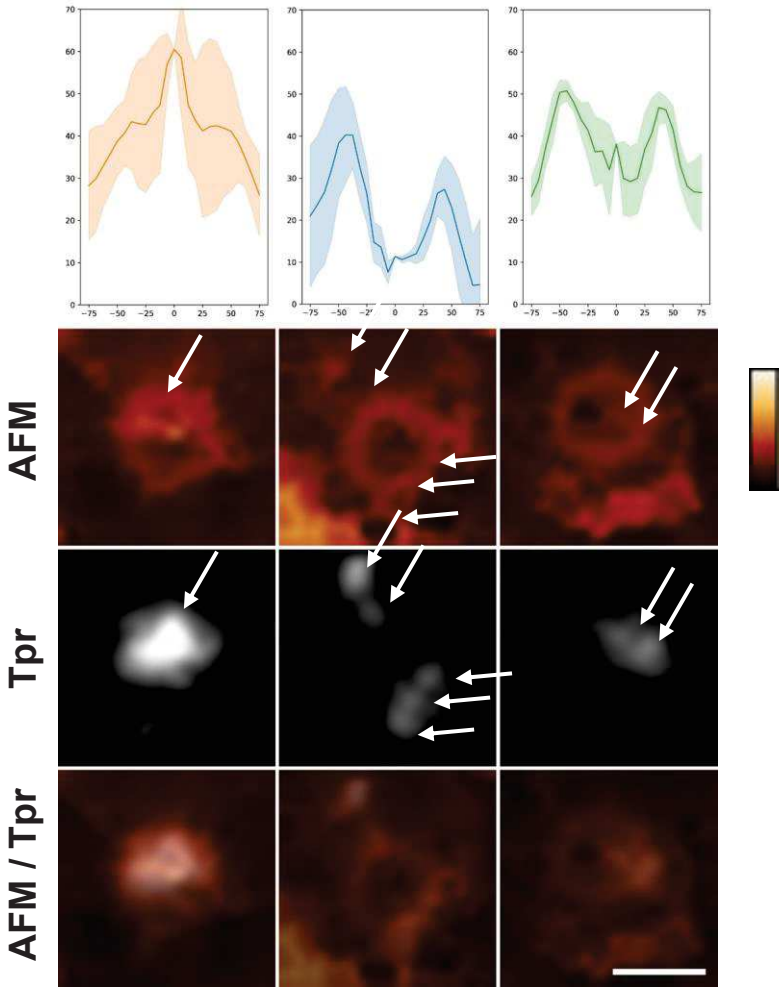

Figure 59: Details of correlative AFM/STORM Tpr conformations and corresponding profile. Left: Tpr STORM signal overlaps with the protruding basket. Center: NPC with a hole in the center and Tpr located on the ring and outside of the NPC. Right: NPC with low and side-shifted basket matches with the corresponding Tpr STORM signal. Scale bar 100 nm. AFM colour scale 0-150 nm.

As STORM was performed before AFM imaging, it was clear that asymmetry and partial disassembly in Tpr organization was not due to perturbations of the structure by the AFM tip. However, the possibility that the biochemical preparation of NEs alters the basket cannot be excluded. Therefore, basket structure was explored in intact cells by 2-color STED microscopy. Tpr and Nup153 were co-labelled in fixed cells by immuno-fluorescence to visualize their relative organization. Two proteins were used as references, Nup153 labelled with two different fluorophores and Elys which is localized in the nucleoplasmic ring and appears as a ring in STED microscopy (Figure 60).

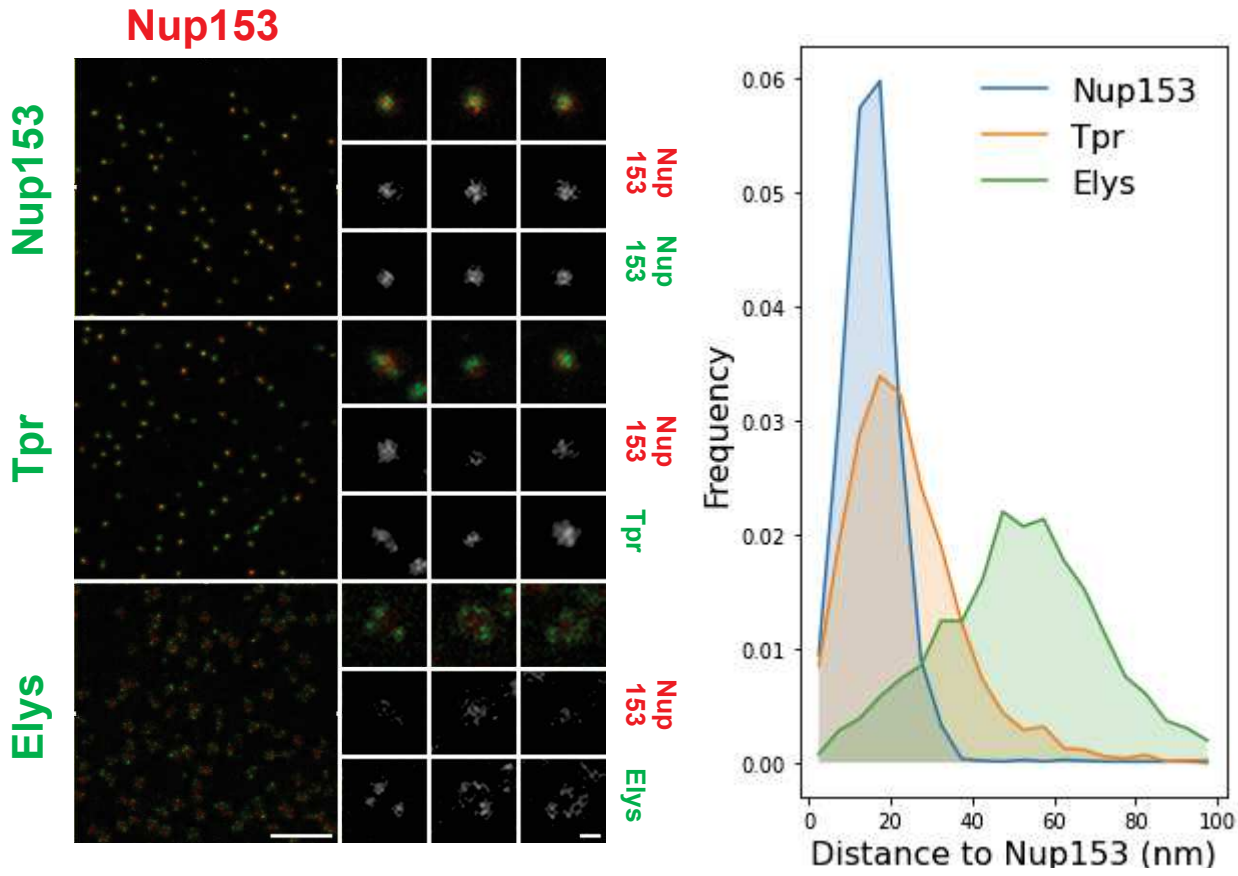

Figure 60: Left: Two colours STED microscopy on fixed cells immuno-labelled with antibodies against Nup153 and Tpr or Elys. Ensemble images and zooms on individual NPCs. Scale bars 1 µm and 100 nm. Right: Distribution of distances to Nup153 between the three previously described conditions, Nup153 (blue), Tpr (orange) and Elys (green).

As expected, Nup153 imaged in both channels renders a very similar signal, and Elys is localized as a rim around Nup153 central dot, with some variability in the labelling efficiency. Regarding Tpr, it usually appears as one -sometimes two- dots that can be well aligned with the Nup153 signal or slightly shifted on the side. To quantify this phenomenon, the distances

between Nup153 labelled with Alexa-594 and the protein of interest labelled with Star-635P were measured (Figure 60, right panel). The distribution shows that a fraction of Tpr is laterally shifted towards the nucleoplasmic ring where Elys resides, as comparison with Elys to Nup153 distance suggests (graph in Figure 60). These results are in good agreement with the topography observed by AFM in open nuclei and demonstrates that these different positions of Tpr are also present in intact cells.

To conclude on this part, AFM and super-resolution microscopy data demonstrate a high variability in the human NPC basket structure. The NPC basket can adopt different conformations and either protrude, sink into the NPC channel and disassemble to completely collapse within the channel or point towards the nucleoplasm. These results are in good agreement with what has also been observed by AFM in *Xenopus laevis* NPCs and question the model of an always protruding NPC basket.

8.3. Contribution of the basket in the NPC structure

Nup153 is known to anchor Tpr at the NPC, and previous studies have shown that Nup153 depletion induces a loss of several Nups of the basket (Walther *et al.*, 2001; Hase and Cordes, 2003). Considering the development presented before in opening human cell nuclei for AFM imaging, it appeared interesting to see how depletion of Nup153 would affect the NPC nucleoplasmic structure. To do so, U2OS cells were treated with siRNA against Nup153 before extracting nuclei and which were opened using the same protocol as in naïve cells.

First, siRNA against Nup153 was performed on U2OS/Nup96-GFP cells to ensure the efficiency of this treatment to disrupt the basket. As expected, pore density dramatically decreased in siRNA-treated cells. Moreover, confocal images (Figure 61A) confirmed that in NPC depleted of Nup153, Tpr was also absent (white arrows in Figure 61A) while Nup96 signal was visible.

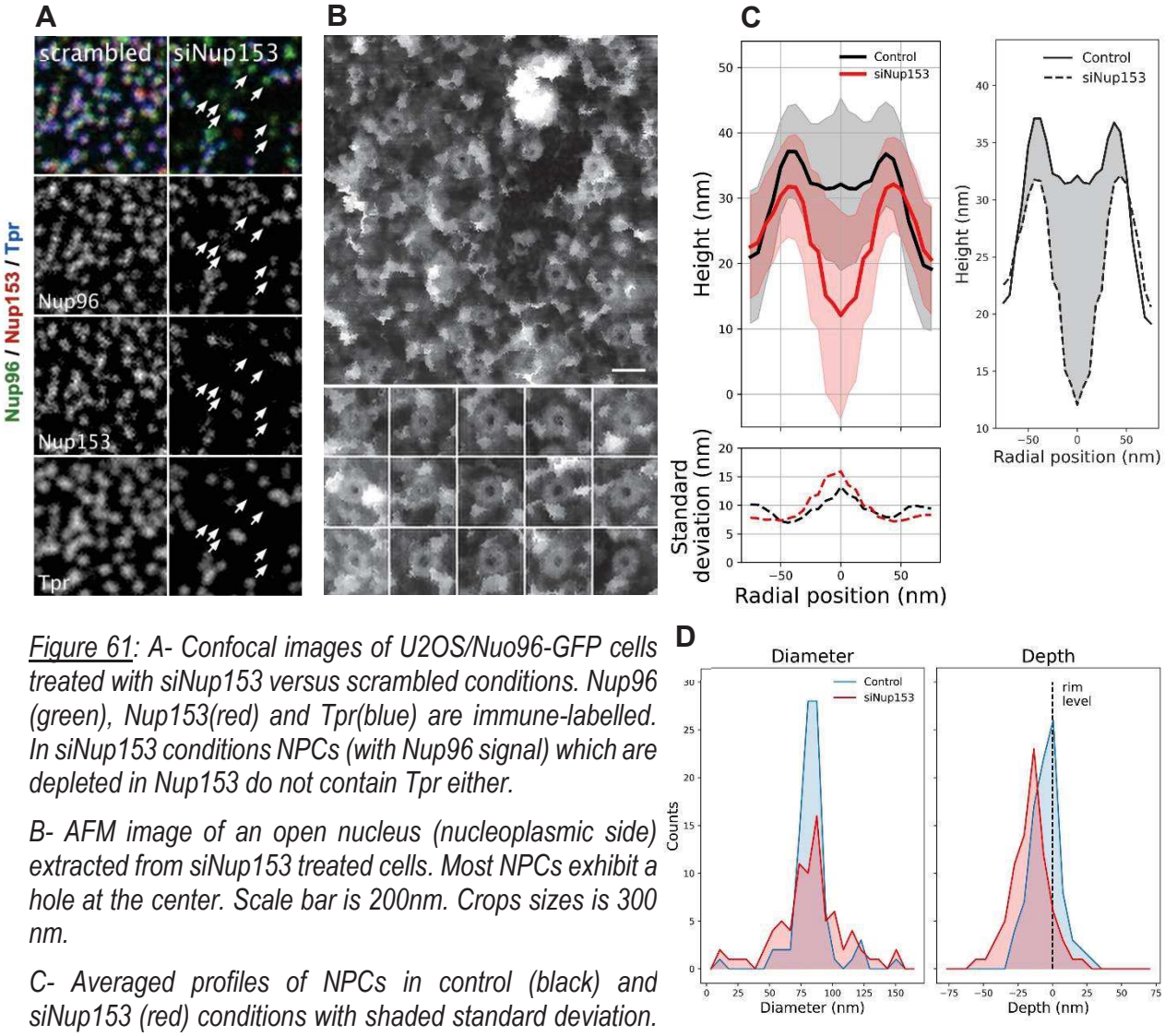

Figure 61: A- Confocal images of U2OS/Nuo96-GFP cells treated with siNup153 versus scrambled conditions. Nup96 (green), Nup153(red) and Tpr(blue) are immune-labelled. In siNup153 conditions NPCs (with Nup96 signal) which are depleted in Nup153 do not contain Tpr either.

B- AFM image of an open nucleus (nucleoplasmic side) extracted from siNup153 treated cells. Most NPCs exhibit a hole at the center. Scale bar is 200nm. Crops sizes is 300 nm.

C- Averaged profiles of NPCs in control (black) and siNup153 (red) conditions with shaded standard deviation. The graph shows a lower topography at the center of the NPC but also on the rim of the nucleoplasmic rim in siNup153 condition.

D- Distribution of diameter (left) and depth of the central channel of NPCs in control (blue) and siNup153 (red) conditions.

Next, AFM imaging of open nuclei treated with siNup153 was performed (Figure 61B). Interestingly, most NPCs viewed from the nucleoplasmic side in these conditions seem to be lacking the basket, exhibiting a deep hole at the center of the NPC. Moreover, in several of them, details of the eight-fold rotational symmetry of the nucleoplasmic ring tend to be visible. Comparison of rotationally averaged profiles of both conditions confirms a deep hole in the center with a topography which generally appears much lower than the lower profiles of the center of the NPC under control condition (Figure 61C). The nucleoplasmic ring height

appears lower than naïve NPCs, suggesting that the basket sits on top of the nucleoplasmic ring. The average contribution of the basket in the NPC structure can be visualized in Figure 61C (right graph) as the shaded area. Nup153 depletion does not seem to affect NPC diameter while depth of the central channel significantly increases. As expected, siRNA against Nup153 prevents the recruitment of Tpr and strongly affects the structure of the NPC basket by preventing its attachment to the rest of the NPC. Interestingly, these results show that siRNA against Nup153 modifies both the central basket structure and the top of the nucleoplasmic ring. This observation might indicate that the linking of Tpr to the NPC is located at the top of the ring, where Nup153 most probably sits. Further investigations depleting only Tpr while recording the change in topography with AFM could confirm this hypothesis.

8.4. Mechanics of NPC nucleoplasmic side

In addition to the structure, QI mode in AFM allows extracting data about the mechanical properties of a sample. Thus, since this imaging mode is used in these experiments, it was possible to verify if the mechanical properties of the NPC could be affected by the deletion of the basket. Using the data processing software from JPK, it was possible to fit the stiffness of the sample, and more specifically NPCs. The slope of the first 20 nm of the repulsive part of the AFM force curves, was analysed starting from the contact point. The contact point was determined using the contact mechanics model of a pyramid shape tip (see details in Material and methods). Stiffness images were then reconstructed and crops around NPCs were extracted for further analysis. Individual NPC topography, stiffness and sometimes STORM signal of TPR could then be assembled (Figure 62A).

Performing profiles on this data, it was possible to better characterize the relationship between topography and mechanics. To come back on the effect of siNup153 on the mechanics, stiffness of control NPCs with that of siNup153 treated nuclei using the same approach of rotationally averaged profiles was compared. Starting from the control conditions (Figure 62B), the nuclear basket generally appeared softer than the nucleoplasmic ring, whose stiffest part correlated with the top of the ring topography. This is very interesting since Tpr is predicted to be composed of coiled-coils which are generally thought of as stiff structures. Averaged profiles (Figure 62B) also indicates slightly higher stiffness at the center of the

basket. This could be due to a higher rigidity when probing all of the eight filaments of the basket. In siNup153 conditions (Figure 62B), disruption of the basket leads to much lower stiffness at the center of the NPC which might indicate that the AFM tip probes the hydrogel present in the central channel. Stiffer part of the profile still correlates with the nucleoplasmic ring.

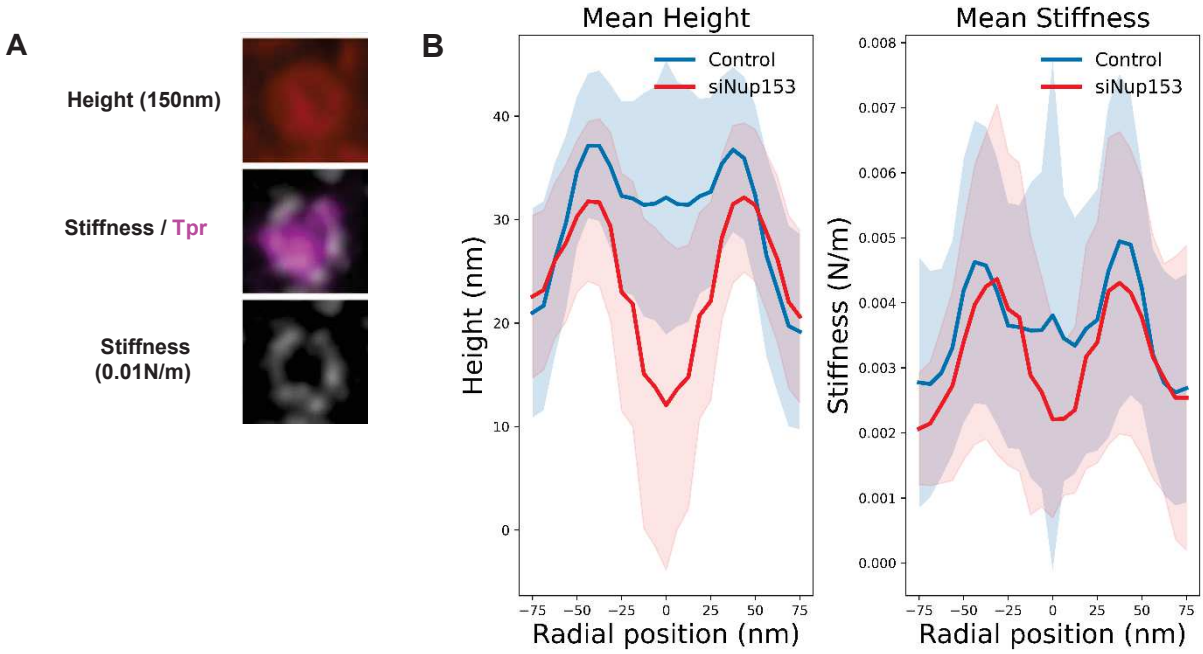

Figure 62: Mechanical analysis of NPCs in control and siNup153 conditions.

A- Height (Z scale 0-150 nm), Stiffness correlated (gray) with Tpr STORM (pink) and stiffness (colour scale 0-0.01 N/m) of a NPC.

B- Mean height and stiffness profiles of NPCs in control (blue) and siNup153 (red) conditions.

In conclusion, I have for the first time imaged by AFM the nanoscale topography of human NPC. This reveals a large flexibility in the conformations adopted by the Tpr basket filaments, supported by the mechanical analysis of NPC basket which indicates it is softer than the rest of the NPC. In addition, siRNA treatments against Nup153 confirmed its role in anchoring Tpr to the NPC since its depletion led to a hole at the place of the expected basket. These NPCs devoid of Tpr also appeared softer at the center of the nucleoplasmic ring where it is likely that the measured stiffness corresponds to the probing of the permeability barrier hydrogel.

9. Interphase assembly

The developed protocol to open nuclei allowed use of AFM as a nanotool to investigate the NPC nucleoplasmic side. Early stages of NPC interphase assembly take place at the INM and involve highly coordinated protein recruitment and membrane remodelling. Thus, the high-resolution topography provided by AFM could resolve the nanometric structure and membrane deformation associated with interphase assembly sites. To do so, correlation with fluorescence microscopy technique was also required to identify and localize these intermediates sites.

9.1. AFM observation of NPC intermediates identified by correlative fluorescence TIRF microscopy

POM121 has been reported as an early player in the interphase assembly of NPC. To identify interphase assembly sites containing POM121, a standard strategy is to use a differential labelling between POM121 and the antibody mAb414. mAb414 is a mouse antibody which recognizes FG-repeats motifs present in Nup358, Nup214, Nup153 and mainly Nup62, which are all peripheral proteins recruited late during the assembly process. mAb414 is thus assumed to be a marker of mature NPCs. By labelling POM121 and NPCs with the mAb414 antibody associated with different fluorescent probes in nuclei from U2OS cells, it is possible to identify NPC interphase intermediates of assembly. In contrast to the mature NPCs which will have both POM121 and mAb414 signal, NPC intermediates will only have POM121 signal. It is important to mention that mAb414 can also slightly recognize some domains present in Nup153 and POM121 which might result in low mAb414 signal in intermediates that is however not comparable with mature NPC signal.

Applying this strategy on our correlative AFM/fluorescence setup using TIRF illumination, it was possible to localize NPC interphase assembly intermediates and to correlate their nanoscale 3D topography recorded by AFM (Figure 63). These intermediates are indicated by a dashed circle in Figure 61 and exhibited a different structure than other pores. Especially the intermediates to the right exhibited a hole in the central channel that is much lower than the INM level suggesting that Nups composing the basket and central permeability barrier were not recruited yet. The other one also presents intriguing side spots present around the nuclear ring.

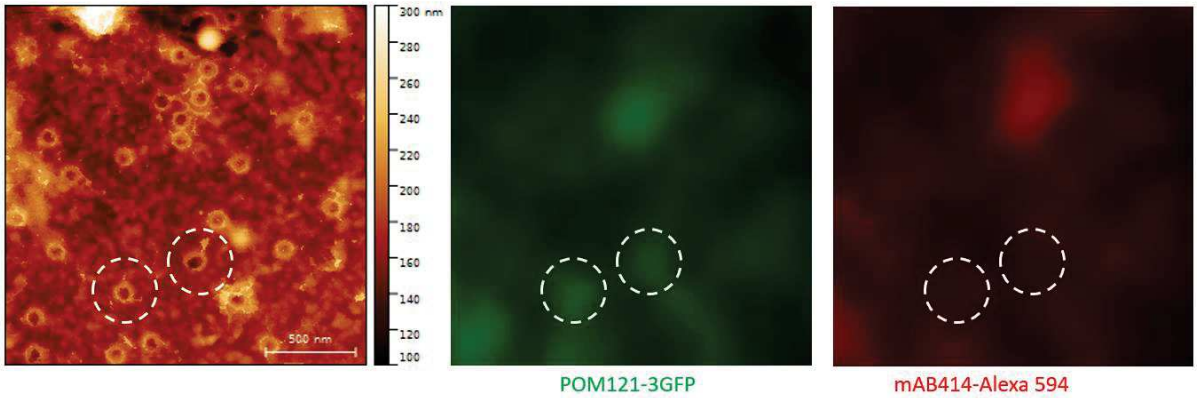

Figure 63: Identification of pore intermediates by differential labelling. Left: AFM images of the INM side where NPCs are visible. Center: TIRF image of POM121-3EGFP.Right: TIRF image of mAb414-Alexa594. Dashed circles indicate NPC intermediates which only contain POM121 fluorescence signal.

While numerous studies revealed the key factors for NPC assembly and the importance of Nups interaction with the membrane, the topology of intermediate NPC structures and how they evolve to form a mature NPC has not been extensively characterized. The best picture we have about this topology of interphase assembly intermediates is given by Otsuka *et al.* in a cryo-EM study (Otsuka *et al.*, 2016). They observed electron-opaque structures at INM growing in depth and diameter and associated with INM deformation. The structure of intermediates obtained on this specific timescale suggests an organization around a central mushroom-like dense complex surrounded by a ring which exhibits an eight-fold symmetry. The initially shallow central complex grows in height and diameter with the progression of the assembly while the surrounding ring grows up to less than 100 nm diameter. It is important to mention that this ring is very similar in terms of organization and diameter to what is observed as nucleoplasmic ring in mature pores.

In comparison, these structures, if they were observed by AFM from the INM, would be visualized as small globular complexes protruding from the membrane for shallow early intermediates. The surrounding ring is expected to be also resolved by AFM in the case it is accessible for the AFM tip. In fact, EM data from Otsuka *et al.* suggest that some protruding elements connect the central complex with the ring and could prevent its direct imaging with AFM. Thus, this structure could also appear as a large globular structure.

We have applied the previously described method and measured the topography of tens of intermediates. Here, it is important to note that interphase assembly is a relatively

rare event at the timescale of the cell cycle. Thus, these events in an open nucleus, where less than half of the NE was preserved and accessible to the AFM tip, were even harder to catch and at maximum a handful of them could be detected during one experiment. In the end, 61 intermediates have been imaged with very variable structures.

Among these structures, several of them exhibit similar aspects and have further been classified based on the topography and rotationally averaged profiles. In the following figures, crops of 290 nm x 290 nm have been grouped by similarity; corresponding height profiles are shown on the right and compared to the average mature pore height profile (dashed black line). All height scales are identical - 0-150nm for color scale and 0-120nm for height profiles – to visualize the progression of the structures:

- First class: seven intermediates exhibit a shallow structure (generally below the height of the NPC ring of mature pores) of relatively small diameter which probably corresponds to early intermediates where only few Nups are present.

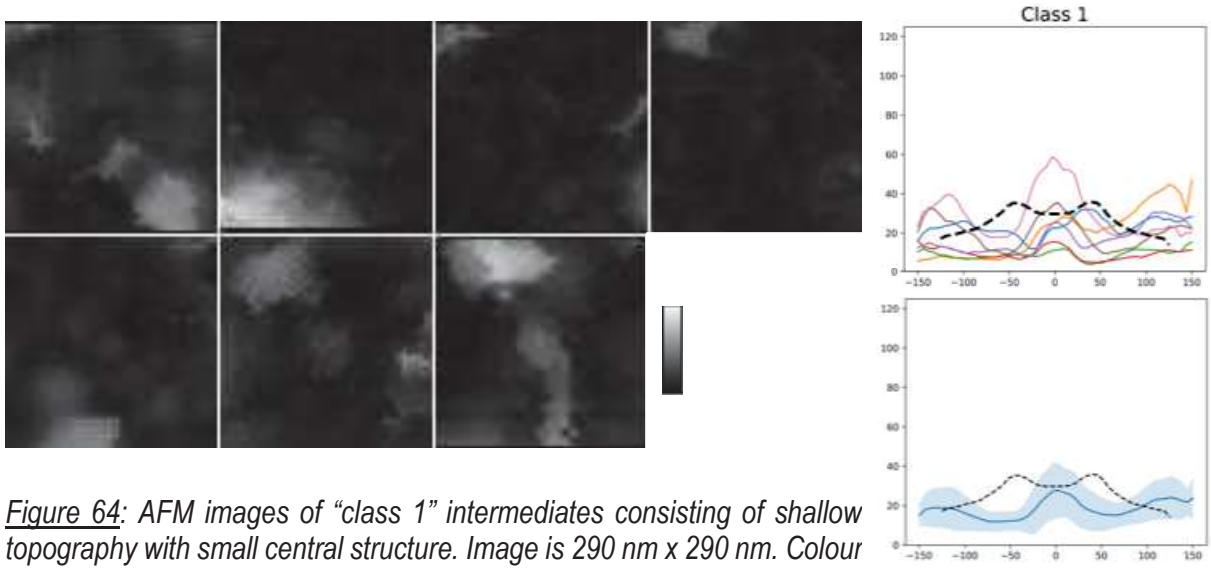

Figure 64: AFM images of "class 1" intermediates consisting of shallow topography with small central structure. Image is 290 nm x 290 nm. Colour scale 0-150 nm. Corresponding profiles (top) and averaged profile with standard deviation (blue) compared to average profile of mature pore (black dashed line).

- Second class (Figure 65): nine intermediates appear as a slightly larger central complex surrounded by a ring structure. The ring diameter is typically in a range from 138 to 215 nm. It is important to mention that it is much larger than what has been observed by EM and thus probably corresponds to different elements. In between the central complex and the ring, a depression with lower topography is visible. The role of this external ring is not clear. It could be a scaffold that helps NPC assembly and/or acts on the membrane to deform it or stabilize its curvature. Indeed, it is sitting right at the edge of the membrane depression. Another hypothesis is that it is a part of the assembling NPC that assembles around it to narrow and join the "mushroom"-like structure.

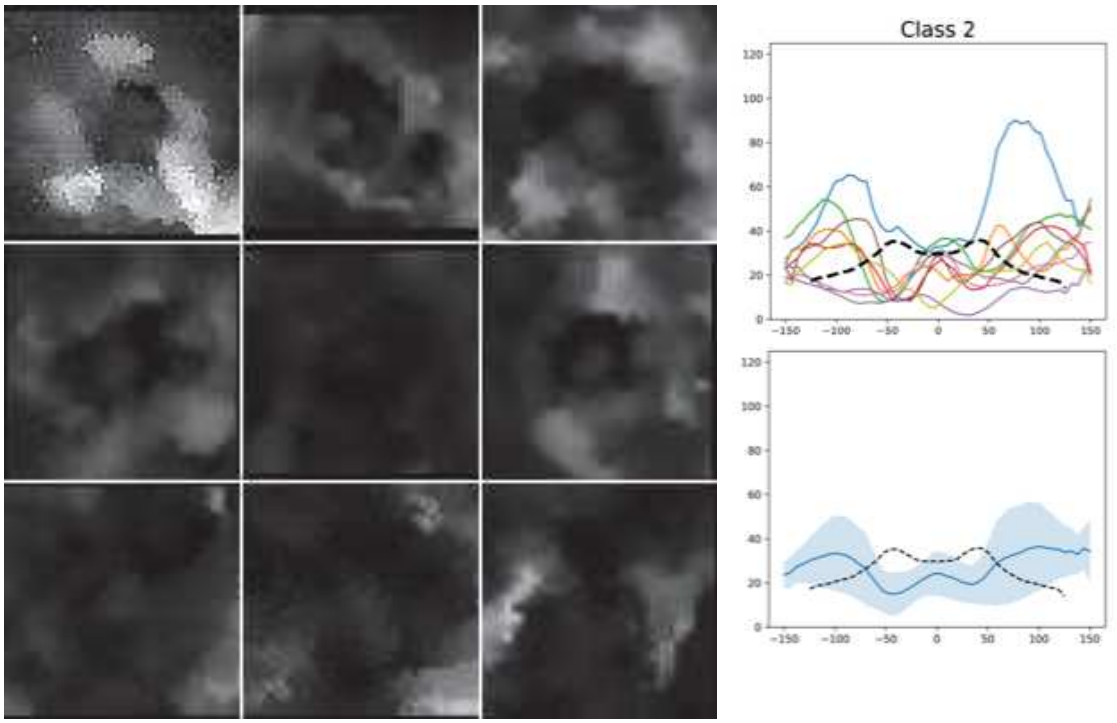

Figure 65: AFM images of "class 2" intermediates consisting of a central density surrounded by a large ring. Image is 290 nm x 290 nm. Colour scale 0-150 nm. Corresponding profiles (top) and averaged profile (bottom) with standard deviation (blue) compared to average profile of mature pore (black dashed line).

- Third class (Figure 66): five intermediates present a central complex with a small annular shape which is still surrounded by a peripheral larger ring; in some cases, the external ring is partially disassembled. Importantly some of them, presented in Figure 66, exhibit a membrane depression surrounding this central complex. One interpretation about these structures is that the previous globular central complex

expanded and matured into a ring-like structure. This ring whose diameter is closer to that of the mature NPCs could correspond to the ring structure observed by EM.

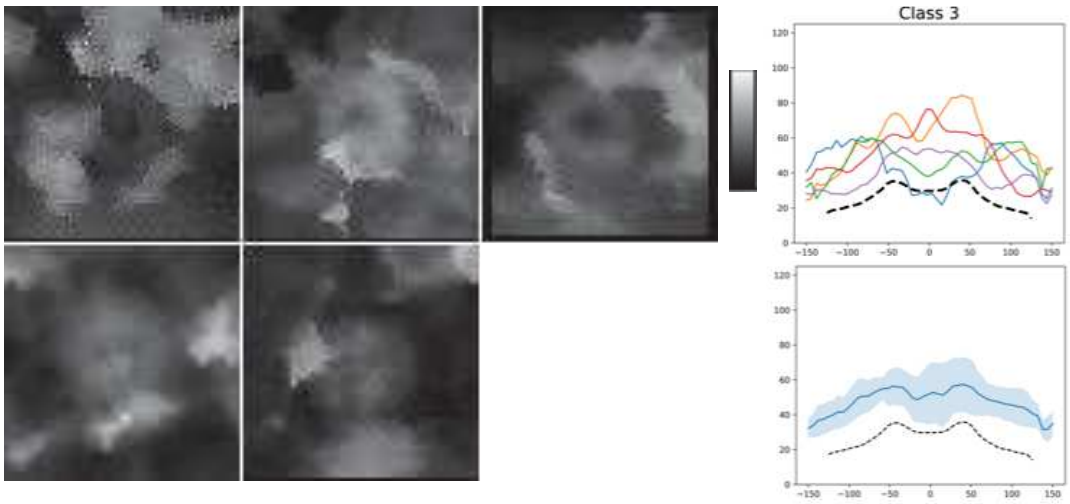

Figure 66: AFM images of "class 3" intermediates consisting of a small annular structure surrounded by a peripheral larger ring. Image is 290 nm x 290 nm. Colour scale 0-150 nm. Corresponding profiles (top) and averaged profile (bottom) with standard deviation (blue) compared to average profile of mature pore (black dashed line).

- Fourth class (Figure 67): besides relatively shallow structures presented before, five intermediates appear as very high and large structures with a diameter around 200 nm and protruding up to approximately 100 nm from the membrane. As most of the assembly process takes place at the INM, these intermediates might be containing most of the Nups required for fusion between the INM and the ONM, located inside the nucleus. This large structure could be the last stage before fusion which would

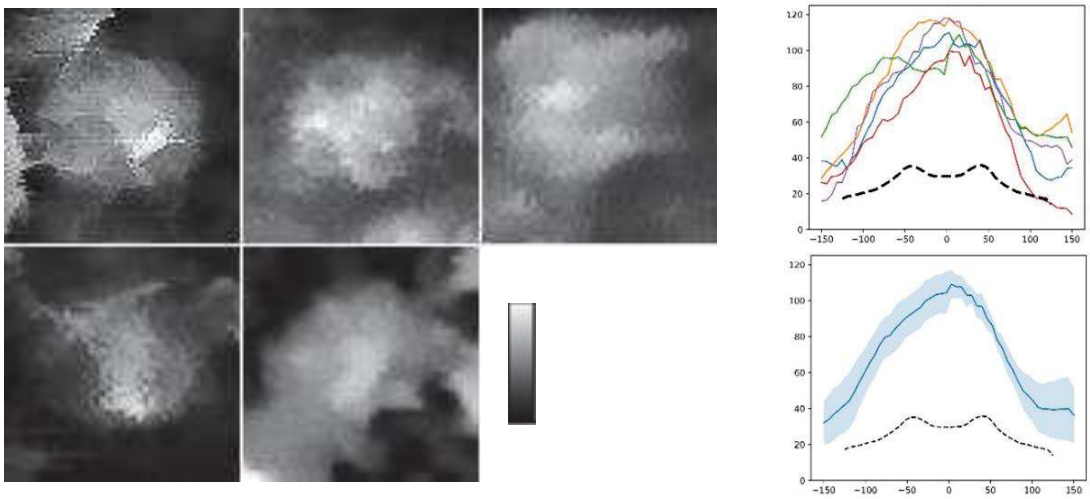

Figure 67: AFM images of "class 4" intermediates consisting of large and very high structures. Crops are 290 nm x 290 nm. Colour scale 0-150 nm. Corresponding profiles (top) and averaged profile (bottom) with standard deviation (blue) compared to average profile of mature pores (black dashed line).

subsequently result in a large rearrangement of the forming pore complex. These stages may correspond to the “mushroom” stage observed by EM (Otsuka *et al.*, 2016).

- Fifth class (Figure 68): sixteen of them appear very similar to fully assembled NPCs with often filaments in the center of the channel. These intermediates are probably late stages of assembly since their ring diameter is close to the size of mature pore. Sometimes a deep hole is observed at its center which might indicate the lack of most of the components of the central channel and basket. Peripheral protruding structures (see white arrows in Figure 68) were also present in these intermediates and might correspond to other proteins that are not members of the NPC involved in its interphase assembly, maybe remnants of the large ring observed in early stages.

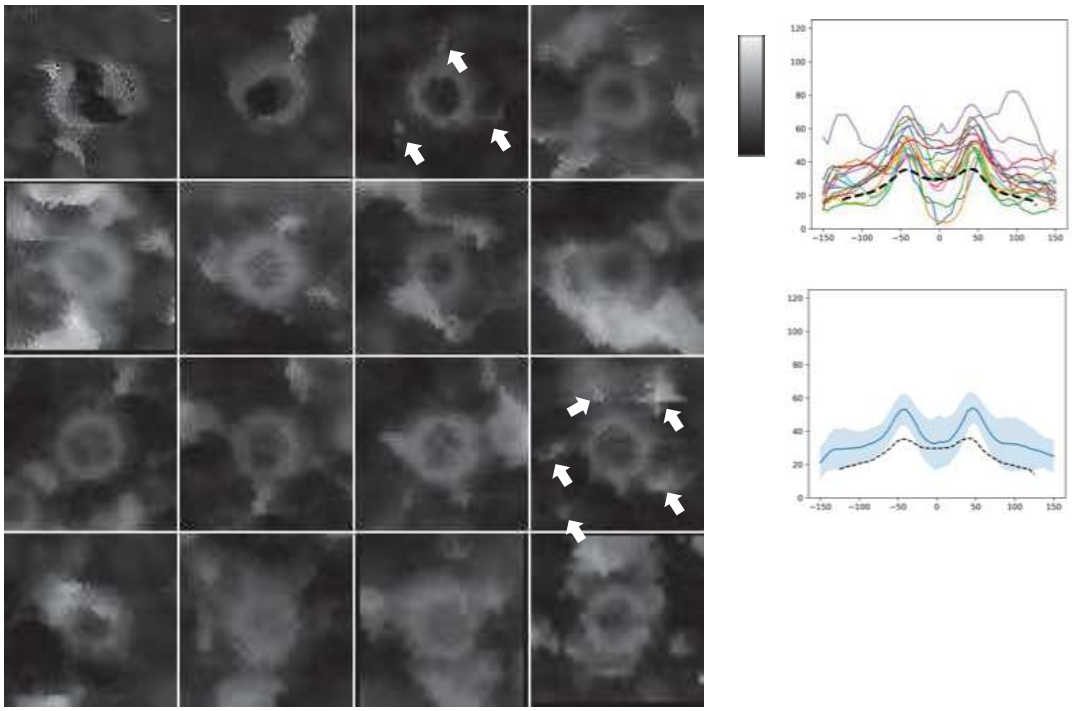

Figure 68: AFM images of “class 5” intermediates consisting of annular structures similar to matures NPCs. Some of them are incomplete (first crop) or lack central channel elements (fourth crop) Peripheral structures are also visible (white arrows for example). Crops are 290 nm x 290 nm. Colour scale 0-150 nm. Corresponding profiles (top) and averaged profile (bottom) with standard deviation (blue) compared to average profile of mature pores (black dashed line).

- Finally, a small subset of intermediates could not be classified since their structure was too different from other ones. This heterogeneity might be due to a rough topography or debris of other cellular components that may interfere with the observation. Some of these “rare intermediate configurations” might also reflect very transient states,

hence their low frequency. One interesting intermediate in this case is probably the one presented in Figure 69 which exhibits a small central complex associated with a large membrane depression surrounded by three punctual structures. This could correspond to a transition between previously mentioned classes 1 and 2, at the very beginning of a large ring formation.

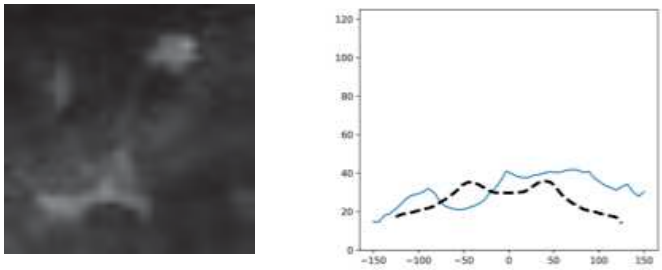

Figure 69: AFM image of an intermediate potentially corresponding to a stage between class 1 and 2. It consists of a very small central complex situated in a large membrane depression and surrounded by three peripheral structures. Image is 290 nm x 290 nm. Colour scale 0-150 nm. Corresponding profile (top) and averaged profile (bottom) with standard deviation (blue) compared to average profile of mature pores (black dashed line)

In conclusion, using correlative AFM/TIRF microscopy, I have been able to visualize the nanoscale topography of tens of NPC intermediates for which structural similarity allowed to arrange them into specific classes. These classes most probably correspond to different stages of NPC interphase assembly, but additional information is necessary to build a logic kinetics of the structure evolution during this process.

9.2. Organization of POM121 within NPC intermediates at different stages

In the intermediates structures presented above, we know from the TIRF image that POM121, an early player of interphase assembly, is present. But no information can be obtained from non-super-resolved TIRF microscopy about the position of POM121 in these substructures. To better understand its role, we thus combined in some experiments STORM microscopy on POM121 with AFM. These experiments revealed new information on few intermediates (Figure 70). First it appears that shallow intermediates in terms of AFM topographical structure generally have low POM121 signal which is concentrated in a point centered on small complexes observed by AFM.

Second, as the size of the structure gets bigger, the POM121 signal gets also larger and more intense which suggests that a progressive recruitment of POM121 was happening.

Finally, for intermediates containing Nup96 (blue rectangle in Figure 70), POM121 was segregated away from the center of the NPC in a step that could be concomitant with the formation of one of the rings composed of Y-complexes that contains Nup96.

In conclusion, correlative AFM and STORM imaging of NPC intermediates show a wide range of conformations. The data obtained on these intermediates indicate that early steps of interphase assembly involve the recruitment of POM121 in a central position that could serve as a nucleation point for further Nups recruitment. The presence of intermediates with a large peripheric structure suggests that a surrounding scaffold helps to build the proto-NPC structure. After this stage, POM121 is segregated from the centre of the intermediates towards the periphery, matching with the recruitment of the Y-complex that includes Nup96. Finally, details in the topography of some intermediate structures in the class 5 with a missing basket which look like siNup153-treated NPCs suggest that the peripheral Nups, like Tpr, join the forming pore at the end.

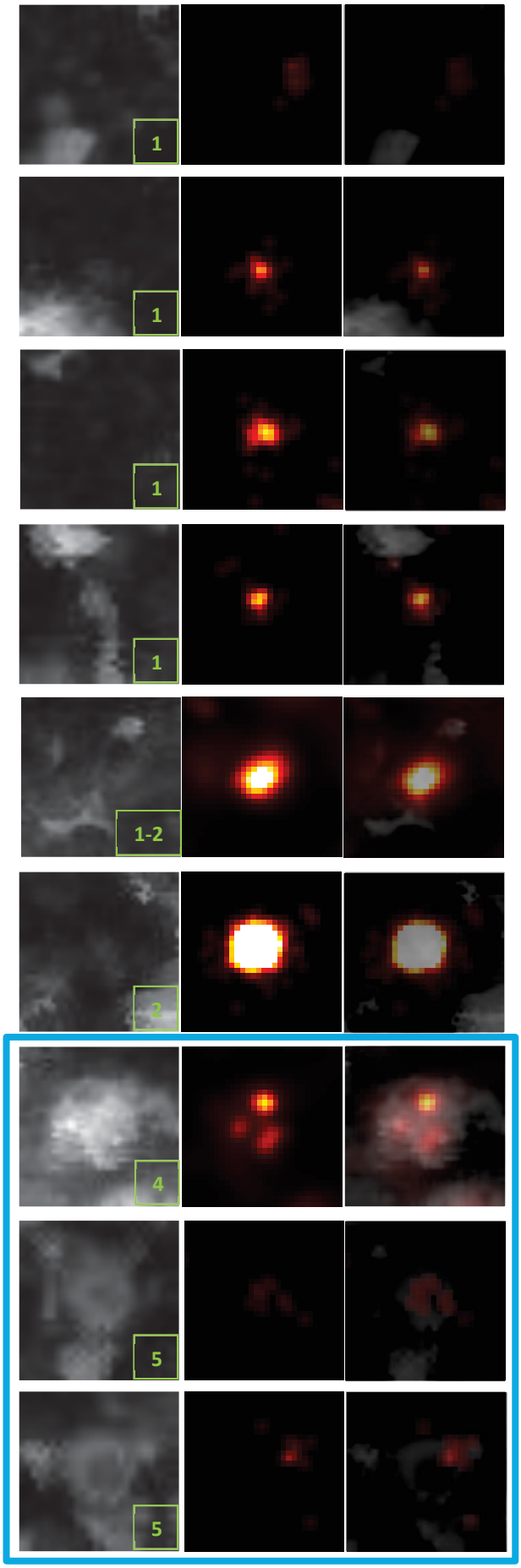

Figure 70: Correlative AFM STORM POM121.

For each intermediate, AFM (left)– STORM POM121 (middle) – correlative image (right). Green label indicates the class in which the intermediates have been previously assigned based on AFM image. Class 1 intermediates show small intermediates structures with weak POM121 signal. Transition from class 1 to class 2 show an increasing central POM121 signal. In class 4 and 5, large AFM intermediates structures in which TIRF microscopy indicated the presence of Nup96-GFP (intermediates in the blue frame) and with POM121 segregated away from the center of the NPC. Crop size 300 nm. AFM Z scale 0-150 nm.

9.3. Organization of SUN1 relative to NPCs

AFM imaging of NPC intermediates showed the presence of structures with an annular organization around some NPC intermediates (white arrows in Figure 68 for example). These structures as well as the large surrounding rings might play a role in the stabilization of the NE during interphase assembly. Similar structures have also been observed around mature NPCs, suggesting they may be remnants of the large rings assembled during NPC formation. We know SUN1 plays a role in maintaining INM and ONM spacing, associated with NPCs and essential for interphase assembly. Thus, we wanted to test if SUN1 is present in these satellite structures. However, co-labelling of POM121 and SUN1 was not possible since both antibodies used were produced in rabbit, which prevented us from colocalizing SUN1 with formally identified pore intermediates.

In consequence, I first analysed the previous AFM data of mature NPC and identified peripheric protrusions around NPC. I then measured their distance from the barycentre of these protrusions to the center of the corresponding pore. The averaged value on 182 of peripheral dots was 89.6 nm, with a standard deviation of 13.1 nm, a minimal distance of 57 nm and a maximum of 137 nm (Figure 71). These results are a bit different from a previous EM study which determined that SUN1 associated with NPC, labelled with gold nanoparticles, was located within a range of 120 nm around the center of the NPC (Liu *et al.*, 2007). Liu et al. measured a typical distance of 66 nm with a standard deviation of 20 nm. However, they are almost all within the 120 nm range from the center and the difference could be explained by the fact that our antibody labels the nucleoplasmic region of SUN1 while Liu *et al.* antibody targets a luminal region.

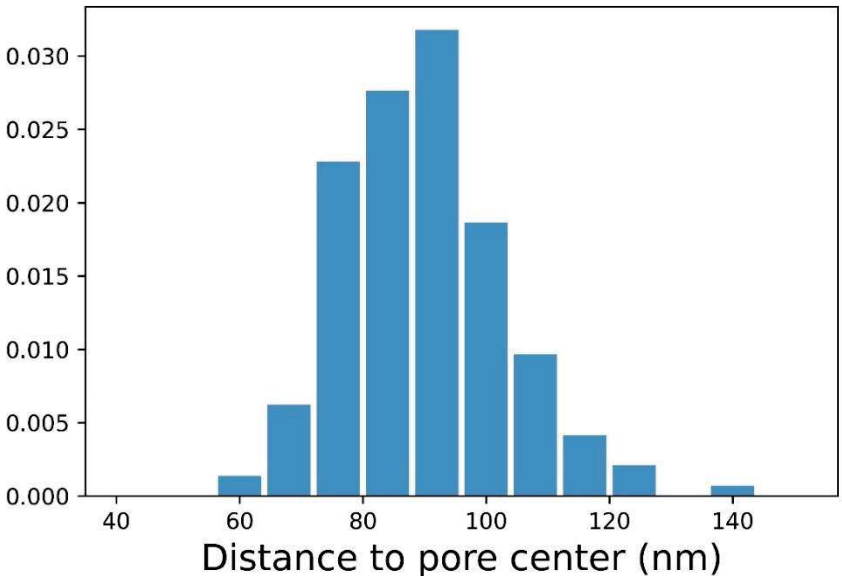

Figure 71: Peripheric protrusions (hypothetically corresponding to SUN1) distance to center of the NPC measured on AFM images of mature NPCs. Average distance of 89.6 nm +/- 13.1 nm (N=182 dots).

To test the position of SUN1 in the structures surrounding NPCs, we performed correlative AFM and STORM on nuclei labelled with mAb414 and SUN1 antibodies. Our images revealed that SUN1 is often but not always associated with NPCs in peripheric protruding structures (Figure 72). Indeed, several peripheral structures do not have SUN1 labelling. This can be due to a problematic accessibility to SUN1 since it is known to be associated with lamin A that could prevent the labelling by the antibody. Indeed, the lamin A binding domain overlaps with the immunogenic region used to raise the antibody (Abcam ab124770). Another explanation is that it could correspond to some of the Tpr since we also observed that Tpr might be present outside of the NPC in similar structures (see one of the white arrows in the central AFM image of Figure 59). Thus, all these protrusions might not correspond to SUN1, and we could not confirm that they are the same as observed around intermediates. However, similarities between the surrounding structures observed in mature NPCs and intermediates suggest that SUN1 could play a role and be present in these structures to constrain the area where interphase assembly occurs by acting as a scaffold around these sites.

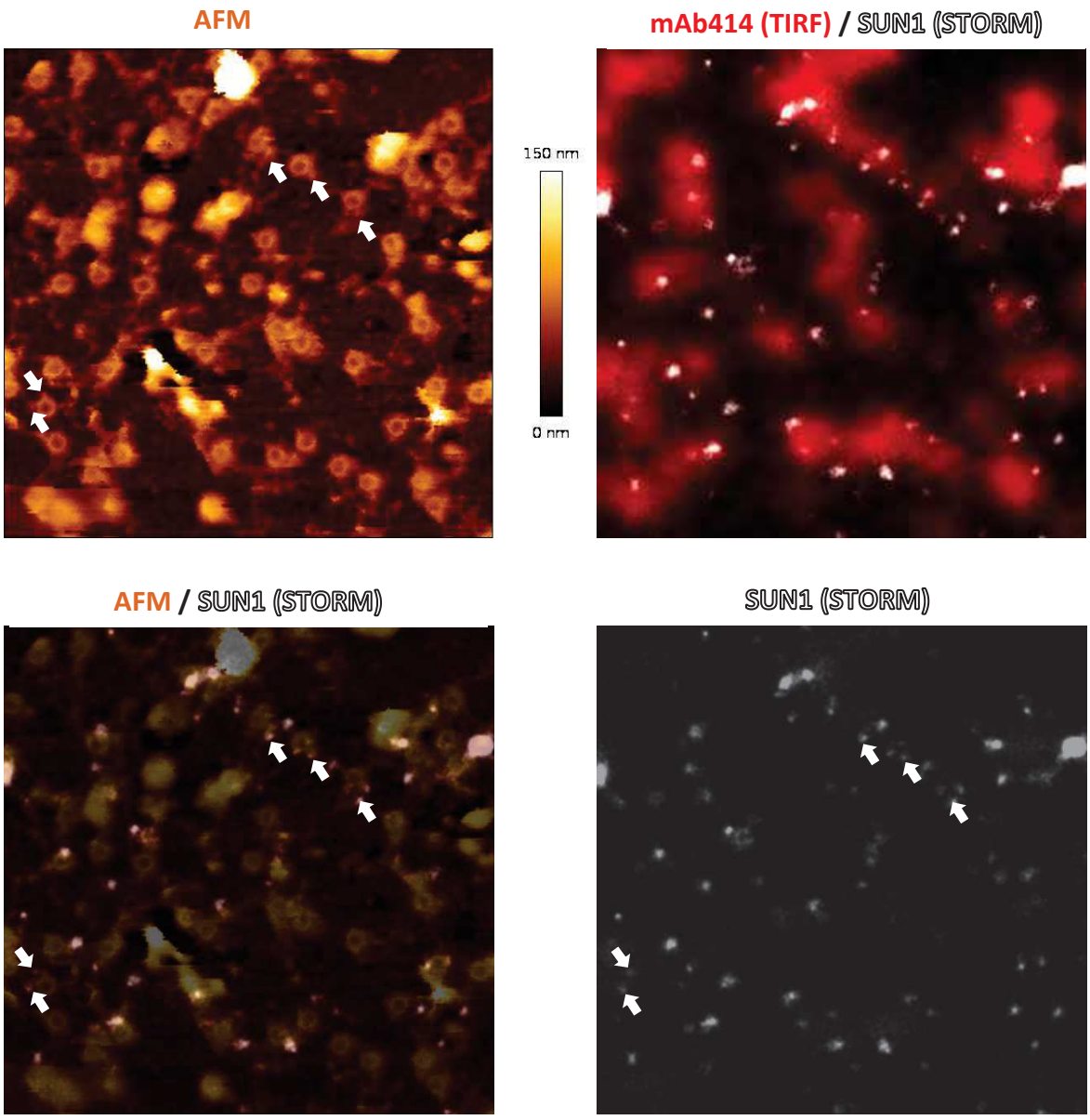

Figure 72: Correlation between AFM image of NPC, SUN1, and mAb414. Top left: AFM image. Scan size is 3µm. Top right: Corresponding fluorescence image correlating mAb414 (red, acquired in TIRF) and SUN1 (white, acquired in STORM). Bottom left: Correlative AFM/STORM on SUN1. Bottom right: STORM on SUN1. White arrows indicate peripheral structures around NPCs correlated with SUN1 STORM signal.

9.4. STED imaging in intact cells - siRNA strategy to confirm the different stages of NPC assembly identified in AFM/STORM correlative microscopy

AFM and STORM correlative experiments that I performed showed that NPC intermediates have a large variety of structures and sizes which most probably correspond to

specific stages of the NPC interphase assembly process. But AFM is a low throughput technique which does not allow a large sampling of the intermediates. To better understand the roles of the different Nups in this assembly process we next used two colours STED to image both mature and intermediates NPC. By immuno-labelling both POM121 and mAb414 with fluorophores suited for STED microscopy in fixed cells, we could obtain high-resolution fluorescence images of both populations. In the left image of the Figure 73 confocal and STED image of NPC labelled with POM121 and mAb414 show the gain of resolution achieved thanks to STED microscopy. This resolution allows us to get details of the NPC and intermediates (right panel in Figure 73). Mature NPC exhibit signals from mAb414 (red) surrounded by a POM121 ring while intermediates with only POM121 have different sizes, reflecting different stages of assembly. In a number of detected NPCs, the POM121 rings are not complete, which is most likely due to incomplete labelling, a problem often encountered in super-resolution imaging of NPCs (Thevathasan *et al.*, 2019).

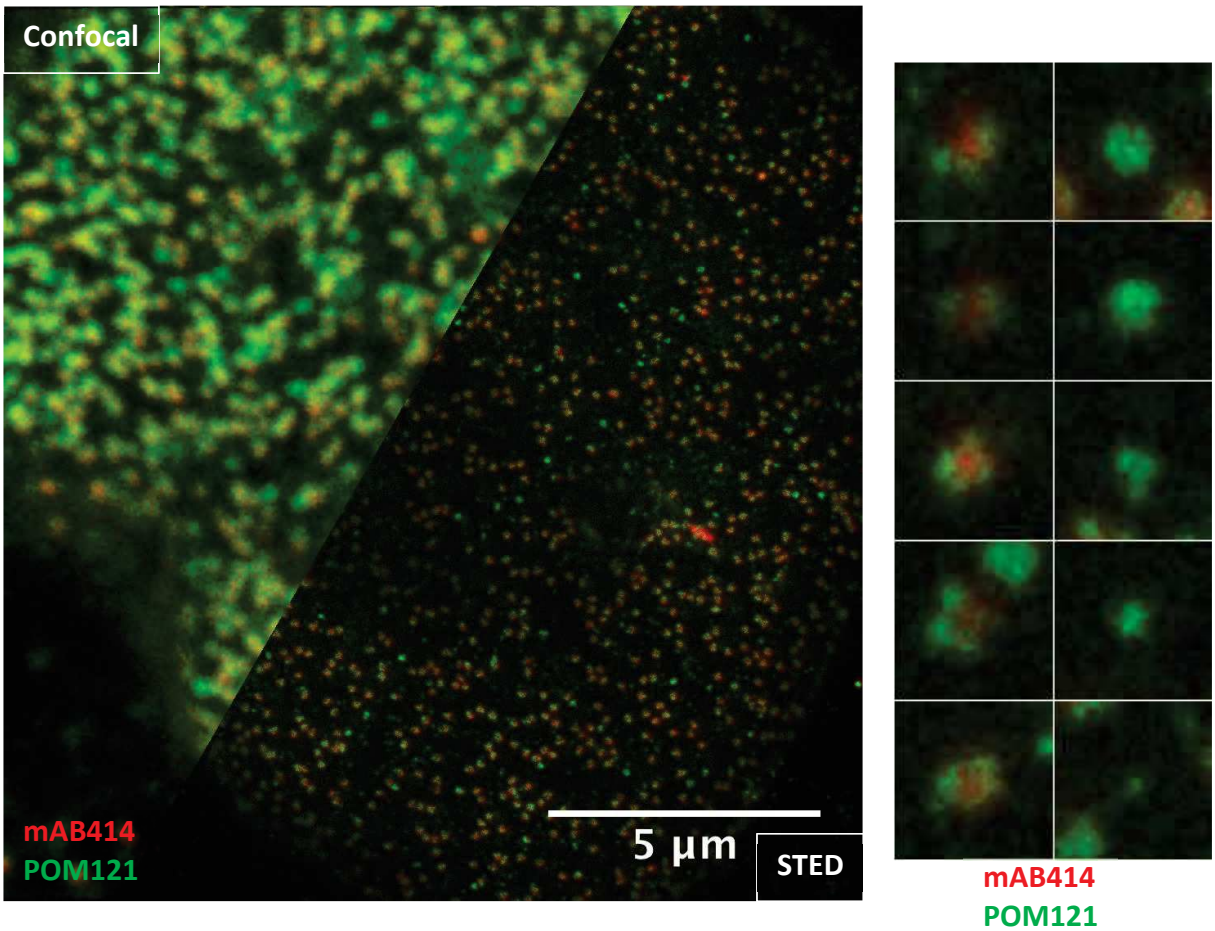

Figure 73: Left: Confocal and STED image of NPCs labelled with mAb414 (red) and POM121 (green). Right: Selection of mature pores (left column) and intermediates (right column). Crop size 300 nm.

To further analyse both mature NPCs and pore intermediates, we developed an algorithm to automatically detect pore coordinates and generate rotationally averaged intensity profiles (see Material and Methods for more details). After automatic detection of mature and intermediate NPCs, their center was determined by fitting the local maxima respectively on mAb414 or POM121 signal. Then an averaged profile around this point was calculated. Depending on the number of subunits labelled by the antibody, mature NPC would exhibit different profiles with one or two side peaks of POM121 (Figure 74). For the intermediates, intensity and diameter would vary, reflecting different stages of assembly.

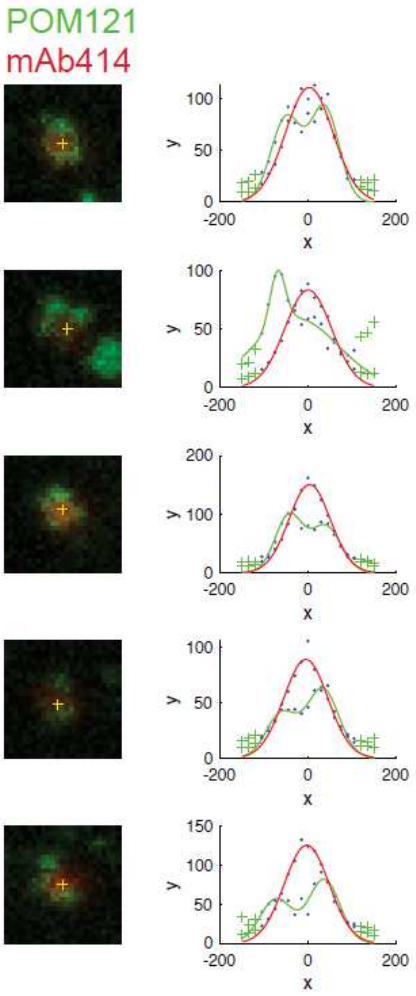

Figure 74: Examples of mature pores labelled with mAb414 (red) and POM121 (green) and corresponding profiles. Crop size is 300 nm.

On these profiles we measured several parameters for individual NPCs. First, in mature pores, mAb414 and POM121 FWHMs and the POM121 diameters are determined by the distance between the two peaks and the FWHM of the POM121 (Figure 75). This

distance provides information about both the structure of the NPC and the central channel for mAb414 signal.

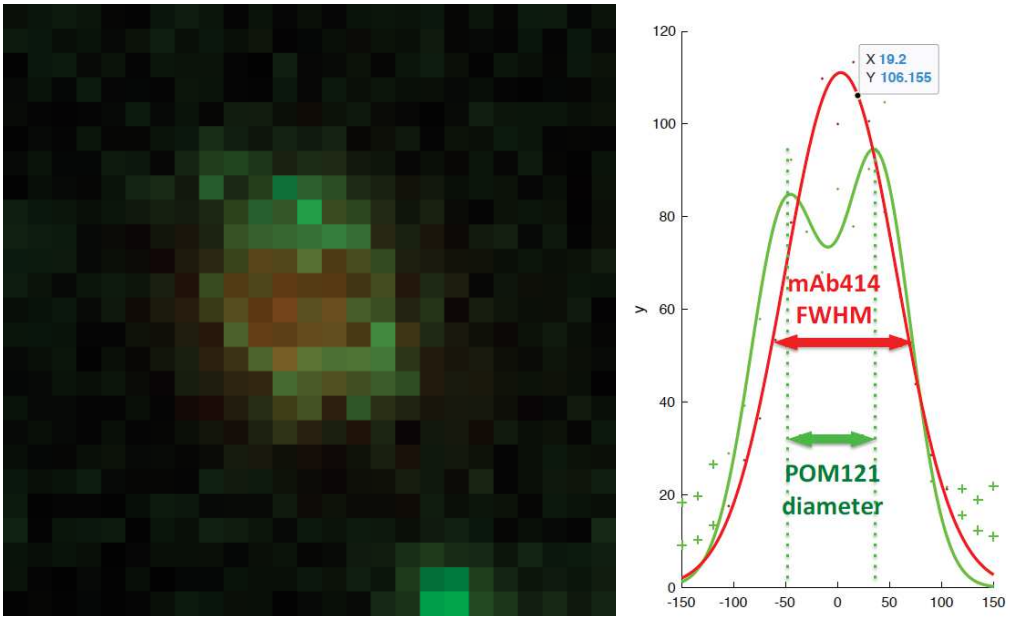

Figure 75: Measurements on STED images. Representative image of a mature NPC labelled with mAb414 (red) an POM121(green). Rotationnally averaged profile on mature NPC exhibit an mAb414 signal which appear as one peak where FWHM can be measure. POM121 signal exhibit two peaks which can be fitted to measure the POM121 diameter.

We then treated cells with siRNA targeting different nucleoporins and proteins involved in NPC interphase assembly to see how their depletion would affect mature and intermediate pore structure and distribution (Figure 76). Depletion of ELYS, SUN1, Nup53, Nup96, Nup133 and Nup153 resulted in a reduced density of NPCs compared to the scramble condition. The depletion of Tpr did not affect the density of mature pore in our experiments and we did not observe the higher density described by McCloskey et al. (McCloskey, Ibarra and Hetzer, 2018).

The most drastic effect on NPC density is observed among siRNA against Nups member of the Y-complex, Nup133, Nup96 and Elys. This result is explained by the fact that the recruitment of Y-complexes is essential in both interphase and post-mitotic assembly while other tested Nups are implicated in only one pathway. siRNA against Nup96 showed an even more drastic reduction in density since Nup96 and Nup98 are co-translated from the same RNA and cleaved. This condition then corresponds to the depletion of both Nup96 and Nup98.

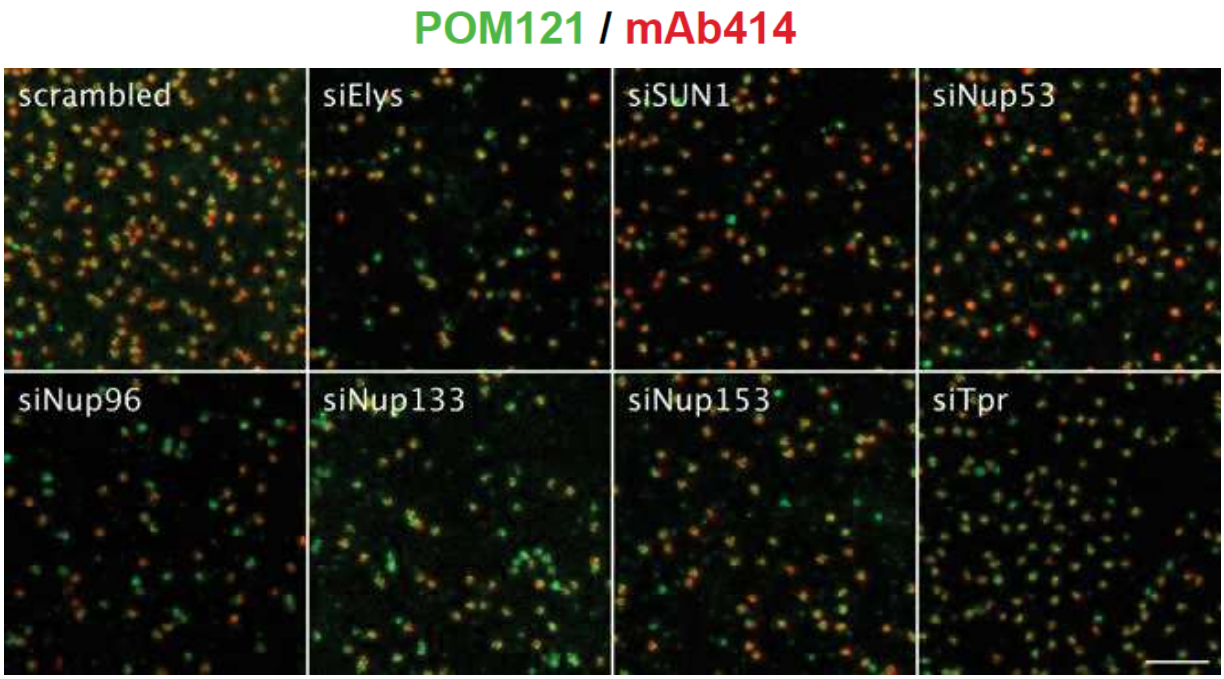

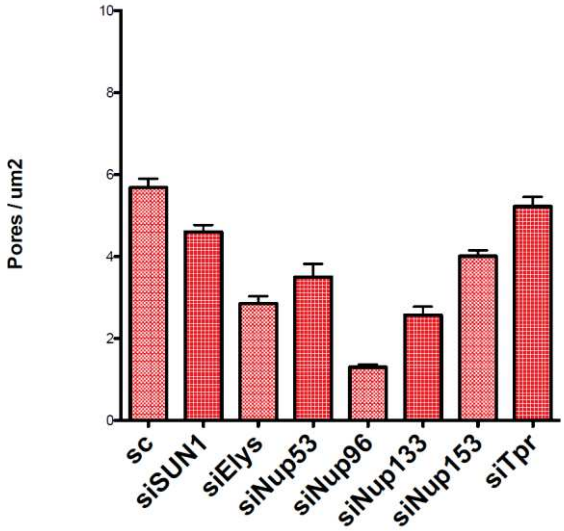

Figure 76: Top-STED images of NPCs labelled with mAb414 (red) and POM121 (green) after treatments with different siRNA in comparison with scrambled conditions. Scale bar is

Bottom-Mature NPC density based on mAb4144 signal in the same conditions.

In addition to the density of mature pores, a change in the ratio of mature versus intermediate pores is clearly visible in cells treated with siRNA (Figure 77). By measuring the density of intermediates and adding them to mature pores to quantify the overall density, it appears that the value obtained in almost all conditions is very similar, around 7 NPCs/µm². This value is only slightly lower than in the scrambled siRNA. The only exception is the siNup96 where the depletion of two Nups strongly affects NPC density. These results suggest that the treatment by siRNA against proteins involved in NPC interphase assembly prevents getting mature pores. By depleting a protein with siRNA, the amount of protein available is then not enough to continue the process of NPC assembly. This process is probably stopped at a specific stage of the assembly which is different for each protein.

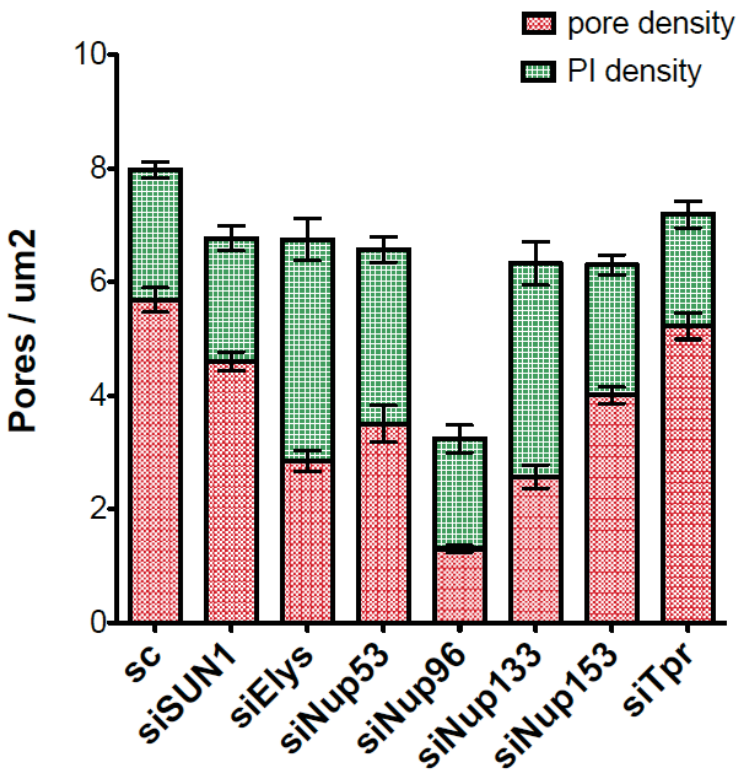

Figure 77: Density of mature NPCs (red) and NPCs intermediates (green) measured by STED quantifications in different siRNA conditions

Correlative AFM/STORM has allowed us to observe NPC interphase assembly intermediates and suggested that the diameter of the POM121 subunits grows in diameter. We have observed from our correlative AFM/STORM study that while assembly progresses, the POM121 pattern as measured from STORM increases in diameter. We thus assume that, similarly, POM121 diameter measured from STED becomes larger along the pore assembly process, until it reaches the size observed in mature NPCs (Figure 78). Since NPC intermediates rarely show a POM121 ring structure in STED microscopy but rather a single dot, we fitted the rotationally averaged profiles with single gaussians and measured the FWHM as a readout of POM121 assembly sizes.

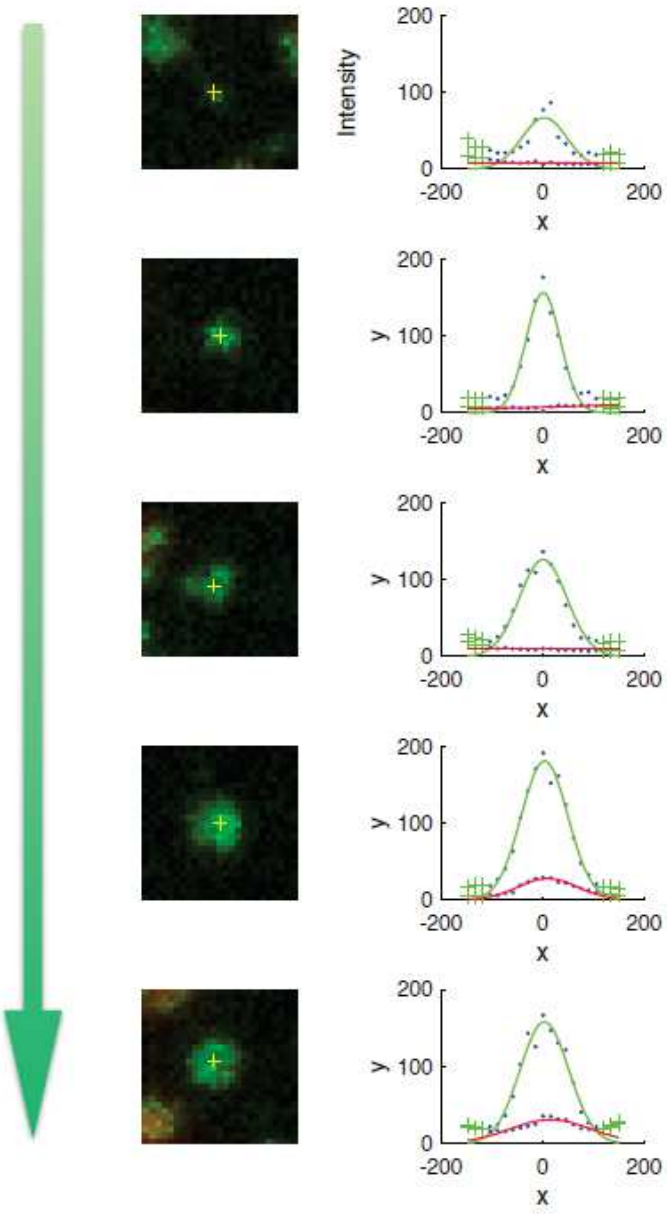

Figure 78: Different intermediates containing only POM121 observed by STED and corresponding intensity profile. The green arrow depicts potential evolution of a growing POM121 signal during interphase assembly. Crop size is 300 nm.

Moreover, we know that the depletion of certain nucleoporins will strongly affect NPC interphase assembly. This effect is determined by the limited amount of a specific nucleoporin available in the cell. Thus, the depletion of a nucleoporin using siRNA would lead to a defect in the assembly process at a specific step where the protein is key to complete it. The arrest in the assembly process will lead to an enriched population of intermediates of a specific size (Figure 79).

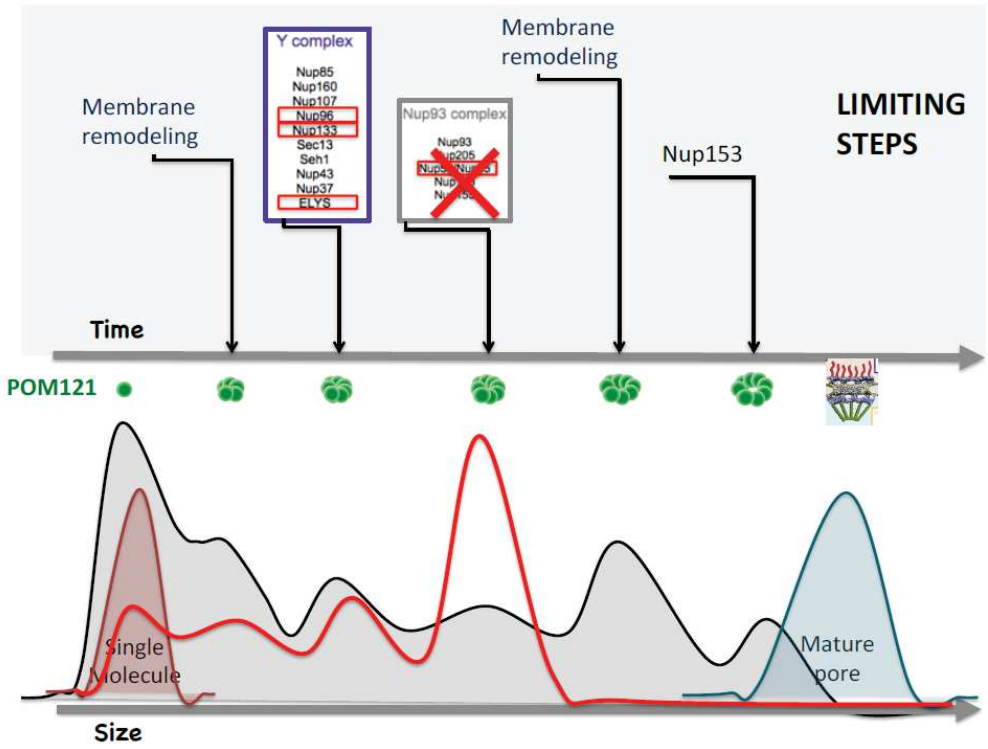

Figure 79: Putative model of assembly stopped by siRNA. The top part represents a hypothetical order of assembly with different limiting steps. Bottom part represents the distribution in size of POM121 containing intermediates (grey curve) which size will range from single molecule signal size (brown curve) to size in mature NPCs (blue curve) The red curve represents a hypothetic change in the distribution of intermediates sizes following siRNA treatment.

We first characterize the distribution of the FWHM of POM121 intermediates in control cells (black curve in Figure 80) and compare it with the same measure done for mature NPCs (black dashed curve in Figure 80). This quantification seems to indicate two main limiting steps in the assembly process, one with a very high peak around 50 nm and another one a bit lower than 100 nm. Importantly, 50nm also corresponds to the resolution limit in our STED imaging conditions. Thus, we cannot exclude that this peak actually comprises several distinct limiting steps. The FWHM of mature NPC is centered around 130 nm.

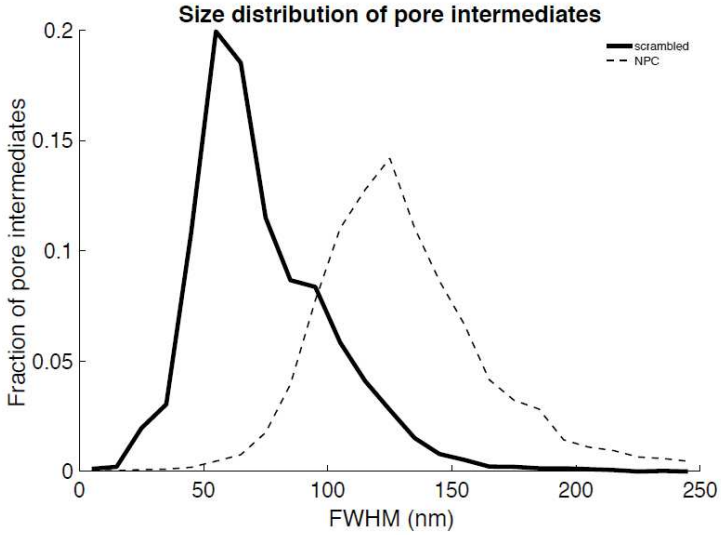

Figure 80: Distribution of POM121 FWHM of scrambled siRNA condition in intermediates (continuous line) and mature (dashed line) NPCs

Then, we treated cells with siRNAs against SUN1, ELYS, Nup53, Nup96, Nup133, Nup153 and Tpr and measured the same parameters to compare with the control condition. In the corresponding graph (Figure 81), where the POM121 size distribution of intermediate pore (continuous lines) and mature pores (dashed lines) are represented, we observe for three conditions, siELYS, siNup96 and siNup153 a higher frequency of small intermediates (around 50 nm FWHM) compared to the control. For ELYS and Nup96, this result is expected since they are members of the Y-complex which is recruited relatively early at the INM for interphase assembly. However, Elys is dispensable for interphase assembly and this increased frequency of small interphase intermediates might be a compensation for the reduced post-mitotic assembly induced by Elys depletion. Since Nup153 mediates the Y-complex recruitment, this is also expected and combined with the lower density of mature NPCs observed before, suggest that the recruitment of Nup153 at the membrane is a key limiting step.

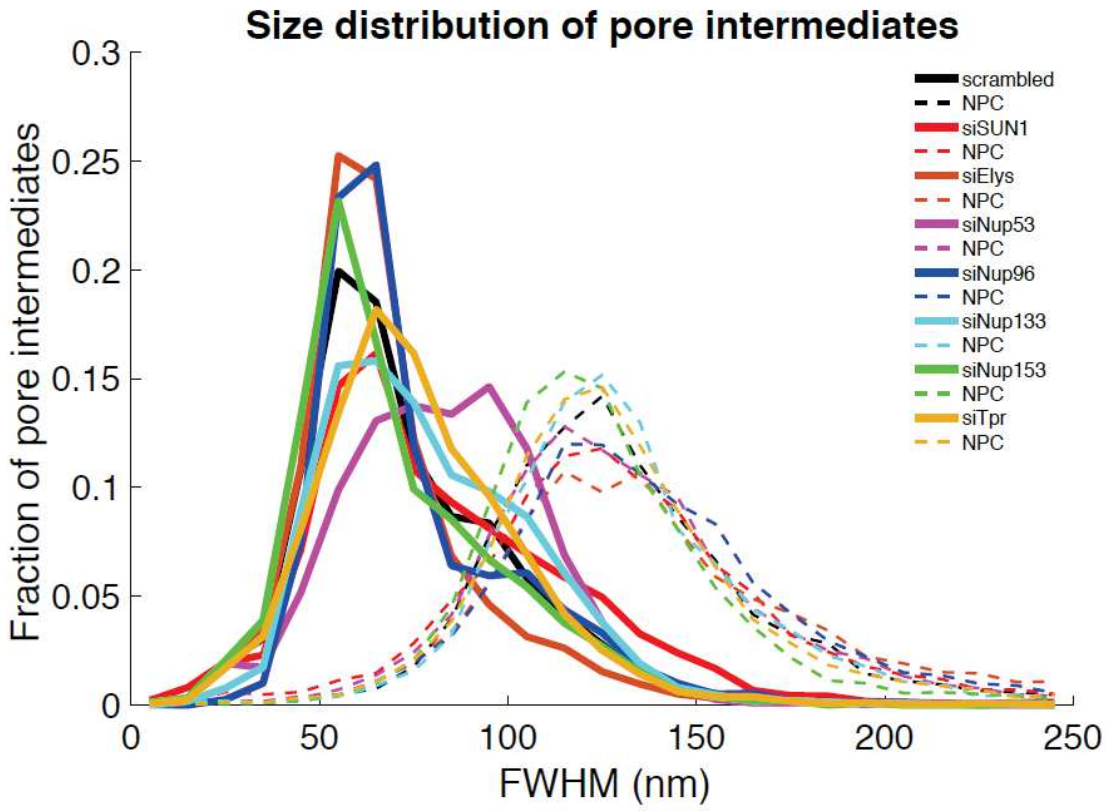

Figure 81: Distribution of POM121 FWHM in different siRNA condition in intermediates (continuous line) and mature (dashed line) NPCs

In comparison siTpr induces a slight shift of the first peak towards larger intermediates. This suggests that Tpr is critical for NPC progression at a step later than Nup153 but still quite early in the process (Figure 82). These results are consistent with the role of Nup153 to recruit Tpr to the NPC. However, they question the fact that Tpr is among the last Nup recruited at the NPC. One interpretation of this data is that Tpr could be present earlier at assembly sites. It might participate in the assembly process and be later relocated to the nucleoplasmic basket at the end of the process. This relocation could be controlled by the large rearrangement operated after the fusion process and visualized in AFM and EM data (Otsuka *et al.*, 2016).

Finally, another typical pattern observed for some conditions is the reduced number of small intermediates and the enrichment in large intermediates, corresponding to the second peak of the control (Figure 85). This was observed for siRNA against SUN1, Nup53 and Nup133. For SUN1 depletion the distribution of intermediates sizes is spread over a large range, even above the control data. One interpretation would be that the constraint applied via the control of the distance between the INM and ONM is reduced and makes it more difficult for NPC subcomplexes to assemble to form a mature NPC.

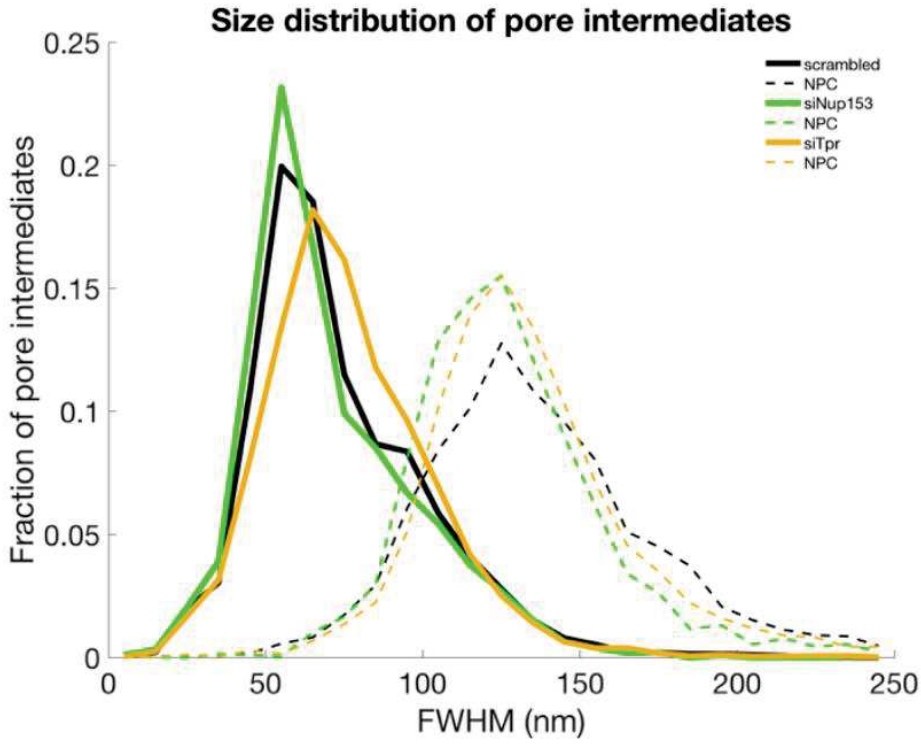

Figure 82: Focus on distribution of POM121 FWHM in siNup153 and siTpr conditions in intermediates (continuous line) and mature (dashed line) NPCs

Nup53 is believed to be an early player of interphase assembly because of its capacity to bind membranes. However, our data seem to indicate that the role of Nup53, presumably including membrane bending, is important for the fusion process. Intermediates' sizes in siNup53 exhibit a large distribution of size dominated by two peaks. This suggests that the assembly process is slowed down in the absence of Nup53 during the first stages of assembly. However, although NPC assembly seems to be able to progress since the size keeps growing, it finally stops at a late stage of assembly indicated by the second peak in intermediates' sizes. This could correspond to the large rearrangement of the assembling NPC structure at the moment of the fusion in which membrane bending properties of Nup53 might be of primary importance.

Experiments with siRNA against Nup133 also show a reduced frequency of small intermediates as well as an increased frequency of larger ones. Several works on Nup133 described contradictory results about its requirement for NPC assembly. While Souquet et al. described it as dispensable for the assembly, Doucet et al. as well as our STED results

shows a strong reduction in the density of mature NPC that support our hypothesis. Souquet et al. described that mutation of Nup133 results in a higher dynamic of Nup153 that would lead to a basket lacking Tpr. What is striking in our data is that Nup133 and Nup96 both belong to the Y-complex, yet their depletion has a very different effect on the size distribution of the intermediates. However, NPCs contain two rings of Y-complexes. Given the asymmetry of the assembling structure, it is possible that these two rings are recruited sequentially, and by different mechanisms. The simplest explanation is that Nup133 recruitment is not critical for early stages of assembly. It is possible that assembly of the first Y-complexes ring is mediated by Nup153 as described by Vollmer *et al.* (Vollmer, Lorenz, Moreno-Andrés, Bodenhöfer, De Magistris, *et al.*, 2015) and thus tolerant to Nup133 depletion, while the recruitment of the second depends on Nup133, as described in (Doucet, Talamas and Hetzer, 2010).

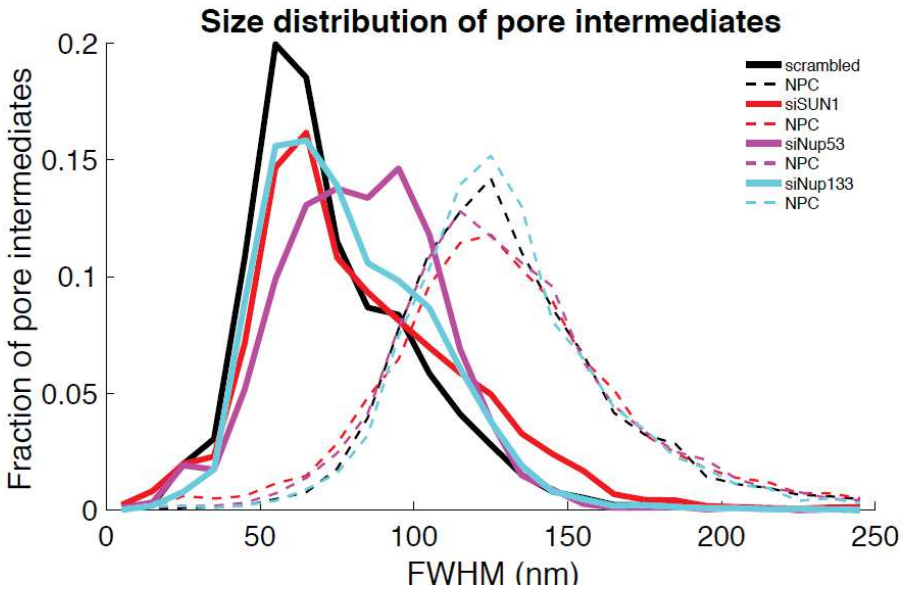

Figure 83: Focus on distribution of POM121 FWHM in siSUN1, siNup53 and siNup133 conditions in intermediates (continuous line) and mature (dashed line) NPCs

Our work using STED as a tool to characterize both size and stages of assembly of NPC interphase intermediates confirms that the POM121 assemblies grow progressively along the NPC formation process. These results are consistent with AFM/STORM correlative data where smaller intermediates structures tend to have small, nucleated signal of POM121 that would segregate to form a ring as observed in late intermediates and mature pores. Our data, although difficult to interpret, also show that different Nups are required at distinct steps.

9.5. Conclusion on interphase assembly

In this work, I have used three complementary methods to try to understand the molecular and structural details of NPC formation during interphase.

Firstly, AFM topography acquired on intermediates detected thanks to correlation with fluorescence confirms the observation made by EM by Otsuka *et al.* (Otsuka *et al.*, 2016): concentric rings that assemble in a very tall structure (mushroom-like) until a large rearrangement leads to the step where INM and ONM membranes fuse.

In addition to this picture, we have observed very precocious assemblies (no ring) where POM121 is present. This observation confirms that POM121 is probably the seeding element of nascent pores during interphase assembly.

Moreover, we have observed very large annular structures that are sometimes discontinuous. These could be subcomplexes recruited in the pore vicinity to get incorporated into the structure, or scaffold elements that could facilitate pore assembly. In this later hypothesis, SUN1 could be a compatible and functionally interesting candidate.

Finally, we have investigated the limiting steps in NPC assembly, and the players involved in each of them. While these data are tricky to interpret, they still clearly show that POM121 assemblies grow in two phases. Nup153 seems to be required very early on, closely followed by Tpr. Interestingly, components of the Y-complex are not equivalent, Nup96 being critical for early steps of assembly while Nup133 is required for progression of the second phase. Nup53 seems to be involved in two successive stages, and especially critical for a late step that could be membrane fusion. SUN1 depletion induces the appearance of wider POM121 assemblies, which can be due to a change in the progression rate of NPC assemblies, or a widening of the structures that may stem from defects in NE luminal spacing.

These observations, while they appear very interesting by showing new details of interphase assembly structure and components, also open up many more questions!

Discussion

10. Discussion and perspectives

During my thesis, the goal was to explore the nanoscale structure of the nucleoplasmic side of the human NPC. The main motivation for this work was to catch NPC interphase assembly events and to measure their topography thanks to AFM, to better understand this complex cellular process. To tackle this challenge, I have developed a specific protocol to purify and open nuclei from U2OS human cells. With this approach, combining AFM and super-resolution microscopy techniques, I have investigated the nanoscale structure, organization and components of both NPC basket and intermediates of assembly. In the following section, I will discuss how to interpret these results and what they mean for the general understanding of NPC structure and interphase assembly. I will further explore the perspectives for deciphering NPC interphase assembly.

10.1. AFM as a nanotool to explore NPC nucleoplasmic structure

The protocol to purify and open nuclei from cultured cells developed in this work allows access to the nucleoplasmic side of NPCs by AFM while preserving its structure. Until now, the NE purified from *Xenopus laevis* were the main sample for the nanoscale investigation of NPCs. Current protocol offers the possibility to open thousands of human nuclei at the same time in a relatively reproducible manner. The application to the human cell nuclei allows investigation of characteristics of NPCs which are known to be important in some aspects of cancer research. Moreover, it is easy to manipulate cultured cells, with siRNA for instance. Thus, this gives access to a better characterization of the different Nups contributions to the structural and functional aspects of the NPC. In addition, composition and relative stoichiometry of Nups have been reported to differ between cell types and tissues. By investigating various cell types, differences could be observed in terms of structure or mechanics, which might reflect functional differences between NPCs in different tissues. The versatility of our approach to study *in situ* NPC structure from cells opens the way to decipher how compositional bias translates into structural diversity. Finally, this approach could be used to investigate both structure and mechanical properties of other components localized at the INM, like

lamins and LINC complexes, with the same correlative AFM/super-resolution microscopy approach. These aspects are especially interesting for the rising field of biomechanics. Indeed, the NE appears as a mechanical hub that physically transmits and biochemically transduces mechanical cues from the cellular environment to the nucleoplasm.

10.2. Structure of the NPC

This approach offered the first AFM images of human NPCs observed from their nucleoplasmic side. Extensive analysis of NPC topography obtained by AFM reveals that its structure is very similar to data from *Xenopus laevis* oocytes. The averaged nucleoplasmic ring diameter we measured was 81.6 nm, compared to the 85 nm observed in Xenopus laevis (Stanley, Fassati and Hoogenboom, 2018). The basket exhibited a large variability which corresponds to previous observations in *Xenopus laevis* (Stanley, Fassati and Hoogenboom, 2018). A large set of basket configurations was observed, from the usual protruding basket to the filaments located inside the pore, below the height of the nucleoplasmic ring. The data from the mechanical analysis also highlight a soft basket structure which is consistent with a certain flexibility. These results question the generally admitted protruding structure of the NPC basket described for instance by EM. Recent super-resolution approaches failed to depict this supposedly very organized protruding basket filaments of Tpr which appeared as a cloud of localizations (Sabinina *et al.*, 2021). Tpr is predicted to contain coiled-coils which are usually described as relatively rigid structures. However, structure predictions from sequence analysis with the PDB identified four coiled-coils regions which could be connected by flexible linkers that could play a role in the flexibility of the conformations. One possibility in the organization of Tpr is that it arranges itself as a tetramer formed of two dimers in antiparallel orientation forming a filaments as suggested by structural data of a fragment of Tpr (Pal *et al.*, 2017). This hypothesis would match with the stoichiometry of 32 Tpr per NPC (Ori *et al.*, 2013), where Tpr would be organized as one tetramer in each of the eight basket filaments. However, this still should be confirmed.

In addition, some NPCs appear to have a basket which is not located in the middle of the nucleoplasmic ring but rather on the top of the ring with sometimes even signals located

outside of the NPC. This suggests that in some conditions the distal ring where filaments join might disrupt and result in NPCs without a structured basket. This supports the idea that some of the dynamic nucleoporins could be envisioned as “a cloud of accessory factors surrounding and constantly exchanging with the NPC *in vivo*” which has been suggested by a recent work (Hakhverdyan *et al.*, 2021).

It is important to remember that NPC structure is highly sensitive to environmental conditions. As soon as samples are prepared, introducing environmental changes, the question arises whether the structures depicted are truly physiological or result from the sample preparation. The fact that a number of baskets are collapsed into NPCs may be due to an artefact of sample preparation since even though we controlled the preservation of the NPC scaffold structure based on Nup96 organization, we cannot exclude that the peripheral structures are damaged during purification. In fact, the fragile structures may be sucked into the core channel because of changes in surface tension (proposed in (Jarnik and Aebi, 1991)). Structure should be also determined with hybrid approaches, relying on different data acquisition methods and various preparation conditions to confirm our results.

Finally, our approach can be used to observe how depleting NPC subunits from human cells can affect the structure and help to better understand the function of each Nup. In this work, this has been demonstrated by the depletion of Nup153 by siRNA which resulted in NPCs without a basket. Interestingly, the topography of these NPCs is very similar to what has been observed in *Xenopus laevis* during apoptosis where Nup153 is degraded and leads to basket disruption (Kramer *et al.*, 2008). We could even refine this analysis by depleting Tpr and thus understand the respective contributions of Nup153 and Tpr in the basket organization.

10.3. Interphase assembly: what did we learn and what does it mean?

Importantly, the approaches that we used to study the process of pore assembly all lack the time dimension. Indeed, our observations are done in fixed samples, and reveal snapshots of frozen instants. We made this choice because it is extremely difficult to detect rare events, especially from the very beginning. It would require imaging areas of the NE until seeding particles of POM121 appear, which would probably require very long acquisitions because of the scarcity of pore assembly events. This would have repercussions on data quality since long imaging can affect fluorescence via photobleaching. In this regard, the trick used by Otsuka *et al* to catch a narrow window in the cell cycle where interphase assembly occurs in a frequent and synchronous manner is very interesting. However, this approach is not adapted to the preparation of NEs.

That said, it is still possible to reconstitute sequences of events from snapshots, provided the representativity of each stage of the sequence is high enough to get statistics, and/or there is additional information (size, fluorescence intensity…) to help us sort the events. Here we used the AFM topography to sort events, knowing they would be growing in size until they reach their final state (mature NPC). In addition, we used POM121 intensity and spatial organization to confirm our analysis in AFM. In STED, we used the POM121 organization to sort events and used statistics to infer kinetics information. We believe these approaches are valuable, but interpretation of the results is not straightforward. Here I will try to integrate our observations as well as data from the literature into a global picture of the pore assembly process.

First, my correlative AFM/STORM data strongly support that POM121 is one of the first proteins contributing to the nascent pore edifice, as it is detected in small structures that are barely detectable by AFM (class 1). However, membrane deformation is visible at this stage, and it is not clear if other factors, either in the lumen or further away from the pore assembling site, induced membrane bending.

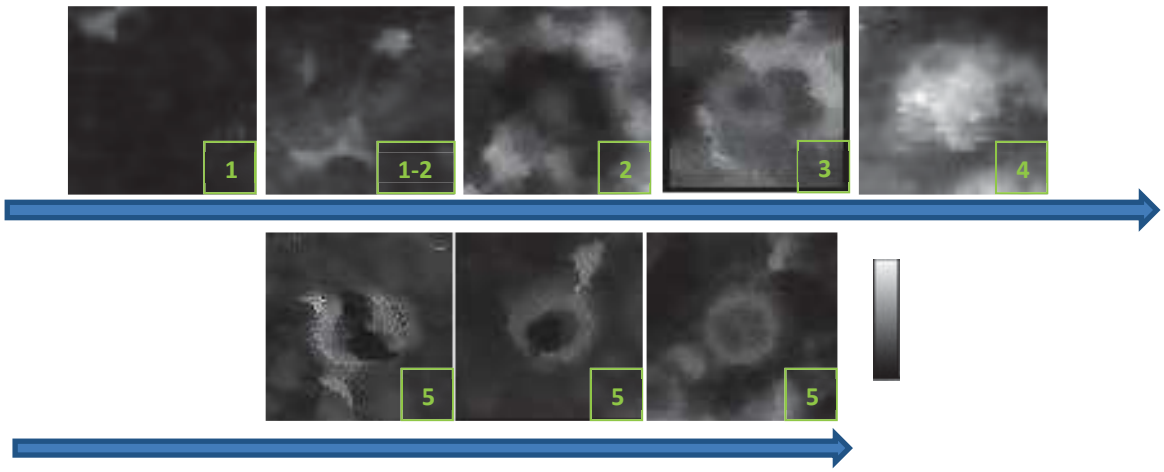

Figure 84: Hypothetical model for topography of the interphase assembly process. Crops 290 nm x 290 nm. Colour scale 0-150 nm. The green label indicates the class assigned based on topography. The blue arrow indicates the progression in the structure.

Furthermore, the STED data suggest that Nup153, then Tpr, are required early on, followed in a second time by Nup53. This was quite a surprise since we expected that peripheral Nups, including Tpr, would be recruited in the last phase of assembly, probably after membrane fusion. However, this observation is supported by a recent work (Otsuka *et al.*, 2021) showing that Tpr is recruited at the NE very early on during interphase pore assembly, shortly following Nup153. Moreover, they also observe that Nup205 and Nup93, which belong to the same subcomplex as Nup53, are recruited in a second phase.

Another unexpected result was the discrepancy between the effects of siRNAs against Nup96 and Nup133, which both belong to the Y-complex. As Nup133 is located at the extremity of the complex, it is possible that its depletion in early events does not prevent the recruitment of subsequent components. Indeed, from the final arrangement of Y-complexes in the NPC architecture, Nup133 mostly interacts with the membrane (von Appen *et al.*, 2015). Thus, our interpretation is that Nup133 is not required in early stages but may be required later during the process. This second phase could either correspond to the recruitment of a second ring of Y-complexes, or reflect the connection of Nup133 with the curved pore membrane via its ALPS motif (Doucet, Talamas and Hetzer, 2010).

Finally, the effect of SUN1 is the most difficult to interpret as it does not dramatically change the ratio of specific peaks in the size distributions, but rather shifts the whole diagram towards larger sizes. This may be an indirect effect of aberrant NE deformations, as SUN1 is

known for its role to maintain mechanical stability of the NE (Rothballer, Schwartz and Kutay, 2013). Interestingly, we have identified SUN1 in protruding structures surrounding mature NPCs which look similar to some of the structures imaged around intermediates. It would be very interesting to test if SUN1 is present in a large circular structure that surrounds NPC assembling sites. However, the labelling strategy I used did not offer the possibility to label at the same time POM121 and SUN1. It would be appealing to develop CRISPR/CAS9 cell line expressing POM121 fused to a SNAP-tag for example, to study how these proteins are organized relative to each other in both mature pores and intermediates to better understand the role of SUN1 in the NPC assembly and its localization relative to pore intermediates.

From a structural point of view now, the obtained AFM data highlighted tens of pore intermediates structures that were qualitatively classified, based on their similarities. We then organized them in a putative chronological order (figure 84), assuming that the assembling structures would grow over the process. This chronology indeed coincides with early and progressive recruitment of POM121 (Figure 70), which was previously shown (Dultz and Ellenberg, 2010). The topography of intermediates observed by EM helped us to sort structures with a very large and high topography (Class 4), that we identified as the mushroom-like assemblies identified by Otsuka *et al.* Thanks to the use of POM121 fluorescence to identify locations of pore intermediates, we were able to catch very early stages, with central structures that do not exhibit annular shape, at least at the resolution of AFM. Interestingly, POM121 co-localizes with these tiny structures, sitting at the center of a concave membrane deformation. This observation is in line with previous reports that POM121 could induce such deformations (Talamas and Hetzer, 2011), even though the mechanisms behind this are not clear yet. Nup153 is another interesting candidate: indeed, it is involved early on during assembly, and has the capacity to bind membranes (Vollmer, Lorenz, Moreno-Andrés, Bodenhöfer, De Magistris, *et al.*, 2015). Moreover, its yeast homologs can bend membranes via an amphipathic helix that is conserved in hNup153 (Mészáros *et al.*, 2015). The central ring seen in the subsequent classes may be composed of Y-complexes. Unfortunately, these events are not very frequent and fluorescence information about the presence of Nup96 was not available in the corresponding experiments.

A very interesting and unexpected result obtained here is the presence of an external annular structure that surrounds the central complexes containing POM121. The diameter of these structures is larger than mature pores, and larger than rings observed by EM (Otsuka *et al.*, 2016). It would be of higher interest to identify the components present in this ring, and would greatly help the comprehension of the assembly mechanism. For now, we have two main models: i) the ring could be an accessory structure that constrains the membrane to help shape it to a concave topology. Indeed, all the elements identified in Nups that can bend membranes are able to induce convex curvature; ii) the ring could contain Nups that are inserted into the edifice at later stages, corresponding for instance to class 4 stage.

Finally, a large rearrangement happens, that probably includes membrane fusion, to lead to late intermediates that are very similar to mature pores, except they sometimes do not possess a basket (Class 5). In our study, we do not have information on the very latest stages of assembly like the recruitment of cytoplasmic filaments. However, a recent study has reported a role of Torsins in INM-ONM fusion (Rampello *et al.*, 2020). Their depletion results in blebbing of the NE, enriched in Nups, and is dependent on the expression of POM121. These blebs might correspond to defective NPC intermediates stalled in the process. Indeed, this blebbing is associated with a diminution of mature pores and Nup358, which is in the lately recruited cytoplasmic filaments, is absent.

In conclusion, in this work, a new protocol for human nuclei purification and opening was established to give access to the inner side of the NPC while preserving the NPC structure. The investigation of the nanoscale topography of the NPC by AFM allowed a better characterization of the NPC basket. Detection of interphase assembly events using correlation with fluorescence microscopy led to the measure of various intermediate NPC structures which have been classified to build a model on the topology of NPC interphase assembly. Finally, using super-resolution microscopy techniques combined with siRNA treatment, the potential roles of different Nups during the interphase assembly were inferred by measuring how their depletion could affect the size of intermediate structures.

Annexes

A. Scientific publications

The following part corresponds to the scientific publications on other projects in which I have been involved during my thesis:

- 1) Correlative AFM and fluorescence imaging demonstrate nanoscale membrane remodelling and ring-like and tubular structure formation by septins.
- 2) Structures of the archaerhodopsin-3 transporter reveal that disordering of internal water networks underpins receptor sensitization.
- 3) Imaging Artificial Membranes Using High-Speed Atomic Force Microscopy.

Volume 13
Number 29
7 August 2021
Pages 12381-12758

Nanoscale

rsc.li/nanoscale

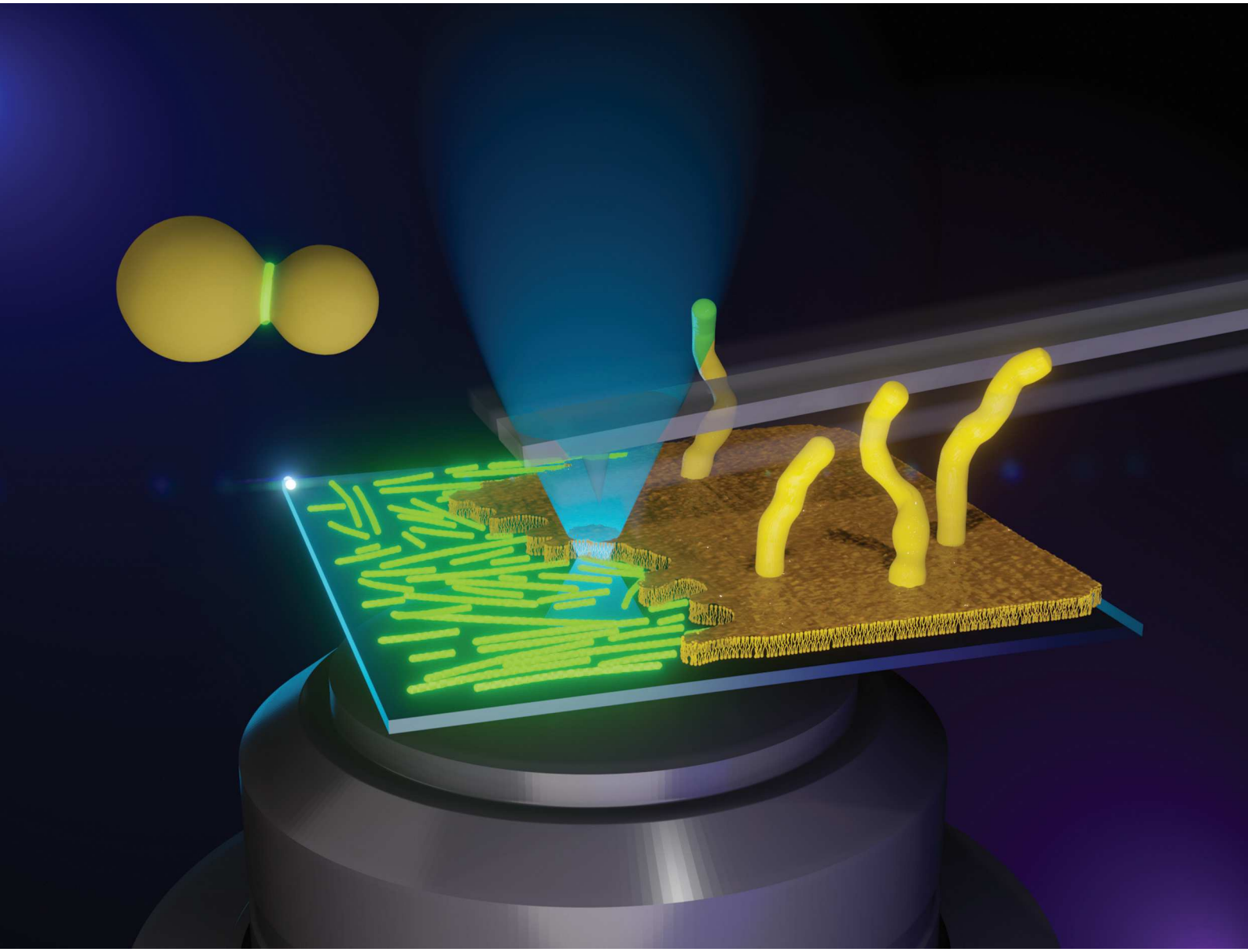

ISSN 2040-3372

ROYAL SOCIETY OF CHEMISTRY

PAPER
Aurélie Bertin, Pierre-Emmanuel Milhiet *et al.*
Correlative AFM and fluorescence imaging demonstrate nanoscale membrane remodeling and ring-like and tubular structure formation by septins

NCNST

Nanoscale

ROYAL SOCIETY OF CHEMISTRY

PAPER

Cite this: *Nanoscale*, 2021, **13**, 12484

Correlative AFM and fluorescence imaging demonstrate nanoscale membrane remodeling and ring-like and tubular structure formation by septins†

Anthony Vial, ‡[a] Cyntia Taveneau,‡§[b] Luca Costa, [a] Brieuc Chauvin,[b] Hussein Nasrallah,[a] Cédric Godefroy,[a] Patrice Dosset,[a] Hervé Isambert,[b] Kien Xuan Ngo,[c] Stéphanie Mangenot,[b] Daniel Levy, [b] Aurélie Bertin *‡[b] and Pierre-Emmanuel Milhiet *‡[a]

Received 29th March 2021,
Accepted 21st June 2021

DOI: 10.1039/d1nr01978c

rsc.li/nanoscale

Septins are ubiquitous cytoskeletal filaments that interact with the inner plasma membrane and are essential for cell division in eukaryotes. In cellular contexts, septins are often localized at micrometric Gaussian curvatures, where they assemble onto ring-like structures. The behavior of budding yeast septins depends on their specific interaction with inositol phospholipids, enriched at the inner leaflet of the plasma membrane. Septin filaments are built from the non-polar self-assembly of short rods into filaments. However, the molecular mechanisms regulating the interplay with the inner plasma membrane and the resulting interaction with specific curvatures are not fully understood. In this report, we have imaged dynamical molecular assemblies of budding yeast septins on PIP2-containing supported lipid bilayers using a combination of high-speed AFM and correlative AFM-fluorescence microscopy. Our results clearly demonstrate that septins are able to bind to flat supported lipid bilayers and thereafter induce the remodeling of membranes. Short septin rods (octamers subunits) can indeed destabilize supported lipid bilayers and reshape the membrane to form 3D structures such as rings and tubes, demonstrating that long filaments are not necessary for septin-induced membrane buckling.

Introduction

Septins are ubiquitous conserved proteins present in eukaryotes and bound to the inner plasma membrane. From palindromic rod-like oligomers, they self-assemble into higher-ordered structures, including filaments, bundles and rings.[1] They participate in a large spectrum of cellular processes including cytokinesis,[2,3] ciliogenesis[4] or cell migration.[5] The poor regulation of septin expression is thus related to numerous pathologies from cancer diseases[6] to infections[7] or neurodegenerative diseases.[8] All septins are GTP-binding proteins that form hetero-oligomeric palindromic assemblies. Studies by Electron Microscopy (EM) and X-rays crystallography[9] have provided pieces of structural information arguing for the conservation of septin ultra-structures across species.

Septins were first discovered in *Saccharomyces cerevisiae*. The *S. cerevisiae* septins are rod-like octameric palindromic units of 32–35 nm long and 4–5 nm in diameter in the presence of more than 150 mM monovalent salt[10] (Fig. 1A, insert). At ionic strengths below 150 mM monovalent salt, septin rods self-associate to form paired filaments of several microns long (Fig. 1A, insert), suggesting that electrostatic interactions drive the assembly of filaments. GTP and/or GDP are necessary to ensure the self-association of stable octameric complexes.[1] However, the role of GTP hydrolysis is not required to ensure proper septin polymerization or promote their interaction with lipids. A recent report[11] suggests, using atomic force microscopy (AFM), that the mica surface is likely to mimic membranes and thus analyzes how septins self-assemble on mica. However, budding yeast septins interact specifically with phosphatidylinositol-4,5-bisphosphate (PIP2) and their polymerization is facilitated in its presence. Indeed, PIP2 is required to observe any budding yeast septins membrane interaction even in the presence of other negatively charged

[a]*Centre de Biochimie Structurale (CBS), Université de Montpellier, CNRS, INSERM, 34090 Montpellier, France. E-mail: pem@cbs.cnrs.fr*
[b]*Institut Curie, Université PSL, Sorbonne Université, CNRS UMR 168, Laboratoire Physico Chimie Curie, 75005 Paris, France. E-mail: aurelie.bertin@curie.fr*
[c]*Nano Life Science Institute (WPI-NanoLSI), Kanazawa University, Japan*
†Electronic supplementary information (ESI) available. See DOI: 10.1039/d1nr01978c
‡Have equally contributed to this work.
§Current address: Department of Biochemistry and Molecular Biology, Monash University, 3800 Clayton, Victoria, Australia.

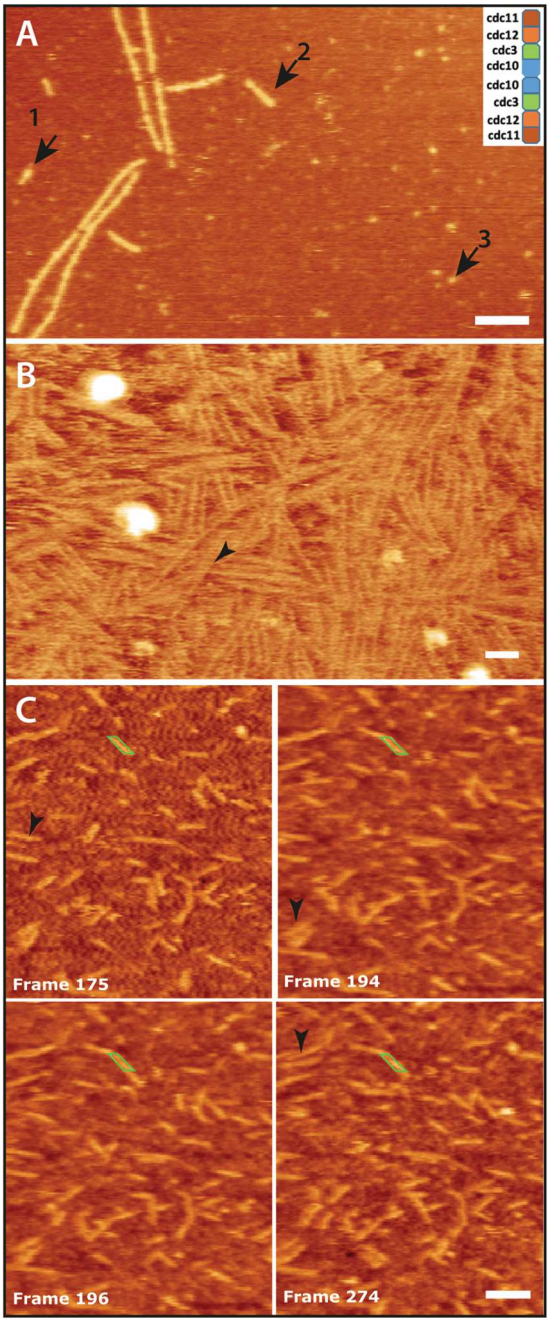

Fig. 1 AFM imaging of purified septin coated on mica. A and B are AFM height images recorded in liquid at low and high density, respectively. Black arrows indicate septin oligomers of different lengths, 36 nm and 76 nm respectively for 1 and (2). The arrow 3 points out a smaller and globular structure (in the range of 10 nm). Black arrowheads in B point out disordered filaments (one can observe that some filaments are at the top of others with different orientation). Scale bars are 100 nm (A) and 50 nm (B) and z scales are 10 nm. The inset in A shows a cartoon of the octameric rod that is the elementary bricks of filaments. Its length is 35 nm.[10] C corresponds to snapshots of Movie 1† recorded with HS-AFM with the number of frames indicated. The 4 height images show the growth of septin filaments over time. The green parallelogram indicates a filament that is growing overtime in both directions. The last frame (274) highlights the fact that the filament could be disrupted during imaging (part of the filament that is perpendicular to the scan axis). Black arrowheads point out paired filaments. The scale bar is 50 nm.

lipids (di-oleoyl-phosphatidylserine, DOPS).[12] Using lipid monolayer assays combined with EM observations, PIP2 was shown to promote budding yeast septin filament assembly and organization.[13] Both their organization and functions are thus closely related to their interplay with lipids.[13] At the membrane, septins have a key role as scaffolds for protein recruitment in signaling pathways. Septins are involved in building diffusion barriers for membrane bound proteins in various tissues. Specifically, during cytokinesis, they have a compartmentalizing role around the cleavage site.[14] Septins also impact cell morphogenesis and can affect the membrane stability and rigidity of migrating cells.[15] *In situ*, septins have been shown to have a role in membrane reshaping, for instance in the context of *endo* lysosomal sorting.[16] Using *in vitro* bottom-up approaches, human septins from extracts were shown to reshape PIP2-containing membranes and induce tubular structures from giant unilamellar vesicles (GUVs).[17] More recently, the curvature sensitivity of septins was analyzed.[18,19] In particular, we demonstrated that septin filaments can reshape liposomes and that the observed reshaping results from a septin filament curvature preference.[20] Bound to a lipid membrane covering an undulated solid surface, filaments can indeed adopt negative curvatures, while septins avoid interacting with highly positive curvatures and would rather lie flat on a biomimetic membrane.

Here, to further understand the molecular mechanisms associated with septin-induced membrane remodeling, we have used AFM and fluorescence microscopy to analyze the self-oligomerization of budding yeast septins, both in the presence and absence of a supported lipid bilayer (SLB). We ensured that the lipid composition mimics the inner leaflet of the plasma membrane. We have thereby analyzed here, for the first time, the behavior of septins interacting with a flat supported lipid bilayer. We employed High-Speed AFM (HS-AFM) to investigate the real-time protein oligomer self-assembly. Supporting previous observations suggesting that septins are able to reshape and remodel membranes spontaneously, we have demonstrated here that septin short rods (octamers) can dramatically disrupt flat 2D lipid bilayers to reshape them into peculiar three-dimensional structures.

Experimental

Protein purification

Yeast-septin complexes containing Cdc11, His6-Cdc12, Cdc10 (±GFP) and Cdc3 were co-expressed in *Escherichia coli* and purified as previously described.[10] Briefly, septins are purified by immobilized nickel affinity, size exclusion and ion exchange chromatography. A Cdc11_His_6-Cdc12_Cdc3_Cdc10_Cdc10_Cdc3-His6-Cdc12_Cdc11 or the version with GFP-tagged Cdc10 and palindromic complex are thus obtained.

Supported lipid bilayers

The lipid mixture was composed of EggPC (EPC), di-oleoyl-phosphatidylethanolamine (DOPE), di-oleoyl-phosphatidylserine (DOPS), cholesterol (Chl), PIP2 at 55 : 10 : 10 : 15 : 10 ratios,

as already described,[20] except in Fig. 4, S2 and Movies 2, 6† where it was composed of palmitoyl-oleoyl-phosphatidylcholine (POPC), palmitoyl-oleoyl-phosphatidylethanolamine (POPE), palmitoyl-oleoyl-phosphatidylserine (POPS), and dioleoyl-phosphatidyl-inositol (PIP2) at 50 : 35 : 10 : 5 molecular ratios. Fluorescence labeling of SLBs was performed using 0.1% GloPIP Bodipy C16 or 0.1% Rhodamine-DOPE. All the lipids were purchased from Avanti Polar lipids except the GloPIP Bodipy C16 that is from Echelon.

Large unilamellar vesicles (100 nm diameter) are prepared in buffer A composed of HEPES 20 mM (pH 7.4) and NaCl 150 mM by extrusion through a polycarbonate filter. The vesicle solution is then added at 40 °C for 40 min on top of the support in the presence of 10 mM $CaCl_2$ to facilitate membrane fusion onto the support.[21,22] Vesicles then adsorbed on the substrate before rupturing and formed a continuous supported bilayer. The bilayer is rinsed with buffer A supplemented with EDTA in order to remove the excess of divalent cations that can reduce the in-plane diffusion of lipids within the membrane on mica.[23]

AFM imaging

The setup was a combination of a Nanowizard 4 microscope (JPK, Berlin) together with a homemade objective-type TIRF inverted optical microscope (Zeiss, Le Pecq, France) equipped for single molecule localization microscopy with an oil-immersion objective (αPlanFluar 100×, 1.45 DIC, Zeiss)(see more details in ref. 24).

HS-AFM was performed with a prototype from Toshio Ando's laboratory and provided by RIBM Research Institute of Biomolecule Metrology Co., Ltd, Tsukuba, Japan.

Imaging was performed in a Tris 50 mM pH 8 buffer supplemented with 50 or 300 mM NaCl.

Confocal fluorescence imaging and image analysis

Confocal experiments were performed on a Nikon Ti inverted microscope. The software EZ-C1 was used to acquire confocal images and a MatLab routine was used to view the stage in real time and acquire movies *via* the camera. The image J radial profile plugin was used to analyse the fluorescence signal on the GUVs.

Results

Septin oligomerization observed by AFM

We first characterized by AFM the different ultra-structures of septins and thus confirmed that the expected rods as well as paired filaments could be observed by atomic force microscopy. To this end, we have incubated septins in solution at low salt conditions and then deposited the solution on mica, a substrate that is atomically flat, allowing high resolution AFM imaging[25] (Fig. 1A and B). At a low density of ~2.6 nM (1 μg mL^{-1}) septin (Fig. 1A), we observed individual octameric rods of 35 nm long and 5 nm diameter as well as longer filaments, with lengths up to several hundreds of nanometers (Fig. S3†), which likely corresponded to the association of small octameric rods as already observed by electron microscopy.[10] Isolated and round-shaped structures were also delineated by the AFM tip and probably from a partial dissociation of the septin complex that occurs in solution.[10] The mean value of the diameter of these small oligomers was 9.3 ± 4.3 nm (mean ± SD), ranging from 5.7 to 25 nm (data not shown). As already observed by EM,[10] fluorescence microscopy,[18,26] and FRET assays,[27,28] paired filaments were also observed, even at low density, suggesting long-range interactions between oligomerized rods. This tendency to associate along the long axis of filaments was more pronounced with 80 nM septin when the density of filaments coating the mica increased (Fig. 1B). A network of disorganized septin filaments was observed with a high proportion of paired structures where the flexible coiled coils connecting paired filaments make the filament-filament distance variable.[10] We next analyzed the dynamics of septin oligomer self-assembly imaging in real-time with HS-AFM, *i.e.* 1–2 frames per s. The complexes were first equilibrated at high ionic strength where septins remain octameric. The buffer was subsequently exchanged with low ionic strength buffer during imaging to induce polymerization. Under these conditions, we observed the formation of filamentous septin oligomers under the AFM tip. Snapshots in Fig. 1C and Movie 1† clearly demonstrate the non-polar growth of septin filaments. Indeed, the oligomers were able to grow from both ends as expected from the palindromic molecular nature of the septin rod structure. In the course of movie acquisition, we observed both self-assembly (elongation as well as pairing, see black arrowheads in Fig. 1C) and disassembly of septin filaments. However, their maximal length remained below 80 nm (Fig. S3A,† right panel) while septin filaments have previously been shown to reach several microns in length.[13,26] These results suggest that septin oligomerization is mitigated by forces below a few tens of pN, the force that we imposed during HS-AFM imaging. Septin scanning sensitivity and oligomerization fragility was also supported by observations carried out using conventional AFM where successive scans of the same area led to the disruption of filaments by pulling out portions of the filaments (Fig. S1†). A recent article using high-speed AFM reports that low ionic strengths do not promote any septin self-assembly into filaments.[11] Instead, the elongation of septins is facilitated in the presence of salt, suggesting that the charges present on the mica surface significantly alter the septin elongation mechanism that is observed in solution. Our current study along with others mentioned above using cryo-EM tends to show that polymerization indeed occurs at low ionic strengths, suggesting that the nature and state of the support surfaces can affect the polymerization of septins.

Septin induced membrane destabilization and remodeling

To mimic the lipid composition of the inner leaflet of the plasma membrane of eukaryotic cells we produced lipid bilayers, composed of a mixture of phosphatidylcholine (PC), phosphatidylethanolamine (PE), phosphatidylserine (PS),

cholesterol, PIP2, and traces of fluorescent PIP2, supported on mica. SLBs were formed on freshly-cleaved thin mica glued on a glass coverslip allowing both AFM (Fig. 2F) and fluorescence microscopy acquisitions (Fig. 2A–D).

80 nM GFP-tagged septins were added to the buffer surrounding the AFM tip under non polymerizing high salt conditions. The buffer was then exchanged to a lower salt solution, thus enabling septin polymerization. The bare control

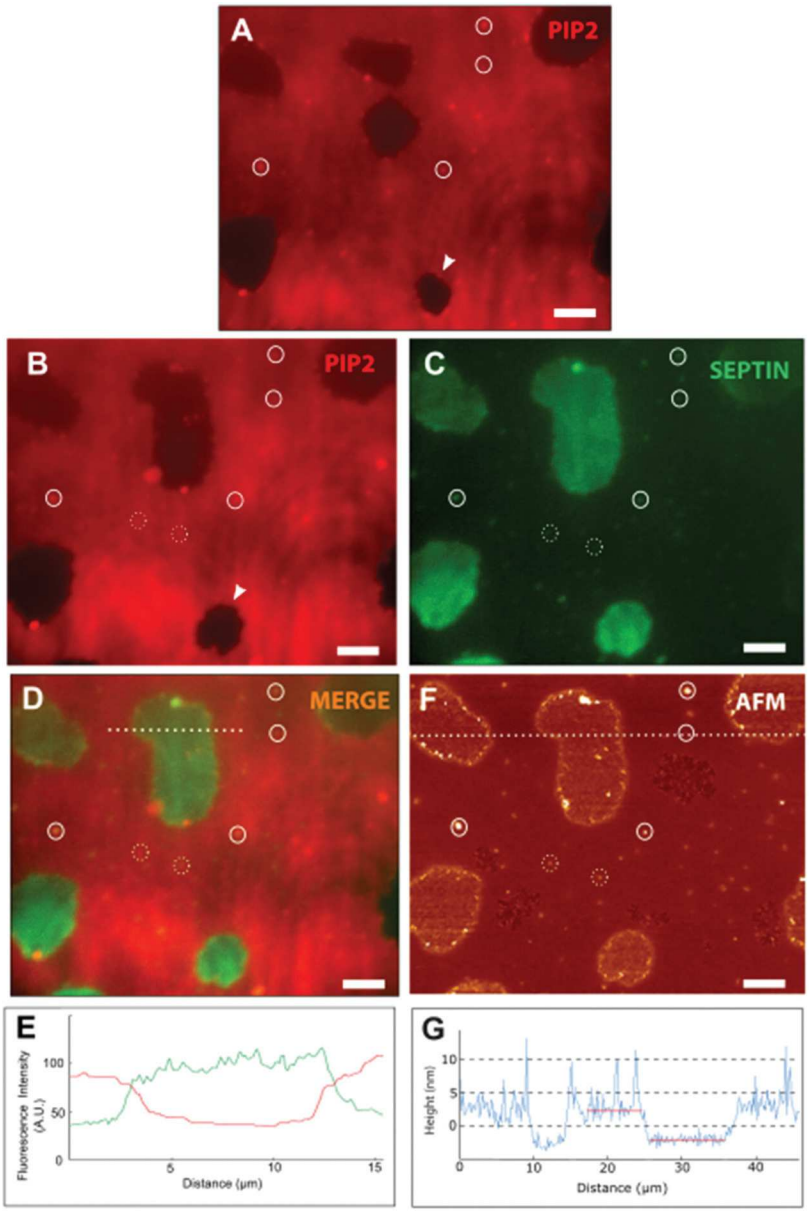

Fig. 2 AFM-fluorescence correlative microscopy of supported lipid membranes incubated with septin. SLB composed of EPC, DOPE, DOPS, Chl, PIP2 at 55 : 10 : 10 : 15 : 10 ratios supplemented with 0.1% GloPIP Bodipy C16 (PIP2 labeling in red) were observed using correlative TIRF-AFM microscopy before (A) or after (B to G) incubation with 80 nM septin GFP-septin. White empty circles are used as fiducial marks in the different images of the figure, including the control A. The white doted cercles are fiducial marks only observed after the addition of septin. Scale bar, 5 µm. (A) Fluorescence imaging of the SLB labelled with fluorescent PIP2 lipids (red signal) before septin incubation. The black holes correspond to membrane defects where mica is accessible. (B to D) Fluorescence imaging of the same area of the SLB after 15 min of incubation with GFP-septin. B and C respectively correspond to the red (PIP2) and green (septin) channels and D is the merge image. The majority of GFP-septin are bound to mica, accessible at membrane holes. In addition, GFP-septin molecules were also detected in interaction with the lipid membrane. Importantly, comparing the surface of the fluorescent patch of septins in C and the area of the holes in B indicates that septins and PIP2 lipids overlap and co-localize at the edge of the membrane (see the intensity profile of the green and red channels in E). After incubation with septin, an increase of the size of the holes into the SLB was observed (see the holes indicated by white arrowheads in A and B). (F) Height AFM image revealing that septins were forming assemblies on mica but also bound to the surface of the membrane, especially at the edge of holes (membrane defects). All the circles are localized at the top or within the SLB. The white line indicates the profile that is shown in G. Height scale, 70 nm. (G) Profile of image F (blue line). The difference between the 2 red lines used as marks is 3.8 nm, suggesting 3D stacking of septin oligomers.

membrane labeled with fluorescent PIP2 (red channel) was often non continuous with some defects (black patterns in the fluorescence micrograph shown in Fig. 2A), allowing the measurement of the bilayer thickness by AFM (>3.5 nm above the mica). Such defects are often observed for membranes containing negatively charged lipids. To minimize it, we added calcium to increase the yield of fusion of small vesicles used to form the SLBs.[29] After 15 min of incubation with GFP-septins, we observed a specific binding of proteins to mica, accessible at membrane holes (Fig. 2C), suggesting a higher affinity for charged mica than for membranes. Additionally, the surface of some of the mica holes in the SLB increases from Fig. 2A–B, suggesting that septins induce membrane remodeling by pulling out the membrane. Septins have been indeed shown to be capable of membrane reshaping on inducing periodic "spikes" on giant unilamellar vesicules or by flattening large unilamellar vesicles.[18] Importantly, we observed septin and PIP2 co-localization close to the edge of the membrane (see the fluorescence profile in Fig. 2E showing an overlap of the 2 channels at the edge of the hole) and also within clusters of PIP2 present before the addition of the protein (see the white circles in Fig. 2B and C and the merge image in 2D). This membrane remodeling was confirmed by AFM showing a corrugated pattern corresponding to septin oligomers surrounded by the smoother bilayer (Fig. 2F and G). Interestingly, the AFM resolution revealed that septins were forming clusters or assemblies on mica but also bound to the surface of the membrane (see empty circles in Fig. 2F), with a high density at their edges. The presence of septins in these clusters, which vary in size, was confirmed by the GFP fluorescence channel (compare Fig. 2C and F and see empty circles used as fiducial marks to compare the 2 fluorescence channels and the AFM image). The layer of septins coated on mica was protruding 3–5 nm above the surrounding membrane, suggesting a 3D stacking of septin oligomers (Fig. 2F and see a profile in Fig. 2G). For longer incubation times (Movie 2 and two snapshots of the movie in Fig. S2†), the GFP-septin signal indicated that both the surface area and the density of septins bound to mica increased over time (white arrowheads in Fig. S2†). The thickness measured by AFM was up to 16 nm (data not shown), strongly suggesting membrane remodeling and 3D stacking of septins. Movie 2† also confirmed the presence of clusters of septin accumulated at the surface of the membrane. Interestingly, filamentous structures up to 2.5 μm in length could also be observed over time. Those filamentous structures were often anchored to the membrane through a single point co-localized with the clusters mentioned above, with the rest of the filament floating in the buffer (Fig. S2B† and snapshots in Fig. S2C†). However, such filaments could not be imaged using AFM, probably because they were swept away during tip scanning, thus reinforcing the idea that septin filaments are sensitive to the resulting scanning force when imaged directly on mica.

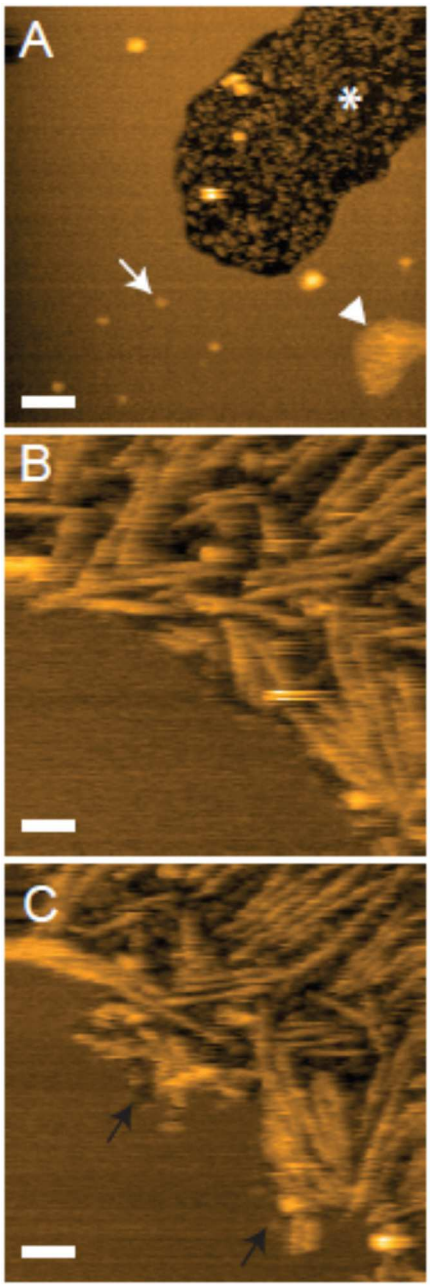

Fig. 3 Septin induces destabilization and remodeling of model membranes. SLB composed of EPC, DOPE, DOPS, Chl, PIP2 at 55 : 10 : 10 : 15 : 10 ratios were observed using HS-AFM in the presence of 80 nM septin in low salt buffer. (A) Height image (snapshot of Movie 3†) recorded at short incubation time (<15 min). The white asterisk indicates a hole (defect) within the bilayer covered by septin assemblies. The white arrowhead and white arrow point out assemblies protruding ~2 nm and ~10 nm above the membrane, respectively. Scale bar, 100 nm. B and (C) Height images recorded for long incubation (>15 min). Septin filaments were observed at the top of mica. C has been recorded 220 s after B and SLB remodeling can be easily observed (black arrows). Scale bar, 50 nm.

To assess the dynamics of both septin oligomerization and its ability to remodel membranes, we imaged SLBs with HS-AFM (Fig. 3 and Movie 3†). Under these conditions, for short incubation times (Fig. 3A), we imaged dynamic septin assemblies, directly interacting with mica, with a size in the range of 10 nm and protruding 2 to 5 nm above the mica. We

also observed round-shaped assemblies at the surface of the lipid bilayer, protruding up to 10 nm above the membrane (white arrow in Fig. 3A). In addition, we sometimes pinpointed larger patches protruding ~2 nm above the membrane (white arrowhead in Fig. 3A) that appeared to be very dynamic, as shown by the diffusion within the patch, likely septins (Movie 3†). The lateral dimensions of such patches could reach several hundreds of nanometers (Fig. 3 and Movie 3†). Because of the sensitivity of septin filaments to the force applied by the AFM tips as mentioned above, we never observed the formation of filaments below the AFM tip in the course of imaging. However, when scanning a neighboring area which had not been imaged yet, longer filaments at the top of mica were clearly observed (Fig. 3B), reinforcing the idea that the mechanical stress imposed by the AFM tip prevents septin polymerization. The length of these filaments varied, from a few tens to a few hundreds of nanometers (see the scatter plot in Fig. S3†). We observed the Brownian movement of these filaments with an amplitude inversely proportional to their length, probably due to their attachment to the substrate that is stronger for a long filament. Interestingly, imaging the same area after a few minutes (Fig. 3C) highlighted the membrane disruption induced by septin oligomerization (see the black arrows and compare with Fig. 3B). Real time membrane disruption that occurs within the intervals of a few minutes could also be observed in Movies 4 and 5.†

3D-organization of septin-lipid assemblies

HS-AFM imaging was able to capture 3D remodeling of membrane/septin assemblies (Fig. 4). The presence of both interacting partners in these arrangements was captured by fluorescence imaging of GFP-septins and red rhodamine-labelled lipids. We captured in real-time the spontaneous formation of doughnut-shaped structures from 2D lipid bilayer organization (Fig. 4A and Movie 6†). The starting structure in the first example was a membrane protruding 6 nm above the SLB underneath (see Movie 6†) that first bent along the main axis (white arrowhead in Fig. 4A1) and then reshaped to produce a

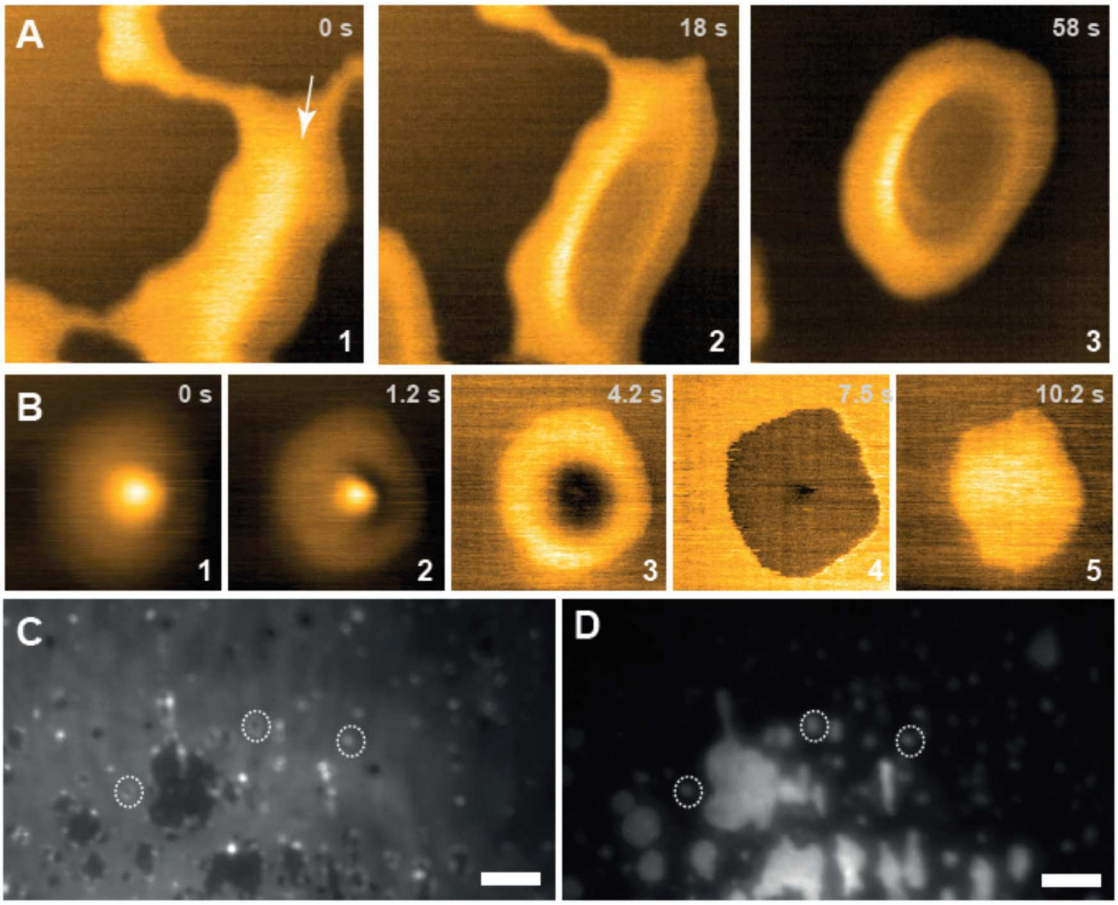

Fig. 4 Septin-induced reshaping of membrane forms doughnut-shaped structures. AFM imaging of SLB composed of POPC, POPE, POPS, PIP2 at 50 : 35 : 10 : 5 ratios after incubation with 80 nM septin. A and (B) HS-AFM height images of two different areas of the sample (A1 to A3, Movie 6,† and B1 to B5, movie not shown). Acquisition times of HS-AFM images are indicated at the upper right of each picture. The white arrow indicates bending of the membrane patch along the main axis (white arrowhead in Fig. 5A1) and its reshaping to produce a doughnut/ring shape of 1.1 μm diameter and 10–20 nm thickness within a few tens of seconds. Scan size 2 μm, Z scale, 20 nm (A) and (B). C and (D) TIRF fluorescent images of SLB supplemented with 0.1% GloPIP Bodipy C16; C and D respectively correspond to PIP2 and septin labeling after 60 min incubation. Images are z projections of 50 frames. The dashed circles indicate doughnut-shaped assemblies similar to A and B. Scale bar, 5 μm.

doughnut/ring shape of 1.1 μm diameter and 10–20 nm thickness (measured at different places on the ring as compared to the membrane underneath) within a few tens of seconds. The width of the loop varied between 150 nm and 250 nm. Importantly, following longer septin incubation times, we observed an increase in the number of doughnut-shaped structures. Some of them were smaller and thus probably resulted from different types of membrane organizations. We also frequently imaged "fried egg-shaped" structures lying on the lipid bilayer (see Fig. 4B1 and B2†). They could be reshaped by increasing the force during imaging into a "doughnut" shaped structure in Fig. 4B3† (350 nm protruding 5 nm above the bilayer). At higher forces, the doughnut was swept away, allowing the AFM tip to image mica (dark area in Fig. 4B4†) that was rapidly covered by septins forming a thick layer protruding from the lipid membrane (Fig. 4B5†). We confirmed the presence of doughnut-shaped structures on larger areas inaccessible with HS-AFM. Indeed, similar structures were also visualized using TIRF fluorescent microscopy (Fig. 4C and D) both in the PIP2 and septin fluorescent channels and ring-like structures of different diameters were also observed (Fig. 4C), the largest having diameters in the micrometer range, in good agreement with the rings observed in Fig. 4A with AFM. The dimensions of the smallest ones were difficult to estimate because of fluorescence microscopy resolution limitations.

These observations are consistent with the spontaneous curvature of membrane-bound septin filaments recently reported on giant unilamellar vesicles (GUVs) as well as with supported bilayer membranes on wavy substrates with locally varying curvature.[18] Such a curvature affinity stems from an increase in surface contact of septin filaments binding along their stretched (rather than compressed) side to the membrane.[18] This corresponds to a spontaneous negative curvature of membrane-bound septin filaments and filament bundles. The balance between binding energy gain and bending energy cost of membrane-bound septin filaments then leads to an optimum radii of curvature in the micrometric range, as well as a minimum radii in the sub-micrometric range, depending on filament bundle sizes.[18] Such a model is in good agreement with the ring like structures surrounded by membrane observed here (Fig. 4) and reminiscent of the ring-like structures observed *in vivo* at sites of constriction in living cells.

Finally, to address the effect of varying septin concentrations, we performed similar fluorescence microscopy experiments using higher 300 nM septin concentrations (Fig. 5 and Movie 7†). Immediately upon septin addition, a few thin and long filaments were observed (Fig. 5A) and the lipid bilayer appeared highly disrupted, with holes through which the surface of mica was apparent (black areas growing over time in Movie 7 and Fig. S4A and B,† white asterisk). In addition, septins accumulated at the lipid bilayer-mica interfaces and, after a few tens of seconds, tubes started arising from the surface of the bilayer, generally from a septin cluster (Fig. S4A and S4D,† white arrowhead). The tube diameters were

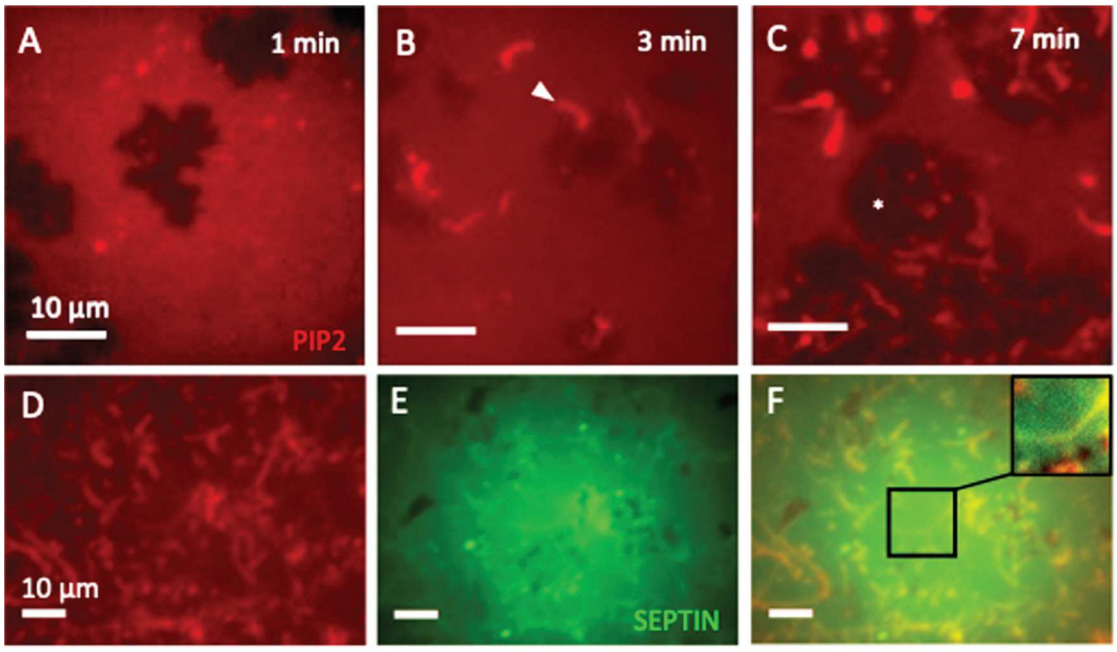

Fig. 5 Formation of membrane tubes from supported membranes induced by septin. Incubation of membranes composed of EPC, DOPE, DOPS, Chl, PIP2 at 55 : 10 : 10 : 15 : 10 ratios supplemented with 0.1% GloPIP Bodipy C16 with 300 nM septin and observed using confocal microscopy. Scale bar, 10 μm. A, B, C: fluorescence imaging (PIP2 red channel) upon septin incubation for 1, 3 and 7 min (A, B, C). The lipid bilayer supported on mica is remodeled leading to the formation of tubes (white arrowhead) at the expense of the membrane, suggesting that lipids are recycled within the visualized tubes (formation of holes within the SLB indicated by a white star). D, E, F: Fluorescence imaging of PIP2 (D, red channel), GFP-septin (E, green channel) and the merge image of the 2 channels (F). Both septins and PIP2 seem to colocalize along those tubes. The inset in F is a zoom as indicated by the black rectangle.

measured between 1 and 2 μm. As tubular structures formed, the surface of the bilayer continually decreased, suggesting that most of the bilayer, upon its interaction with a high density of septins, is largely altered and recycled within the visualized tubes (easily observable in Movie 7†). After about five minutes, the process seemed to reach an equilibrium. Hence, upon a higher septin density, the observed doughnuts reshape the membranes, converting them into tubes. In addition, both septins and PIP2 seem to colocalize along these tubes (Fig. 5D–F). A few rings and filaments were also observed in Fig. S4B (white arrow) and in Movie 7.† Interestingly, this behavior was not observed when similar bilayers were deposited on glass surfaces. When supported by glass, bilayers were not altered by septin addition likely due to a stronger interaction with the surfaces. Indeed, FRAP (Fluorescence Recovery After Photobleaching) indicated that PIP2 lipids move freely within a bilayer deposited on mica, while the diffusion of PIP2 molecules is constrained when embedded within a bilayer deposited on glass (data not shown).

Discussion

Until recently, septins have been considered primarily as scaffolding proteins enabling the establishment of diffusion barriers and recruiting different factors. However, our observations unambiguously demonstrate that septins can remodel and reshape membranes by remodeling supported lipid bilayers and generating peculiar deformations in 3D. Our findings are in agreement with previous bottom-up experiments where membrane deformations were directly induced by septins. Human septins were shown to generate tubulations from giant unilamellar vesicles.[30] Additionally, we have demonstrated that budding yeast septins can either trigger the formation of "spiky" structures on GUVs or flatten unilamellar vesicles.[18] Taken together, these observations suggest that septins might have a crucial and underestimated role in membrane reshaping in different cellular contexts and functions. Indeed, septins have been shown to be implicated in the formation of membrane protrusions in detached tumor cells.[31] Septins have also been shown to be involved in preserving the rigidity of the plasma membrane and tuning the plasma membrane morphology by reducing spontaneous membrane blebbing during cell motility.[32] Notably, the dimensions of the ring or tubular shapes observed in this report correspond to the dimensions of ring-like architectures of septins visualized at the constriction sites of budding yeast during cell division (hundreds of nanometers to 1–2 μm). Moreover, these micrometric curvatures are also found within metazoa at the base of cilia,[33] at the annulus of spermatozoa[34] or even at the base of dendrites[35] where septins localize. Hence, the spontaneous reshaping of membranes within tubular or ring (doughnut-like) architectures reflects the localization of septins *in situ* and a specific sensitivity to micrometric curvatures (see ref. 18 and 19). Even though the concentrations of septins used for bottom-up assays might be higher than septin densities *in situ*, we are nevertheless convinced that the observed reshaping is relevant. The concentration of septin in cell is not known. However, septin concentrate at the plama membrane and self-assemble. By analogy, the concentration of septin in our bottom assays reproduce this high concentration at the proximity of the membrane. Furthermore, in our hands, no other protein has ever displayed such an uncommon behavior. Importantly, septin and PIP2 are co-localized in both rings and tubes, questioning the driving force involved in both membrane remodeling and the formation of 3D structures. Septin subunits contain several basic residues, *e.g.* at the N-terminal that are candidates to interact with PIP2.[36] Such residues would concentrate locally PIP2 forming seeds for the filaments and larger assemblies of septin. In budding yeast, at the constriction site, the density of PIP2 is indeed enhanced.[37] This is in good agreement with small septin oligomers that were observed diffusing at the SLB surface and that immobilized over time (data not shown). In addition, as shown in Movie 7 and Fig. S4,† it is clear that the formation of tubes emerged from PIP2-enriched areas.

As observed by AFM, septin filaments are rather fragile and sensitive to piconewton forces applied by the AFM tip, either directly bound to mica (Fig. S1†) or in interaction with SLBs (septin swept away during scanning can be easily observed using correlative AFM-fluorescence microscopy, Movie 8†). The action of the AFM tip is indeed capable of displacing long septin filaments, fragmenting them and, to a certain extent, preventing septins from polymerizing. The polymerization of septins is thus highly sensitive to mechanical stress, suggesting that septin ultrastructures can be easily remodeled *in vivo* as well to undergo major conformational remodeling. However, septins are able to collectively remodel membranes in a spectacular fashion. Not only are membranes reshaped by long filamentous septins as described in several papers (see introduction) but it appears that short filaments or even septin protomeric rods can also disrupt membranes, as visualized by high-speed AFM. Small rods can enlarge holes by destabilizing the lipid bilayer (Movies 4 and 5†). Once a hole or a defect within the bilayer emerges, septin filaments seem sometimes to grow beneath the lipid bilayer to induce its detachment from the mica surface (data not shown). This does not exclude the possibility that septin–lipid interactions destabilize the lipid bilayer by perturbing membrane line tension. The visualized growing holes imaged by AFM are most likely coupled to the generation of 3D structures. However, the AFM tip certainly disrupts the tubes which are displaced and thereby cannot be detected by AFM. It is then tempting to propose that long septin filaments role may have been overestimated in membrane destabilization, at least at early stages of the process. Indeed, they were removed by tip scanning and were not visualized associated to doughnuts and tubes using either AFM or fluorescence microscopy, though we cannot completely exclude their presence in 3D structures. Octameric rods or small septin assemblies could be functional units involved in membrane remodeling, with the cellular cytosol acting as a reservoir of septins (cytosolic septins are in small com-

plexes[26]). This assumption is supported by our previous work showing septin-induced reshaping of GUVs, where no long filaments were observed to interact with the vesicle.[18] Our results also indicate that small oligomers are not sensitive to the curvature, whereas septin filaments sense nanometer or micrometer-scale curvature.[19] Indeed, we clearly observed that filaments can interact with flat membranes, and the preferential interaction of septin with curved membranes is probably valid only when proteins are organized in long filaments.

Conclusion

Taken together, our results clearly demonstrate that small assemblies/rods of septin can destabilize supported lipid bilayers and reshape the membrane to form 3D structures, reinforcing their role as membrane organizers when interacting with PIP2. This phenomenon, which is not energy-dependent, could be explained by the propensity of septins to form and/or bind PIP2-enriched clusters, inducing membrane bending through an increase in membrane pressure that cannot be counterbalanced by the tension in the plane of the membrane.[38]

Author contributions

P. E. M., A. B. and D. L. conceived the study. A. B. and C. T. purified the protein. A. V., L. C., C. T., C. G., H. N., K. X. N. and P. E. M. performed the AFM experiments. B. C. and S. M. performed some of the fluorescence microscopy experiments. H. I. contributed in interpreting the data. P. D. developed HS-AFM software. A. B., D. L. and P. E. M. interpreted the data and wrote the manuscript.

Conflicts of interest

The authors declare that they have no conflicts of interest with the contents of this article.

Acknowledgements

We acknowledge the support from FranceBioImaging (FBI, ANR10INSB04), the Agence Nationale pour la Recherche (ANR-13-JSV8-0002-01 Septime, ANR-16-CE11-0004-01 Neopore), and the EpiGenMed Labex (ANR-10-LABX-12-01) and the GIS IBISA (Infrastructures en Biologie Santé et Agronomie). AV is a recipient of the Fondation pour la Recherche sur le Cancer (ARC) and CT has been supported by Labex CelTisPhyBio (ANR-11-LABX0038). We are indebted to the Bio-AFM Summer School organized by the Nano Life Science Institute (WPI NanoLSI) in Kanazawa (Japan) led by Pr Toshio Ando, especially to Motonori Imamura (current address: Bio-AFM-Lab, Weill Cornell Medicine, New York, USA).

References

1 S. Mostowy and P. Cossart, *Nat. Rev. Mol. Cell Biol.*, 2012, **13**, 183–194.
2 A. Berlin, A. Paoletti and F. Chang, *J. Cell Biol.*, 2003, **160**, 1083–1092.
3 J. C. Adam, J. R. Pringle and M. Peifer, *Mol. Biol. Cell*, 2000, **11**, 3123–3135.
4 O. Palander, M. El-Zeiry and W. S. Trimble, *Front. Cell Dev. Biol.*, 2017, **5**, 36.
5 L. Dolat, J. L. Hunyara, J. R. Bowen, E. P. Karasmanis, M. Elgawly, V. E. Galkin and E. T. Spiliotis, *J. Cell Biol.*, 2014, **207**, 225–235.
6 C. Poüs, L. Klipfel and A. Baillet, *Front. Cell Dev. Biol.*, 2016, **4**, 126.
7 J. Pfanzelter, S. Mostowy and M. Way, *J. Cell Biol.*, 2018, **217**, 2911–2929.
8 M. Marttinen, K. M. Kurkinen, H. Soininen, A. Haapasalo and M. Hiltunen, *Mol. Neurodegener.*, 2015, **10**, 16.
9 N. F. Valadares, H. d' Muniz Pereira, A. P. Ulian Araujo and R. C. Garratt, *Biophys. Rev.*, 2017, **9**, 481–500.
10 A. Bertin, M. A. McMurray, P. Grob, S.-S. Park, G. Garcia, I. Patanwala, H.-L. Ng, T. Alber, J. Thorner and E. Nogales, *Proc. Natl. Acad. Sci. U. S. A.*, 2008, **105**, 8274–8279.
11 F. Jiao, K. S. Cannon, Y.-C. Lin, A. S. Gladfelter and S. Scheuring, *Nat. Commun.*, 2020, **11**, 5062.
12 J. Zhang, C. Kong, H. Xie, P. S. McPherson, S. Grinstein and W. S. Trimble, *Curr. Biol.*, 1999, **9**, 1458–1467.
13 A. Bertin, M. A. McMurray, L. Thai, G. Garcia, V. Votin, P. Grob, T. Allyn, J. Thorner and E. Nogales, *J. Mol. Biol.*, 2010, **404**, 711–731.
14 J. Dobbelaere and Y. Barral, *Science*, 2004, **305**, 393–396.
15 A. J. Tooley, J. Gilden, J. Jacobelli, P. Beemiller, W. S. Trimble, M. Kinoshita and M. F. Krummel, *Nat. Cell Biol.*, 2009, **11**, 17–26.
16 K. Song, G. Russo and M. Krauss, *Front. Cell Dev. Biol.*, 2016, **4**, 124.
17 Y. Tanaka-Takiguchi, M. Kinoshita and K. Takiguchi, *Curr. Biol.*, 2009, **19**, 140–145.
18 A. Beber, C. Taveneau, M. Nania, F.-C. Tsai, A. Di Cicco, P. Bassereau, D. Lévy, J. T. Cabral, H. Isambert, S. Mangenot and A. Bertin, *Nat. Commun.*, 2019, **10**, 420.
19 K. S. Cannon, B. L. Woods, J. M. Crutchley and A. S. Gladfelter, *J. Cell Biol.*, 2019, **218**, 1128–1137.
20 A. Beber, M. Alqabandi, C. Prevost, F. Viars, D. Levy, P. Bassereau, A. Bertin and S. Mangenot, *Cytoskeleton*, 2019, **76**(1), 92–103.
21 H. Nasrallah, A. Vial, N. Pocholle, J. Soulier, L. Costa, C. Godefroy, E. Bourillot, E. Lesniewska and P.-E. Milhiet, *Methods Mol. Biol.*, 2019, **1886**, 45–59.
22 D. E. Leckband, C. A. Helm and J. Israelachvili, *Biochemistry*, 1993, **32**, 1127–1140.
23 A. Berquand, D. Lévy, F. Gubellini, C. Le Grimellec and P.-E. Milhiet, *Ultramicroscopy*, 2007, **107**, 928–933.

24 S. Dahmane, C. Doucet, A. Le Gall, C. Chamontin, P. Dosset, F. Murcy, L. Fernandez, D. Salas, E. Rubinstein, M. Mougel, M. Nollmann and P.-E. Milhiet, *Nanoscale*, 2019, **11**, 6036–6044.
25 B. Seantier, M. C. Giocondi, C. Le Grimellec and P. E. Milhiet, *Curr. Opin. Colloid Interface Sci.*, 2008, **13**, 326–337.
26 A. A. Bridges, H. Zhang, S. B. Mehta, P. Occhipinti, T. Tani and A. S. Gladfelter, *Proc. Natl. Acad. Sci. U. S. A.*, 2014, **111**, 2146–2151.
27 E. A. Booth and J. Thorner, *Methods Cell Biol.*, 2016, **136**, 35–56.
28 E. A. Booth, E. W. Vane, D. Dovala and J. Thorner, *J. Biol. Chem.*, 2015, **290**, 28388–28401.
29 R. Richter, A. Mukhopadhyay and A. Brisson, *Biophys. J.*, 2003, **85**, 3035–3047.
30 M. Kinoshita, C. M. Field, M. L. Coughlin, A. F. Straight and T. J. Mitchison, *Dev. Cell*, 2002, **3**, 791–802.
31 K. Østevold, A. V. Meléndez, F. Lehmann, G. Schmidt, K. Aktories and C. Schwan, *Oncotarget*, 2017, **8**, 76686–76698.
32 J. K. Gilden, S. Peck, Y.-C. M. Chen and M. F. Krummel, *J. Cell Biol.*, 2012, **196**, 103–114.
33 Q. Hu, L. Milenkovic, H. Jin, M. P. Scott, M. V. Nachury, E. T. Spiliotis and W. J. Nelson, *Science*, 2010, **329**, 436–439.
34 M. Ihara, A. Kinoshita, S. Yamada, H. Tanaka, A. Tanigaki, A. Kitano, M. Goto, K. Okubo, H. Nishiyama, O. Ogawa, C. Takahashi, S. Itohara, Y. Nishimune, M. Noda and M. Kinoshita, *Dev. Cell*, 2005, **8**, 343–352.
35 H. Ewers, T. Tada, J. D. Petersen, B. Racz, M. Sheng and D. Choquet, *PLoS One*, 2014, **9**, e113916.
36 D. A. Brown, *Chem. Phys. Lipids*, 2015, **192**, 33–40.
37 L. S. Garrenton, C. J. Stefan, M. A. McMurray, S. D. Emr and J. Thorner, *Proc. Natl. Acad. Sci. U. S. A.*, 2010, **107**, 11805–11810.
38 J. Gilden and M. F. Krummel, *Cytoskeleton*, 2010, **67**, 477–486.

nature COMMUNICATIONS

ARTICLE

https://doi.org/10.1038/s41467-020-20596-0 OPEN

Structures of the archaerhodopsin-3 transporter reveal that disordering of internal water networks underpins receptor sensitization

Juan F. Bada Juarez [1,9], Peter J. Judge [1,9], Suliman Adam [2], Danny Axford [3], Javier Vinals[1], James Birch [3,4], Tristan O. C. Kwan [4,5], Kin Kuan Hoi [6], Hsin-Yung Yen[7], Anthony Vial [8], Pierre-Emmanuel Milhiet [8], Carol V. Robinson [6], Igor Schapiro [2], Isabel Moraes [4,5]✉ & Anthony Watts [1]✉

Many transmembrane receptors have a desensitized state, in which they are unable to respond to external stimuli. The family of microbial rhodopsin proteins includes one such group of receptors, whose inactive or dark-adapted (DA) state is established in the prolonged absence of light. Here, we present high-resolution crystal structures of the ground (light-adapted) and DA states of Archaerhodopsin-3 (AR3), solved to 1.1 Å and 1.3 Å resolution respectively. We observe significant differences between the two states in the dynamics of water molecules that are coupled via H-bonds to the retinal Schiff Base. Supporting QM/MM calculations reveal how the DA state permits a thermodynamic equilibrium between retinal isomers to be established, and how this same change is prevented in the ground state in the absence of light. We suggest that the different arrangement of internal water networks in AR3 is responsible for the faster photocycle kinetics compared to homologs.

[1] Biochemistry Department, Oxford University, South Parks Road, Oxford OX1 3QU, UK. [2] Fritz Haber Center for Molecular Dynamics Research, Institute of Chemistry, Hebrew University of Jerusalem, Jerusalem 9190401, Israel. [3] Diamond Light Source, Harwell Science and Innovation Campus, Didcot OX11 0DE, UK. [4] Research Complex at Harwell, Rutherford Appleton Laboratory, Harwell Science and Innovation Campus, Didcot OX11 0FA, UK. [5] National Physical Laboratory, Hampton Road, Teddington, London TW11 0LW, UK. [6] Chemistry Research Laboratory, Oxford University, Mansfield Road, Oxford OX1 3TA, UK. [7] OMass Therapeutics, The Schrodinger Building, Oxford Science Park, Oxford OX4 4GE, UK. [8] Centre de Biochimie Structurale (CBS), INSERM, CNRS, University of Montpellier, Montpellier, France. [9] These authors contributed equally: Juan F. Bada Juarez, Peter J. Judge. ✉email: isabel.moraes@npl.co.uk; anthony.watts@bioch.ox.ac.uk

Transmembrane (TM) receptor proteins are ubiquitous in biology. They enable cells to sense and to respond to their environment by undergoing conformational changes on ligand binding or light absorption. In addition to their active and resting states, several receptor proteins have a desensitized or inactive form, in which their responsiveness to external stimuli is reduced. Desensitization results in the uncoupling of the receptor from its downstream effectors, thus reducing the magnitude of the cellular response.

Desensitization is commonly achieved through reversible covalent or non-covalent modifications, which typically modulate intramolecular bonding networks, to stabilize a conformation which is distinct from the active resting or ground state of the receptor[1]. In the case of some G-protein coupled receptors (GPCRs), including rhodopsin and the β_2 adrenergic receptor[2], a Ser/Thr kinase phosphorylates residues on the cytosolic face of the protein, which promotes the recruitment of an arrestin that in turn blocks the binding site for Gα[3]. Other GPCR desensitization mechanisms involve changes in glycosylation patterns (e.g., for the dopamine D3 receptor[4]) and fatty acid conjugation (e.g., for the vasopressin receptor V2R[5]). In the case of ion channels, desensitization may occur in the persistent presence of a ligand[6] and may be achieved through a relatively subtle conformational change to produce a closed state, which is distinct from the resting state[7–9].

Archaerhodopsin-3 (AR3, from the archaebacterium *Halorubrum sodomense*) is a photoreceptor which, like all eukaryotic GPCRs, has seven TM helices. Although the wild-type protein is more usually classified as a light-driven proton pump, mutants of AR3 are commonly used in optogenetics experiments to enable individual neurons to be stimulated or silenced (by altering the permeability of the cell membranes to cations when illuminated at specific wavelengths) or as membrane voltage sensors[10–13]. AR3 is particularly suitable for these applications, since the protein has been suggested to have faster photocycle kinetics than many of its homologs[13] (including bacteriorhodopsin (bR) from *Halobacterium salinarum*), although the current produced by recombinant AR3 expressed in *Xenopus* oocytes has been measured as comparable to that of bR[14]. Development of AR3 mutants (commonly termed Arch in the optogenetics field) has been hampered both by the absence of high-resolution structural information[15–18] and by a lack of understanding of the mechanisms of receptor desensitization[19–22].

Although it is not a direct homolog of the Class A GPCR rhodopsin, AR3 undergoes a similar, highly ordered sequence of conformational changes (known collectively as the photocycle) after the ground state of the protein is stimulated by a photon of appropriate wavelength. To enable them to absorb light, the immature forms of AR3 and rhodopsin are modified after translation by the addition of retinal, which is covalently conjugated to a lysine sidechain via a Schiff Base (SB) linkage to produce the retinylidene chromophore. It is a light-induced change in the isomerization state of the retinal, detected by the surrounding receptor, that initiates the progression around the photocycle[23–25].

The desensitized form of archaeal, retinal-containing photoreceptors (the so-called dark-adapted (DA) state) is established in the absence of light and is characterized by a thermal equilibrium between at least two conformations, one with all-*trans* retinal (in common with the ground state) and the other with 13-*cis* 15-*syn* retinal. (Many of the early photocycle intermediates contain 13-*cis* 15-*anti* retinal[26–28].) To date, it has been unclear how the change in chromophore isomerization occurs with no apparent input of energy, to produce the DA state from the ground state or light-adapted (LA) state. It is also not clear why a thermal equilibrium between *cis* and *trans* retinal is established in the DA form, but only all-*trans* retinal is found in the LA state[26–29].

In this work, we have determined the crystal structures of the DA and LA states of the wild-type AR3 photoreceptor, solved to 1.3 and 1.1 Å, respectively. Our structures reveal the different conformations of the chromophore and the internal hydrogen-bonding networks that control the molecular mechanism of receptor desensitization and resensitization. Using quantum mechanical/molecular mechanical (QM/MM) approaches, our study explores the differences between the two states in both the activation energy barrier for conversion between *cis* and *trans* retinal, and also the equilibrium position between the two isomers. We propose that the apparent re-arrangement of internal water networks in AR3 may be a more general feature of receptor activation and deactivation beyond the family of archaeal photoreceptors.

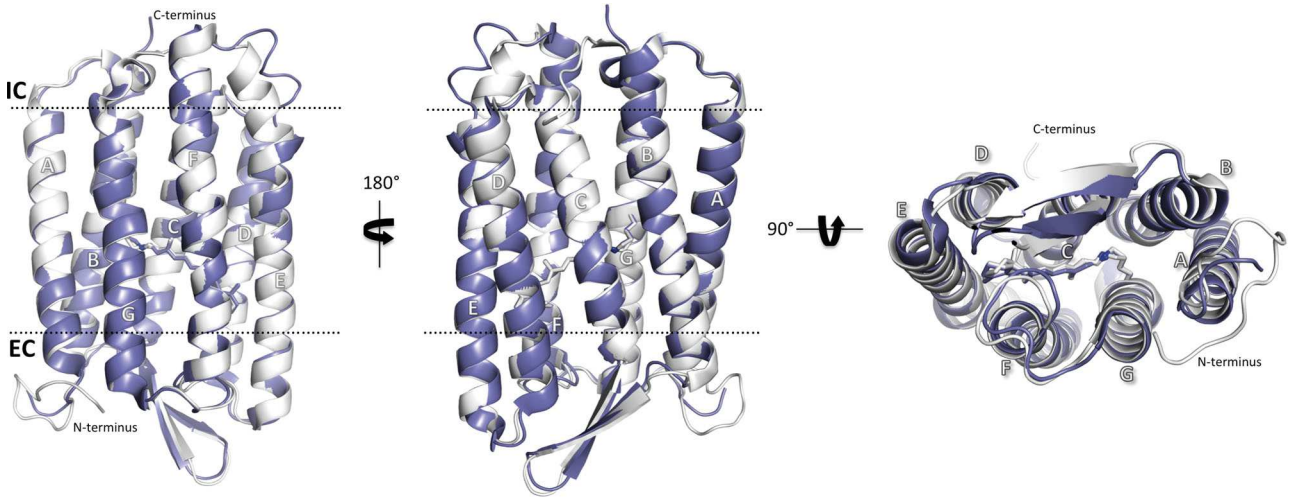

Fig. 1 Comparison of the light-adapted (LA) AR3 (6S6C [http://doi.org/10.2210/pdb6S6C/pdb], white) and bR (5ZIM [http://doi.org/10.2210/pdb5ZIM/pdb] purple) crystal structures. The approximate positions of the extracellular (EC) and intracellular (IC) membrane interfaces are shown as black dotted lines. The retinylidene chromophore (formed by the post-translational conjugation of retinal to a lysine sidechain) is shown in stick representation. The transmembrane helices (shown in ribbon representation) are labeled from A to G. The N termini of both proteins face the extracellular (EC) side of the membrane and the C-termini face the intracellular (IC) side.

Results

Crystal structures of the DA and LA states of AR3 solved at atomic resolution. Wild-type AR3 was purified from *H. sodomense* cells that had not been genetically modified and protein crystals were grown in lipidic cubic phase (LCP) (Supplementary Fig. 1)[30,31]. Both purification and crystallization of AR3 were performed in the absence of detergents ("Methods"). The LA ground-state structure of AR3 was solved from crystals which had been illuminated under a white tungsten light for two minutes prior to *cryo*-freezing. Crystals that had not been exposed to light were used to determine the structure of DA AR3. Diffraction data (Supplementary Fig. 1) from different crystals were merged to obtain the final data sets. Both structures were solved by molecular replacement using the coordinates of Archaerhodopsin-1 (AR1, 1UAZ [https://doi.org/10.2210/pdb1UAZ/pdb])[32] to a resolution of 1.3 and 1.1 Å for the DA and LA states respectively (Supplementary Table 1).

Similar to its homologs (including bR, with which it shares 59% sequence identity, Supplementary Fig. 2), AR3 has seven TM helices and a single, extracellular-facing, two-stranded β-sheet (Fig. 1), consistent with circular dichroism data (Supplementary Fig. 3a). In addition, retinal is covalently bound, via a SB to residue Lys226, thus creating the retinylidene chromophore. Ultraviolet-visible spectra suggest that AR3-rich membranes also contain a bacterioruberin pigment (Supplementary Fig. 3b); however, unlike in the case of Archaerhodopsin-2 (AR2)[33], this molecule could not be resolved from the residual electron density during refinement. Several lipid fragments and a large number of water molecules are also observed across the structures. Although crystallographic data shows one molecule in the asymmetric unit, atomic force microscopy images of patches of the claret membrane from wild-type *H. sodomense* cells (Supplementary Fig. 4) suggest that, like bR, AR3 is trimeric and forms a hexagonal lattice in the native organism[34].

Retinal is resolved in two conformations in each state. A striking aspect of the two high-resolution *cryo*-temperature structures is that the retinal conformations are very well resolved in both cases (Fig. 2 and Supplementary Fig. 5a, d). When all-*trans* or 13-*cis* retinal isomers are fitted at 100% occupancy for the DA and LA structures, strong positive and negative peaks from the calculated mF_{obs}–DF_{cal} maps are observed around the SB lysine and the β-ionone ring, suggesting a second retinal conformation (Supplementary Fig. 5) in each state.

In the DA state (6GUX [https://doi.org/10.2210/pdb6GUX/pdb]), 13-*cis* and all-*trans* retinal isomers are modeled into the electron density in a calculated occupancy ratio of 70% and 30%, respectively (Fig. 2, left). The isomer ratio observed in the AR3 DA structure is therefore similar to that previously reported from liquid chromatography studies for the DA state of other photoreceptor homologs (67%:33%)[35]. Although the positions of the carbon atoms nearest the SB (C12, C13, C14, C20) show the largest displacement when the isomers are compared, there are no significant differences in the positions of the SB nitrogen atom itself or the remainder of the Lys226 sidechain.

The conformations of the two retinal isomers in the 6GUX [https://doi.org/10.2210/pdb6GUX/pdb] structure were subsequently optimized using a QM/MM approach. The calculated structure of the *cis* isomer was in excellent agreement with the coordinates of the crystal structure. The calculated *trans* structure has a reduced twist along the main axis of the chromophore, when compared to the crystal structure, with the greatest discrepancies observed for the C10-C13 atoms in the retinal backbone as well as the C20 methyl group (Supplementary Fig. 6).

In the LA ground-state structure (6S6C [https://doi.org/10.2210/pdb6S6C/pdb]), retinal is resolved as two different conformations of the same all-*trans* isomer (Fig. 2, right), with relative occupancies of 75% and 25%. In this state, the greatest differences in atom position are observed in the Lys226 side chain (specifically Cδ) and the SB nitrogen atom. The calculated structures show an even larger difference between the two forms and suggest both a reduction in the axial twisting in the major conformation (trans1, Supplementary Fig. 6) and an increase in the twist in the minor conformation (trans2, Supplementary Fig. 6). The crystal and calculated structures are however in agreement that the significant difference in the position of the SB N atom is sufficient to cause a break in the H-bond to internal water molecule W402 (Supplementary Fig. 6).

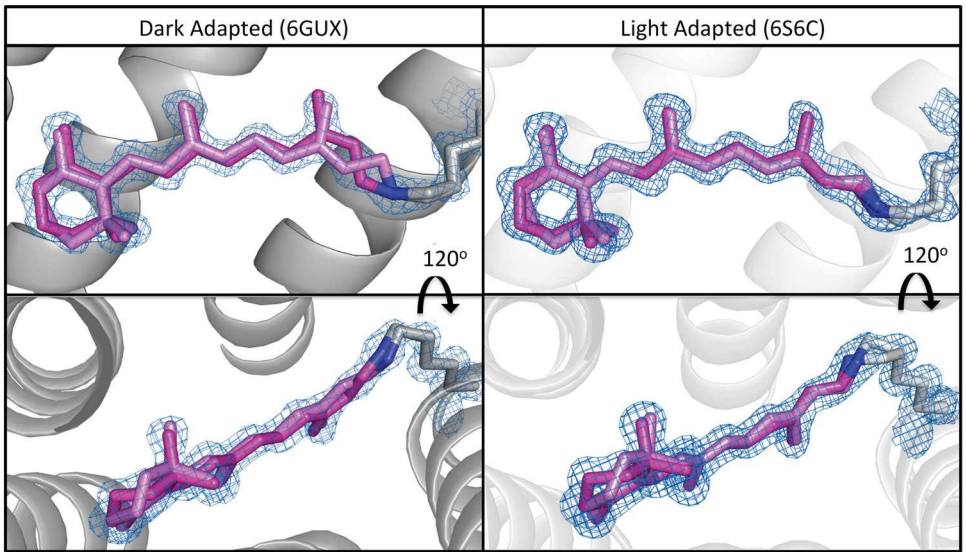

Fig. 2 Comparison of the conformations of retinal in the DA (6GUX [http://doi.org/10.2210/pdb6GUX/pdb]) and LA (6S6C [http://doi.org/10.2210/pdb6S6C/pdb]) states of AR3. In the DA state (left) the C13 = C14 retinal bond has been modeled with 70% *cis* and 30% *trans* isomers (colored in dark and light pink, respectively). In the LA state (right) retinal (colored in dark and light pink respectively) is modeled in the all-*trans* state only, but as two different conformers. Movement of the β-ionone ring is also observed in both structures. The $2F_{obs}$–F_{calc} electron density maps (blue mesh) around the retinal and Lys226 are contoured at 1.2σ.

Two variants of the puckering of the β-ionone ring are also observed in each crystal structure, characterized by a movement of the C3 atom of ~1.1 Å perpendicular to the plane of the ring (Supplementary Fig. 5a–f, left). The distance from C3 to Ser151 in the DA state is 3.4 Å for the *cis* form and 4.4 Å for the *trans* isomer. The changes in this part of the chromophore are also visible in the structures calculated by QM/MM (Supplementary Fig. 6). Nuclear magnetic resonance studies of inactive rhodopsin in the dark state also suggest that there is disorder around the C3 position of the β-ionone ring[36]. We therefore interpret this ring puckering (also observed in the calculated retinal structures, Supplementary Fig. 6) to indicate that this part of the chromophore is less constrained by the protein environment and is more disordered than has been previously reported in lower-resolution structures of homologs.

With the exception of the atoms in the β-ionone ring, the carbon skeleton (C6 to C15 inclusive) of the all-*trans* retinal in the DA state crystal structure, matches exactly the major conformation of the chromophore in the LA state. (There are significant differences in the position of the C atoms nearest the SB in the second conformation of all-*trans* retinal in the LA state.) There would therefore appear to be at least two independent mechanisms for receptor sensitization. In the first mechanism, the population of DA receptors with all-*trans* retinal may be directly stimulated by light to enter the photocycle. As this DA-*trans* population is depleted, the thermal equilibrium between the isomers acts to convert the 13-*cis* isomer and under continuous illumination produces a population of active LA AR3 proteins. A second mechanism is also proposed, in which the 13-*cis* population is capable of being excited under illumination to produce a 13-*trans*,15-*syn* chromophore, which then rapidly relaxes to the 13-*trans*,15-*anti* isomer observed in the ground or resting state. It would be possible for the two mechanisms to occur simultaneously and in parallel.

The SB electronic environment determines the relative stability of retinal isomers. The stability of the 13-*cis* and all-*trans* retinal in the two structures was compared by calculating the potential of mean force (PMF) for the rotation about the C13 = C14 double bond for all conformers (Fig. 3 and Supplementary Fig. 7). For DA AR3, the 13-*cis* isomer is energetically more favorable than the all-*trans* isomer ($\Delta G_{cis\text{-}trans} = -1.9$ kcal/mol), which is in qualitative agreement with the presence of the two isomers in the deposited crystal structure (with the *cis* isomer being the dominant species). In the case of LA AR3, the all-*trans* isomer is more stable, ($\Delta G_{cis\text{-}trans} = 10.9$ kcal/mol). The larger energy difference means that the 13-*cis* isomer is far less likely to be observed than the all-*trans* isomer in the LA state, consistent with the crystal electron density maps in which only all-*trans* retinal can be detected (Fig. 2). The activation energy for interconversion between the retinal isomers is calculated to be 4.4 kcal/mol higher for the LA form (21.5 kcal/mol) compared to the DA form (17.1 kcal/mol). These calculations are consistent with experimental observations of other microbial rhodopsins that show that, in the DA form, both retinal isomers can be found at room temperature, consistent with a thermal isomerization in the absence of light ($kT_{298K} = 0.59$ kcal/mol); however, in the LA form, absorption of a photon is required to convert between the two isomers[37,38].

Finally, although the position of the SB nitrogen atom of retinal appears to change little between the *cis* and *trans* forms in the DA structure (6GUX [https://doi.org/10.2210/pdb6GUX/pdb], Supplementary Fig. 5b,c), a subtle movement of 0.5 Å in the position of the same atom in the LA structure (6S6C [https://doi.org/10.2210/pdb6S6C/pdb]) is observed (Supplementary Fig. 5e,f). Similarly, the Lys226 side chain is resolved in only one position in the DA structure (Fig. 2 left and Supplementary Fig. 5a–c), whereas in the LA structure this side chain is resolved in two conformations (see Fig. 2 right and Supplementary Fig. 5d–f). In the LA state, these sidechain movements allow the SB nitrogen atom to approach to within 2.9 Å of the Thr99 side chain and may support an H-bond at this position, which is not achievable in the DA state (Supplementary Table 4). Since there is no significant change in the position of the hydrophobic residues that line the retinal binding pocket (including Tyr93, Trp96, Leu103, Met155, Trp192, and Trp199), it would appear that the differences in the relative stabilities of the *cis* and *trans* retinal isomers in the DA and LA states are solely dependent on the different electronic environments around the SB[39].

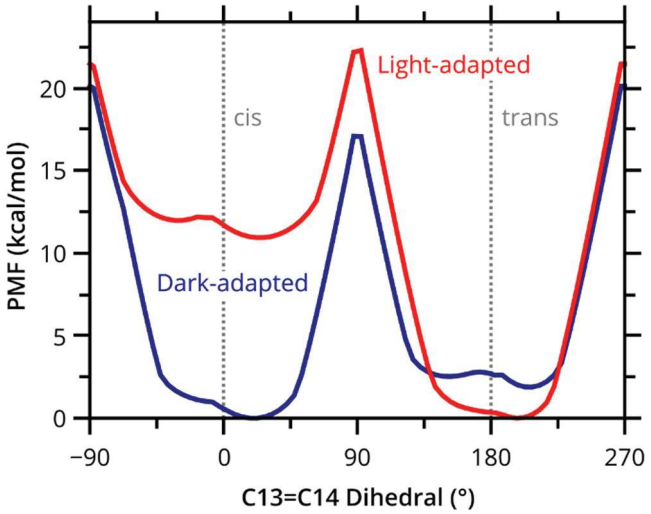

Fig. 3 Calculated potentials of mean force (PMF) for the isomerization of the C12–C13 = C14–C15 dihedral of retinal in DA (blue) and LA (red) AR3. The PMF was computed by sampling the retinal isomerization from all-*trans* to 13-*cis* and vice versa. Each point on the curve is generated from two independent 0.5 ns QM(SCC-DFTB)/MM MD trajectories, initiated from two separated equilibrated starting structures. The protein backbone was fixed in place; however, all other atoms (including those in the chromophore and amino acid sidechains) were allowed to move.

The SB N atom position influences internal water dynamics. Light-driven proton pumps such as AR3 rely on a precisely coordinated network of internal water molecules to mediate proton translocation across membranes[37,38]. The movement of internal water molecules in bovine rhodopsin has previously been shown, using MD simulations, to respond to changes in chromophore conformation[40]. As in bR, both the LA and the DA structures of AR3 reveal a "quasi-planar" pentagonal hydrogen-bonding network in the SB region, formed by three internal water molecules (W402, W401, and W406) and two negatively charged sidechains (Asp95 and Asp222) (Fig. 4a, b and Supplementary Fig. 8)[41–45]. This region is known to undergo structural changes during the early stages of the microbial rhodopsin photocycle and plays a key role in the transfer of an H^+ ion from the protonated SB to the proton release complex (PRC)[41–45]. By comparing the occupancies and static positions of water molecules and amino acid side chains resolved in the two *cryo* crystal structures, we can infer information about their likely dynamics at physiological temperatures.

Close inspection of the structures reveals the coupling between the chromophore and the pentagonal H-bond network. The greater ambiguity in the position of the retinal SB N atom in the AR3 LA state, compared with the DA state, would appear to

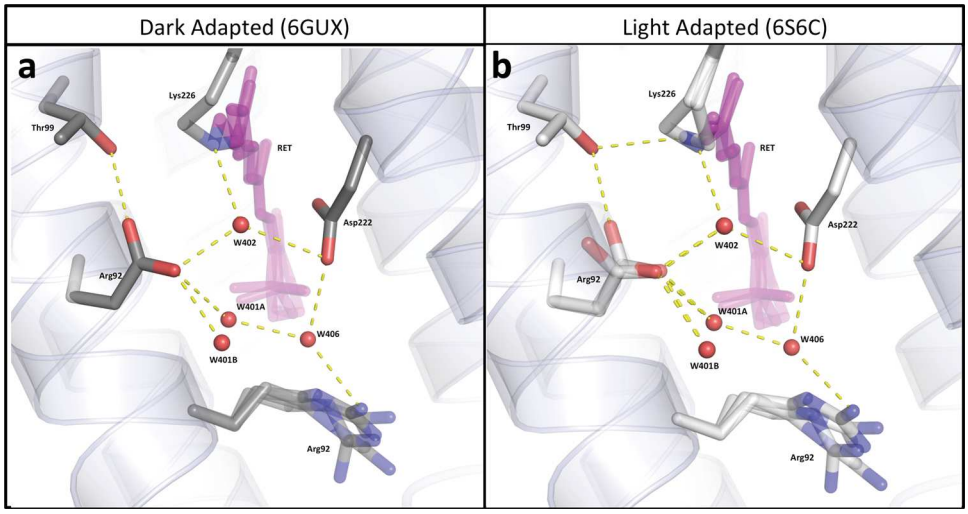

Fig. 4 Structures of the pentagonal H-bond networks in AR3. Predicted H-bonds are represented by yellow dashes (for distances see Supplementary Table 4) for DA (**a**) and LA AR3 (**b**). Selected amino acid sidechains are shown in stick representation with atoms colored using the CPK convention. Water molecules are shown as red spheres and retinal is colored pink. Wat401 is seen in two positions (A and B) at partial occupancy and the sidechain of Arg92 is seen in four conformations for both AR3 structures. Wat402 has single occupancy in AR3 (b) and bR (Wat602 in Supplementary Fig. 8b) in the LA state.

influence the order of the internal water molecules, both directly through W402 and indirectly via Thr99. Although W402 is well resolved in the 6GUX [https://doi.org/10.2210/pdb6GUX/pdb] structure, positive and negative electron density features are observed for this molecule in the 6S6C [https://doi.org/10.2210/pdb6S6C/pdb] structure confirming that it is more disordered in the LA state. In addition, in the AR3 LA state, the Asp95 side chain (which makes a direct H-bond to W402) is seen in two conformations and conversion between the two rotamers appears to involve the making/breaking of an H-bond with Thr99. It is possible that the stronger interaction that the SB N atom makes with the Thr99 side chain in the AR3 LA state, compensates for the partial breaking of the Asp95-Thr99 H-bond.

A second water molecule (W401) in the pentagonal network forms a H-bond to Asp95 and is also coupled to the chromophore isomerization state. In both AR3 structures, W401 is seen in two positions (A and B) ~1.5 Å apart (Fig. 4a, b), whereas in most bR ground-state structures[46], it is only present in one position (matching the W401B position in 6GUX [https://doi.org/10.2210/pdb6GUX/pdb] and 6S6C [https://doi.org/10.2210/pdb6S6C/pdb], Supplementary Fig. 9). In part, this difference in mobility appears to arise from the sequence Ser64-Ala65-Ala66 on Helix B of AR3, which replaces Phe67-Thr68-Met69 in bR and releases additional space to accommodate W401 oscillations. However, the mobility difference is also dependent on the order of the Asp95 side chain, since the relative occupancies of the two positions of W401 change between the two states of AR3. The Asp95-W401-W406 bond angle is increased to 146.5° in the LA state (compared to 140° in the DA state, Supplementary Table 5) further destabilizing the pentagonal H-bond network. The disorder observed in W401 (Supplementary Table 3) is consistent with previous Fourier-transform infrared spectroscopy (FTIR) experiments, which have suggested greater movement of W401 in AR3 than in bR[29]. It is interesting to note that W401 and $Thr89_{bR}$ are implicated in maintaining the $Asp85_{bR}$ sidechain pKa at ~2.2[47] and weaker equivalent bonds in AR3 would be consistent with a higher pKa for $Asp95_{AR3}$.

Classical MD simulations were used to evaluate the positions of water molecules in the vicinity of the SB, as observed in the crystal structures (Supplementary Figs. 9 and 10). An additional mobile water molecule is predicted in the vicinity of Asp95 in the LA form and also possible in the DA-*cis* retinal structure. These discrepancies are interpreted as confirming the considerable disorder in the hydrogen-bonded water network, especially in the LA form, and could explain why larger currents are produced by the protein when expressed recombinantly in neurons, compared with other rhodopsins such as bR and halorhodopsin[13].

Although it does not directly form part of the pentagonal network of H-bonds, Arg92 stabilizes this arrangement by forming an H-bond to W406 from its Nε atom. In bR, the angle of the side chain ($Arg82_{bR}$) alters between the DA and LA states, pointing more towards the PRC in the latter (Supplementary Fig. 8)[46]. In contrast, in both the AR3 LA and DA states, Arg92 is resolved in four conformations, with similar occupancies and amplitudes of motion (Fig. 5). It therefore appears that changes in the rotamer populations of this residue do not provide a significant contribution to the transition between DA and LA states in AR3.

Network of H-bonded water molecules between Arg92 and the PRC. Several water molecules form a complex H-bond network between the two Glu residues (Glu204, Glu214) that together form the PRC on the extracellular face of AR3, and Arg92 (Fig. 5 and Supplementary Fig. 11). Several water molecules are resolved with partial occupancy, and the different conformations of Arg92 appear to stabilize different H-bonded networks that lead to the two Glu residues (Supplementary Fig. 11). The complexity of H-bonds in this region is possible because of a larger cavity in AR3 than bR. We suggest that this extensive water molecule network forms multiple interconnected pathways, which would appear to allow H^+ transfer from the SB region to the PRC, independent of the orientation of the Arg92 sidechain. In bR, H^+ release to the extracellular medium occurs during the M-state (which is itself divided into three substates)[48] and previous FTIR data have suggested that the differences in the organization of water molecules between bR and AR3 are even more pronounced in the M and N states than in the ground state[49]. We therefore suggest that the water-mediated parallel pathways for ion transfer, observed in the ground state, play a significant role in later photocycle stages and might reduce the time taken for H^+ release and uptake.

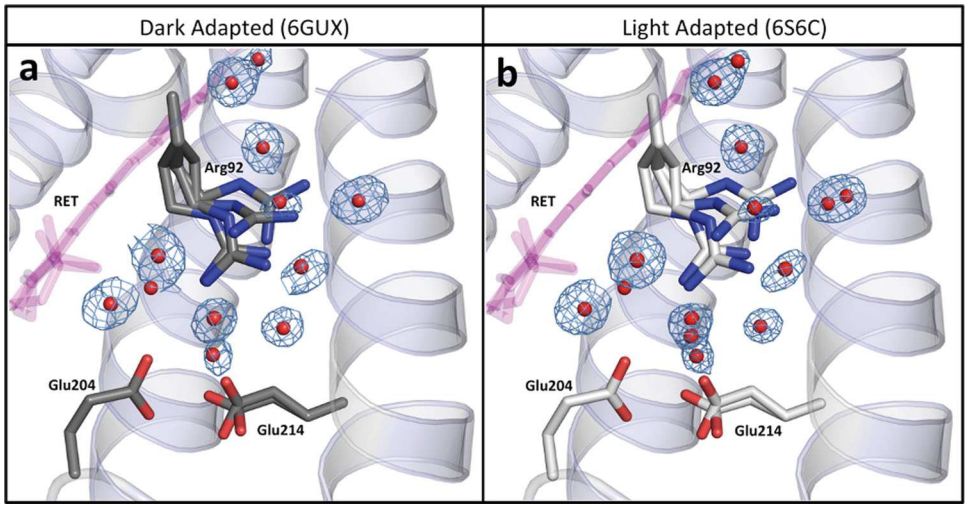

Fig. 5 Structures of the Proton Release Complex (PRC) of AR3. Glu204, Glu214 and the associated network of H-bonded water molecules in DA (6GUX [http://doi.org/10.2210/pdb6GUX/pdb]) (**a**) and LA AR3 (6S6C [http://doi.org/10.2210/pdb6S6C/pdb]) (**b**). Selected amino acid sidechains are shown in stick representation with atoms colored using the CPK convention. Water molecules are shown as red spheres and retinal is colored pink. The $2F_{obs}$–F_{calc} electron density maps (blue mesh) around the water molecules are contoured at 1.2σ.

The PRC is highly conserved across microbial rhodopsins. In a recent high-resolution structure of bR (5ZIM [https://doi.org/10.2210/pdb5ZIM/pdb]), both glutamate side chains are observed in different conformations, with rotations about the Cβ-Cγ and Cγ-Cδ bonds. In both the AR3 DA and LA structures, only Glu214 is present in two conformations (at 0.5 partial occupancies), distinguished by an 87.4° rotation around the Cγ-Cδ bond (Fig.5). In AR3, the distances between the two Glu214 sidechain conformations and Glu204 is 2.3 Å (consistent with the distance previously reported for AR2) and 2.9 Å. Free-energy QM/MM calculations suggest that in both the DA and LA states, Glu214 is most likely to be protonated and that the Glu204 side chain is fully ionized, as observed in the ground state and early photo-intermediates in bR (Supplementary Fig. 12).

Post-translational modifications and lipid binding. Post-translational modifications of the protein were identified using nano electrospray ionization mass spectrometry (nESI MS) with protein solubilized in detergent (*n*-Octyl-β-glucoside) (Supplementary Fig. 13). An exact mass of 27,238 ± 0.9 Da for AR3 was determined, implying an extensively modified N terminus, with the removal of Met1-Leu6 and the conversion of Gln7 to a pyroglutamate (PCA) residue, as previously reported for bR[50,51] (Supplementary Figs. 13–15). Our AR3 structures reveal the post-translational modification of the N terminus, in agreement with the MS data. In addition, the nESI MS data suggests that the C terminus is also truncated with the removal of Asp258 (Supplementary Figs. 13 and 15); however, this region is not resolved in the structures presented here.

A non-covalent ligand with a mass of 1.06 kDa was observed bound to AR3 by MS and is most likely the archaeal lipid 1-*O*-[6"-sulfo-α-D-Mannosyl-1"-2'-α-D-Glucosyl]-*sn*-2,3-di-*O*-phytanylglycerol (S-DGD) (Supplementary Fig. 13b, c). This lipid is thought to stabilize the lipid bilayer during changes in osmolarity[52,53] and has been suggested as a proton donor for microbial rhodopsins[54,55]. S-DGD could not be resolved from the electron density of either of the AR3 structures presented here.

Omega loop. A so-called "omega loop structure" (formed by residues Asp11–Arg17) is observed in both crystal structures, the sequence of which (DLLxDGR) is highly conserved between archaerhodopsins (Fig. 6). This loop appears to form a binding site for an Na^+ ion, which coordinates with polar groups on the peptide backbone. During a 300 ns MD simulation, the ion was observed to exchange with water several times, without perturbing the conformation of the protein. We therefore conclude that Na^+ is not essential for maintenance of the loop structure, consistent with the deposited crystal structure of AR2 (3WQJ [https://doi.org/10.2210/pdb3WQJ/pdb]), in which water is modeled at this position[56].

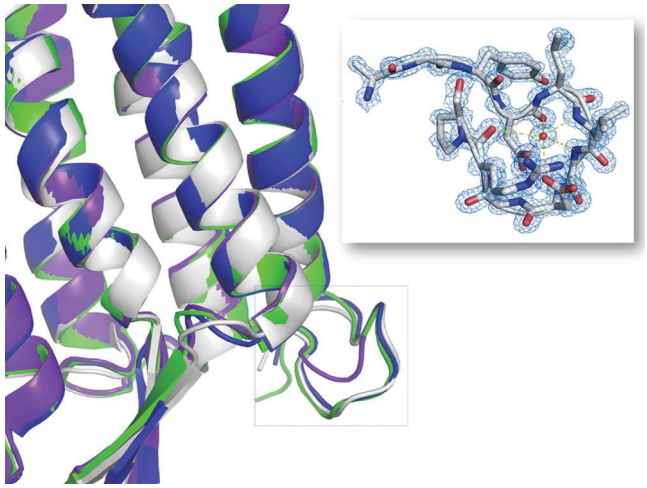

Fig. 6 Comparison of the structures the N termini of AR3 and related microbial rhodopsins. Overlay of structures of bR (5ZIM [http://doi.org/10.2210/pdb5ZIM/pdb] purple), AR1 (1UAZ [http://doi.org/10.2210/pdb1UAZ/pdb] green), AR2 (3WQJ [http://doi.org/10.2210/pdb3WQJ/pdb] blue), and LA AR3 (6S6C [http://doi.org/10.2210/pdb6S6C/pdb], white) showing the extracellular-facing omega loop, which is present in AR1, AR2, and AR3 but absent in bR. The inset shows details of the 6S6C [http://doi.org/10.2210/pdb6S6C/pdb] AR3 omega loop. Amino acids are shown in stick representation with atoms colored using the CPK convention. The $2F_{obs}$–F_{calc} electron density map (blue mesh) is contoured at 2.3σ.

In AR2, the omega loop has been proposed to form the intracellular end of the bacterioruberin binding site, which runs orthogonal to the membrane between helices E and F[32,33]. In the LA AR3 structure, the analogous site is partially occupied by lipid

tails and is occluded near the center of the membrane by the Phe150 side chain. We cannot exclude the possibility that the absence of the second chromophore in the structures reported here is an artifact of the crystallization process. Loss of bacterioruberin may also have induced monomerization of the protein during crystallization, although the crystals obtained do have the characteristic scarlet color observed in the native membranes (Supplementary Fig. 1).

Discussion

The archaeal photoreceptor AR3 harvests energy from sunlight to transport H^+ ions from the cytoplasm of *H. sodomense* cells to the extracellular medium, creating a TM proton gradient for ATP synthesis. Like other members of the microbial rhodopsin superfamily, it has seven TM helices, which are arranged to create an internal channel linking the two sides of the membrane[37,38]. The crystal structures presented here, show that this channel is occluded by the retinylidene chromophore, which is formed by the post-translational, covalent conjugation of retinal to Lys226 via a SB. The water molecules within the channel form strong H-bonds to the conserved residues (including Arg92, Asp95, Asp106, Glu204, and Glu214), which are implicated in the mechanism of ion transport. Two AR3 structures have been determined. The first (6S6C [https://doi.org/10.2210/pdb6S6C/pdb]), which contains two forms of all-*trans* retinal, corresponds to the LA ground state. The second (6GUX [https://doi.org/10.2210/pdb6GUX/pdb]), which corresponds to the desensitized DA state, includes both 13-*cis* and all-*trans* retinal in a 7:3 isomer ratio.

A comprehensive understanding of the mechanism of photoreceptor desensitization has been hampered by the absence of high-resolution crystal structures of the DA forms of microbial rhodopsins. Long-standing questions in the field have concerned the energetics of the transformation from the LA ground state to the DA state and, in particular, how the thermodynamic equilibrium between all-*trans* and 13-*cis* retinal in the DA state is established in the absence of light and with no apparent input of energy. (There is limited structural data for the DA states of other microbial rhodopsins and the only DA crystal structure currently deposited in the PDB is for bR[27,57].) It is perhaps surprising that, in AR3, there are minimal changes in the positions of the side chains that line the retinal binding pocket between the two states and it would therefore appear that the favoring of the *cis* isomer in the DA state, does not arise from changes in the binding energy of the chromophore. Instead, our QM/MM calculations (which use the crystal structures as a starting point) show that the subtle changes in partial charge distribution around the SB (in the low dielectric environment of the center of the membrane) and the lower mobility of the Lys226 sidechain in the DA form, reduce the activation energy for retinal isomerization (compared to the LA form). Our calculations also show, that the difference in energy between *cis* and *trans* retinal is approximately ten times less in the DA form than the LA form, consistent with the thermodynamic equilibrium between the two isomers, observed in the DA states of several microbial rhodopsins.

These crystal structures also allow us to gain a better understanding of the extent to which the conformation of the chromophore is coupled to the networks of internal water molecules. The movement of the SB nitrogen atom in the LA state appears to destabilize the quasi-planar pentagonal network of H-bonded groups—directly via W402 and indirectly via Thr99 and Asp95. From this study alone, it is not clear the extent to which the observed differences in this region between the DA and LA states are important for the mechanism of proton pumping. Although we can be confident from the all-*trans* retinal, that the LA crystal structure presented here does indeed correspond to the AR3 ground state, it shares some features with the early intermediates of the bR photocycle: first, time-resolved X-ray free-electron laser experiments on bR have shown that, in the 100 s fs after light absorption, Wat402 is displaced away from the SB nitrogen atom[43]. Second, the H-bond between $Thr89_{bR}$ and $Asp85_{bR}$ ($Thr99_{AR3}$-$Asp95_{AR3}$), which breaks during the formation of the bR M-state[41], is already partially broken in the ground state LA AR3 structure. Third, Wat401 becomes disordered within 13.8 µs of photon absorption in bR[42], whereas this molecule is resolved in two distinct positions in both AR3 structures reported here. We would therefore suggest that the AR3 ground state is "more advanced" in photocycle terms than the bR ground state and that this might have an influence on the kinetics of ion transport.

Atomic force microscopy images of the *H. sodomense* claret membrane (Supplementary Fig. 4) indicate that AR3 is a trimer in vivo; however, the structures presented here are monomeric and were obtained from a three-dimensional crystal in which packing between adjacent molecules differs from that of the native environment. Several studies have examined the functional differences between monomeric and trimeric forms of the microbial rhodopsins and of bR in particular. The dissociation of oligomers is generally characterized by a hypsochromic shift in the absorption spectrum, which is primarily caused by the loss of exciton coupling between the chromophores, rather than by structural changes within the monomers[58–60]. Although the photocycles of monomeric and trimeric bR are qualitatively the same[61,62], the kinetics of individual steps vary, in particular those later stages that involve larger conformational changes[63]. Dencher et al.[64] reported that the equilibrium position between 13-*cis* and all-*trans* retinal in DA bR is perturbed by monomerization. The dissociation of AR3 oligomers will inevitably alter the interactions between the individual molecules and their environment. This may, in turn, perturb the behavior of dynamic structural elements within the interior of the protein, including amino acid side chains (thereby influencing their protonation state), water molecules and the chromophore itself. It is therefore essential that structures of DA microbial rhodopsins, crystallized as trimers, be obtained in order to determine the influence of oligomerization state on the mechanisms of receptor desensitization and resensitzation.

We have attempted to mitigate the effects that the crystallization process might have on the LA and DA states of AR3, by preparing wild-type protein, expressed in its native organism and purified without any detergents that might remove closely associated native lipids and bacterioruberin. We have crystallized the protein in LCP, to provide an environment which more closely resembles the native membrane than can be provided by micelle-based methods. Although our QM/MM calculations are in qualitative agreement with the expected chromophore isomer ratio, we cannot exclude the possibility that crystal contacts influence the conformational flexibility of the protein and that this might give rise to non-physiological behavior.

The structures of DA and LA AR3 presented here, also have implications for our wider understanding of the process of desensitization in other receptor families. They highlight how minimal displacements of charged and hydrophilic groups within the low dielectric environment of the membrane can induce changes in ligand conformation and vice versa. Finally, these structures also provide information that increases our understanding of the mechanism of H^+ translocation by AR3, and will facilitate the design of further, more efficient Arch mutants for applications in optogenetics.

Methods

Protein expression and purification. *H. sodomense* (ATCC-33755) cells were purchased from LGC Standards Ltd (Teddington, UK) and were grown without any genetic modification (see Supplementary Information). Cells were collected by centrifugation (8000 × *g*; 30 min; 4 °C) and the pellets were resuspended in 4 M NaCl and DNAse I (Sigma, UK). The solution was stirred for 2 h before being manually homogenized. The preparation was dialyzed overnight in 0.1 M NaCl, and centrifuged (70,000 × *g*; 50 min; 4 °C). Sucrose density gradient ultra-centrifugation was used to isolate the AR3-rich membrane, using a step gradient consisting of layer of 4 mL of sucrose at densities of 30, 40, 50, and 60% w/v, and centrifuged at 110,000 × *g* for 15 h at 15 °C. The lower band with a pink/purple color was collected, and the sucrose remaining in the sample was removed through overnight dialysis against distilled water. The sample was then further centrifuged (70,000 × *g*, 50 min, 4 °C), and the pellet was resuspended in distilled water to a final concentration of 20 mg/ml. Using SDS-polyacrylamide gel electrophoresis, the AR3 content of the samples was estimated to be 78 ± 2% (w/w) of the total protein, which is comparable to bR purified by the same method[65,66]. Samples were stored at 4 °C prior to spectroscopic experiments and crystallization.

Crystallization in LCP. The non-delipidated AR3 protein sample was mixed with molten monoolein lipid (Nu-Check) in a 40:60 volume ratio using two gas-tight Hamilton syringes connected by a TTP Labtech syringe coupler[67]. The LCP mixture was dispensed onto a 96-well glass crystallization plate using a TTP LCP-Mosquito crystallization robot (TTP Labtech) at 18/1 ratio (540 nL reservoir + 30 nL of LCP). The LCP plate was sealed with a glass cover and stored at 20 °C. All crystallization procedures were performed under dim light.

Crystals of AR3 appeared after 2–3 days in a precipitant solution containing 30% v/v polyethylene glycol 600 (Fluka Analytical), 100 mM MES buffer pH 5.5, 150 mM NaCl, and 150 mM Ca^{2+} (Supplementary Fig. 1a). Crystals were collected using Dual-Thickness MicroMounts *cryo*-loops (MiTeGen, Ithaca USA), then flash-frozen and stored in liquid nitrogen.

X-ray data collection and processing. X-ray data were collected from different crystals at 100 K on the I24 microfocus beamline at Diamond Light Source (Harwell, UK) using a beam size of 6 µm × 9 µm and a Pilatus3 6 M detector (DECTRIS).

Diffraction patterns were integrated using DIALS (version 1.10.1) and several data sets were all combined using BLEND (version 0.6.23)[68] with default parameters. The diffraction data from individual crystals were integrated using the Xia2 pipeline (0.3.8.0)[69] running DIALS and then, in a separate step, merged using AIMLESS (version 0.0.14)[70]. Phases for the AR3 *cryo* structures were obtained by molecular replacement using the Phaser software (version 2.7.17) from the CCP4 Suite (version 7.0.066)[71] with the deposited structure for AR1 (1UAZ [https://doi.org/10.2210/pdb1UAZ/pdb][32]) as the search model. The initial electron density maps were inspected, and the model was built using Coot (0.8.9.1)[72,73]. The structure models were refined using PHENIX (version 1.18.2)[74] and Refmac5[75]. Retinal occupancy ratio for both structures were determined using several tools such as occupancy refinement in PHENIX[74], observation of the retinal B factors before and after refinement (using different occupancies values), observation of the calculated mF_{obs}–DF_{calc} maps corresponding to each occupancy value and ligand validation tools in PHENIX, Coot, and wwPDB[76,77]. In the deposited PDB files, amino acid residues were numbered according to the deposited UNIPROT sequence BACR3_HALSD and water molecules were numbered following the convention used in the 1C3W [https://doi.org/10.2210/pdb1C3W/pdb] structure for bR.

QM/MM optimization. Each of the two retinal conformations found in the DA and LA crystal structures were optimized with a hybrid QM/MM approach using the ChemShell software package (version 3.7.0)[78,79]. The QM region contained retinal and the side chain of Lys216, while the MM region consisted of the remainder of the protein and crystal waters. The B3LYP[79–83] functional with the cc-pVDZ[84,85] basis set was used as the QM method. The MM region was described with the CHARMM36 protein force field[86] and the TIP3P water model[87]. During the optimization only the QM region was allowed to relax, while all other atoms were constrained to their crystal positions.

Computation of potentials of mean force. PMFs were generated by using QM/MM in combination with the Weighted Histogram Approach Method (WHAM)[88] as implemented by Alan Grossfield[89]. This approach was used in earlier work that utilized WHAM for proton transfer computations[90] and a more detailed description of the methodology can be found there. To ensure sufficient sampling of the reaction coordinates, the self-consistent charge density functional tight binding method with full third-order extension[91–95] was applied to the QM region. The MM region used the CHARMM protein force field[86] and TIP3P water model[87].

For the proton transfer between Glu204 and Glu214, the reaction coordinate was defined as the difference between donor–hydrogen distance and acceptor–hydrogen distance. For the retinal isomerization the reaction coordinate was defined as the C12–C13–C14–C15 dihedral of retinal. The reaction pathways were sampled for a reaction coordinate of −1.7 to 1.7 Å and from −90° to 270° for proton transfer and retinal isomerization, respectively. The reaction coordinate was restrained with a harmonic potential of 150 kcal/mol and sampled in steps of 0.1 Å for proton transfer and 5° for retinal isomerization, with each point being sampled for 0.5 ns. The final PMF profiles were obtained by combing sampling initiated from the 13-*cis* and all-*trans* retinal conformation in the case of 6GUX [https://doi.org/10.2210/pdb6GUX/pdb] and from the minor and major *trans* states in the case of 6S6C [https://doi.org/10.2210/pdb6S6C/pdb].

Reporting summary. Further information on research design is available in the Nature Research Reporting Summary linked to this article.

Data availability

Structures and diffraction data have been deposited in the protein databank (https://www.rcsb.org). The accession codes are 6GUX [https://doi.org/10.2210/pdb6GUX/pdb] for dark-adapted AR3 and 6S6C [https://doi.org/10.2210/pdb6S6C/pdb] for light-adapted AR3. Mass spectrometry data are available for download [https://doi.org/10.6084/m9.figshare.13293203.v1]. Other data are available from the corresponding authors upon reasonable request.

Received: 9 June 2020; Accepted: 10 December 2020;
Published online: 27 January 2021

References

1. Rajagopal, S. & Shenoy, S. K. GPCR desensitization: acute and prolonged phases. *Cell. Signal.* https://doi.org/10.1016/j.cellsig.2017.01.024 (2018).
2. Azevedo, A. W. et al. C-terminal threonines and serines play distinct roles in the desensitization of rhodopsin, a G protein-coupled receptor. *Elife* https://doi.org/10.7554/eLife.05981 (2015).
3. Moore, C. A. C., Milano, S. K. & Benovic, J. L. Regulation of receptor trafficking by GRKs and arrestins. *Annu. Rev. Physiol.* https://doi.org/10.1146/annurev.physiol.69.022405.154712 (2007).
4. Min, C. et al. N-linked Glycosylation on the N-terminus of the dopamine D2 and D3 receptors determines receptor association with specific microdomains in the plasma membrane. *Biochim. Biophys. Acta Mol. Cell Res.* https://doi.org/10.1016/j.bbamcr.2014.09.024 (2015).
5. Naumenko, V. S. & Ponimaskin, E. Palmitoylation as a functional regulator of neurotransmitter receptors. *Neural Plast.* https://doi.org/10.1155/2018/5701348 (2018).
6. Gielen, M. & Corringer, P. J. The dual-gate model for pentameric ligand-gated ion channels activation and desensitization. *J. Physiol.* https://doi.org/10.1113/JP275100 (2018).
7. Kinde, M. N. et al. Conformational changes underlying desensitization of the pentameric ligand-gated ion channel ELIC. *Structure* https://doi.org/10.1016/j.str.2015.03.017 (2015).
8. Schauder, D. M. *et al.* Glutamate receptor desensitization is mediated by changes in quaternary structure of the ligand binding domain. *Proc. Natl Acad. Sci. USA* https://doi.org/10.1073/pnas.1217549110 (2013).
9. Plested, A. J. R. Structural mechanisms of activation and desensitization in neurotransmitter-gated ion channels. *Nat. Struct. Mol. Biol.* https://doi.org/10.1038/nsmb.3214 (2016).
10. Han, X. et al. A high-light sensitivity optical neural silencer: development and application to optogenetic control of non-human primate cortex. *Front. Syst. Neurosci.* **5**, 18 (2011).
11. Wiegert, J. S., Mahn, M., Prigge, M., Printz, Y. & Yizhar, O. Silencing neurons: tools, applications, and experimental constraints. *Neuron* **95**, 504–529 (2017).
12. Govorunova, E. G., Sineshchekov, O. A., Li, H. & Spudich, J. L. Microbial rhodopsins: diversity, mechanisms, and optogenetic applications. *Annu. Rev. Biochem.* **86**, 845–872 (2017).
13. Chow, B. Y. et al. High-performance genetically targetable optical neural silencing by light-driven proton pumps. *Nature* **463**, 98–102 (2010).
14. Vogt, A., Wietek, J. & Hegemann, P. Gloeobacter rhodopsin, limitation of proton pumping at high electrochemical load. *Biophys. J.* https://doi.org/10.1016/j.bpj.2013.08.031 (2013).
15. Rost, B. R., Schneider-Warme, F., Schmitz, D. & Hegemann, P. Optogenetic tools for subcellular applications in neuroscience. *Neuron* **96**, 572–603 (2017).
16. Hochbaum, D. R. et al. All-optical electrophysiology in mammalian neurons using engineered microbial rhodopsins. *Nat. Methods* **11**, 825–833 (2014).
17. Flytzanis, N. C. et al. Archaerhodopsin variants with enhanced voltage-sensitive fluorescence in mammalian and Caenorhabditis elegans neurons. *Nat. Commun.* **5**, 1–9 (2014).
18. McIsaac, R. S. et al. Directed evolution of a far-red fluorescent rhodopsin. *Proc. Natl Acad. Sci. USA* **111**, 13034–13039 (2014).

19. Yizhar, O., Fenno, L. E., Davidson, T. J., Mogri, M. & Deisseroth, K. Optogenetics in neural systems. *Neuron* https://doi.org/10.1016/j.neuron.2011.06.004 (2011).
20. Yawo, H., Asano, T., Sakai, S. & Ishizuka, T. Optogenetic manipulation of neural and non-neural functions. *Dev. Growth Differ.* https://doi.org/10.1111/dgd.12053 (2013).
21. Ferenczi, E. A., Tan, X. & Huang, C. L. H. Principles of optogenetic methods and their application to cardiac experimental systems. *Front. Physiol.* https://doi.org/10.3389/fphys.2019.01096 (2019).
22. Fenno, L., Yizhar, O. & Deisseroth, K. The development and application of optogenetics. *Annu. Rev. Neurosci.* https://doi.org/10.1146/annurev-neuro-061010-113817 (2011).
23. Ihara, K. et al. Evolution of the archaeal rhodopsins: Evolution rate changes by gene duplication and functional differentiation. *J. Mol. Biol.* https://doi.org/10.1006/jmbi.1998.2286 (1999).
24. Palczewski, K. et al. Crystal structure of rhodopsin: a G protein-coupled receptor. *Science* https://doi.org/10.1126/science.289.5480.739 (2000).
25. Clair, E. C. Saint, Ogren, J. I., Mamaev, S., Russano, D. & Kralj, J. M. Near-IR resonance Raman spectroscopy of archaerhodopsin 3: 2 effects of transmembrane potential 1. *J. Phys. Chem. B* **2**, 14592–14601 (2012).
26. Casadio, R., Gutowitz, H., Mowery, P., Taylor, M. & Stoeckenius, W. Light-dark adaptation of bacteriorhodopsin in Triton-treated purple membrane. *BBA Bioenerg.* **590**, 13–23 (1980).
27. Nishikawa, T., Murakami, M. & Kouyama, T. Crystal structure of the 13-cis isomer of bacteriorhodopsin in the dark-adapted state. *J. Mol. Biol.* **352**, 319–328 (2005).
28. Brown, M. F. et al. Solid-State2H NMR spectroscopy of retinal proteins in aligned membranes. *Biochim. Biophys. Acta Biomembr.* **1768**, 2979–3000 (2007).
29. Saint Clair, E. C. et al. Near-IR resonance Raman spectroscopy of archaerhodopsin 3: effects of transmembrane potential. *J. Phys. Chem. B* **116**, 14592–14601 (2012).
30. Caffrey, M. A comprehensive review of the lipid cubic phase or in meso method for crystallizing membrane and soluble proteins and complexes. *Acta Crystallogr. Sect. F Struct. Biol. Commun.* **71**, 3–18 (2015).
31. Caffrey, M. On the mechanism of membrane protein crystallization in lipidic mesophases. *Cryst. Growth Des.* **8**, 4244–4254 (2008).
32. Enami, N. et al. Crystal structures of archaerhodopsin-1 and -2: common structural motif in archaeal light-driven proton pumps. *J. Mol. Biol.* **358**, 675–685 (2006).
33. Yoshimura, K. & Kouyama, T. Structural role of Bacterioruberin in the trimeric structure of Archaerhodopsin-2. *J. Mol. Biol.* **375**, 1267–1281 (2008).
34. Yamashita, H. et al. Role of trimer-trimer interaction of bacteriorhodopsin studied by optical spectroscopy and high-speed atomic force microscopy. *J. Struct. Biol.* https://doi.org/10.1016/j.jsb.2013.02.011 (2013).
35. Ihara, K., Amemiya, T., Miyashita, Y. & Mukohata, Y. Met-145 is a key residue in the dark adaptation of bacteriorhodopsin homologs. *Biophys. J.* **67**, 1187–1191 (1994).
36. Creemers, A. F. L. et al. 1H and 13C MAS NMR evidence for pronounced ligand-protein interactions involving the ionone ring of the retinylidene chromophore in rhodopsin. *Proc. Natl Acad. Sci. USA* https://doi.org/10.1073/pnas.112677599 (2002).
37. Kandori, H. Ion-pumping microbial rhodopsins. *Front. Mol. Biosci.* **2**, (2015).
38. Ernst, O. P. et al. Microbial and animal rhodopsins: Structures, functions, and molecular mechanisms. *Chem. Rev.* **114**, 126–163 (2014).
39. Baudry, J., Crouzy, S., Roux, B. & Smith, J. C. Simulation analysis of the retinal conformational equilibrium in dark- adapted bacteriorhodopsin. *Biophys. J.* https://doi.org/10.1016/S0006-3495(99)77349-2 (1999).
40. Leioatts, N. et al. Retinal ligand mobility explains internal hydration and reconciles active rhodopsin structures. *Biochemistry* https://doi.org/10.1021/bi4013947 (2014).
41. Wickstrand, C., Dods, R., Royant, A. & Neutze, R. Bacteriorhodopsin: Would the real structural intermediates please stand up? *Biochim. Biophys. Acta Gen. Subj.* **1850**, 536–553 (2015).
42. Nango, E. et al. A three-dimensionalmovie of structural changes in bacteriorhodopsin. *Science* **354**, 1552–1557 (2016).
43. Nogly, P. et al. Retinal isomerization in bacteriorhodopsin captured by a femtosecond x-ray laser. *Science* **361**, 1–15 (2018).
44. Lesca, E., Panneels, V. & Schertler, G. F. X. The role of water molecules in phototransduction of retinal proteins and G protein-coupled receptors. *Faraday Discuss.* **207**, 27–37 (2018).
45. Gerwert, K., Freier, E. & Wolf, S. The role of protein-bound water molecules in microbial rhodopsins. *Biochim. Biophys. Acta Bioenerg.* **1837**, 606–613 (2014).
46. Hasegawa, N., Jonotsuka, H., Miki, K. & Takeda, K. X-ray structure analysis of bacteriorhodopsin at 1.3 Å resolution. *Sci. Rep.* **8**, 13123 (2018).
47. Chang, C.-H., Jonas, R., Govindjee, R. & Ebrey, T. G. Regeneration of blue and purple membranes from deionized bleached membranes of *Halobacterium halobium*. *Photochem. Photobiol.* **47**, 261–265 (1988).
48. Lanyi, J. K. Proton transfers in the bacteriorhodopsin photocycle. *Biochim. Biophys. Acta Bioenerg.* **1757**, 1012–1018 (2006).
49. Clair, E. C. S., Ogren, J. I., Mamaev, S., Kralj, J. M. & Rothschild, K. J. Conformational changes in the archaerhodopsin-3 proton pump: Detection of conserved strongly hydrogen bonded water networks. *J. Biol. Phys.* **38**, 153–168 (2012).
50. Khorana, H. G. et al. Amino acid sequence of bacteriorhodopsin. *Proc. Natl Acad. Sci. USA* **76**, 5046–5050 (1979).
51. Seehra, J. S. & Khorana, H. G. Bacteriorhodopsin precursor. *J. Biol. Chem.* **259**, 4187–4193 (1984).
52. Lobasso, S., Lopalco, P., Lattanzio, V. M. T. & Corcelli, A. Osmotic shock induces the presence of glycocardiolipin in the purple membrane of *Halobacterium salinarum*. *J. Lipid Res.* **44**, 2120–2126 (2003).
53. Lopalco, P., Lobasso, S., Babudri, F. & Corcelli, A. Osmotic shock stimulates de novo synthesis of two cardiolipins in an extreme halophilic archaeon. *J. Lipid Res.* **45**, 194–201 (2004).
54. Kamekura, M. & Kates, M. Structural diversity of membrane lipids in members of halobacteriaceae. *Biosci. Biotechnol. Biochem.* **63**, 969–972 (1999).
55. Yoshinaga, M. Y., Kellermann, M. Y., Valentine, D. L. & Valentine, R. C. Phospholipids and glycolipids mediate proton containment and circulation along the surface of energy-transducing membranes. *Prog. Lipid Res.* **64**, 1–15 (2016).
56. Kouyama, T. et al. Structure of archaerhodopsin-2 at 1.8Å resolution. *Acta Crystallogr. Sect. D. Biol. Crystallogr.* **70**, 2692–2701 (2014).
57. Kooijman, L. et al. Dynamics of bacteriorhodopsin in the dark-adapted state from solution nuclear magnetic resonance spectroscopy. *Angew. Chem.* https://doi.org/10.1002/ange.202004393 (2020).
58. Pescitelli, G. & Woody, R. W. The exciton origin of the visible circular dichroism spectrum of bacteriorhodopsin. *J. Phys. Chem. B* https://doi.org/10.1021/jp212166k (2012).
59. Fujimoto, K. J. Transition-density-fragment interaction approach for exciton-coupled circular dichroism spectra. *J. Chem. Phys.* https://doi.org/10.1063/1.3480015 (2010).
60. Hasselbacher, C. A., Spudich, J. L. & Dewey, T. G. Circular dichroism of halorhodopsin: comparison with bacteriorhodopsin and sensory rhodopsin I. *Biochemistry* https://doi.org/10.1021/bi00407a041 (1988).
61. Fukuda, K., Ikegami, A., Nasuda-Kouyama, A. & Kouyama, T. Effect of partial delipidation of purple membrane on the photodynamics of bacteriorhodopsin. *Biochemistry* https://doi.org/10.1021/bi00460a006 (1990).
62. Milder, S. J., Thorgeirsson, T. E., Kliger, D. S., Miercke, L. J. W. & Stroud, R. M. Effects of detergent environments on the photocycle of purified monomeric bacteriorhodopsin. *Biochemistry* **30**, 1751–1761 (1991).
63. Váró, G. & Lanyi, J. K. Effects of the crystalline structure of purple membrane on the kinetics and energetics of the bacteriorhodopsin photocycle. *Biochemistry* https://doi.org/10.1021/bi00243a018 (1991).
64. Dencher, N. A., Kohl, K. D. & Heyn, M. P. Photochemical cycle and light-dark adaptation of monomeric and aggregated bacteriorhodopsin in various lipid environments. *Biochemistry* https://doi.org/10.1021/bi00275a002 (1983).
65. Oesterhelt, D. & Stoeckenius, W. Isolation of the cell membrane of *Halobacterium halobium* and its fractionation into red and purple membrane. *Methods Enzymol.* https://doi.org/10.1016/0076-6879(74)31072-5 (1974).
66. Hendler, R. W. & Dracheva, S. Importance of lipids for bacteriorhodopsin structure, photocycle, and function. *Biochemistry (Moscow)* https://doi.org/10.1023/A:1013143621346 (2001).
67. Cherezov, V. Crystallizing membrane proteins using lipidic mesophases. *Nat. Protoc.* https://doi.org/10.1038/nprot.2009.31 (2009).
68. Foadi, J. et al. Clustering procedures for the optimal selection of data sets from multiple crystals in macromolecular crystallography. *Acta Crystallogr. Sect. D. Biol. Crystallogr.* **69**, 1617–1632 (2013).
69. Winter, G. & McAuley, K. E. Automated data collection for macromolecular crystallography. *Methods* https://doi.org/10.1016/j.ymeth.2011.06.010 (2011).
70. Evans, G., Axford, D., Waterman, D. & Owen, R. L. Macromolecular microcrystallography. *Crystallogr. Rev.* https://doi.org/10.1080/0889311X.2010.527964 (2011).
71. McCoy, A. J. et al. Phaser crystallographic software. *J. Appl. Crystallogr.* **40**, 658–674 (2007).
72. Emsley, P. & Cowtan, K. Coot -model building tools for molecular graphics. *Acta Crystallogr. D. Biol. Crystallogr.* **D60**, 2126–2132 (2004).
73. Emsley, P., Lohkamp, B., Scott, W. G. & Cowtan, K. Features and development of Coot. *Acta Crystallogr. Sect. D Biol. Crystallogr.* https://doi.org/10.1107/S0907444910007493 (2010).
74. Adams, P. D. et al. PHENIX: a comprehensive Python-based system for macromolecular structure solution. *Acta Crystallogr. Sect. D. Biol. Crystallogr.* **66**, 213–221 (2010).

75. Murshudov, G. N. et al. REFMAC5 for the refinement of macromolecular crystal structures. *Acta Crystallogr. Sect. D Biol. Crystallogr.* https://doi.org/10.1107/S0907444911001314 (2011).
76. Emsley, P., Lohkamp, B., Scott, W. G. & Cowtan, K. Using Coot to model N-linked carbohydrates model building and structure refinement. *Acta Crystallogr. Sect. D Biol. Crystallogr. Opin. Struct. Biol.* (2017).
77. Williams, C. J. et al. MolProbity: more and better reference data for improved all-atom structure validation. *Protein Sci.* https://doi.org/10.1002/pro.3330 (2018).
78. Sherwood, P. et al. QUASI: a general purpose implementation of the QM/MM approach and its application to problems in catalysis. *J. Mol. Struct. Theochem.* https://doi.org/10.1016/s0166-1280(03)00285-9 (2003).
79. Kästner, J. et al. DL-FIND: an open-source geometry optimizer for atomistic simulations*. *J. Phys. Chem. A* https://doi.org/10.1021/jp9028968 (2009).
80. Becke, A. D. Density-functional thermochemistry. III. The role of exact exchange. *J. Chem. Phys.* https://doi.org/10.1063/1.464913 (1993).
81. Vosko, S. H., Wilk, L. & Nusair, M. Accurate spin-dependent electron liquid correlation energies for local spin density calculations: a critical analysis. *Can. J. Phys.* https://doi.org/10.1139/p80-159 (1980).
82. Stephens, P. J., Devlin, F. J., Chabalowski, C. F. & Frisch, M. J. Ab Initio calculation of vibrational absorption and circular dichroism spectra using density functional force fields. *J. Phys. Chem.* https://doi.org/10.1021/j100096a001 (1994).
83. Lee, C., Yang, W. & Parr, R. G. Development of the Colle-Salvetti correlation-energy formula into a functional of the electron density. *Phys. Rev. B* https://doi.org/10.1103/PhysRevB.37.785 (1988).
84. Dunning, T. H. Gaussian basis sets for use in correlated molecular calculations. I. The atoms boron through neon and hydrogen. *J. Chem. Phys.* https://doi.org/10.1063/1.456153 (1989).
85. Davidson, E. R. Comment on "Comment on Dunning's correlation-consistent basis sets". *Chem. Phys. Lett.* https://doi.org/10.1016/0009-2614(96)00917-7 (1996).
86. Best, R. B. et al. Optimization of the additive CHARMM all-atom protein force field targeting improved sampling of the backbone φ, ψ and side-chain χ1 and χ2 dihedral angles. *J. Chem. Theory Comput.* https://doi.org/10.1021/ct300400x (2012).
87. Jorgensen, W. L., Chandrasekhar, J., Madura, J. D., Impey, R. W. & Klein, M. L. Comparison of simple potential functions for simulating liquid water. *J. Chem. Phys.* https://doi.org/10.1063/1.445869 (1983).
88. Kumar, S., Rosenberg, J. M., Bouzida, Swendsen, R. H. & Kollman, P. A. THE weighted histogram analysis method for free-energy calculations on biomolecules. I. The method. *J. Comput. Chem.* https://doi.org/10.1002/jcc.540130812 (1992).
89. Grossfield, A. WHAM: the weighted histogram analysis method. Available at: http://membrane.urmc.rochester.edu/wordpress/?page_id=126.
90. Adam, S. & Bondar, A. N. Mechanism by which water and protein electrostatic interactions control proton transfer at the active site of channelrhodopsin. *PLoS ONE* https://doi.org/10.1371/journal.pone.0201298 (2018).
91. Elstner, M. et al. Self-consistent-charge density-functional tight-binding method for simulations of complex materials properties. *Phys. Rev. B Condens. Matter Mater. Phys.* https://doi.org/10.1103/PhysRevB.58.7260 (1998).
92. Gaus, M., Cui, Q. & Elstner, M. DFTB3: Extension of the self-consistent-charge density-functional tight-binding method (SCC-DFTB). *J. Chem. Theory Comput.* https://doi.org/10.1021/ct100684s (2011).
93. Gaus, M., Goez, A. & Elstner, M. Parametrization and benchmark of DFTB3 for organic molecules. *J. Chem. Theory Comput.* https://doi.org/10.1021/ct300849w (2013).
94. Grimme, S., Antony, J., Ehrlich, S. & Krieg, H. A consistent and accurate ab initio parametrization of density functional dispersion correction (DFT-D) for the 94 elements H-Pu. *J. Chem. Phys.* https://doi.org/10.1063/1.3382344 (2010).
95. Grimme, S., Ehrlich, S. & Goerigk, L. Effect of the damping function in dispersion corrected density functional theory. *J. Comput. Chem.* https://doi.org/10.1002/jcc.21759 (2011).

Acknowledgements

We thank Dr. Robin Owen and Dr. Darren Sherrell, and the I24 beamline staff (Diamond Light Source) for their support during data collection under the MX proposals 19152 and 11386. We thank Juan Escobar and Peter Fisher (Oxford) for technical assistance, and Dr. Agata Butryn (Diamond Light Source) and Dr Rosana Reis (NPL) for helpful discussions. We are grateful for support from the Membrane Protein Laboratory under Wellcome Trust grant number 20289/Z16/Z, including the award of experimental time (SM15222) on the B23 Beamline at Diamond Light Source (UK) and we acknowledge the support of Dr. Giuliano Siligardi, Dr. Rohanah Hussain and Dr. Charlotte Hughes. We acknowledge funding from United Kingdom Department of Business, Energy and Industrial Strategy (BEIS) to I.M., from the European Research Council (ERC) under the European Union's Horizon 2020 research and innovation program (Grant Agreement number 678169, ERC Starting Grant "PhotoMutant") to I.S., from DSTL UK (grant number DSTLX-1000099768) and BBSRC (grant number BB/N006011/1) to A.W. We thank the Minerva Stiftung for a post-doctoral fellowship within the framework of the Minerva Fellowship Program to SA and the DFG for a Mercator Fellowship to I.S. (Grant number SFB 1078).

Author contributions

P.J.J., I.M., and A.W. conceived the study and all authors were involved in designing experiments and interpreting data. AR3 protein was expressed and purified by J.F.B.J. and J.V. Crystallization was performed by J.F.B.J., P.J.J., J.B., T.O.C.K., and I.M. Diffraction data were acquired by J.F.B.J., P.J.J., D.A., and I.M. High-resolution structures were solved by P.J.J., D.A., and I.M. Simulations were performed by S.A. and I.S. Mass spectrometry data were acquired by K.K.H., H.Y.Y., and C.V.R. Atomic force microscopy images were acquired by A.V. and P.E.M. J.F.B.J., P.J.J., I.M., and A.W. wrote the paper with assistance from all authors. J.F.B.J. and P.J.J. contributed equally to this paper.

Competing interests

The authors declare no competing interests.

Additional information

Supplementary information is available for this paper at https://doi.org/10.1038/s41467-020-20596-0.

Correspondence and requests for materials should be addressed to I.M. or A.W.

Peer review information *Nature Communications* thanks Michael Brown, Dimitrios Fotiadis, and other, anonymous, reviewers for their contributions to the peer review of this work. Peer review reports are available.

Reprints and permission information is available at http://www.nature.com/reprints

Publisher's note Springer Nature remains neutral with regard to jurisdictional claims in published maps and institutional affiliations.

Chapter 3

Imaging Artificial Membranes Using High-Speed Atomic Force Microscopy

Hussein Nasrallah, Anthony Vial, Nicolas Pocholle, Jérémy Soulier, Luca Costa, Cédric Godefroy, Eric Bourillot, Eric Lesniewska, and Pierre-Emmanuel Milhiet

Abstract

Supported lipid bilayers represent a very attractive way to mimic biological membranes, especially to investigate molecular mechanisms associated with the lateral segregation of membrane components. Observation of these model membranes with high-speed atomic force microscopy (HS-AFM) allows the capture of both topography and dynamics of membrane components, with a spatial resolution in the nanometer range and image capture time of less than 1 s. In this context, we have developed new protocols adapted for HS-AFM to form supported lipid bilayers on small mica disks using the vesicle fusion or Langmuir-Blodgett methods. In this chapter we describe in detail the protocols to fabricate supported artificial bilayers as well as the main guidelines for HS-AFM imaging of such samples.

Key words Atomic force microscopy, Lipid, Artificial membrane, Supported lipid bilayer, Vesicle fusion, Langmuir, Dynamics

1 Introduction

Cell membranes are very complex structures, consisting of a multitude of different lipids and proteins. They are essential for life, delineating intracellular compartments or forming a protective barrier for the cell, such as the plasma membrane of eukaryotic cells. By organizing its components in space and time, cell plasma membranes play a pivotal role in many biological processes including cell recognition, signaling, selective-ion transfer, adhesion, and fusion. In order to investigate the molecular mechanisms associated to these functions, the complexity of biomembranes has led over the past years to the use of model membranes. By simplifying the system, it is possible to systematically study the subcomponents of cellular membranes and therefore gain valuable insights into the lateral segregation of membrane components and their implications

Nuno C. Santos and Filomena A. Carvalho (eds.), *Atomic Force Microscopy: Methods and Protocols*, Methods in Molecular Biology, vol. 1886, https://doi.org/10.1007/978-1-4939-8894-5_3,

in membrane remodeling. There are currently two main categories of model membranes: (i) free-standing membranes like giant unilamellar vesicles (GUV) that are very popular to study dynamic events and have been widely used to explore lipid domain formation using single molecule optical microscopy [1]. This approach, however, is restricted by the diffraction-limited resolution and is therefore not suitable to probe membrane on the mesoscopic scale and (ii) planar model membranes supported by a substrate and named supported lipid bilayer (SLB) [2]. The substrates are generally glass, silicon, or mica. SLBs are robust systems that are compatible with most surface-based biophysical techniques including fluorescence microscopy, ellipsometry, and atomic force microscopy (AFM).

AFM is nowadays recognized as an outstanding technique in the membrane field [3]. Vertical and lateral resolution in the nanometer range can be achieved in buffer, a great advantage as compared to other structural biology techniques. In addition, due to a high signal-to-noise ratio, AFM often does not require image averaging, limiting the number of acquisitions required. AFM has been widely used to probe both the topography at the nanoscale of artificial SLBs [4] and their physical properties [5]. Major advances have been made in the understanding of lateral organization in biological membranes using SLBs analyzed by AFM. Lipid membrane microdomains and the importance of certain lipids such as cholesterol (Chl), gangliosides, or ceramides have been characterized using AFM [6–8]. Membrane partition of proteins associated with membrane microdomains have also been measured by AFM imaging of lipid phase-separated membranes, e.g., GPI-anchored alkaline phosphatase (reviewed in ref. 9). In addition to its use in characterizing membrane microdomains, AFM is suitable to acquire images of proteins reconstituted within SLB with subnanometer resolution such as the light-harvesting complex of bacterial photosynthetic apparatus [10] or pore-forming proteins such as cytolysin [11]. Finally AFM has been applied in membrane-bioinspired nanotechnology [12].

Conventional AFM is limited by the time to acquire one image, in the minute range, and AFM imaging was therefore unable to provide information about the dynamics of most biological processes. However tremendous progresses in AFM during the last 10 years enabled the development of high-speed (HS) AFM able to capture images of fragile biological samples up to the video rate [13]. Early developments came from the group of Paul Hansma and Toshio Ando in the early 90s. The latter pushed the limits of AFM speed and developed a new setup that is now commercially available (*see* the history of HS-AFM developments in ref. 14). Main advances reside in the development of small cantilevers oscillating in the MHz range in liquid and new feedback control technique such as dynamic PID control [13]. Nowadays the majority of

companies offer new microscopes allowing fast AFM imaging in the range of one frame per second. High-speed AFM has been already used to visualize in real time the formation of SLB from tubular membranes composed of a ternary phospholipid mixture with a sampling rate better than one image per second [15]. Real-time visualization of the assembly of a sphingomyelin-specific pore-forming toxin on planar lipid membranes was also performed, this protein forming hexagonal close-packed structures whose assembly was driven by reorganization of lysenin oligomers including association/dissociation and rapid diffusion along the membrane [16]. More recently, thanks to the development of temperature-controlled HS-AFM, it was possible to observe both topography and dynamics of lipid phase transition from ripple phase to fluid phase [17].

In this chapter, we detail two protocols for preparing SLBs suitable for HS-AFM as well as imaging conditions and microscope tuning. Examples of real-time imaging of model membranes are also provided.

2 Materials

2.1 Supplies

1. 2 mm diameter glass rods from RIBM (Research Institute of Biomolecule Metrology Co., Ltd., Tsukuba, Japan).
2. Muscovite mica from Goodfellow (France) or from RIBM Co. (Japan).
3. Polyether ether ketone (PEEK) chemically modified with hydroxyapatite (HA) by the plasma spray technique (PEEK-OPTIMA HA, Invibio, UK).
4. Araldite® glue.
5. Silicon nitride AFM tips are from Olympus (AC10FS, $k = 0.1$ N/m) or from Nanoworld (USC-F1.2, Neuchâtel, Switzerland, $k = 0.15$ N/m). Both tips are functionalized with a carbon nano fiber (CNF).

2.2 Reagents

1. Lipids: Lipid reagents must be of the highest purity and can be purchased from Avanti Polar Lipids (Alabaster, USA) or other suppliers. Lipid mixtures that we used include 1,2-dioleoyl-sn-glycero-3-phosphocholine (DOPC), 1,2-dipalmitoyl-sn-glycero-3-phosphocholine (DPPC), and cholesterol (Chl). Lipid stock solutions are stored at −80 °C in $CHCl_3$ solution or in powder and kept under argon 6–12 months according to the supplier's recommendations. Working solutions are prepared at 10 mM in 2:1 $CHCl_3$/MeOH and stored at −20 °C.
2. Phosphate buffered saline (PBS) at pH 7.4 and 10 mM Tris, 150 mM KCl, pH 7.4.

2.3 Instrumentation

1. Avanti mini extruder (Avanti, USA).
2. Langmuir-Blodgett balance KSV NIMA (Biolin Scientific, Sweden).
3. Homemade 10 × 20 mm dipping plate in PEEK with three holes for 1 mm diameter glass rods for HS-AFM.
4. Standard Infuse/Withdraw Pump 11 Elite dual programmable syringe Pump (Harvard Apparatus, US) with infusion tubing polyethylene (PE-10/100) and female Luer stubs to connect infusion tubing to 150 µL Hamilton syringes.
5. Infuse/Withdraw tip associated with two manual probe positioners (Probe Head DDP105, Cascade Microtech Co., USA) with a resolution of 3 µm for travel range over 5–25 mm in order to bring the fluid on each side of the HS-AFM cantilever holder.
6. HS-AFM was performed with a prototype from Toshio Ando's laboratory and provided by RIBM Research Institute of Biomolecule Metrology Co., Ltd., Tsukuba, Japan). The microscope can be equipped with of 1, 5, or 40 µm scanner (respectively $x = 1$ µm/$y = 4$ µm/$z = 1$ µm, $x = 5$ µm/$y = 5$ µm/$z = 2$ µm and $x = 40$ µm/$y = 40$ µm/$z = 6$ µm).
7. RF plasma etcher (Diener, Intco France).
8. HS-AFM cantilever holder for cantilever etching (homemade).

3 Methods

3.1 Preparation of Artificial Supported Lipid Bilayers for HS-AFM

3.1.1 Vesicle Fusion Method

Different methods have been developed to prepare SLB but the most popular remains the fusion of large unilamellar lipid vesicles (LUVs) on a solid surface [18]. LUVs are prepared via extrusion and the vesicle solution is then added on top of the support. Vesicles then adsorb on the substrate before rupturing and form a continuous supported bilayer. We often use phase-separated lipid bilayers (e.g., DOPC/DPPC SLBs) in order to assess the formation of a continuous membrane (phase separation is easily observed with AFM) [19]. DOPC is known to have a transition temperature of −16.5 °C and therefore exists in the fluid like liquid crystalline state ($L\alpha$) at room temperature whereas DPPC has a transition temperature of 41.3 °C and therefore exists in the solid-like gel state ($L\beta$) at this temperature. The main steps of the protocol described below are for HS-AFM experiments. The protocol for conventional AFM has already been published in another Methods in Molecular Biology issue [10].

1. Glue a 2 mm diameter mica disk with Araldite® at the top of a glass rod and let it dry at least overnight.

2. Add the lipids solubilized in organic solvent in a Pyrex® tube at 30 °C and dry them under nitrogen using a dry block for at least 2 h. If a lipid mixture is used, vortex the tube before drying.
3. Suspend the dried lipids at 0.125 mM in PBS buffer by 1 min strong vortexing under argon in the presence of 2 mm glass beads to form multilamellar vesicles (MLV). Alternatively, longer vortexing without beads can be used.
4. Extrude MLVs using a suitable extruder (e.g., Avanti Mini-Extruder) through a 100 nm diameter polycarbonate membrane to produce LUVs. Their homogeneity can be easily controlled using dynamic light scattering.
5. There are two possible methods to deposit the SLB from the LUV suspension. *Method A*: Cleave the small mica disk glued at the top of the glass rod under a binocular to assess the quality of cleavage, deposit 2 μL LUV suspension onto it (*see* Fig. 1a) and allow the LUVs to adsorb and fuse during 35 min at 60 °C in the oven for a DOPC/DPPC mixture (perform the incubation at 20 °C above the fusion temperature of the lipids allowing them to form a homogeneous fluid phase). The sample is then cooled down for 5 min at room temperature and rinsed with PBS. This procedure however led to some problems of reproducibility in the quality of the membrane (shape of DPPC domains, holes, double membrane) that we interpret as the consequence of the partial evaporation of the tiny drop upon incubation at 60 °C. This evaporation is difficult to control and can change salt and lipid concentration influencing the fusion process (*see* **Note 1** below). The protocol described in Fig. 1b prevents such drawbacks. *Method B:* A large mica disc of about 1 cm is punched in the center leaving a hole of 2 mm diameter that will hold the glass rod with the small mica disc glued on top. After being cleaved, holding the large disc by tweezers so that the glass rod is not affected or contaminated, both will be inserted sidewise into the bottom of a 2 mL microtube and covered by 50 μL of lipids. This tube was then incubated (standing vertically) under the conditions described above (60 °C, in a water bath). The tube is then cooled down for 5 min at room temperature and then the sample rinsed with PBS.
6. After rinsing the glass rod is glued to the top of the z piezo of the scanner (schematized in Fig. 1b) using nail polish or Loctite®.
7. The piezo scanner is then placed over the liquid cell holding the cantilever chip according the detailed protocol provided by Uchihashi et al. [20].

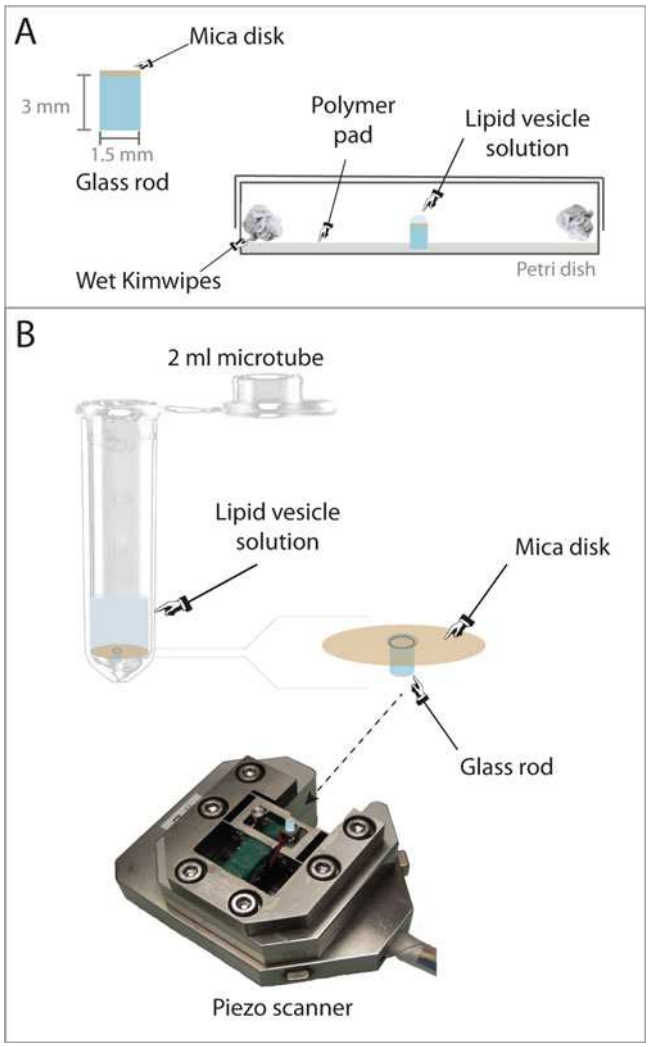

Fig. 1 Formation of supported lipid bilayers from lipid vesicles. The first method (**a**) is adapted from ref. 20 and the second method (**b**) has been developed to improve the reproducibility of the fabrication. (**a**) A mica disk is glued at the top of a glass rod and placed on a polymer pad in a Petri dish. The lipid vesicle solution is deposited on mica, incubated in an oven in a water-saturated atmosphere thanks to wet Kimwipes® in the dish closed by a lid. After rinsing, the glass rod is glued at the top of the piezo scanner shown in **b**. (**b**) A mica disk of ~1 cm diameter with a punched hole of 2 mm in the center is positioned at the bottom of a 2 mL microtube. A glass rod of 2 mm diameter, the HS-AFM sample holder, with a 2 mm mica disk glued at the top, is placed in the hole. The two mica disks should be at the same level. A solution of lipid vesicles is then deposited at the top of the sample and incubated in a water bath (*see* Subheadings 2 and 3). After incubation, the glass rod is picked up with tweezers and glued with Loctite® glue on the z piezo of the scanner

3.1.2 Langmuir Balance

The main drawback of the vesicle fusion method is the symmetry of SLBs that are obtained, imperfectly mimicking biological membranes. Another approach to form SLBs on a solid support is the use of the Langmuir-Blodgett or Langmuir Schaefer technique. Both consist of the transfer of a lipid monolayer (inner leaflet) onto a hydrophilic support by pulling it vertically through a lipid monolayer at the air-water interface. The outer leaflet is then transferred using either another vertical passage of the support through the lipid monolayer at the air-water interface (Blodgett) or by dipping horizontally the support into the lipid monolayer at the air-water interface (Schaefer). The advantage of the double transfer methods is that asymmetrical bilayers can be produced. We describe below a protocol to produce SLBs supported on mica which are suitable for HS-AFM imaging (Fig. 2):

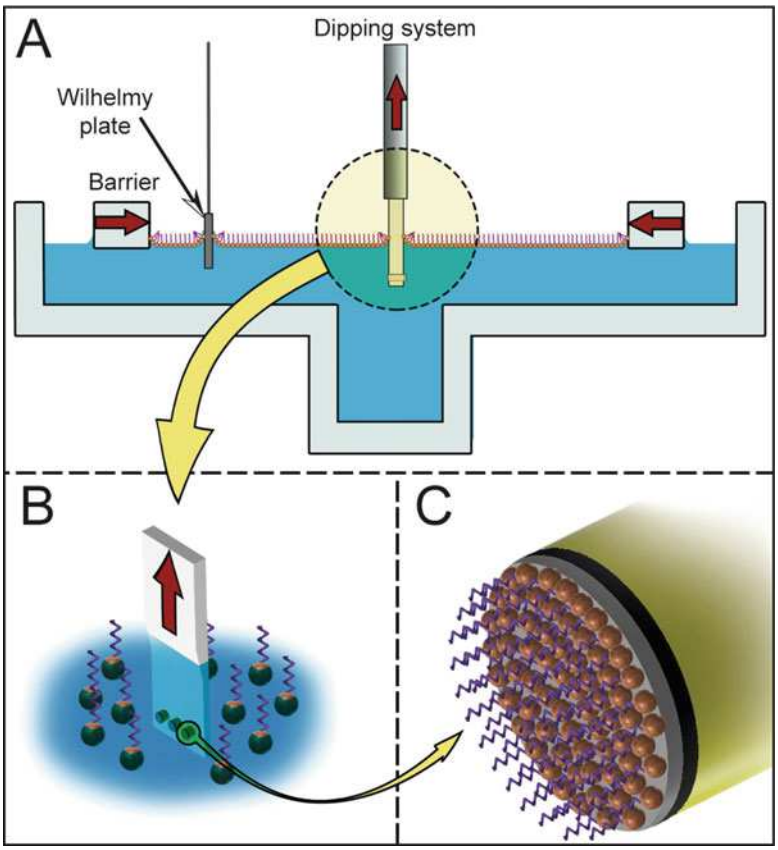

Fig. 2 Fabrication of supported lipid bilayers using Langmuir Blodgett technique. (**a**) Schematic view of the Langmuir balance; (**b**) zoom on the dipping system made in polyether ether ketone (PEEK), chemically modified and biologically inert. Glass rods with mica disk glued at the top, similar to those shown in Fig. 1, are inserted in holes in the polymer plate; (**c**) zoom on mica, glued at the top of a glass rod and covered by a lipid monolayer

1. Install the Langmuir-Blodgett apparatus on a vibration isolation table and inside a complete enclosure box with temperature control (22 °C in our case).
2. Before an experiment and after each run, it is crucial to clean the Langmuir trough and barriers. Wash with hot water and a commercial detergent and always use gloves to manipulate each element in order to minimize contamination.
3. Use a soft brush soaked with ethanol for mechanical and chemical cleaning of LB elements. Rinse thoroughly with Milli-Q water (18 MΩ).
4. Clean the platinum Wilhelmy plate over a blue flame (Bunsen burner) hot enough to make the plate glow red in just a few seconds. Rinse with ethanol and water.
5. Place the trough, the barriers, and the Wilhelmy plate in the frame.
6. Solvent quality and its nature (volatile or not) impact the Langmuir isotherm. Equilibrium time and subphase temperature should be maintained constant during the process.
7. Fill the LB trough with pure water (the subphase) in order to get a positive meniscus of 2 mm high on the Wilhelmy plate.
8. Open the barriers and zero the LB balance (associate to the Wilhelmy plate).
9. Close the barriers. The surface pressure should not change (less than 0.2 mN/m). If the surface pressure change, it is caused by contaminants. A new cleaning process should be performed.
10. We designed and used a specific hydrophilic and bio-inert holder (PEEK treated with hydroxyapatite) to dip three HS-AFM mica substrates at the same time (Fig. 2b). It was also cleaned in the same way as the LB barriers. Cleave the three mica disks and immerse the dipping system just before adding the lipids (*see* below).
11. Fill a precision pipette-puller with a suitable volume (20 μL of lipids in our case) of the prepared solution of lipids in a volatile organic solvent (chloroform). The organic solvent should be nonpolar to prevent miscibility in water and volatile so that it will evaporate at the air-water interface.
12. Gently add the lipids at the interface by depositing the drop in contact with water (do not let the drop fall down from the needle as part of the sample might be lost in the subphase as micelles). Do not touch the water with the needle.
13. Wait 15–20 min for the pressure surface to reach equilibrium (the time for the solvent to evaporate).
14. Start the experiment according to the protocol provided by the LB equipment manufacturer (*see* an example in [21]:

(a) Compress the lipid film at a rate of 5 mm^2/min up to a pressure mimicking that of a biological membrane (typically 30–35 mN/m). The maximum pressure for the LB film collapsing should be determined when using a new lipid mixture.

(b) The dipping mechanism holds the substrate and enables controlled deposition cycles. Monolayers should be deposited at a constant surface pressure of 30 mN/m, after a 5-min relaxation time, by raising vertically (0.5 mm/min) freshly cleaved mica through the air-water interface (Fig. 2c).

(c) The deposited sample is left 30 min in a desiccator under nitrogen and in darkness in order to limit oxidation of unsaturated aliphatic chains and a second deposition is performed in order to get a second leaflet producing a bilayer.

3.2 HS-AFM Imaging

The procedure described in Subheading 3.1.1 led to a flat supported lipid bilayer with a root mean square (rms) in the Angstrom range (*see* examples in Fig. 3). In order to image such SLB at scanning rate up to ten images/second, we used the HS-AFM setup developed by Toshio Ando's group in oscillating mode with optimized high-resolution imaging parameters to minimize the force applied by the tip on the sample, an important parameter for biological AFM imaging. Typically, short cantilevers designed for HS-AFM (length < 10 μm, a spring constant of 0.1–0.2 N/m, a resonance frequency of 600 kHz and a quality factor of ~2 in solution) were oscillated at free amplitude of a few nm (below 0.5 V amplitude voltage). The amplitude set point was set at 80–90% of the free amplitude. The scanning rate was generally one or two frames/second with a 400 × 400 pixels sampling but largely depended on the scanner used (basically, we were not able to achieve more than one image/second with the 40 μm scanner) and on the scanning area (generally 4–5 μm for observing SLB structure). Another important feature is the presence of an electron beam deposited tip at the end of the cantilever [20]. It is very important for high-resolution imaging since this EBD tip can be sharpened using plasma etching, and it also increases the distance between the sample and the cantilever, minimizing hysteresis during fast scanning.

Using this setting, we have been able to image in real time the formation of SLB composed of an equal mixture of DOPC and DPPC. We observed the formation of the SLB from unilamellar vesicles that can be identified in the HS-AFM images (Fig. 1a–d). Over time we observed the fusion of vesicles on mica leading to formation of a flat supported membrane. Vesicle fusion was however too fast for HS-AFM to capture intermediate shapes of vesicle

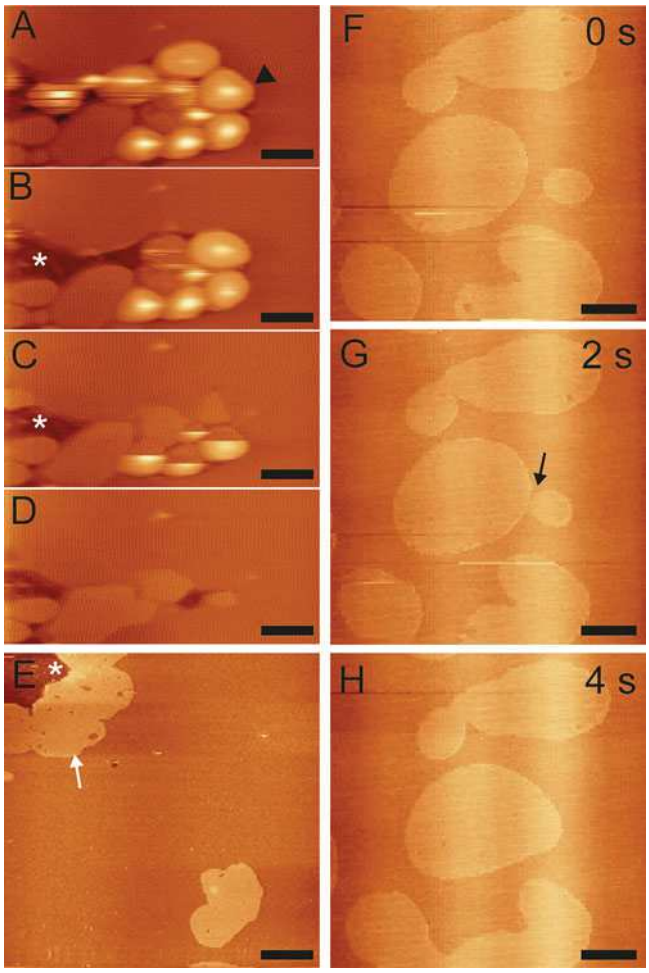

Fig. 3 Imaging supported lipid bilayer and its formation using HS-AFM. (**a**–**d**) 2 s time lapse showing real-time formation of DOPC-DPPC (1:1) SLB on mica. The black arrowhead indicates a non-fused vesicle that is surrounded by a brown matrix corresponding to an already formed SLB. From **a** to **d**, the number of intact vesicles decreases over time and a lipid phase transition can be observed in **d**. The white asterisk points a defect in the membrane where no membrane is present. (**e**) Typical pattern obtained at the end of the vesicle fusion for a DOPC-DPPC bilayer. Three regions are clearly distinguishable, mica (white asterisk), DOPC, and DPPC, from the darkest to the brightest, respectively. (**f**–**h**) 2 s time lapse showing a DOPC-DPPC-Chl (1:1:0.35) SLB. The dynamics of the liquid-ordered (lighter) domains in terms of shape and position and their coalescence can be observed in real time (black arrow in Fig. 1g). Scale bars are 100 nm (**a**–**d**), 500 nm (**e**), and 1 μm (**f**, **g**). The z scale is automatically adjusted and in the 20 nm range

during this process. Importantly we cannot completely exclude that part of this fusion is induced or favored by tip scanning. This hypothesis is in good agreement with the pattern observed in Fig. 3c where the vesicles seem to be partially fused with a separation between the two states along the scan axis. The picture in Fig. 3e shows a classical pattern of DOPC-DPPC membrane with three domains: a light domain corresponding to DPPC enriched domains in gel phase protruded from a darker matrix made of DOPC enriched fluid domains (white arrow). The height difference between the two domains was 1.2 ± 0.2 nm and fitted well with lipid phase separation between fluid and gel phases. The darkest domain corresponded to the mica substrate that is around 4–5 nm lower than the DOPC domain, a value that fits well with the thickness of a lipid bilayer with a thin layer of buffer between the lipid polar heads and the substrate. Importantly this pattern cannot be obtained just after the vesicle fusion since phase separation requires lipids to laterally segregate according to their physical properties [22]. During this membrane remodeling, HS-AFM imaging can be difficult due to lipid diffusion.

It is well documented that components of biological membranes are very dynamic and HS-AFM represents a very attractive tool to monitor 2D-diffusion in real time. It has already been used to investigate diffusion and dynamic interaction of membrane proteins [13] and a recent paper described the dynamics of lipid phases during transition [17]. HS-AFM is therefore an outstanding tool to probe cholesterol effects in membrane organization. Indeed this lipid plays a major role in the regulation of the fluidity and mechanical stiffness of membranes [23]. This ability of cholesterol to modulate the fluidity of membranes is thought to be important in the formation of membrane microdomains [24] and associated to many biological processes, including cell fusion [25] or development of Alzheimer's disease [26, 27] (in fact, the biological significance of cholesterol-induced changes in membrane fluidity is vast, and these reflect only a small proportion of affected areas). A glance into the benefit of using HS-AFM for imaging Chl-containing SLB is shown in Fig. 3 (right column) describing Chl effect on the basic DOPC/DPPC mixture. Using the vesicle fusion method, a mixture composed of DOPC/DPPC/Chl (1:1:0.35) led to the formation of ordered lipid domains surrounded by a fluid phase. The shape of ordered domains was a little bit different as compared to the DOPC/DPPC reference mixture with more round-shaped domains, most likely composed of DPPC in interaction with Chl. These two lipids are known to preferentially interact with each other as compared to the DOPC/Chl pair [28]. Chl is known to increase the fluidity of ordered domains (here DPPC) and probably reduced the line tension within the membrane, which supports the shape of ordered domains. The images captured with HS-AFM also showed that the membrane is dynamic and that DPPC/Chl

domains could diffuse in the fluid DOPC matrix and even coalesce to form larger domains (black arrow in Fig. 3g).

Using the Langmuir-Blodgett technique, phase-separated lipid membranes can also be observed on mica with a pattern that is similar to that obtained with SLB made using the vesicle fusion method (compare Figs. 3e and 4a). A DOPC matrix surrounded gel phase domains. SLBs obtained at 32 mN/m surface pressure covered about 80% of the whole investigated area, as shown in Fig. 4a, b. DPPC domains were relatively stable in shape and position as compared to mica area devoid of lipids. Membrane dynamics could nevertheless be observed in some places (black asterisks in Fig. 4a, b). Importantly we observed that membrane

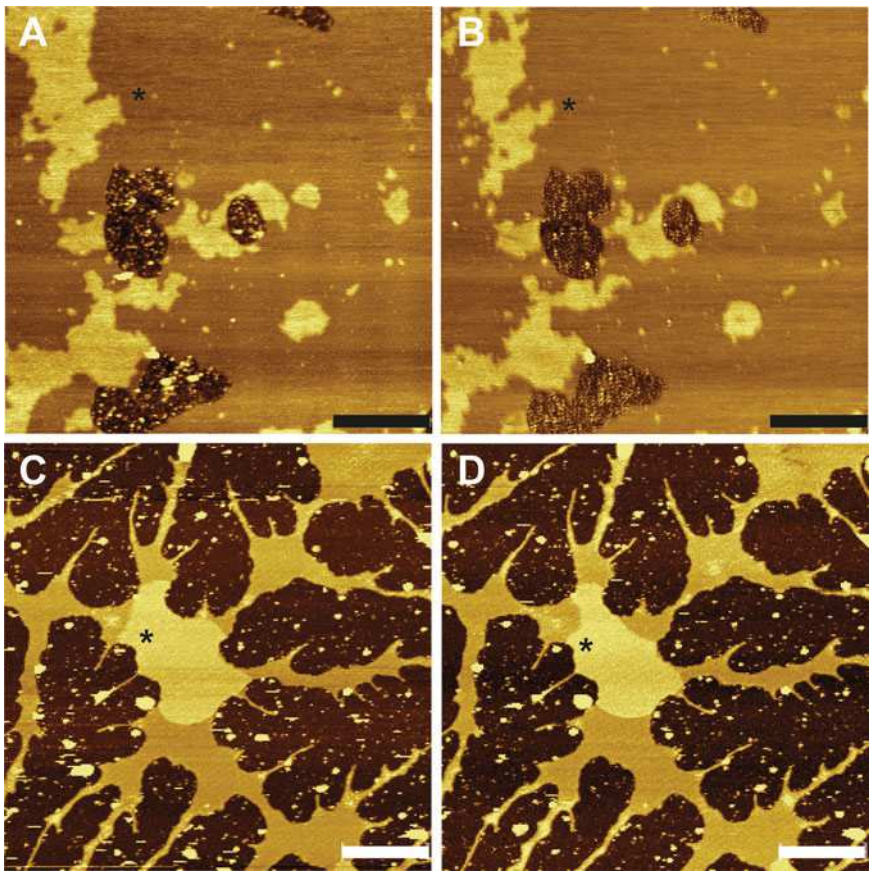

Fig. 4 HS-AFM imaging of DOPC/DPPC (1:1) SLB using Langmuir Blodgett technique. (**a**, **b**) Topography of a DOPC/DPPC bilayer supported on mica, transferred at 32 mN/m surface pressure. Three regions are clearly distinguishable, mica, DOPC, and DPPC, from the darkest to the brightest, respectively. The pattern is similar to SLB obtained by vesicle fusion and membrane covered ~80% mica surface. The black asterisk indicates an area where DPPC remodeling can be observed. The time between **a** and **b** is 30 s; (**c**, **d**) Topography of a DOPC/DPPC bilayer supported on mica, made at 12 mN/m surface pressure. Membrane coverage is lower as compared to **a** and **b** and large mica area are devoid of membrane (dark area). The time between **c** and **d** is 30 s. HS-AFM scan rate, 4 s/frame; scale bars, 1 μm

mica coverage depends on surface pressure transfer. Indeed decreasing surface pressure applied to the lipid film during the transfer to 12 mN/m led to a huge decrease in membrane coverage, below 30%. Under these conditions, membrane dynamics can be observed over time, e.g., DPPC domain remodeling in Fig. 4c, d. Such small membranes were very sensitive to tip scanning and membrane patches could be easily removed by the tip.

3.3 Conclusion and Perspectives

HS-AFM is assuredly an outstanding technique to probe both structure and dynamics of membrane assemblies. The shape of lipid domains can be easy delineated with the tip scanning at several images per second and HS-AFM is also very useful to study membrane-protein interactions in real time [29]. In the future, further improvements in scanning speed would help in better understanding membrane organization since lipid diffusion is very high (in the $\mu m^2/s$ range). In addition, SLB imaging with HS-AFM would benefit from its combination with fluorescence or Raman microscopy in order to identify membrane components delineated by the tip.

4 Notes

1. It is important to stress again that the small size of the sample holder is critical for SLB imaging using AFM. Some tricks similar to what we described in Fig. 1b need to be developed to prevent any evaporation or dewetting problems.
2. In Langmuir-Blodgett experiments, the optimal surface pressure obtained by plotting surface pressure-area isotherm depends on the composition in lipids of the monolayer and is established empirically (typically 30–35 mN/m for DOPC-DPPC). The surface pressure-area isotherm can also provide a measure of the average area per molecule and the compressibility of the monolayer.
3. Surface hydrophilicity of the PEEK plate can be increased by treating the dipping part by 172-nm Xenon excimer radiation to generate hydroxyl and carbonyl groups.
4. An important parameter to control is the power of the laser diode reflected on the cantilever. Therefore for laser over 0.2 mW for the Olympus cantilever and 0.4 mW for the Nanoworld cantilever, we could observe the melting of the DPPC phase, strongly suggesting that the temperature locally increases beneath the tip during imaging (no increase of temperature was recorded in the buffer bathing the cantilever). DPPC melting temperature is about 40 °C.

5. The composition of the buffer used for vesicle fusion has to be finely tuned for optimal mica coverage. For instance, adsorption of negatively charged vesicles made from a mixture of palmitoyl-oleoyl-phosphoglycerol (POPG)/palmitoyl-oleoyl-phosphatidyletha-nolamine (POPE) lipids on a mica (also negatively charged) is only possible in the presence of divalent cations [30].
6. It is sometimes useful to tune lipid concentration and fusion buffer composition for optimizing substrate coverage. The duration of SLB cooling-down can also influence vesicle fusion.
7. Tip contamination is one of the main problems, especially in HS-AFM where tip scanning is very rapid. Fortunately the EBD-functionalized tips can be easily cleaned using plasma etching [20].
8. Mica needs to be cleaved just before the addition of lipids.

Acknowledgments

The research has been supported by CNRS (PEM and EL), INSERM (PEM), Institut Carnot (EL), and by the ANR program (ANR-11-nano-009-04, ANR-08-NANO-010-03, ANR-08-PCVI-0003-02, the EpiGenMed Labex ANR-10-LABX-12-01 and the French Infrastructure for Integrated Structural Biology (FRISBI) ANR-10-INBS-05). We are grateful to our collaborators involved in the project, P. Dosset, J. Kokavecz, and C. Le Grimellec.

References

1. Kahya N (2006) Targeting membrane proteins to liquid-ordered phases: molecular self-organization explored by fluorescence correlation spectroscopy. Chem Phys Lipids 141:158–168
2. Sackmann E (1996) Supported membranes: scientific and practical applications. Science 271:43–48
3. Muller DJ (2008) AFM: a nanotool in membrane biology. Biochemistry 47:7986–7998
4. El Kirat K, Morandat S, Dufrêne Y (2010) Nanoscale analysis of supported lipid bilayers using atomic force microscopy. Biochim Biophys Acta 1798:750–765
5. Garcia-Manyes S, Sanz F (2010) Nanomechanics of lipid bilayers by force spectroscopy with AFM: a perspective. Biochim Biophys Acta 1798:741–749
6. Goksu EI, Vanegas JM, Blanchette CD, Lin WC, Longo ML (2009) AFM for structure and dynamics of biomembranes. Biochim Biophys Acta 1788:254–266
7. Johnston I, Johnston LJ (2006) Ceramide promotes restructuring of model raft membranes. Langmuir 22:11284–11289
8. Seantier B, Giocondi M, Le Grimellec C, Milhiet P (2008) Probing supporting model and native membranes using afm. Curr Opin Colloid Interface Sci 13:326–337
9. Giocondi M-C, Seantier B, Dosset P, Milhiet P-E, Le Grimellec C (2008) Characterizing the interactions between GPI-anchored alkaline phosphatases and membrane domains by AFM. Pflüg Arch Eur J Physiol 456:179–188
10. Levy D, Milhiet P-E (2013) Imaging of transmembrane proteins directly incorporated within supported lipid bilayers using atomic force microscopy. Methods Mol Biol 950:343–357

11. Czajkowsky DM, Hotze EM, Shao Z, Tweten RK (2004) Vertical collapse of a cytolysin prepore moves its transmembrane β-hairpins to the membrane. EMBO J 23:3206–3215
12. Yu C, Groves JT (2010) Engineering supported membranes for cell biology. Med Biol Eng Comput 48:955–963
13. Ando T, Uchihashi T, Scheuring S (2014) Filming biomolecular processes by high-speed atomic force microscopy. Chem Rev 114:3120–3188
14. Ando T, Uchihashi T, Kodera N, Yamamoto D, Miyagi A, Taniguchi M et al (2008) High-speed AFM and nano-visualization of biomolecular processes. Pflugers Arch 456:211–225
15. Giocondi MC, Yamamoto D, Lesniewska E, Milhiet PE, Ando T, Le Grimellec C (2010) Surface topography of membrane domains. Biochim Biophys Acta 1798:703–718
16. Yilmaz N, Kobayashi T (2015) Visualization of lipid membrane reorganization induced by a pore-forming toxin using high-speed atomic force microscopy. ACS Nano 9:7960–7967
17. Takahashi H, Miyagi A, Redondo-Morata L, Scheuring S (2016) Temperature-controlled high-speed AFM: real-time observation of ripple phase transitions. Small 12:6106–6113
18. McConnell HM, Watts TH, Weis RM, Brian AA (1986) Supported planar membranes in studies of cell-cell recognition in the immune system. Biochim Biophys Acta 864:95–106
19. Almeida PF, Vaz WL, Thompson TE (1992) Lateral diffusion and percolation in two-phase, two-component lipid bilayers. Topology of the solid-phase domains in-plane and across the lipid bilayer. Biochemistry 31:7198–7210
20. Uchihashi T, Kodera N, Ando T (2012) Guide to video recording of structure dynamics and dynamic processes of proteins by high-speed atomic force microscopy. Nat Protoc 7:1193–1206
21. Milhiet PE, Domec C, Giocondi MC, Van Mau N, Heitz F, Le Grimellec C (2001) Domain formation in models of the renal brush border membrane outer leaflet. Biophys J 81:547–555
22. Giocondi MC, Vié V, Lesniewska E, Milhiet PE, Zinke-Allmang M, Le Grimellec C (2001) Phase topology and growth of single domains in lipid bilayers. Langmuir 17:1653–1659
23. Needham D, McIntosh TJ, Evans E (1988) Thermomechanical and transition properties of dimyristoylphosphatidylcholine/cholesterol bilayers. Biochemistry 27:4668–4673
24. Brown DA, London E (1998) Functions of lipid rafts in biological membranes. Annu Rev Cell Dev Biol 14:111–136
25. Nakanishi M, Hirayama E, Kim J (2001) Characterisation of myogenic cell membrane: II. Dynamic changes in membrane lipids during the differentiation of mouse C2 myoblast cells. Cell Biol Int 25:971–979
26. Yip CM, Elton EA, Darabie AA, Morrison MR, McLaurin J (2001) Cholesterol, a modulator of membrane-associated Abeta-fibrillogenesis and neurotoxicity. J Mol Biol 311:723–734
27. Chochina SV, Avdulov NA, Igbavboa U, Cleary JP, O'Hare EO, Wood WG (2001) Amyloid beta-peptide1-40 increases neuronal membrane fluidity: role of cholesterol and brain region. J Lipid Res 42:1292–1297
28. Fritzsching KJ, Kim J, Holland GP (2013) Probing lipid-cholesterol interactions in DOPC/eSM/Chol and DOPC/DPPC/Chol model lipid rafts with DSC and (13)C solid-state NMR. Biochim Biophys Acta 1828:1889–1898
29. Rangl M, Rima L, Klement J, Miyagi A, Keller S, Scheuring S (2017) Real-time visualization of phospholipid degradation by outer membrane phospholipase a using high-speed atomic force microscopy. J Mol Biol 429:977–986
30. Picas L, Carretero-Genevrier A, Montero MT, Vazquez-Ibar JL, Seantier B, Milhiet PE et al (2010) Preferential insertion of lactose permease in phospholipid domains: AFM observations. Biochim Biophys Acta 1798:1014–1019

Bibliography

Allen, T. D. *et al.* (1997) 'Macromolecular substructure in nuclear pore complexes by in-lens field-emission scanning electron microscopy', *Scanning*, 19(6), pp. 403–410. doi: 10.1002/sca.4950190603.

Anderson, D. J. *et al.* (2009) 'Recruitment of functionally distinct membrane proteins to chromatin mediates nuclear envelope formation in vivo', *Journal of Cell Biology*, 186(2), pp. 183–191. doi: 10.1083/jcb.200901106.

Anderson, D. J. and Hetzer, M. W. (2007) 'Nuclear envelope formation by chromatin-mediated reorganization of the endoplasmic reticulum.', *Nature Cell Biology*, 9(10), pp. 1160–1166. doi: 10.1038/ncb1636.

Anderson, D. J. and Hetzer, M. W. (2008) 'Reshaping of the endoplasmic reticulum limits the rate for nuclear envelope formation', *Journal of Cell Biology*, 182(5), pp. 911–924. doi: 10.1083/jcb.200805140.

Antonin, W. *et al.* (2005) 'The integral membrane nucleoporin pom121 functionally links nuclear pore complex assembly and nuclear envelope formation', *Molecular Cell*, 17(1), pp. 83–92. doi: 10.1016/j.molcel.2004.12.010.

von Appen, A. *et al.* (2015) 'In situ structural analysis of the human nuclear pore complex', *Nature*, 526(7571), pp. 140–143. doi: 10.1038/nature15381.

Asally, M. *et al.* (2011) 'Nup358, a nucleoporin, functions as a key determinant of the nuclear pore complex structure remodeling during skeletal myogenesis', *FEBS Journal*, 278(4), pp. 610–621. doi: 10.1111/j.1742-4658.2010.07982.x.

Belgareh, N. *et al.* (2001) 'An evolutionarily conserved NPC subcomplex, which redistributes in part to kinetochores in mammalian cells', *Journal of Cell Biology*, 154(6), pp. 1147–1160. doi: 10.1083/jcb.200101081.

Bestembayeva, A. *et al.* (2015) 'Nanoscale stiffness topography reveals structure and mechanics of the transport barrier in intact nuclear pore complexes', *Nature Nanotechnology*, 10(1), pp. 60–64. doi: 10.1038/nnano.2014.262.

Betzig, E. *et al.* (2006) 'Imaging intracellular fluorescent proteins at nanometer resolution', *Science*, 313(5793), pp. 1642–1645. doi: 10.1126/science.1127344.

Bolhy, S. *et al.* (2011) 'A Nup133-dependent NPC-anchored network tethers centrosomes to the nuclear envelope in prophase', *Journal of Cell Biology*, 192(5), pp. 855–871. doi: 10.1083/jcb.201007118.

Brohawn, S. G. *et al.* (2009) 'The Nuclear Pore Complex Has Entered the Atomic Age', *Structure*, 17(9), pp. 1156–1168. doi: 10.1016/j.str.2009.07.014.

Callan, H. G., Randall, J. T. and Tomlin, S. G. (1949) 'An electron microscope study of the nuclear membrane [1]', *Nature*, p. 280. doi: 10.1038/163280a0.

Capelson, M. *et al.* (2010) 'Chromatin-Bound Nuclear Pore Components Regulate Gene Expression in Higher Eukaryotes', *Cell*, 140(3), pp. 372–383. doi: 10.1016/j.cell.2009.12.054.

Chatel, G. and Fahrenkrog, B. (2011) 'Nucleoporins: Leaving the nuclear pore complex for a successful mitosis', *Cellular Signalling*. Elsevier Inc., 23(10), pp. 1555–1562. doi: 10.1016/j.cellsig.2011.05.023.

Chatton, E. (1925) Pansporella perplexa: Réflexions sur la Biologie et la Phylogénie des Protozoaires

Collart-Dutilleul, P. Y. *et al.* (2014) 'Initial stem cell adhesion on porous silicon surface: molecular architecture of actin cytoskeleton and filopodial growth', *Nanoscale Research Letters*, 9(1), pp. 1–10. doi: 10.1186/1556-276X-9-564.

D'Angelo, M. A. *et al.* (2006) 'Nuclear pores form de novo from both sides of the nuclear envelope', *Science*, 312(5772), pp. 440–443. doi: 10.1126/science.1124196.

D'Angelo, M. A. *et al.* (2012) 'A Change in Nuclear Pore Complex Composition Regulates Cell

Differentiation', *Developmental Cell*. Elsevier Inc., 22(2), pp. 446–458. doi: 10.1016/j.devcel.2011.11.021.

D'Angelo, M. A. (2018) 'Nuclear pore complexes as hubs for gene regulation', *Nucleus*. Taylor & Francis, 9(1), pp. 142–148. doi: 10.1080/19491034.2017.1395542.

Dahmane, S. *et al.* (2019) 'Nanoscale organization of tetraspanins during HIV-1 budding by correlative dSTORM/AFM', *Nanoscale*. Royal Society of Chemistry, 11(13), pp. 6036–6044. doi: 10.1039/C8NR07269H.

Davis, L. I. and Blobel, G. (1986) 'Identification and characterization of a nuclear pore complex protein', *Cell*, 45(5), pp. 699–709. doi: 10.1016/0092-8674(86)90784-1.

Dawlaty, M. M. *et al.* (2008) 'Resolution of Sister Centromeres Requires RanBP2-Mediated SUMOylation of Topoisomerase IIα', *Cell*, 133(1), pp. 103–115. doi: 10.1016/j.cell.2008.01.045.

Dawson, T. R. *et al.* (2009) 'ER membrane - bending proteins are necessary for de novo nuclear pore formation', *Journal of Cell Biology*, 184(5), pp. 659–675. doi: 10.1083/jcb.200806174.

Doucet, C. M. *et al.* (2015) 'Membrane curvature sensing by amphipathic helices is modulated by the surrounding protein backbone', *PLoS ONE*, 10(9), pp. 1–24. doi: 10.1371/journal.pone.0137965.

Doucet, C. M. and Hetzer, M. W. (2010) 'Nuclear pore biogenesis into an intact nuclear envelope', *Chromosoma*, 119(5), pp. 469–477. doi: 10.1007/s00412-010-0289-2.

Doucet, C. M., Talamas, J. A. and Hetzer, M. W. (2010) 'Cell cycle-dependent differences in nuclear pore complex assembly in metazoa', *Cell*. Elsevier Ltd, 141(6), pp. 1030–1041. doi: 10.1016/j.cell.2010.04.036.

Dultz, E. *et al.* (2008) 'Systematic kinetic analysis of mitotic dis- and reassembly of the nuclear pore in living cells', *Journal of Cell Biology*, 180(5), pp. 857–865. doi: 10.1083/jcb.200707026.

Dultz, E. and Ellenberg, J. (2010) 'Live imaging of single nuclear pores reveals unique assembly kinetics and mechanism in interphase', *Journal of Cell Biology*, 191(1), pp. 15–22. doi: 10.1083/jcb.201007076.

Eisenhardt, N., Redolfi, J. and Antonin, W. (2014) 'Interaction of Nup53 with Ndc1 and Nup155 is required for nuclear pore complex assembly', *Journal of Cell Science*, 127(4), pp. 908–921. doi: 10.1242/jcs.141739.

Elosegui-Artola, A. *et al.* (2017) 'Force Triggers YAP Nuclear Entry by Regulating Transport across Nuclear Pores', *Cell*. Elsevier Inc., 171(6), pp. 1397-1410.e14. doi: 10.1016/j.cell.2017.10.008.

Eriksson, C., Rustum, C. and Hallberg, E. (2004) 'Dynamic properties of nuclear pore complex proteins in gp210 deficient cells', *FEBS Letters*, 572(1–3), pp. 261–265. doi: 10.1016/j.febslet.2004.07.044.

Fernandez-Martinez, J. *et al.* (2016a) 'Structure and Function of the Nuclear Pore Complex Cytoplasmic mRNA Export Platform', *Cell*. Elsevier Inc., 167(5), pp. 1215-1228.e25. doi: 10.1016/j.cell.2016.10.028.

Fernandez-Martinez, J. *et al.* (2016b) 'Structure and Function of the Nuclear Pore Complex Cytoplasmic mRNA Export Platform', *Cell*. Elsevier Inc., 167(5), pp. 1215-1228.e25. doi: 10.1016/j.cell.2016.10.028.

Fichtman, B. *et al.* (2010) 'Inner/outer nuclear membrane fusion in nuclear pore assembly: Biochemical demonstration and molecular analysis', *Molecular Biology of the Cell*, 21(23), pp. 4197–4211. doi: 10.1091/mbc.E10-04-0309.

Field, M. C. and Rout, M. P. (2019) 'Pore timing: the evolutionary origins of the nucleus and nuclear pore complex', *F1000Research*, 8, p. 369. doi: 10.12688/f1000research.16402.1.

Franks, T. M. *et al.* (2016) 'Evolution of a transcriptional regulator from a transmembrane nucleoporin', *Genes and Development*, 30(10), pp. 1155–1171. doi: 10.1101/gad.280941.116.

Franz, C. *et al.* (2007) 'MEL-28/ELYS is required for the recruitment of nucleoporins to chromatin and postmitotic nuclear pore complex assembly', *EMBO Reports*, 8(2), pp. 165–172. doi: 10.1038/sj.embor.7400889.

Frey, S., Richter, R. P. and Görlich, D. (2006) 'FG-rich repeats of nuclear pore proteins form a three-

dimensional meshwork with hydrogel-like properties', *Science*, 314(5800), pp. 815–817. doi: 10.1126/science.1132516.

Funakoshi, T. *et al.* (2011) 'Localization of Pom121 to the inner nuclear membrane is required for an early step of interphase nuclear pore complex assembly', *Molecular Biology of the Cell*, 22(7), pp. 1058–1069. doi: 10.1091/mbc.E10-07-0641.

Gall, J. G. (1967) 'Octagonal nuclear pores.', *The Journal of cell biology*, 32(2), pp. 391–399. doi: 10.1083/jcb.32.2.391.

Göttfert, F. *et al.* (2013) 'Coaligned dual-channel STED nanoscopy and molecular diffusion analysis at 20 nm resolution', *Biophysical Journal*, 105(1), pp. 6–8. doi: 10.1016/j.bpj.2013.05.029.

Griffis, E. R. *et al.* (2002) 'Nup98 Is a Mobile Nucleoporin with Transcription-dependent Dynamics', *Molecular Biology of the Cell*. Edited by J. Gall, 13(4), pp. 1282–1297. doi: 10.1091/mbc.01-11-0538.

Gwosch, K. C. *et al.* (2019) 'MINFLUX nanoscopy delivers multicolor nanometer 3D-resolution in (living) cells', *bioRxiv*. Springer US, p. 734251. doi: 10.1101/734251.

Hakhverdyan, Z. *et al.* (2021) 'Dissecting the Structural Dynamics of the Nuclear Pore Complex', *Molecular Cell*, 81(1), pp. 153-165.e7. doi: 10.1016/j.molcel.2020.11.032.

Hampoelz, B. *et al.* (2016) 'Pre-assembled Nuclear Pores Insert into the Nuclear Envelope during Early Development', *Cell*, 166(3), pp. 664–678. doi: 10.1016/j.cell.2016.06.015.

Hase, M. E. and Cordes, V. C. (2003) 'Direct interaction with nup153 mediates binding of Tpr to the periphery of the nuclear pore complex.', *Molecular biology of the cell*, 14(5), pp. 1923–40. doi: 10.1091/mbc.e02-09-0620.

Hase, M. E., Kuznetsov, N. V. and Cordes, V. C. (2001) 'Amino acid substitutions of coiled-coil protein Tpr abrogate anchorage to the nuclear pore complex but not parallel, in-register homodimerization', *Molecular Biology of the Cell*, 12(8), pp. 2433–2452. doi: 10.1091/mbc.12.8.2433.

Hawryluk-Gara, L. A. *et al.* (2008) 'Nup53 Is Required for Nuclear Envelope and Nuclear Pore Complex Assembly', *Molecular Biology of the Cell*. Edited by K. Weis, 19(4), pp. 1753–1762. doi: 10.1091/mbc.e07-08-0820.

Hawryluk-Gara, L. A., Shibuya, E. K. and Wozniak, R. W. (2005) 'Vertebrate Nup53 Interacts with the Nuclear Lamina and Is Required for the Assembly of a Nup93-containing Complex', *Molecular Biology of the Cell*, 16(5), pp. 2382–2394. doi: 10.1091/mbc.e04-10-0857.

Heilemann, M. *et al.* (2008) 'Subdiffraction-resolution fluorescence imaging with conventional fluorescent probes', *Angewandte Chemie - International Edition*, 47(33), pp. 6172–6176. doi: 10.1002/anie.200802376.

Hell, S. W. and Wichmann, J. (1994) 'Breaking the diffraction resolution limit by stimulated emission: stimulated-emission-depletion fluorescence microscopy', *Optics Letters*, 19(11), p. 780. doi: 10.1364/ol.19.000780.

Hess, S. T., Girirajan, T. P. K. and Mason, M. D. (2006) 'Ultra-high resolution imaging by fluorescence photoactivation localization microscopy', *Biophysical Journal*, 91(11), pp. 4258–4272. doi: 10.1529/biophysj.106.091116.

Hezwani, M. and Fahrenkrog, B. (2017) 'The functional versatility of the nuclear pore complex proteins', *Seminars in Cell and Developmental Biology*. Elsevier Ltd, 68, pp. 2–9. doi: 10.1016/j.semcdb.2017.05.004.

Huang, G. *et al.* (2020) 'Structure of the cytoplasmic ring of the Xenopus laevis nuclear pore complex by cryo-electron microscopy single particle analysis', *Cell Research*. Springer US, 30(6), pp. 520–531. doi: 10.1038/s41422-020-0319-4.

Imachi, H. *et al.* (2020) 'Isolation of an archaeon at the prokaryote–eukaryote interface', *Nature*. Springer US, 577(7791), pp. 519–525. doi: 10.1038/s41586-019-1916-6.

Israelachvili, J. N. (1992) 'Israelachvili J.N. Intermolecular and surface forces (AP 1992).pdf'.

Jacinto, F. V., Benner, C. and Hetzer, M. W. (2015) 'The nucleoporin Nup153 regulates embryonic stem cell pluripotency through gene silencing', *Genes and Development*, 29(12), pp. 1224–1238. doi: 10.1101/gad.260919.115.

Jäggi, R. D., Franco-Obregón, A. and Ensslin, K. (2003) 'Quantitative Topographical Analysis of Nuclear Pore Complex Function Using Scanning Force Microscopy', *Biophysical Journal*, 85(6), pp. 4093–4098. doi: 10.1016/S0006-3495(03)74821-8.

Jahed, Z. *et al.* (2016) 'The LINC and NPC relationship - it's complicated!', *Journal of Cell Science*, 129(17), pp. 3219–3229. doi: 10.1242/jcs.184184.

Jarnik, M. and Aebi, U. (1991) 'Toward a more complete 3-D structure of the nuclear pore complex', *Journal of Structural Biology*, 107(3), pp. 291–308. doi: 10.1016/1047-8477(91)90054-Z.

Joseph, J. *et al.* (2004) 'The RanGAP1-RanBP2 Complex Is Essential for Microtubule-Kinetochore Interactions In Vivo', *Current Biology*, 14(7), pp. 611–617. doi: 10.1016/j.cub.2004.03.031.

Kalverda, B. *et al.* (2010) 'Nucleoporins Directly Stimulate Expression of Developmental and Cell-Cycle Genes Inside the Nucleoplasm', *Cell*, 140(3), pp. 360–371. doi: 10.1016/j.cell.2010.01.011.

Kehat, I. *et al.* (2011) 'Modulation of chromatin position and gene expression by HDAC4 interaction with nucleoporins', *Journal of Cell Biology*, 193(1), pp. 21–29. doi: 10.1083/jcb.201101046.

Khater, I. M., Nabi, I. R. and Hamarneh, G. (2020) 'A Review of Super-Resolution Single-Molecule Localization Microscopy Cluster Analysis and Quantification Methods', *Patterns*. Elsevier Inc., 1(3), p. 100038. doi: 10.1016/j.patter.2020.100038.

Kim, S. J. *et al.* (2018) 'Integrative structure and functional anatomy of a nuclear pore complex', *Nature*. Nature Publishing Group. doi: 10.1038/nature26003.

Knockenhauer, K. E. and Schwartz, T. U. (2016) 'The Nuclear Pore Complex as a Flexible and Dynamic Gate', *Cell*. Elsevier Inc., 164(6), pp. 1162–1171. doi: 10.1016/j.cell.2016.01.034.

Kosinski, J. *et al.* (2016) 'Molecular architecture of the inner ring scaffold of the human nuclear pore complex.', *Science (New York, N.Y.)*, 352(6283), pp. 363–5. doi: 10.1126/science.aaf0643.

Kramer, A. *et al.* (2007) 'A pathway separate from the central channel through the nuclear pore complex for inorganic ions and small macromolecules', *Journal of Biological Chemistry*, 282(43), pp. 31437–31443. doi: 10.1074/jbc.M703720200.

Kramer, A. *et al.* (2008) 'Apoptosis leads to a degradation of vital components of active nuclear transport and a dissociation of the nuclear lamina.', *Proceedings of the National Academy of Sciences of the United States of America*, 105(32), pp. 11236–41. doi: 10.1073/pnas.0801967105.

Krull, S. *et al.* (2004) 'Nucleoporins as Components of the Nuclear Pore Complex Core Structure and Tpr as the Architectural Element of the Nuclear Basket', *Molecular Biology of the Cell*, 15(9), pp. 4261–4277. doi: 10.1091/mbc.e04-03-0165.

Kuznetsov, N. V. *et al.* (2002) 'The evolutionarily conserved single-copy gene for murine Tpr encodes one prevalent isoform in somatic cells and lacks paralogs in higher eukaryotes', *Chromosoma*, 111(4), pp. 236–255. doi: 10.1007/s00412-002-0208-2.

Lau, C. K., Delmar, V. A. and Forbes, D. J. (2006) 'Topology of yeast Ndc1p: Predictions for the human NDC1/NET3 homologue', *Anatomical Record - Part A Discoveries in Molecular, Cellular, and Evolutionary Biology*, 288(7), pp. 681–694. doi: 10.1002/ar.a.20335.

Lautier, O. *et al.* (2021) 'Co-translational assembly and localized translation of nucleoporins in nuclear pore complex biogenesis', *Molecular Cell*, pp. 1–11. doi: 10.1016/j.molcel.2021.03.030.

Lénárt, P. and Ellenberg, J. (2003) 'Nuclear envelope dynamics in oocytes: From germinal vesicle breakdown to mitosis', *Current Opinion in Cell Biology*, 15(1), pp. 88–95. doi: 10.1016/S0955-0674(02)00011-X.

Lewin, J. M. *et al.* (2007) 'The Direct Effect of Nuclear Pores on Nuclear Chemotherapeutic Concentration in Multidrug Resistant Bladder Cancer: The Nuclear Sparing Phenomenon', *Journal of Urology*, 177(4), pp. 1526–1530. doi: 10.1016/j.juro.2006.11.048.

Liang, Y. *et al.* (2013) 'Dynamic Association of NUP98 with the Human Genome', *PLoS Genetics*, 9(2). doi: 10.1371/journal.pgen.1003308.

Liashkovich, I. *et al.* (2011) 'Exceptional structural and mechanical flexibility of the nuclear pore complex', *Journal of Cellular Physiology*, 226(3), pp. 675–682. doi: 10.1002/jcp.22382.

Liashkovich, I. *et al.* (2012) 'Structural organization of the nuclear pore permeability barrier', *Journal of*

Controlled Release. Elsevier B.V., 160(3), pp. 601–608. doi: 10.1016/j.jconrel.2012.02.016.

Liashkovich, I. *et al.* (2015) 'Clathrin inhibitor Pitstop-2 disrupts the nuclear pore complex permeability barrier', *Scientific Reports*. Nature Publishing Group, 5, pp. 1–9. doi: 10.1038/srep09994.

Liashkovich, I. and Shahin, V. (2017) 'Functional implication of the common evolutionary origin of nuclear pore complex and endomembrane management systems', *Seminars in Cell and Developmental Biology*. Elsevier Ltd, 68, pp. 10–17. doi: 10.1016/j.semcdb.2017.04.006.

Lim, K. S. and Wong, R. W. (2018) 'Targeting Nucleoporin POM121-Importin β Axis in Prostate Cancer', *Cell Chemical Biology*. Elsevier Ltd, 25(9), pp. 1056–1058. doi: 10.1016/j.chembiol.2018.09.003.

Lin, D. H. and Hoelz, A. (2019) 'The Structure of the Nuclear Pore Complex (An Update)', *Annual Review of Biochemistry*, 88(1), pp. 725–783. doi: 10.1146/annurev-biochem-062917-011901.

Liu, H.-L. *et al.* (2009) 'The three fungal transmembrane nuclear pore complex proteins of Aspergillus nidulans are dispensable in the presence of an intact An-Nup84-120 complex.', *Molecular biology of the cell*, 20(2), pp. 616–30. doi: 10.1091/mbc.e08-06-0628.

Liu, Q. *et al.* (2007) 'Functional association of Sun1 with nuclear pore complexes', *Journal of Cell Biology*, 178(5), pp. 785–798. doi: 10.1083/jcb.200704108.

Löschberger, A. *et al.* (2014) 'Correlative super-resolution fluorescence and electron microscopy of the nuclear pore complex with molecular resolution', *Journal of Cell Science*, 127(20), pp. 4351–4355. doi: 10.1242/jcs.156620.

Lussi, Y. C. *et al.* (2010) 'The nucleoporin Nup153 affects spindle checkpoint activity due to an association with Mad1', *Nucleus*, 1(1), pp. 71–84. doi: 10.4161/nucl.1.1.10244.

Mackay, D. R., Elgort, S. W. and Ullman, K. S. (2009) 'The Nucleoporin Nup153 Has Separable Roles in Both Early Mitotic Progression and the Resolution of Mitosis', *Molecular Biology of the Cell*. Edited by S. L. Schmid, 20(6), pp. 1652–1660. doi: 10.1091/mbc.e08-08-0883.

Mansfeld, J. *et al.* (2006) 'The Conserved Transmembrane Nucleoporin NDC1 Is Required for Nuclear Pore Complex Assembly in Vertebrate Cells', *Molecular Cell*, 22(1), pp. 93–103. doi: 10.1016/j.molcel.2006.02.015.

Many, M. C. *et al.* (1981) 'Morphometry of nuclear pore complexes in thyroid cells during hyperplasia and involution', *Molecular and Cellular Endocrinology*, 23(2), pp. 137–149. doi: 10.1016/0303-7207(81)90065-4.

Marelli, M. *et al.* (2001) 'A link between the synthesis of nucleoporins and the biogenesis of the nuclear envelope', *Journal of Cell Biology*, 153(4), pp. 709–723. doi: 10.1083/jcb.153.4.709.

Martins, F. *et al.* (2020) 'Nuclear envelope dysfunction and its contribution to the aging process', *Aging Cell*, 19(5), pp. 1–17. doi: 10.1111/acel.13143.

Mateos-Langerak, J. *et al.* (2007) 'Nuclear architecture: Is it important for genome function and can we prove it?', *Journal of Cellular Biochemistry*, 102(5), pp. 1067–1075. doi: 10.1002/jcb.21521.

Maul, G. G. *et al.* (1972) 'Time sequence of nuclear pore formation in phytohemagglutinin-stimulated lymphocytes and in hela cells during the cell cycle', *Journal of Cell Biology*, 55(2), pp. 433–447. doi: 10.1083/jcb.55.2.433.

Maul, G. G., Price, J. W. and Lieberman, M. W. (1971) 'Formation and distribution of nuclear pore complexes in interphase', *Journal of Cell Biology*, 51(2), pp. 405–418. doi: 10.1083/jcb.51.2.405.

McCloskey, A., Ibarra, A. and Hetzer, M. W. (2018) 'Tpr regulates the total number of nuclear pore complexes per cell nucleus.', *Genes & development*, pp. 1–11. doi: 10.1101/gad.315523.118.

Mészáros, N. *et al.* (2015) 'Nuclear Pore Basket Proteins Are Tethered to the Nuclear Envelope and Can Regulate Membrane Curvature', *Developmental Cell*, 33(3), pp. 285–298. doi: 10.1016/j.devcel.2015.02.017.

Mimura, Y. *et al.* (2017) 'A statistical image analysis framework for pore-free islands derived from heterogeneity distribution of nuclear pore complexes', *Scientific Reports*. Springer US, 7(1), pp. 1–14. doi: 10.1038/s41598-017-16386-2.

Mohamed, M. S. *et al.* (2017) 'High-Speed Atomic Force Microscopy Reveals Loss of Nuclear Pore

Resilience as a Dying Code in Colorectal Cancer Cells', *ACS Nano*, p. acsnano.7b00906. doi: 10.1021/acsnano.7b00906.

Mohamed, M. S. *et al.* (2020) 'Spatiotemporally tracking of nano-biofilaments inside the nuclear pore complex core', *Biomaterials*. Elsevier, 256(December 2019), p. 120198. doi: 10.1016/j.biomaterials.2020.120198.

Olsson, M., Schéele, S. and Ekblom, P. (2004) 'Limited expression of nuclear pore membrane glycoprotein 210 in cell lines and tissues suggests cell-type specific nuclear pores in metazoans', *Experimental Cell Research*, 292(2), pp. 359–370. doi: 10.1016/j.yexcr.2003.09.014.

Onischenko, E. *et al.* (2017) 'Natively Unfolded FG Repeats Stabilize the Structure of the Nuclear Pore Complex', *Cell*. Elsevier Inc., 171(4), pp. 904-917.e19. doi: 10.1016/j.cell.2017.09.033.

Onischenko, E. *et al.* (2020) 'Maturation Kinetics of a Multiprotein Complex Revealed by Metabolic Labeling', *Cell*. Elsevier Inc., 183(7), pp. 1785-1800.e26. doi: 10.1016/j.cell.2020.11.001.

Ori, A. *et al.* (2013) 'Cell type-specific nuclear pores: a case in point for context-dependent stoichiometry of molecular machines.', *Molecular systems biology*, 9(1), p. 648. doi: 10.1038/msb.2013.4.

Ori, A., Andrés-Pons, A. and Beck, M. (2014) 'The use of targeted proteomics to determine the stoichiometry of large macromolecular assemblies', *Methods in Cell Biology*, 122, pp. 117–146. doi: 10.1016/B978-0-12-417160-2.00006-0.

Otsuka, S. *et al.* (2016) 'Nuclear pore assembly proceeds by an inside-out extrusion of the nuclear envelope', *eLife*, 5(September2016), pp. 1–23. doi: 10.7554/eLife.19071.

Otsuka, S. *et al.* (2018) 'Postmitotic nuclear pore assembly proceeds by radial dilation of small membrane openings', *Nature Structural and Molecular Biology*. Springer US, 25(1), pp. 21–28. doi: 10.1038/s41594-017-0001-9.

Otsuka, S. and Ellenberg, J. (2018) 'Mechanisms of nuclear pore complex assembly – two different ways of building one molecular machine', *FEBS Letters*, 592(4), pp. 475–488. doi: 10.1002/1873-3468.12905.

Otsuka, S. *et al.* (2021) A quantitative map of nuclear pore assembly reveals two distinct mechanisms, *bioRxiv* doi: 10.1101/2021.05.17.444137

Pal, K. *et al.* (2017) 'Structural Basis of TPR-Mediated Oligomerization and Activation of Oncogenic Fusion Kinases', *Structure*. Elsevier Ltd., 25(6), pp. 867-877.e3. doi: 10.1016/j.str.2017.04.015.

Patel, S. S. *et al.* (2007) 'Natively Unfolded Nucleoporins Gate Protein Diffusion across the Nuclear Pore Complex', *Cell*, 129(1), pp. 83–96. doi: 10.1016/j.cell.2007.01.044.

Ponten, J. and Saksela, E. (1967) 'Two established in vitro cell lines from human mesenchymal tumours', *International Journal of Cancer*, 2(5), pp. 434–447. doi: 10.1002/ijc.2910020505.

Rabut, G., Doye, V. and Ellenberg, J. (2004) 'Mapping the dynamic organization of the nuclear pore complex inside single living cells', *Nature Cell Biology*, 6(11), pp. 1114–1121. doi: 10.1038/ncb1184.

Raices, M. and D'Angelo, M. A. (2017) 'Nuclear pore complexes and regulation of gene expression', *Current Opinion in Cell Biology*, 46, pp. 26–32. doi: 10.1016/j.ceb.2016.12.006.

Rampello, A. J. *et al.* (2020) 'Torsin ATPase deficiency leads to defects in nuclear pore biogenesis and sequestration of MLF2', *Journal of Cell Biology*, 219(6). doi: 10.1083/JCB.201910185.

Rasala, B. A. *et al.* (2006) 'ELYS is a dual nucleoporin/kinetochore protein required for nuclear pore assembly and proper cell division', *Proceedings of the National Academy of Sciences of the United States of America*, 103(47), pp. 17801–17806. doi: 10.1073/pnas.0608484103.

Rico, F. *et al.* (2005) 'Probing mechanical properties of living cells by atomic force microscopy with blunted pyramidal cantilever tips', *Physical Review E - Statistical, Nonlinear, and Soft Matter Physics*, 72(2), pp. 1–10. doi: 10.1103/PhysRevE.72.021914.

Ries, J. (2020) 'SMAP: a modular super-resolution microscopy analysis platform for SMLM data', *Nature Methods*. Springer US, 17(9), pp. 870–872. doi: 10.1038/s41592-020-0938-1.

Rodriguez-Bravo, V. *et al.* (2018) 'Nuclear Pores Promote Lethal Prostate Cancer by Increasing POM121-Driven E2F1, MYC, and AR Nuclear Import', *Cell*. Elsevier Inc., 174(5), pp. 1200-1215.e20.

doi: 10.1016/j.cell.2018.07.015.

Rothballer, A., Schwartz, T. U. and Kutay, U. (2013) 'LINCing complex functions at the nuclear envelope', *Nucleus*, 4(1), pp. 29–36. doi: 10.4161/nucl.23387.

Rout, M. P. and Field, M. C. (2017) 'The Evolution of Organellar Coat Complexes and Organization of the Eukaryotic Cell', *Annual Review of Biochemistry*, 86(1), pp. 637–657. doi: 10.1146/annurev-biochem-061516-044643.

Rust, M. J., Bates, M. and Zhuang, X. (2006) 'Sub-diffraction-limit imaging by stochastic optical reconstruction microscopy (STORM)', *Nature Methods*, 3(10), pp. 793–795. doi: 10.1038/nmeth929.

Sabinina, V. J. *et al.* (2021) 'Three-dimensional superresolution fluorescence microscopy maps the variable molecular architecture of the nuclear pore complex', *Molecular Biology of the Cell*. Edited by J. Lippincott-Schwartz, 32(17), pp. 1523–1533. doi: 10.1091/mbc.E20-11-0728.

Sakiyama, Y. *et al.* (2016) 'Spatiotemporal dynamics of the nuclear pore complex transport barrier resolved by high-speed atomic force microscopy', *Nature Nanotechnology*. Nature Publishing Group, 11(May), pp. 1–6. doi: 10.1038/nnano.2016.62.

Sakuma, S. *et al.* (2021) 'Inhibition of Nuclear Pore Complex Formation Selectively Induces Cancer Cell Death', *Cancer Discovery*, 11(1), pp. 176–193. doi: 10.1158/2159-8290.CD-20-0581.

De Sandre-Giovannoli, A. *et al.* (2003) 'Lamin A truncation in Hutchinson-Gilford progeria', *Science*, 300(5628), p. 2055. doi: 10.1126/science.1084125.

Sang, H. L. *et al.* (2008) 'Tpr directly binds to Mad1 and Mad2 and is important for the Mad1-Mad2-mediated mitotic spindle checkpoint', *Genes and Development*, 22(21), pp. 2926–2931. doi: 10.1101/gad.1677208.

Sapp, J. (2005) 'The Prokaryote-Eukaryote Dichotomy: Meanings and Mythology', *Microbiology and Molecular Biology Reviews*, 69(2), pp. 292–305. doi: 10.1128/mmbr.69.2.292-305.2005.

Savas, J. N. *et al.* (2012) 'Extremely long-lived nuclear pore proteins in the rat brain', *Science*, 335(6071), p. 942. doi: 10.1126/science.1217421.

Savulescu, A. F. *et al.* (2011) 'Nuclear import of an intact preassembled proteasome particle', *Molecular Biology of the Cell*. Edited by M. W. Hetzer, 22(6), pp. 880–891. doi: 10.1091/mbc.e10-07-0595.

Schillers, H. *et al.* (2017) 'Standardized Nanomechanical Atomic Force Microscopy Procedure (SNAP) for Measuring Soft and Biological Samples', *Scientific Reports*, 7(1), pp. 1–9. doi: 10.1038/s41598-017-05383-0.

Schlune, A. *et al.* (2006) 'Plugs in nuclear pores: Transcripts in early oocyte development identified with nanotechniques', *Journal of Cellular Biochemistry*, 98(3), pp. 567–576. doi: 10.1002/jcb.20742.

Schmidt, H. B. and Görlich, D. (2016) 'Transport Selectivity of Nuclear Pores, Phase Separation, and Membraneless Organelles', *Trends in Biochemical Sciences*. Elsevier Ltd, 41(1), pp. 46–61. doi: 10.1016/j.tibs.2015.11.001.

Schwartz, T. U. (2016) 'The Structure Inventory of the Nuclear Pore Complex', *Journal of Molecular Biology*, 428(10), pp. 1986–2000. doi: 10.1016/j.jmb.2016.03.015.

Sellés, J. *et al.* (2017) 'Nuclear pore complex plasticity during developmental process as revealed by super-resolution microscopy', *Scientific Reports*, 7(1), pp. 1–8. doi: 10.1038/s41598-017-15433-2.

Sommerville, J. (2010) 'Using oocyte nuclei for studies on chromatin structure and gene expression', *Methods*. Elsevier Inc., 51(1), pp. 157–164. doi: 10.1016/j.ymeth.2010.02.002.

Soupart, P. and Strong, P. A. (1974) 'Ultrastructural observations on human oocytes fertilized in vitro', *Fertility and Sterility*. Elsevier Masson SAS, 25(1), pp. 11–44. doi: 10.1016/s0015-0282(16)40150-0.

Souquet, B. *et al.* (2018) 'Nup133 Is Required for Proper Nuclear Pore Basket Assembly and Dynamics in Embryonic Stem Cells', *Cell Reports*, pp. 2443–2454. doi: 10.1016/j.celrep.2018.04.070.

Spindler, M. and Hemleben, C. (1982) 'Formation and possible function of annulate lamellae in a planktic foraminifer', *Journal of Ultrasructure Research*, 81(3), pp. 341–350. doi: 10.1016/S0022-5320(82)90062-4.

Splinter, D. *et al.* (2010) 'Bicaudal D2, dynein, and kinesin-1 associate with nuclear pore complexes and regulate centrosome and nuclear positioning during mitotic entry', *PLoS Biology*, 8(4). doi: 10.1371/journal.pbio.1000350.

Stanley, G. J. *et al.* (2019) 'Quantification of Biomolecular Dynamics Inside Real and Synthetic Nuclear Pore Complexes Using Time-Resolved Atomic Force Microscopy', *ACS Nano*, 13(7), pp. 7949–7956. doi: 10.1021/acsnano.9b02424.

Stanley, G. J., Fassati, A. and Hoogenboom, B. W. (2017) 'Biomechanics of the transport barrier in the nuclear pore complex', *Seminars in Cell and Developmental Biology*. Elsevier Ltd, 68, pp. 42–51. doi: 10.1016/j.semcdb.2017.05.007.

Stanley, G. J., Fassati, A. and Hoogenboom, B. W. (2018) 'Atomic force microscopy reveals structural variability amongst nuclear pore complexes', *Life Science Alliance*, 1(4), p. e201800142. doi: 10.26508/lsa.201800142.

Stavru, F. *et al.* (2006) 'Nuclear pore complex assembly and maintenance in POM121- and gp210-deficient cells', *Journal of Cell Biology*, 173(4), pp. 477–483. doi: 10.1083/jcb.200601002.

Strawn, L. A. *et al.* (2004) 'Minimal nuclear pore complexes define FG repeat domains essential for transport', *Nature Cell Biology*, 6(3), pp. 197–206. doi: 10.1038/ncb1097.

Talamas, J. A. and Hetzer, M. W. (2011) 'POM121 and sun1 play a role in early steps of interphase NPC assembly', *Journal of Cell Biology*, 194(1), pp. 27–37. doi: 10.1083/jcb.201012154.

Thevathasan, J. V. *et al.* (2019) 'Nuclear pores as versatile reference standards for quantitative superresolution microscopy', *Nature Methods*, 16(10), pp. 1045–1053. doi: 10.1038/s41592-019-0574-9.

Thompson, R. E., Larson, D. R. and Webb, W. W. (2002) 'Precise nanometer localization analysis for individual fluorescent probes', *Biophysical Journal*. Elsevier, 82(5), pp. 2775–2783. doi: 10.1016/S0006-3495(02)75618-X.

Torbati, M., Lele, T. P. and Agrawal, A. (2016) 'Ultradonut topology of the nuclear envelope', *Proceedings of the National Academy of Sciences*, p. 201604777. doi: 10.1073/pnas.1604777113.

Turgay, Y. *et al.* (2017) 'The molecular architecture of lamins in somatic cells', *Nature*. Nature Publishing Group, 543(7644), pp. 261–264. doi: 10.1038/nature21382.

Vial, A. *et al.* (2021) 'Correlative AFM and fluorescence imaging demonstrate nanoscale membrane remodeling and ring-like and tubular structure formation by septins', *Nanoscale*. Royal Society of Chemistry, 13(29), pp. 12484–12493. doi: 10.1039/d1nr01978c.

Vietri, M. *et al.* (2015) 'Spastin and ESCRT-III coordinate mitotic spindle disassembly and nuclear envelope sealing', *Nature*, 522(7555), pp. 231–235. doi: 10.1038/nature14408.

Vollmer, B. *et al.* (2012) 'Dimerization and direct membrane interaction of Nup53 contribute to nuclear pore complex assembly', *The EMBO Journal*, 31(20), pp. 4072–4084. doi: 10.1038/emboj.2012.256.

Vollmer, B., Lorenz, M., Moreno-Andrés, D., Bodenhöfer, M., De Magistris, P., *et al.* (2015) 'Nup153 Recruits the Nup107-160 Complex to the Inner Nuclear Membrane for Interphasic Nuclear Pore Complex Assembly', *Developmental Cell*, pp. 1–12. doi: 10.1016/j.devcel.2015.04.027.

Vollmer, B., Lorenz, M., Moreno-Andrés, D., Bodenhöfer, M., De Magistris, P., *et al.* (2015) 'Nup153 Recruits the Nup107-160 Complex to the Inner Nuclear Membrane for Interphasic Nuclear Pore Complex Assembly', *Developmental Cell*, 33(6), pp. 717–728. doi: 10.1016/j.devcel.2015.04.027.

Walther, T. C. *et al.* (2001) 'The nucleoporin Nup153 is required for nuclear pore basket formation, nuclear pore complex anchoring and import of a subset of nuclear proteins', *EMBO Journal*, 20(20), pp. 5703–5714. doi: 10.1093/emboj/20.20.5703.

Walther, T. C. *et al.* (2003) 'The conserved Nup107-160 complex is critical for nuclear pore complex assembly', *Cell*, 113(2), pp. 195–206. doi: 10.1016/S0092-8674(03)00235-6.

Watson, M. L. (1959) 'Further Observations on the Nuclear Envelope of the Animal Cell', *The Journal of Biophysical and Biochemical Cytology*, 6(2), pp. 147–156. doi: 10.1083/jcb.6.2.147.

Wei, F. *et al.* (2016) 'Poroelasticity of cell nuclei revealed through atomic force microscopy characterization', 213701. doi: 10.1063/1.4968191.

Wente, S. R. (2000) ‘Gatekeepers of the Nucleus’, *Science*, 288(5470), pp. 1374–1377. doi: 10.1126/science.288.5470.1374.

Wente, S. R. and Rout, M. P. (2010) ‘The nuclear pore complex and nuclear transport.’, *Cold Spring Harbor perspectives in biology*, pp. 1–20. doi: 10.1101/cshperspect.a000562.

Winey, M. *et al.* (1997) ‘Nuclear pore complex number and distribution throughout the Saccharomyces cerevisiae cell cycle by three-dimensional reconstruction from electron micrographs of nuclear envelopes’, *Molecular Biology of the Cell*, 8(11), pp. 2119–2132. doi: 10.1091/mbc.8.11.2119.

Xie, W. *et al.* (2016) ‘A-type Lamins Form Distinct Filamentous Networks with Differential Nuclear Pore Complex Associations’, *Current Biology*. Elsevier Ltd., 26(19), pp. 2651–2658. doi: 10.1016/j.cub.2016.07.049.

Yavuz, S. *et al.* (2010) ‘NLS-mediated NPC functions of the nucleoporin Pom121’, *FEBS Letters*. Federation of European Biochemical Societies, 584(15), pp. 3292–3298. doi: 10.1016/j.febslet.2010.07.008.

Zhang, Y. *et al.* (2020) ‘Molecular architecture of the luminal ring of the Xenopus laevis nuclear pore complex’, *Cell Research*, 30(6), pp. 532–540. doi: 10.1038/s41422-020-0320-y.

Zimmerli, C. E. *et al.* (2020) ‘Nuclear depletion pores constrict upon energy’, (1495).

Zuccolo, M. *et al.* (2007) ‘The human Nup107-160 nuclear pore subcomplex contributes to proper kinetochore functions’, *EMBO Journal*, 26(7), pp. 1853–1864. doi: 10.1038/sj.emboj.7601642.